SEARCH FOR SUPERSYMMETRY USING MULTILEPTONIC SIGNATURES IN PROTON-PROTON COLLISIONS WITH THE CMS DETECTOR AT THE LHC

Zur Erlangung des akademischen Grades eines
DOKTORS DER NATURWISSENSCHAFTEN
an der Fakultät für Physik des
Karlsruher Instituts für Technologie (KIT)
Helmholtz-Gemeinschaft

genehmigte

DISSERTATION

von

Dipl.-Phys. Daniel Cedric Tröndle

aus Achern

Tag der mündlichen Prüfung: 04.05.2012

Referent: Prof. Dr. W. de Boer
Institut für Experimentelle Kernphysik

Korreferent: Prof. Dr. G. Quast
Institut für Experimentelle Kernphysik

Je planmäßiger die Menschen vorgehen, desto wirksamer vermag sie der Zufall treffen.

Friedrich Dürrenmatt

Contents

1 Introduction **1**

2 The Standard Model of Particle Physics **5**
2.1 Introduction . . . 5
2.2 Lagrange Formalism . . . 7
2.3 Local Gauge Invariance . . . 8
2.4 The Standard Model Lagrangian . . . 10
2.5 Frontiers of the Standard Model . . . 14
2.6 Recent CMS Measurements . . . 15

3 Supersymmetry **19**
3.1 Introduction - Supersymmetry . . . 19
3.2 Particle Spectrum of the MSSM . . . 20
3.3 Supersymmetric Lagrangian . . . 21
3.4 SUSY Mass Spectrum . . . 24
3.5 Constraints on cMSSM . . . 28

4 The CMS Experiment at the Large Hadron Collider **33**
4.1 The Large Hadron Collider . . . 34
4.2 The Compact Muon Solenoid . . . 35
4.2.1 The Coordinate System . . . 36
4.2.2 Inner Tracking System . . . 36
4.2.3 Electromagnetic Calorimeter . . . 37
4.2.4 Hadron Calorimeter . . . 39
4.2.5 Magnet . . . 40
4.2.6 Muon System . . . 40
4.3 Trigger and Data Acquisition System . . . 41

5 Software Tools and Event Reconstruction **51**
5.1 CMSSW: CMS Software Framework . . . 51
5.2 Monte Carlo Event Generation . . . 52
5.3 Detector Simulation . . . 53
5.4 Event Reconstruction . . . 53
5.4.1 Track Reconstruction . . . 54
5.4.2 Vertex Reconstruction . . . 55
5.4.3 Electron and Photon Reconstruction . . . 55
5.4.4 Muon Reconstruction . . . 57
5.4.5 Tauon Reconstruction . . . 58
5.4.6 Jet Reconstruction . . . 60
5.4.7 Missing transverse Energy Reconstruction . . . 61
5.5 CMS Computing Model . . . 62
5.6 Statistical Procedure . . . 66

6 Search for Supersymmetry **69**
6.1 Multilepton Production in SUSY Models . . . 70
6.2 Standard Model Backgrounds . . . 80

7 Prerequisites **85**
7.1 Data and MC Samples . . . 85
7.2 Pile Up Events . . . 86
7.3 Object Definition and Selection . . . 88
7.3.1 Lepton Selection Efficiency . . . 91
7.4 Trigger Selection and Efficiency . . . 95
7.5 Event Selection . . . 98

8 SM Background Prediction **103**
8.1 Dilepton - Data Driven Fake Background Calibration . . . 104
8.1.1 Drell-Yan . . . 105
8.1.2 $t\bar{t}$ . . . 111
8.1.3 $WW \rightarrow l\nu l\nu$ . . . 118
8.1.4 Systematic Uncertainties & Summary . . . 120
8.2 Initial/Final State Radiation . . . 123
8.3 Prompt Lepton Background . . . 129
8.3.1 WZ/γ^* . . . 129
8.3.2 $ZZ, Z\gamma*, \gamma*\gamma*$ . . . 131
8.4 Summary . . . 134

9 Results **139**
9.1 Systematic Uncertainties . . . 146
9.2 Interpretation of the Results . . . 149
9.2.1 cMSSM ($tan\beta = 10$) . . . 149

9.2.2 cMSSM ($tan\beta = 40$) 151
9.2.3 Simplified Model Spectra (SMS) 157

10 Conclusion **163**

Appendices **165**

A DATA and MC Samples **167**

B Private Madgraph Production **169**
B.1 $ZZ + 0, 1, 2$ Jets including $\gamma*$ and Internal Photon Conversions 169

C Trigger Efficiency **177**

D Vertex Reweighting **185**

E Detailed Result Tables **187**

F cMSSM $tan\beta = 10$: Selection Efficiencies **201**

G cMSSM $tan\beta = 40$: Selection Efficiencies **209**

H Event Displays **217**

Bibliography **220**

CHAPTER 1

Introduction

High energy particle physics studies the smallest objects and their interactions as summarized in the so-called Standard Model (SM) which was developed over the last decades. The SM is one of the most scrutinized theories ever written down. It describes a large variety of phenomena seen in nature and is incredible successful in describing all known interactions tested at particle physics experiments with an amazing precision. All particles proposed by the theory were discovered so far, except the Higgs boson, a scalar neutral particle, which is predicted to be responsible for the masses of the elementary particles. Recent measurements published by the two experiments CMS and ATLAS at the LHC might have shown first hints for a Higgs boson with a mass around 125 GeV [1, 2]. But even in case of a discovery of the Higgs boson in the near future, the SM is far from being complete.

There are a few aspects indicating new physics beyond the Standard Model. Impressive astrophysical measurements of the matter composition in the universe have shown, that around 80% of the matter in the universe consists of a new kind of weakly interacting massive particles (WIMP) forming the so called cold dark matter [3]. The SM has no suitable candidate with the right properties to account for this massive abundance of matter.

Another frontier of the SM is the so called Higgs fine tuning problem, where the self-energy correction of the fermions to the Higgs field are orders of magnitude larger than the electroweak breaking scale, if one assumes the SM to be valid to a much larger scale [4]. An unwanted high precision fine tuning is needed to avoid the Higgs mass to blow up, which is a thorn in many physicists flesh.

A solution to these and several other problems of the SM can be achieved by an extension of the theory called Supersymmetry (SUSY). SUSY is a new symmetry between bosons and fermions, which immediately solves various problems. For each Standard Model particle with spin $s = j$ a new particle has to be introduced with spin $s' = j \pm 1/2$. Since none of these new particles were observed so far the symmetry must be a broken symmetry increasing the SUSY masses compared to their SM partners. SUSY models solves the fine tuning problem in an elegant way, because opposite sign amplitudes for bosons and fermions in the Higgs self energy corrections cancel each other [5]. Assuming the lightest supersymmetric particle (LSP) to be stable, it has all the properties expected for the dark

matter in the universe. In many supersymmetric models not only the LSP is introduced, but also the LSP annihilation cross section is predicted to be in agreement with calculations of the required WIMP annihilation cross section to form the measured relic density in our universe. This remarkable coincidence is often called the "WIMP Miracle" [6]. Furthermore if one introduces SUSY particles in the calculations of the running coupling of the strong and weak interactions, a unification of all three forces can be achieved at a scale around 10^{16} GeV [7].

With the start of the Large Hadron Collider (LHC) at CERN (Conseil Européan pour la Recherche Nucléaire) near Geneva Switzerland in 2009 offers a perfect tool for physicists around the world to jump into a new energy regime and hopefully answer many open questions. The LHC is a proton proton collider with a circumference of 27 km accelerating counter rotating proton beams up to 3.5 TeV. Two large general purpose detectors, CMS and ATLAS, are installed at different interaction points with the main purpose to discover the Higgs boson and observe hints for, and finally also discover, new physics beyond the SM, especially SUSY.

The SUSY particle production cross section is tiny, compared to the total SM background production rate. Thus the challenge of searches for SUSY extensions is to distinguish the rare SUSY events on top of a huge background. This can be achieved in multileptonic signatures, namely final states with at least three leptons including electrons, muons and taus. Those signatures are often referred as the "Golden Channel" since its is a clean signature, clean in the sense that SM processes with three prompt leptons are rare, whereas it can be enhanced in many SUSY models.

In SUSY models isolated leptons are produced dominantly in the leptonic decay of the next to lightest neutralino ($\tilde{\chi}_2^0 \rightarrow ll\tilde{\chi}_1^0$) and the lightest chargino ($\tilde{\chi}_1^{\pm} \rightarrow l\nu\tilde{\chi}_1^0$). The simultaneous production of neutralinos and charginos with the subsequent decay to leptons leads to multileptonic signatures, whereas in the Standard Model prompt leptons results from boson decays ($W^{\pm}$, $Z/\gamma*$) including top quark decays $t \rightarrow Wb$. The dominant irreducible background with three/four prompt leptons is formed by the double boson production ($W^{\pm}Z$, ZZ). An additional dangerous background consists of dileptonic SM processes like Drell-Yan or $t\bar{t}$ with the subsequent decay to leptons accompanied by so called fake leptons mimicking a multileptonic signature. Fake leptons are mainly leptons from heavy flavor decays in jets and false identification as prompt leptons.

The search for supersymmetric models in trilepton signatures were studied in former experiments at the Tevatron proton anti-proton collider situated at Fermilab near Chicago USA [8–11]. The study presented in this thesis was published the for first time in 2099 with the first recorded data $\mathcal{L} = 35\,\text{pb}^{-1}$ [12–14] and substantially extended the excluded parameter space from the Tevatron data. The analysis improved through the second year of data taking. Preliminary results were published in Summer 2011 corresponding to an integrated luminosity $\mathcal{L} = 2.1\,\text{fb}^{-1}$ [15]. Further improvements with the full data set of 2011 corresponding to an integrated luminosity of $\mathcal{L} = 4.7\,\text{fb}^{-1}$ are presented in this thesis.

The thesis is organized as follows: In Chapter 2 the Standard Model of particle physics is reviewed and in Chapter 3 the theoretical framework of SUSY is discussed. The LHC and the CMS experiment are presented in Chapter 4. Software tools used for reconstruction of physics objects embedded in the CMS software framework are discussed in Chapter 5. The analysis is described in the Chapters 6-9. First SUSY multileptonic production mechanisms and properties and expected SM background processes are discussed in Chapter 6. Some prerequisites are reported in Chapter 7 and followed by

the SM background predictions in Chapter 8. The results and SUSY interpretations are discussed in Chapter 9. A conclusion is given in Chapter 10.

CHAPTER 2

The Standard Model of Particle Physics

The Standard Model (SM) of elementary particle physics is one of the most scrutinized theories ever written down in modern physics. It describes the world around us with an impressive precision and is continuously being tested and confirmed by a long list of experiments. Three of the four known forces - electromagnetic, weak and strong interaction - and as well the elementary particles and their properties are included in a mathematically consistent and beautiful framework, beautiful in the sense that the SM is a theory based on fundamental symmetries. However, even today not all phenomena seen in nature can be explained by the SM. The most stringent issues are the masses of the gauge bosons, which cannot be explained without an ad hoc mechanism including a new scalar boson. Also the unification of the electromagnetic and weak force into the so called electroweak theory was an incredible achievement, but the unification of all three forces is not possible without certain theoretical extensions to the SM. There are more issues which will be discussed after a short introduction to the Standard Model.

2.1 Introduction

The basic constituents of all matter in our universe, as well as their fundamental ineractions can be described by a set of particles called fermions with a half integer spin forming the matter constituents and four different forces: gravitation, electromagnetism, weak and strong interactions distinguished by their strength, range and type. The SM combines the fermions and three of the four forces (w/o gravitation) in a widely accepted theory. Within the theory the interactions are mediated via so called bosons, i.e. particles with an integer spin. Table 2.1 summarizes all SM fermions and bosons with their corresponding quantum numbers: electric charge Q , hypercharge Y and the third component of the weak isospoin I_3.
The fermions are ordered in two groups: leptons and quarks. Both groups appear in three generations, where particles within the different generations have the same quantum numbers, except their masses, e.g. the lefthanded up-type quarks u_L, c_L and t_L have the same electric charge $Q = 2/3$, hypercharge

Table 2.1: Particle spectrum of the Standard Model. The quantum numbers electric charge Q, hypercharge Y and the third component of the weak isospin I_3 are given.

Fermions Spin = 1/2						
	1. Gen.	2. Gen.	3. Gen.	Q	Y	I_3
Quarks	$\begin{pmatrix} u \\ d \end{pmatrix}_L$	$\begin{pmatrix} c \\ s \end{pmatrix}_L$	$\begin{pmatrix} t \\ b \end{pmatrix}_L$	$2/3$ $-1/3$	$1/3$	$1/2$ $-1/2$
	u_R	c_R	t_R	$2/3$	$4/3$	0
	d_R	s_R	b_R	$-1/3$	$-2/3$	0
Leptons	$\begin{pmatrix} \nu_e \\ e \end{pmatrix}_L$	$\begin{pmatrix} \nu_\mu \\ \mu \end{pmatrix}_L$	$\begin{pmatrix} \nu_\tau \\ \tau \end{pmatrix}_L$	0 -1	-1	$1/2$ $-1/2$
	e_R	μ_R	τ_R	-1	-2	0

Bosons Spin = 1				
Interaction	Boson	Q	Y	I_3
Electromagnetic	γ	0	0	0
Weak	Z^0	0	0	0
	$W^\pm$	± 1	0	± 1
Strong	$g_1 \cdots g_8$	0	0	0

$Y = 1/3$ and the third component of the weak isospin $I_3 = 1/2$ with masses $m_u = 1.7 - 3.3\,\text{MeV}$, $m_c = 1.27^{+0.07}_{-0.09}\,\text{GeV}$ and $m_t = 172 \pm 0.9 \pm 1.3\,\text{GeV}$ respectively [16]. For each fermion there exists also an anti-particle with same mass, but opposite quantum numbers, e.g. $Q_u = 2/3$ and $Q_{\bar{u}} = -2/3$. The mediator of the electromagnetic interaction is the photon γ, which couples to the electric charge of the particles, whereas the weak interactions is described by the exchange of the $W^\pm$ and Z bosons. The $W^\pm$ bosons couples to the weak isospin and hence it couples with the same strength to quarks and leptons. On the other hand the Z boson couples to the isospin and the electric charge as well.
The lefthanded quarks of a doublet of weak interaction eigentstates denoted as d', s' and b' do not correspond to the mass eigenstates but rather to a linear combination of theses mass eigenstates d, s and b. Hence there are rare transitions between doublets of different generations. The 3×3 matrix describing the connection between both representations is the *Cabbibo-Kobayashi-Maskawa* (CKM) matrix

$$\begin{pmatrix} d' \\ s' \\ b' \end{pmatrix} = \begin{pmatrix} V_{ud} & V_{us} & V_{ub} \\ V_{cd} & V_{cs} & V_{cb} \\ V_{td} & V_{ts} & V_{tb} \end{pmatrix} \begin{pmatrix} d \\ s \\ b \end{pmatrix} , \tag{2.1}$$

where the V_{ij} element specifies the coupling of one quark flavor i to another j [17].

Quarks are the only fermions underlying the strong interaction with its mediators, called gluons, which couples to the so called color charge of particles. Baryons and mesons are composite particles made of two or three quarks. The existence of the Ω^- particle [18], a meson which consists of three s quarks with a total spin $s = 3/2$, required a new degree of freedom. Due to Pauli's principle particles with half integer spin quantum number follow the fermi statistics and hence the wavefunction should be anti-symmetric under permutation of the composite partons. This discrepancy could be solved by introducing a new quantum number *color* with three different values *red*, *green* and *blue* and the opposite colors *anti-red/green/blue* as well. A combination of all three colors or anti-color leads to $white$ referring to optics. The invariance of the theory under rotation in the color space yields finally eight gluons, where the nineth is a color singlet and non-relevant for the interactions.

2.2 Lagrange Formalism

The Lagrange formalism in classical mechanics is a complementary descriptions of Newton's second law introduced by Joseph Louis Lagrange in 1788, where the Lagrangian L is given by

$$L = T - V \tag{2.2}$$

with $T = \frac{1}{2}\mathrm{mv}^2$ the kinetic energy of a particle in a scalar potential V, where T and V are functions of the generalized space coordinates q_i and their derivatives $\dot{q}_i$. In a relativistic field theory it is conventional to use instead of L the Lagrange density $\mathcal{L}$ in order to describe the field as function of space and time, hence the Lagrange density is a function of the field ϕ_i itself and its covariant derivatives $\partial_\mu \phi_i = \partial \phi_i / \partial x^\mu$ with the space time coordinates x^μ.
The equations of motions of a desired Lagrange density can be derived from the generalized Euler-Lagrange equations

$$\frac{d}{dt}\left(\frac{\mathcal{L}}{\partial(\partial_\mu \phi_i)}\right) = \frac{\mathcal{L}}{\partial \phi_i} \quad , \; i = 1, 2, 3.. \, . \tag{2.3}$$

In the following *Lagrangian* will be used instead of *Lagrange density* for simplicity.
In high energy physics its all about the determination of the Lagrangian $\mathcal{L}$. If the Lagrangian is known the equations of motion can be determined and predictions can be tested in experiments. The general model building, i.e. the construction of the Lagrangian is based on three axioms:

1. Gauge Symmetry,

2. (Irreducible) Representations of fermions and scalars, i.e. the field content,

3. Spontaneous symmetry breaking (SSB),

where $\mathcal{L}$ is the most general and renormalizable Lagrangian. The next sections will review the given axioms followed by the corresponding Standard Model Lagrangian.

2.3 Local Gauge Invariance

Symmetries play a crucial role in quantum field theory. Emmy Noether showed in 1918 that a group of transformations on fields ϕ, where the corresponding Lagrangian is invariant under this transformations, yields one or more conserved quantities. This implies that symmetries imply conservation laws. The theory of Quantum Electrodynamics (QED) showed impressively that local gauge symmetry under the desired symmetry groups U(1) gives also the correct interaction terms in the Lagrangian of QED and similar principles have been successfully applied in electroweak and strong interactions. Local gauge symmetries are groups of transformations with space time dependent phases $\alpha_a = \alpha_a(x)$. A general transformation $SU(N)$, where N is an array of $N \times N$ matrices with determinant 1, are given by

$$\psi \to \psi'(x) = e^{i\alpha_a(x)T_a}\psi(x) \,, \tag{2.4}$$

where T_a are the generators of the group $SU(N)$ and underly the corresponding group algebra

$$[T^a, T^b] = if^{abc}T^c \,, \tag{2.5}$$

with f^{abc} the structure constants. If the commutator vanishes, e.g. $f^{abc} = 0$, the underlying group is called *abelian*.

Local gauge Invariance of Abelian Groups

The effect of the local gauge invariance of abelian groups will be illustrated for the QED. Free massive fermions with spin $s = 1/2$ can be described by the Lagrangian

$$\mathcal{L} = i\bar{\psi}\gamma^\mu\partial_\mu\psi - m\bar{\psi}\psi \,, \tag{2.6}$$

with the dirac γ-matrices, ψ a four component dirac spinor and $\bar{\psi} = \psi^\dagger\gamma^0$. The first part corresponds to a kinetic term and the second is the mass term. As an example one can consider a simple transformation of the U(1) group , also known as the circle group, due to the fact that U(1) is the multiplicative group of all complex numbers with absolute value 1. A transformation of the dirac spinor ψ under U(1) can be written as

$$\psi \to \psi'(x) = e^{i\alpha(x)}\psi(x) \,. \tag{2.7}$$

Considering an electron field the transformation can be interpreted as a simple transformation of the local phase angle by $\alpha(x)$. Since the derivative term applied acting on the phase $\alpha(x)$ does not vanish, because

$$\begin{aligned}\mathcal{L}' &= i\bar{\psi}'\gamma^\mu\partial_\mu\psi' - m\bar{\psi}'\psi' \\ &= \mathcal{L} - \underbrace{\bar{\psi}\gamma^\mu(\partial_\mu\alpha(x))\psi}_{\neq 0} \,,\end{aligned}$$

i.e. the Lagrangian considered for free massive fermions is not invariant under this transformation, because $\mathcal{L}'$ differs from $\mathcal{L}$. The invariance can be achieved by introducing a new gauge field $A_\mu(x)$, referring to classical electromagnetism, which transforms under U(1) like

$$A_\mu(x) \to A'_\mu(x) = A_\mu(x) - \frac{1}{e}\partial_\mu \alpha(x) \tag{2.8}$$

and replacing the derivative ∂_μ by the so called covariant derivative D_μ

$$\partial_\mu \to D_\mu = \partial_\mu + ieA_\mu \,, \tag{2.9}$$

which finally leads to a Lagrangian invariant under a local phase transformations

$$\mathcal{L} = i\bar{\psi}\gamma^\mu D_\mu \psi - m\bar{\psi}\psi = i\bar{\psi}\gamma^\mu \partial_\mu \psi - e\bar{\psi}\gamma^\mu A_\mu \psi - m\bar{\psi}\psi \,. \tag{2.10}$$

The terms $i\bar{\psi}\gamma^\mu\partial_\mu\psi$ and $m\bar{\psi}\psi$ describe a free massive fermion as introduced in Eq. 2.6 and the term $e\bar{\psi}\gamma^\mu A_\mu\psi$ corresponds to a coupling of the fermions to a new gauge field A_μ. Adding an additional kinetic term for the massless A_μ with spin $s = 1$ yields the complete QED Lagrangian, which describes electron/positron interactions with photons (A_μ).

$$\mathcal{L}_{\text{QED}} = i\bar{\psi}\gamma^\mu\partial_\mu\psi - e\bar{\psi}\gamma^\mu A_\mu\psi - m\bar{\psi}\psi + \frac{1}{4}F_{\mu\nu}F^{\mu\nu} \tag{2.11}$$

with $F^{\mu\nu} = \partial^\mu A^\nu - \partial^\nu A^\mu$ is the field strength tensor. The introduced new gauge field has to be massless because adding a mass term of the form $1/2mA^\mu A_\mu$ for spin 1 particles is not invariant under an U(1) transformation, since

$$A^\mu A_\mu \to A'^\mu A'_\mu = A^\mu A_\mu - \underbrace{\frac{1}{e}A^\mu\partial_\mu\alpha(x) - \frac{1}{e}(\partial^\mu\alpha(x))A_\mu - \frac{1}{e^2}(\partial^\mu\alpha(x))(\partial_\mu\alpha(x))}_{\neq 0}$$

is not invariance under a local phase transformation.
To summarize: for the example of QED it has been shown, that constructing a Lagrangian for fermions and photons (2. axiom: field content), which is invariant under an U(1) transformation (1. axiom: gauge invariance) yields a Lagrangian with the correct coupling to photons. The last axiom of the model building for the requirement of spontaneous symmetry breaking will be introduced in the context of the electroweak theory.

Local Gauge Invariance of Non-Abelian Groups

The gauge invariance principle applied in QED for constructing a quantum field theory of interacting fields on basis of fundamental symmetries was further investigated and applied to the weak and strong interactions. As an example of Non-Abelian symmetries the three dimensional rotation group SU(2) will be shortly discussed, where the impact of gauge invariance under a transformation of the SU(2) group was evaluated by Yang and Mills [19] with respect to an isospin rotation of the proton-neutron doublet. The SU(2) group consists of 2×2 unitary matrices which can be written as

$$U = e^{-i\alpha_a \frac{\sigma_a}{2}} \tag{2.12}$$

with σ_a the generators of the group for which the components are the Pauli matrices

$$\sigma_1 = \begin{pmatrix} 0 & 1 \\ 1 & 0 \end{pmatrix} \quad \sigma_2 = \begin{pmatrix} 0 & -i \\ i & 0 \end{pmatrix} \quad \sigma_3 = \begin{pmatrix} 1 & 0 \\ 0 & -1 \end{pmatrix} \,. \tag{2.13}$$

The SU(2) has three degrees of freedom given four real numbers (2×2 matrices) and one constraint (det(U)=1). Following the same procedure used for the U(1) group applied to the QED Lagrangian, one will encounter additional complication, due to three orthogonal symmetry motions, which do not commute. The covariant derivative can be written as [20]:

$$D^{\mu} = \partial^{\mu} + igA^{\mu}_{a}\frac{\sigma^{a}}{2} \,. \tag{2.14}$$

For each of the group generator σ^a a new vector field A^a_μ is required which finally leads to a Lagrangian of fermions interacting with three massless vector gauge fields

$$\mathcal{L} = i\bar{\psi}\gamma^{\mu}D_{\mu}\psi - m\bar{\psi}\psi - \frac{1}{4}(F^{i}_{\mu\nu})^{2} \tag{2.15}$$

where $F^i_{\mu\nu} = \partial_\nu A^i_\nu - \partial_\nu A^i_\mu + g\epsilon^{ijk}A^j_\mu A^k_\nu$ is the field strength tensor. The structure of this Lagrangian is quite similar to the QED Lagrangian, but it contains also cubic and quartic terms in A^i_μ which result in interactions between the vector gauge fields and depends on two parameters: the fermion mass parameter m and the coupling constant g. This famous Lagrangian is commonly quoted as *Yang-Mills Lagrangian*.

2.4 The Standard Model Lagrangian

After reviewing the prerequisites of local gauge symmetry the standard model Lagrangian and its components will be discussed in the following section. Glashow, Weinberg and Salam were able to unify the electromagnetic and weak interactions in the so called GSW-model [21–23]. The natural follow-up question is the question of the possibility of the unification of strong and electroweak interaction. Wihin the SM this is not possile. Starting with a short discussion of the strong interaction with its underlying symmetry property the electroweak interaction will be discussed, where the principle of spontaneous symmetry breaking has to be introduced in order to describe the measured masses of the weak vector gauge bosons.

Strong Interaction

The concept of the strong interaction was introduced due to the fact of stable nuclei in spite of repulsive electromagnetic forces and the existence of the Ω^- [18]. A particle consisting of three similar quarks (sss) with parallel spins. A new quantum number called color with its colors (red, blue green) had to be introduced in order to preserve the Pauli principle. Referring to optics the theory of strong interaction is called *Quantum Chromo Dynamics* (QCD). The first full formulation of the theory was evaluated in 1973 by Fritzsch, Gross, Wilczek and Weinberg [24–26]. The symmetry group $SU(3)_C$ consisting of 3×3 matrices describes the quark sector. Analogous considerations as for the SU(2) discussed before can be applied here. A symmetry transformation of the $SU(3)_C$ group can be expressed as:

$$U = e^{-i\alpha_a T^a} \,, \tag{2.16}$$

with the generators of the group $T^a = \frac{\lambda^a}{2}$, where λ^a are the Gell-Mann matrices. Introducing the covariant derivative

$$D^\mu = \partial^\mu + i g_s G_a^\mu T^a \,, \tag{2.17}$$

where G_a^μ are the gluon fields and g_s is the gauge coupling. Adding a gauge invariant term representing the dynamics of the gluon fields yields finally the QCD Lagrangian[1]

$$\mathcal{L}_{QCD} = \frac{1}{4} F^a_{\mu\nu} F^{a\,\mu\nu} + \bar{q}_j [(i\gamma^\mu \partial_\mu - m)\delta_{jk} - g_s \gamma^\mu G_{\mu a} T^a_{jk}] q_k \,, \tag{2.18}$$

with $F^a_{\mu\nu} = \partial_\nu A^a_\nu - \partial_\nu A^a_\mu + g_s f^{abc} A^a_\mu A^b_\nu$ and q are the quark fields. Cubic and quartic terms in A_μ results in gluon self couplings. A more detailed evaluation of the QCD Lagrangian can be found elsewhere [20, 27].

Electroweak Interaction

The transition of quarks and leptons is mediated via the weak interaction. Experiments have shown that leptons are ordered in doublets of left-handed and singlets of right-handed leptons (Table 2.1). Same applies for quarks as well. A new spin quantity I referred as the weak isospin was introduced. The weak interaction violates the parity first observed in the beta decay of cobalt 60 [28], where the violation was realized in the way, that only left-handed electrons and right-handed anti-neutrinos were produced.
Glashow, Weinberg and Salam unified the electromagnetic and weak interaction within the GSW-model into the so called *electroweak* interaction. The symmetry group of the electroweak interaction is the

$$SU(2)_L \otimes U(1)_Y \,, \tag{2.19}$$

where Y is the generator of the U(1) symmetry group and is called hypercharge. A local phase transformation of such combined group can be written as

$$\begin{aligned} \psi_L \to \psi'_L &= \psi_L e^{-i\alpha_a T^a} e^{-i\alpha} \\ \psi_R \to \psi'_R &= \psi_R e^{-i\alpha} \end{aligned}$$

with $\psi_{L/R}$ corresponds to the left/right-handed fermion fields and T^a the generators of the $SU(2)_L$ and Y of the $U(1)_Y$, respectivly. We saw before, that the generator $U(1)_{EM}$ of QED was the electric charge, which is related to the hypercharge Y by the identity

$$Q = \frac{Y}{2} + I_3 \,, \tag{2.20}$$

where I_3 is the third component of the weak isospin. In total three vector gauge fields W^i_μ acting on left-handed fermions and one scalar field B acting also on right-handed fields are required. Introducing the covariant derivative

$$\partial_\mu \to D_\mu = \partial_\mu + i\frac{g}{2} W_{\mu i} \sigma^i + i\frac{g'}{2} B^0_\mu Y \tag{2.21}$$

[1] There is an additional freedom in choosing the quantization of the eight gluon fields which leads to so called ghost fields. These ghost fields can be removed by a certain choice of gauge, thus they can be ignored in the calculations.

where σ^u are the Pauli matrices and $g(g')$ are the corresponding couplings, which leads finally to a local gauge invariant Lagrangian for the electroweak theory

$$\begin{aligned}\mathcal{L}_{EW} =& i\bar{\psi}\gamma^\mu\partial_\mu\psi - \frac{1}{4}W^i_{\mu\nu}W_i^{\mu\nu} - \frac{1}{4}B_{\mu\nu}B^{\mu\nu} \\ & - \frac{g}{2}\bar{\psi}\gamma^\mu\sigma^i W_{\mu i}\psi - \frac{g'}{2}\bar{\psi}\gamma^\mu B_\mu\psi \qquad (2.22)\end{aligned}$$

$$(2.23)$$

with $W^i_{\mu\nu} = \partial_\nu W^i_\mu - \partial_\mu W^i_\nu + g\epsilon^{ijk}W^j_\mu W^k_\nu$ and $B_{\mu\nu} = \partial_\nu B_\mu - \partial_\mu B_\nu$. The actual gauge bosons $W^\pm$, Z^0 and A_μ are linear combinations of the four gauge fields W^i_μ and the B^0:

$$\begin{aligned}W^\pm &= \frac{1}{\sqrt{2}}(W^1 \mp iW^2) \\ Z^0 &= -sin(\theta_W)B^0 + cos(\theta_W)W^3 \\ A_\mu &= cos(\theta_W)B^0 + sin(\theta_W)W^3\end{aligned}$$

with the Weinberg angle θ_W measured to be [16]

$$sin^2(\theta_W) \approx 0.232\ . \qquad (2.24)$$

In summary requiring a Lagrangian invariant under local gauge transformation of the unified electromagnetic and weak interaction into a combined $SU(2)_L \otimes U(1)_Y$ symmetry group introduces the four gauge bosons $W^\pm_\mu$, Z^0 and A_μ. However since mass terms for the gauge bosons would spoil the gauge invariance, the observation of massive $W^\pm$ and Z^0 is in contradiction to the theory.

Spontaneous Symmetry Breaking and the Higgs Mechanism

The dilemma of the electroweak theory predicting massless gauge bosons is resolved using the principle of spontaneous symmetry breaking proposed by Higgs, Brout, Guralnik Hagen, Englert and Kibble [29–31]. Spontaneous symmetry breaking is a principle formerly known from ferromagnetism in solid state physics. Bosons and fermions get their masses by coupling to the *Higgs* field. The Higgs field is a complex scalar $SU(2)$ doublet carrying weak hypercharge $Y = 1$ consisting of a charged and neutral part

$$\Phi = \begin{pmatrix}\Phi^+ \\ \Phi^0\end{pmatrix} = \begin{pmatrix}\Phi_1 + i\Phi_2 \\ \Phi_3 + i\Phi_4\end{pmatrix} \qquad (2.25)$$

described by the Lagrangian

$$\mathcal{L}_{Higgs} = (D^\mu\Phi)^\dagger(D_\mu\Phi) - V(\Phi) \qquad (2.26)$$

where $D_\mu = \partial_\mu + i\frac{g}{2}W_{\mu i}\sigma^i + \frac{g'}{2}B^0_\mu Y$ is the covariant derivative and $V(\Phi)$ is the Higgs potential given in the most general renormalizable and $SU(2)_L$ invariant form by

$$V(\Phi) = \mu^2|\Phi^\dagger\Phi| + \lambda(|\Phi^\dagger\Phi|)^2 \qquad (2.27)$$

with a positive and real parameter λ. The shape of the potential is shown in Fig. 2.1 for $\mu^2 < 0$ (right panel) and $\mu^2 > 0$ (left panel). In case of $\mu^2 > 0$ the ground state of the Higgs field is at the

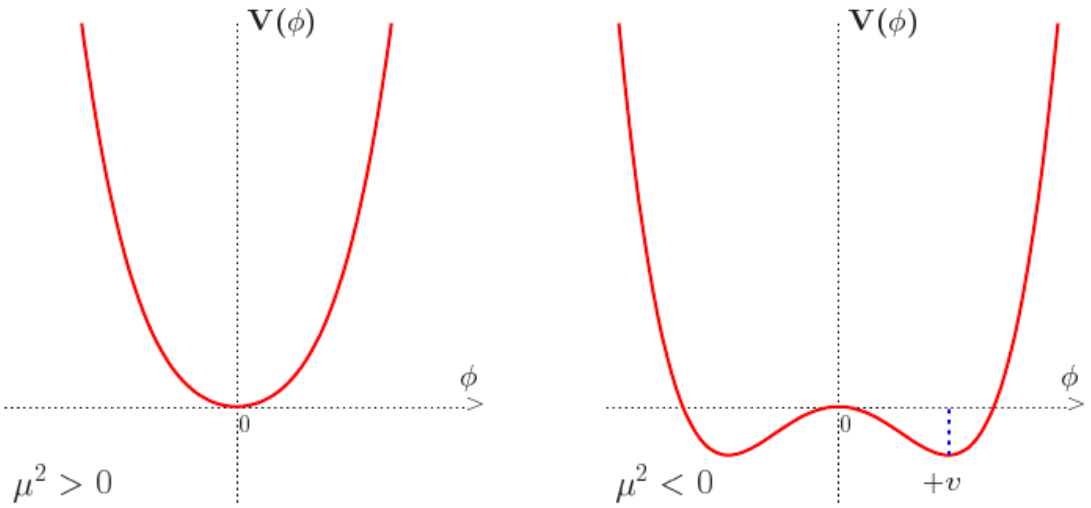

Figure 2.1: The Higgs potential for $\lambda > 0$ and $\mu^2 > 0$ (left) and $\mu^2 < 0$ (right). Picture is taken from [32].

minimum of the potential, here chosen to be $\Phi = 0$, and thus the vacuum expectation value vanishes $|\langle 0|\Phi|0\rangle| = 0$. More interesting is the case of $\mu^2 < 0$. For $\mu^2 < 0$ the vacuum expectations values are non zero:

$$|\langle 0|\Phi|0\rangle| = \sqrt{\frac{-\mu^2}{2\lambda}} = \frac{v}{\sqrt{2}} \,. \tag{2.28}$$

The ground state with its vacuum expectation value can be obtained by different field configurations (Φ^+,Φ^0). Hence a transformation of the $SU(2)_L \otimes U(1)_Y$ symmetry group rotates one ground state into another, thus breaking the symmetry. Since the vacuum expectation value is not changed by this transformation of the ground state, the actual Lagrangian is still invariant. This mechanism is known as spontaneous symmetry breaking.
The ground state can be chosen to be neutral, e.g. $\Phi^+ = 0$, since the vacuum is known to be neutral.

$$\Phi_0 = \frac{1}{\sqrt{2}} \begin{pmatrix} 0 \\ v \end{pmatrix} \tag{2.29}$$

The scalar field can be written as

$$\Phi' = \frac{1}{\sqrt{2}} e^{i\chi^a \tau^a} \begin{pmatrix} 0 \\ v + h \end{pmatrix} \tag{2.30}$$

where χ^a are three massless *goldstone bosons*, which can be easily eliminated by a appropriate gauge transformation $\Phi \rightarrow e^{-i\chi^a \tau^a} \Phi'$, where Φ is the scalar field in the so called *unitary gauge*. Substituting Φ into the Lagrangian given in Eq. 2.26 and considering only the scalar kinetic energy term yields

$$(D^\mu \Phi)^\dagger (D_\mu \Phi) = \frac{1}{2} \left(0, v\right) \left(\frac{g}{2} \sigma^\mu W_\mu - \frac{g'}{2} B_\mu Y\right)^2 \begin{pmatrix} 0 \\ v \end{pmatrix} + \text{h-terms} \,. \tag{2.31}$$

Substitution with $W^{\pm} = \frac{1}{\sqrt{2}}(W^1 \mp iW^2)$, $Z^0 = -sin(\theta_W)B^0 + cos(\theta_W)W^3$ and $A_\mu = cos(\theta_W)B^0 + sin(\theta_W)W^3$ introduced in the context of the electroweak theory before results in masses of the physical gauge fields

$$\begin{aligned} M^2_{W^\pm} &= \frac{1}{4}g^2v^2 \\ M^2_Z &= \frac{1}{4}(g^2 + g'^2)v^2 \\ M_A &= 0\,. \end{aligned}$$

Since the massless photon couples with the electromagnetic strength e and the Weinberg-angle θ_W is related with the couplings g and g', the following relations can de derived:

$$\begin{aligned} e &= g\, sin(\theta_W) \\ e &= g'\, cos(\theta_W) \\ tan(\theta_W) &= \frac{g'}{g} \end{aligned}$$

and the connection between the Z and $W^\pm$ masses can be expressed by

$$cos(\theta_W) = \frac{M_{W^\pm}}{M_Z} \tag{2.32}$$

The introduction of fermions (quarks, leptons) interacting with the Higgs field and so getting their mass can be included in a similar fashion as above for the gauge bosons. A detailed description of these calculation can be found elsewhere [20]. In summary requiring local gauge invariance under a transformation of the $SU(2)_L \otimes U(1)_y$ and introducing a new scalar field in the context of the unified electroweak theory yields three massive ($W^\pm$,Z^0) and one massless gauge boson (A).

Standard Model Lagrangian

The Standard Model of particle physics is a gauge theory of the strong, weak and electromagnetic interactions with the symmetry group

$$SU(3)_C \otimes SU(2)_Y \otimes U(1)_Y \tag{2.33}$$

The corresponding Lagrangians can be factorized as:

$$\mathcal{L}_{SM} = \mathcal{L}_{SU(3)} + \mathcal{L}_{SU(2)\otimes U(1)_Y} \tag{2.34}$$

Putting the QCD Eq. 2.18, electroweak Eq. 2.22 and the Higgs Eq. 2.26 Lagrangian together yields the standard model Lagrangian:

$$\begin{aligned} \mathcal{L}_{SM} = &\sum_f i\bar{\Psi}_f\gamma^\mu D_\mu \Psi_f && \textit{fermion term} \\ &- \frac{1}{4}(B_{\mu\nu}B^{\mu\nu} + W^a_{\mu\nu}W^{\mu\nu}_a + G^b_{\mu\nu}G^{\mu\nu}_b) && \textit{gauge term} \\ &+ (D^\mu\Phi)^\dagger(D_\mu\Phi) - V(\Phi) && \textit{Higgs term} \\ &+ h^i_e\bar{L}^i\Phi e^i_R + h^{ij}_d\bar{Q}^i\Phi d^{ij}_R + h^{ij}_u\bar{Q}^i\Phi^C u^{ij}_R + h.c. && \textit{Yukawa term} \end{aligned} \tag{2.35}$$

with $D_\mu = \partial_\mu + i\frac{g}{2}W_{\mu a}\sigma^a + i\frac{g'}{2}B^0_\mu Y + i\frac{g_s}{2}G_{\mu b}\lambda^b$. The last and before not explicitly discussed *Yukawa term* of the SM Lagrangian describes interaction of fermions (quarks, leptons) with the Higgs fields, where h^{ij} are the yukawa couplings with the generation indicies i and j.

2.5 Frontiers of the Standard Model

The Standard Model describes nature with an incredible high precision down to at least 10^{-16} cm (electroweak scale $\sim$ 100 GeV) . However the standard model consists of at least 18 free parameters, which is seen to be just too much arbitrariness for a fundamental theory. There are other open questions in the SM, some of which are listed below:

- **Charge Quantization Problem**: Why do all particles have charges which are multiplets of e/3? The SM incorporates, but cannot explain this fact, which is of fundamental importance for the electrical neutrality of atoms.
- **Hierarchy Problem**: The hierarchy problem can be summarized with the question why the Higgs mass, which has to be in the same order as the vector gauge boson mass of the weak interaction, is small compared to the fundamental Planck mass $\sim 10^{19}$ GeV.
- **Fine tuning Problem**: Huge quantum corrections are expected to increase the Higgs mass to values many orders of magnitude higher than the electroweak scale, unless an incredible fine-tuning of parameters leads to cancellation of correction terms.
- **Gravitation Problem**: The theoretical consideration of the fourth force, namely the gravitation, is missing in the SM. Writing down a consitent quantum theory of gravity has not been realized so far. For energy regimes, which can be tested in modern high energy particle physics experiments, the gravitational contributions are negligible. At (much) higher energies it has to be taken into account into theoretical considerations.
- **Dark Matter Problem**: The SM provides no appropriate candidate for the so called *cold Dark Matter* in the universe, while it is known from cosmological observations that the contribution of Dark Matter to the total energy density of the universe is about 23% [3].
- **Origin of the Electroweak Symmetry Breaking**: The new scalar Higgs field is introduced "by hand". The squared mass parameter μ^2 is chosen arbitray to be negative and there is no fundamental motivation for this choice.
- **Gauge Coupling Unification**: The couplings g, g' and g_s of the electroweak and strong interaction depend on the energy scale described by the renormalization group equations. In the framework of the SM an accurate unification of all gauge coupling is not realizable so far.

2.6 Recent CMS Measurements

From the standard model Lagrangian,cross sections can be determined and tested in experiments. A small summary of recent measurements published by the CMS Collaboration of SM production

cross sections and properties relevant for this study are presented. The shown results are only a small piece of the SM puzzle and many more results measured in various experiments can be found in the literature.

In Fig. 2.2 the production cross sections for $W^{\pm}$, Z and double boson combinations $W\gamma$, $Z\gamma$, WW, WZ and ZZ measured with the CMS experiment in proton proton collisions at a center of mass energy $\sqrt{s} = 7\,\text{TeV}$ are shown. The measured cross section are in good agreement with the theoretical predictions. Similar in Fig. 2.3 the latest $t\bar{t}$ production cross section measurements in the various signatures of the top decays are summarzied. A complete overview of the latest results published by the CMS Collaboration can be found in Ref. [33].

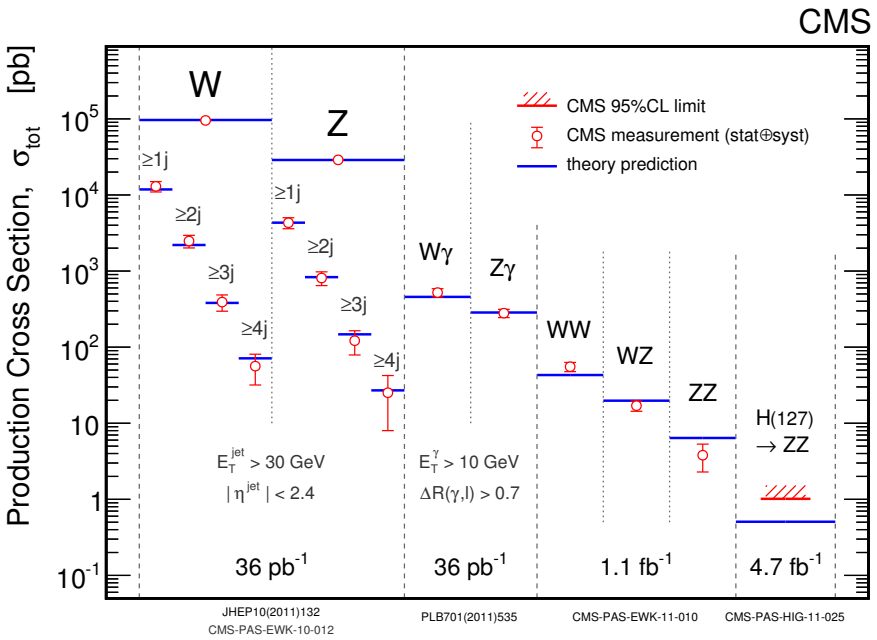

Figure 2.2: Electroweak production cross section measured with the CMS experiment. The plot is taken from [33].

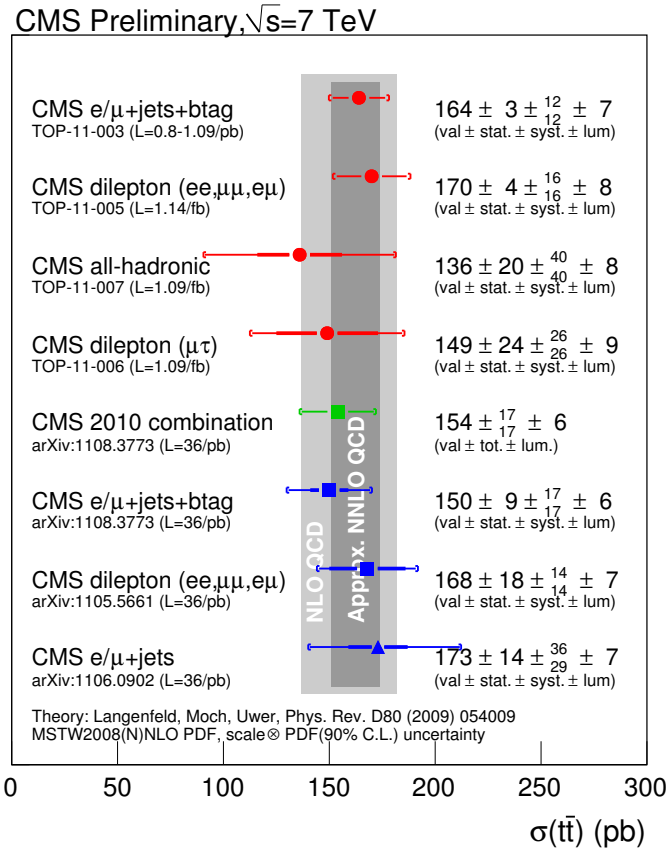

Figure 2.3: $t\bar{t}$ production cross section measured with the CMS experiment. The plot is taken from [33].

CHAPTER 3

Supersymmetry

In the last chapter the Standard Model of particle physics has been discussed. Within the theoretical framework several issues observed in nature can not be described. Hence, new theories expanding the Standard Model have to be evaluated and tested in experiments. As already discussed model building in particle physics follows three axioms: (1) gauge invariance, (2) field content and (3) spontaneous symmetry breaking. Following these axioms an extension of the SM based on a symmetry called *SUperSYmmetry* (SUSY) will be discussed and the Lagrangian invariant under supersymmetric transformations with its particle spectrum will be presented in this chapter.

3.1 Introduction - Supersymmetry

The supersymmetric extension of the Standard Model is based on an additional symmetry between fermions and bosons [34]:

$$Q|\text{Fermion}\rangle \propto |\text{Boson}\rangle \quad , \quad Q|\text{Boson}\rangle \propto |\text{Fermion}\rangle \, , \tag{3.1}$$

with Q the generator of the SUSY algebra follows the (anti-)commutator relations:

$$\{Q_\alpha, Q_\beta\} = \{Q^\dagger_\alpha, Q^\dagger_\beta\} = 0 \tag{3.2}$$

$$\{Q_\alpha, Q^\dagger_\beta\} = 2\sigma^\mu_{\alpha\beta} P_\mu \tag{3.3}$$

$$[P^\mu, Q] = [P^\mu, Q^\dagger] = 0 \, , \tag{3.4}$$

where σ^μ are the Pauli matrices and P_μ is the four-momentum generator of spacetime translations. Supersymmetry defined like above is a spacetime symmetry since the operators Q and $Q^\dagger$ (hermitian conjugate of Q) are carrying spin angular momentum $s = 1/2$ (fermionic operators). The minimal supersymmetric extension of the SM (MSSM[1]) is an $N = 1$ SUSY model with N referring to

[1] MSSM: **M**inimal **S**upersymmetric **S**tandard **M**odel

the number of generators $Q \rightarrow Q_i(i = 1, 2, ...N)$. The irreducible representation of the supersymmetric algebra (*supermultiplets*) contains an equal number of fermions and bosons, where particles transforming under Q ($Q^\dagger$) into each other are called *superpartners*. Q and $Q^\dagger$ commute with the generators of the gauge transformations and hence all superpartners must have the same electric charges, weak isospin and color degrees of freedom except the spin, which differs by $1/2$. Due to the fact that P^μ commutes with $Q(Q^\dagger)$ also the squared mass parameter $-P^2$ commutes and hence all superpartners in a supermultiplet must have equal masses.
Up to now no evidence for any supersymmetric particles have been observed in high energy particle physics experiments, which can only be realized if the masses of the superpartners are large. This is in contrast to the theory prediction. Breaking the symmetry resolves this issue, i.e. the SM particles and their superpartners would have different masses, where the mass difference depends on the breaking mechanism.

The introduction of a set of new particles solves immediately several problems of the SM:

Fine Tuning: The new particles have similar radiative corrections to the Higgs mass as their partners of the SM unless the symmetry is broken. The only difference is the sign of those corrections, which are opposite and cancel each other. This property solves the fine tuning problem. If SUSY is broken the superpartner masses are different and therefore the cancellations depend on the mass differences. To avoid unnatural fine tuning the SUSY breaking scale has to be $M_{SUSY} \leq 1\,\text{TeV}$.

Hierarchy Problem: Similar to the fine tuning the cancellation of quantum corrections induced by the new particles can explain the large difference of the weak and unification scale. In SUSY models electroweak symmetry breaking is not ad-hoc introduced, but is triggered by radiative corrections from the top-quark Yukawa coupling to the Higgs sector. One of the Higgs squared masses are driven to negative values by this coupling. The logarithmic energy dependency of the relative corrections lead to large differences of the two scales.

Unification: Introducing new particles changes the energy scale dependent slope of the gauge couplings. Setting the scale of the new particles at the TeV scale the unification of all gauge couplings can be achieved, which can be seen in Fig. 3.1.

Dark Matter: Introducing an new quantum number (R-parity) and assuming it to be conserved yields a massive stable lightest supersymmetric particle (LSP). The LSP would be a perfect candidate for the cold dark matter in the universe.

3.2 Particle Spectrum of the MSSM

As a first step the naming convention for the supersymmetric partners of the SM particles is discussed. The superpartner names of quarks and leptons, i.e. supersymmetric bosons, are constructed by adding a "s" to the name. So, generically *squarks* are the superpartners of the quarks and *sleptons* of leptons. Since the fermions have two spin states, whereas their superpartners are scalars, there are actual two

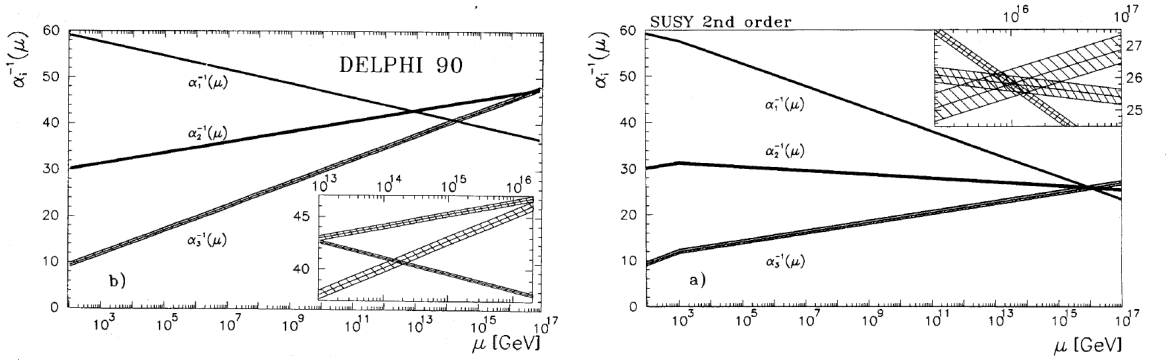

Figure 3.1: Evolution of the three coupling constants of the electroweak and strong interaction using the measured values for M_Z and $\alpha(M_Z)$ from the Delphi experiment for the SM (left) and the similar evolution but including contributions of the minimal SUSY model (right). Plots are taken from the original paper published in 1991, where the effect of gauge coupling unification with a fit to the SUSY mass scale has been shown for the first time [7].

superpartners for each fermion. In an analogous manner the superpartners of the SM bosons get an "-ino" attached, e.g. the wino is the superpartner of the W boson, whereas the partner of the Higgs bosons are called higgsinos. In the context of the MSSM a second Higgs multiplet has to be introduced with both multiplets having a weak hypercharge $Y = \pm 1/2$, because only $Y = +1/2$ Higgs chiral multiplets can give masses to up-type quarks (up, charm, top) and only $Y = -1/2$ Higgs chiral multiplets can give masses to down-type quarks (down, strange, charm). The Higgs multiplets corresponding to $Y = 1/2$ and $Y = -1/2$ are named H_u and H_d, respectively.
Finally, the particle spectrum has the following form: left-handed quarks and leptons as well as gauge bosons and Higgs doublets build multiplets with their superpartners, whereas right-handed quarks and leptons are arranged in doublets with their superpartners. The particle spectrum is presented in Table 3.1, where supersymmetric particles are denoted with a "$\sim$" on top.

3.3 Supersymmetric Lagrangian

After defining the symmetry and the field content the supersymmetric Lagrangian can be evaluated. The MSSM Lagrangian should be invariant under the $SU(3)_C \otimes SU(2)_L \otimes U(1)_Y$ gauge group similar to the SM, but include the superfields listed in Table 3.1. Additional terms breaking the supersymmetry have to be added. The Lagrangian consists of two parts: the supersymmetric generalization of the standard model Lagrangian ($\mathcal{L}_{\text{SUSY}}$) and the SUSY breaking term ($\mathcal{L}_{\text{SUSY-Break}}$)

$$\mathcal{L}_{\text{MSSM}} = \mathcal{L}_{\text{SUSY}} + \mathcal{L}_{\text{SUSY-Break}} \,, \tag{3.5}$$

where the first term can be divided further into a gauge part, consisting of the supersymmetric generalized terms of the kinetic energy of the gauge fields and terms describing the interaction of gauge and fermion fields, and the Yukawa interactions.

$$\mathcal{L}_{\text{SUSY}} = \mathcal{L}_{\text{gauge}} + \mathcal{L}_{\text{Yukawa}} \tag{3.6}$$

Superfield	Bosons	Fermions	$SU(3)_C$	$SU(2)_L$	$U(1)_Y$
Gauge					
$\mathbf{G^a}$	g^a	$\tilde{g}^a$	8	0	0
$\mathbf{V^k}$	W^k $(W^\pm, Z_0)$	$\tilde{w}^k$ $(\tilde{w}^\pm, \tilde{z}_0)$	1	3	0
$\mathbf{V'}$	B/γ	$\tilde{b}$ / $\tilde{\gamma}$	1	1	0
Matter					
$\mathbf{L_i}$	Sleptons $\begin{cases} \tilde{L}_i = (\tilde{\nu}, \tilde{e})_L \\ \tilde{E}_i = \tilde{e}_R \end{cases}$	Leptons $\begin{cases} L_i = (\nu, e)_L \\ E_i = e_R \end{cases}$	1	2	-1
$\mathbf{E_i}$			1	1	2
$\mathbf{Q_i}$	Squarks $\begin{cases} \tilde{Q}_i = (\tilde{u}, \tilde{d})_L \\ \tilde{U}_i = \tilde{u}_R \\ \tilde{D}_i = \tilde{d}_R \end{cases}$	Quarks $\begin{cases} Q_i = (u, d)_L \\ U_i = u_R \\ D_i = d_R \end{cases}$	3	2	$1/3$
$\mathbf{U_i}$			3	1	$-4/3$
$\mathbf{D_i}$			3	1	$2/3$
Higgs					
$\mathbf{H_u}$	Higgs $\begin{cases} H_u \\ H_d \end{cases}$	Higgsino $\begin{cases} \tilde{H}_u \\ \tilde{H}_d \end{cases}$	1	2	-1
$\mathbf{H_d}$			1	2	1

Table 3.1: The particle spectrum of the MSSM [35]. $i = 1, 2, 3$ corresponds to the three generations, $a = 1...8$ is the index of the $SU(3)_C$ and $k = 1, 2, 3$ is the index of the $SU(2)_L$. For completeness the quantum numbers for the internal symmetries are given in the last columns.

The Yukawa interaction term is given by the *superpotenial* W_R:

$$W_R = \epsilon_{ij}(h_U^{ab} Q_a^j U_b^C H_d^i + h_D^{ab} Q_a^j D_b^C H_u^i + h_L^{ab} L_a^j E_b^C H_u^i + \mu H_u^i H_d^j) + h.c.\,, \tag{3.7}$$

with i, j the $SU(2)_L$ indices, $a, b = 1, 2, 3$ are the three generation indices, $h_{U,D,L}$ are the Yukawa couplings and ϵ_{ij} is the total anti-symmetric tensor. All fields included are superfields, where the charge conjugated fields are labeled with a C. The superpotenial has a similar form compared to the Standard Model Yukawa term (Eq. 2.35) except the last term describing the Higgs mixing, which is absent in the SM.

R-parity

In principle, the superpotential given in Eq. 3.7 can be extended by additional renormalizable terms invariant under gauge transformations. These terms allow transitions of quarks and leptons, which leads to lepton and baryon number violating processes. In order to suppress such terms in the superpotential a new symmetry called R-parity is introduced, where fields have to be invariant under discrete transformations $\Phi \to e^{\pm iR\pi}\Phi$. R-parity is a multiplicative quantum number defined as:

$$R = (-1)^{3(B-L)+2S}\,, \tag{3.8}$$

with B the baryon number, L is the lepton number and S is the spin of the particle [34]. SM particles have $R = +1$, whereas SUSY particles $R = -1$. The multiplicative nature of the quantum number and the requirement of conserved R-parity has several consequences:

1. Existence of a *stable* lightest supersymmetric particle (LSP), since a decay to SM particles would violate the R-parity.
2. SUSY particles can only be produced in pairs and each decaying subsequently to the LSP.
3. Those properties of R-parity conserving supersymmetric models imply that at collider experiments sparticle production results in final states with an odd number of LSPs. This leads in case of neutral LSPs to signatures including large missing transverse energy.

SUSY Breaking Mechanism

So far no supersymmetric particles have been discovered. Hence, if supersymmetry is realized in nature, it has to be a broken symmetry, which yields larger masses of the supersymmetric particles. In the last decades large efforts have been mobilized to understand the *soft supersymmetry breaking*, soft in the sense that the mass splitting between standard model particles and their superpartners can not be too large, in order to still cancel the radiative correction to the Higgs mass on a "natural" level. The most general form of such breaking terms are :

$$\begin{aligned}\mathcal{L}_{\text{SUSY-Break-Soft}} =& m_{H_d}^2 H_d^\dagger H_d + m_{H_u}^2 H_u^\dagger H_u + B\mu(H_u^T i\tau_2 H_d + h.c.) \\ &+ \sum_i (\tilde{m}_{Q_i}^2 \tilde{Q}_i^\dagger \tilde{Q}_i + \tilde{m}_{L_i}^2 \tilde{L}_i^\dagger \tilde{L}_i + \tilde{m}_{U_i}^2 \tilde{U}_i^\dagger \tilde{U}_i + \tilde{m}_{D_i}^2 \tilde{D}_i^\dagger \tilde{D}_i + \tilde{m}_{E_i}^2 \tilde{E}_i^\dagger \tilde{E}_i + h.c.) \\ &+ \sum_{i,j} (A_u^{ij} h_u^{ij} \tilde{U}_i H_u \tilde{Q}_j + A_d^{ij} h_d^{ij} \tilde{D}_i H_d \tilde{Q}_j + A_e^{ij} h_e^{ij} \tilde{\tilde{L}}_i H_d \tilde{L}_j + h.c.) \\ &+ \frac{1}{2} \sum_{l=1}^{3} M_l \tilde{\lambda}_l \tilde{\lambda}_l + h.c. \end{aligned} \tag{3.9}$$

where μ is the Higgs mass parameter introduced in the superpotential Eq. 3.7, B is the bilinear coupling, $A_{u,d,e}^{ij}$ are the trilinear couplings with the generation indices $i, j = 1, 2, 3$ and $\tilde{\lambda}_l$ and M_l are the supersymmetric partners of the gauge bosons and their masses corresponding to the three gauge groups ($l = 1, 2, 3$). Introducing the most general soft symmetry breaking terms yield more than 100 free parameters (masses, phases and mixing angles) [36]. In order to reduce the number of parameters, relations between the soft breaking terms have to be determined. The detailed mechanism of the SUSY breaking is unknown, but a common approach assumes, that the breaking occurs in a *hidden sector* that has no direct couplings to the *visible sector* and the breaking is mediated by messengers.
The most popular approaches for the mediating interactions are *gravity mediated* and *gauge mediated* supersymmetry breaking. In **G**auge **M**ediated **S**upersymmetry **B**reaking (GMSB) models the messenger particles are new chiral multiplets, which have $SU(3)_C \otimes SU(2)_L \otimes U(1)_Y$ interactions. Gravity mediated supersymmetry breaking scenarios assume symmetry breaking via gravitational interactions. In this study a $N = 1$ supergravity (mSUGRA/cMSSM) [37] will be used as a reference model. At the GUT scale M_{GUT} the following unifications are assumed:

$$M_1(M_{GUT}) = M_2(M_{GUT}) = M_3(M_{GUT}) \equiv m_{1/2} \tag{3.10}$$

$$\tilde{m}_{E,L,U^i,D^i,Q^i}(M_{GUT}) \equiv m_0 \tag{3.11}$$

$$A_t(M_{GUT}) = A_b(M_{GUT}) = A_\tau(M_{GUT}) \equiv A_0 \tag{3.12}$$

where $m_{1/2}$ is the unified gaugino mass, m_0 is the unified scalar mass and A_0 the unified trilinear coupling at the GUT scale. In Eq. 3.9 it can be seen, that the trilinear couplings only appear in company with the corresponding Yukawa couplings and since the Yukawa couplings of the first two generations can be neglected, it is sufficient to consider only the trilinear couplings of the third generation. The arbitrariness of more than 100 free parameters is reduced to a total of 5 parameters:

- $\mathbf{m_{1/2}}$: unified gaugino mass $m_{1/2}$ at the GUT scale M_{GUT}
- $\mathbf{m_0}$: unified scalar mass m_0 at the GUT scale M_{GUT}
- $\mathbf{A_0}$: unified trilinear coupling A_0 at the GUT scale M_{GUT}
- $sign(\mu)$: the sign of the Higgs mass parameter connecting the two Higgs multiplets
- B: bilinear coupling

The bilinear coupling B can be also equivalently replaced by the ratio of the vacuum expectation values of the two Higgs multiplets $tan\beta = v_u/v_d$.

3.4 SUSY Mass Spectrum

The mass spectrum of the MSSM can be calculated by solving the renormalization group equations (RGE), which can be derived from the Lagrangian Eq. 3.5 [38]. In Fig. 3.1 the solution of the RGEs for the gauge couplings is shown and in Fig. 3.2 for the gaugino masses, sfermion mass breaking terms and the Higgs potential parameters for a typical cMSSM boundary condition ($m_0 = 200\,\text{GeV}$, $m_{1/2} = -A_0 = 600\,\text{GeV}$, $tan(\beta) = 10$ and $sign(\mu) = +1$).

Neutralinos and Charginos

The higgsinos and gauginos mix with each other, where the neutral higgsinos ($\tilde{H}_u^0$ and $\tilde{H}_d^0$) and the neutral gauginos ($\tilde{B}$, $\tilde{W}^0$) form the four mass eigenstates of the so called *neutralinos* denoted with $\tilde{\chi}_i^0$ ($i = 1, 2, 3, 4$). The corresponding neutralino mass matrix is

$$\mathcal{M}_{\tilde{\chi}^0} = \begin{pmatrix} M_1 & 0 & -m_Z \cos\beta \sin\theta_W & m_Z \sin\beta \sin\theta_W \\ 0 & M_2 & m_Z \cos\beta \cos\theta_W & -m_Z \sin\beta \cos\theta_W \\ -m_Z \cos\beta \sin\theta_W & m_Z \cos\beta \cos\theta_W & 0 & -\mu \\ m_Z \sin\beta \sin\theta_W & -m_Z \sin\beta \cos\theta_W & -\mu & 0 \end{pmatrix} \tag{3.13}$$

with the gaugino masses M_1, M_2, the weak mixing angle θ_W, the Higgs mass parameter μ and the ratio of the two Higgs vacuum expectation values $tan(\beta)$. The eigenstates of the mass matrix can be obtained by diagonalizing and are denoted by $\tilde{m}_{\tilde{\chi}_1^0} < \tilde{m}_{\tilde{\chi}_2^0} < \tilde{m}_{\tilde{\chi}_3^0} < \tilde{m}_{\tilde{\chi}_4^0}$, where $\tilde{m}_{\tilde{\chi}_1^0}$ is the lightest neutralino. In many supersymmetric models the $\tilde{\chi}_1^0$ is the LSP and stable, unless R-parity is violated. Since it is neutral and only weakly interacting it would be a perfect candidate for the Dark Matter.

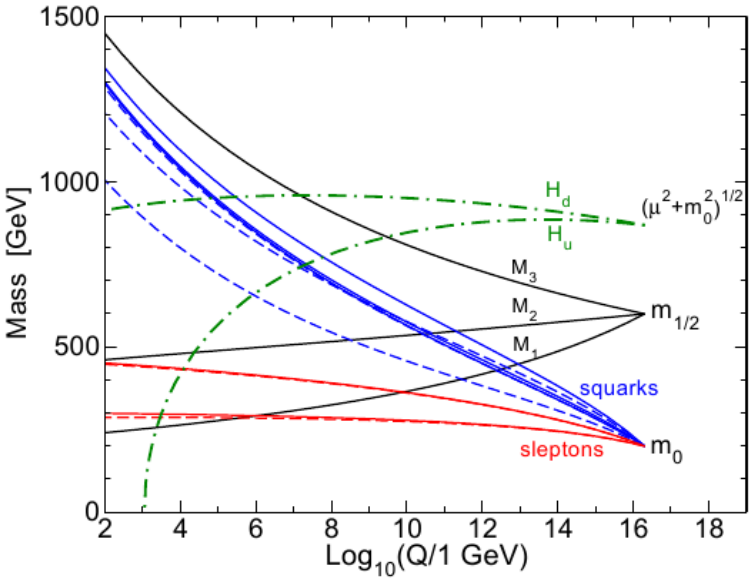

Figure 3.2: MSSM RGE solutions for the gaugino masses, sfermion mass breaking terms and the Higgs potential parameters for a typical cMSSM boundary condition ($m_0 = 200\,\text{GeV}$, $m_{1/2} = -A_0 = 600\,\text{GeV}$, $tan(\beta) = 10$ and $sign(\mu) = +1$)

Charginos are mixtures of the charged higgsino ($\tilde{H}_u^+$ and $\tilde{H}_d^-$) and charged wino ($\tilde{W}^+$ and $\tilde{W}^-$) components and are denoted analogous with $\tilde{\chi}_{1,2}^{\pm}$. The chargino mass matrix can be related to the 2×2 matrix

$$\mathcal{M}_{\tilde{\chi}^{\pm}} = \begin{pmatrix} M_2 & \sqrt{2} m_W sin(\beta) \\ \sqrt{2} m_W cos(\beta) & \mu \end{pmatrix} . \tag{3.14}$$

After diagonalizing the matrix 3.14, two eigenstates with masses $\tilde{m}_{\tilde{\chi}_{i,j}^{\pm}}$ can be obtained, where the (double generated) mass eigenvalues are given by:

$$\begin{aligned} \tilde{m}_{\chi_{i,j}^{\pm}} = & \frac{1}{2} \Big[|M_2|^2 + |\mu|^2 + 2m_W^2 \\ & \mp \sqrt{(|M_2|^2 + |\mu|^2 + 2m_W^2)^2 - 4|\mu M_2 - m_W^2 sin(2\beta)|^2} \Big] \end{aligned} \tag{3.15}$$

Gluino

The gluino is the only color octet fermion in the MSSM and does not mix with any other particle. Its mass is defined by the gaugino mass parameter $\tilde{m}_{\tilde{g}} = M_3$. For typical cMSSM boundary conditions the bino and wino mass parameters are related to the gluino mass via the RGE which yield approximately

$$M_3 : M_2 : M_1 = 6 : 2 : 1 \tag{3.16}$$

near the TeV scale [4].

Squarks and Sleptons

Sleptons and squarks are the superpartners of the leptons and quarks. Left and right-handed fermions must have similar masses, but their superpartners are bosons, whose masses can vary, hence in the following the partners of left and right-handed fermions will be distinguished. Non negligible Yukawa couplings lead to a mixing between the interaction eigenstates and in order to obtain the mass eigenstates of the MSSM sleptons and squarks, one should diagonalize three 6×6 matrices (up-type squarks, down-type squarks, charged sleptons) and one 3×3 matrix for the sneutrinos. For the first and second generation the Yukawa couplings and therefore also the mixing angles are negligible and the mass eigenstates correspond to the interaction eigenstates

$$\tilde{m}^2_{e_L} = \tilde{m}^2_{L_i} + m^2_{E_i} + m^2_Z \cos(2\beta)\left(-\frac{1}{2} + \sin^2\theta_W\right) \tag{3.17}$$

$$\tilde{m}^2_{\nu_L} = \tilde{m}^2_{L_i} + m^2_Z \cos(2\beta)\left(\frac{1}{2}\right) \tag{3.18}$$

$$\tilde{m}^2_{e_R} = \tilde{m}^2_{E_i} + m^2_{E_i} - m^2_Z \cos(2\beta)\left(\sin^2\theta_W\right) \tag{3.19}$$

$$\tilde{m}^2_{u_L} = \tilde{m}^2_{Q_i} + m^2_{U_i} + m^2_Z \cos(2\beta)\left(+\frac{1}{2} + \sin^2\theta_W\right) \tag{3.20}$$

$$\tilde{m}^2_{d_L} = \tilde{m}^2_{Q_i} + m^2_{D_i} + m^2_Z \cos(2\beta)\left(-\frac{1}{2} + \frac{1}{3}\sin^2\theta_W\right) \tag{3.21}$$

$$\tilde{m}^2_{u_R} = \tilde{m}^2_{U_i} + m^2_{U_i} + m^2_Z \cos(2\beta)\left(\frac{2}{3}\sin^2\theta_W\right) \tag{3.22}$$

$$\tilde{m}^2_{d_R} = \tilde{m}^2_{D_i} + m^2_{D_i} - m^2_Z \cos(2\beta)\left(\frac{1}{3}\sin^2\theta_W\right) \quad , \tag{3.23}$$

where $i = 1, 2, 3$ indicates the three generations. The terms labeled with an "$\sim$" are the solutions of the RGEs of the soft symmetry breaking terms in Eq. 3.9, all other terms without represent SM particles.
In contrast, sfermions of the third generation can have substantial mixing and the corresponding mass matrices can be expressed as:

$$\mathcal{M}_{\tilde{t}} = \begin{pmatrix} \tilde{m}^2_{t_L} & m_t(A_t - \mu\cot\beta) \\ m_t(A_t - \mu\cot\beta) & \tilde{m}^2_{t_R} \end{pmatrix} \tag{3.24}$$

$$\mathcal{M}_{\tilde{b}} = \begin{pmatrix} \tilde{m}^2_{b_L} & m_b(A_b - \mu\tan\beta) \\ m_b(A_b - \mu\tan\beta) & \tilde{m}^2_{b_R} \end{pmatrix} \tag{3.25}$$

$$\mathcal{M}_{\tilde{\tau}} = \begin{pmatrix} \tilde{m}^2_{\tau_L} & m_\tau(A_\tau - \mu\tan\beta) \\ m_\tau(A_\tau - \mu\tan\beta) & \tilde{m}^2_{\tau_R} \end{pmatrix} \quad , \tag{3.26}$$

where the mass eigenstates after diagonalization are given by:

$$m^2_{\tilde{t}_{1,2}} = \frac{1}{2}\left(\tilde{m}^2_{t_L} + \tilde{m}^2_{t_R}\right) \pm \sqrt{\frac{1}{4}\left(\tilde{m}^2_{t_L} - \tilde{m}^2_{t_R}\right)^2 + m_t^2\left(A_t - \mu\cot\beta\right)^2} \tag{3.27}$$

$$m^2_{\tilde{b}_{1,2}} = \frac{1}{2}\left(\tilde{m}^2_{b_L} + \tilde{m}^2_{b_R}\right) \pm \sqrt{\frac{1}{4}\left(\tilde{m}^2_{b_L} - \tilde{m}^2_{b_R}\right)^2 + m_b^2\left(A_b - \mu\tan\beta\right)^2} \tag{3.28}$$

$$m^2_{\tilde{\tau}_{1,2}} = \frac{1}{2}\left(\tilde{m}^2_{\tau_L} + \tilde{m}^2_{\tau_R}\right) \pm \sqrt{\frac{1}{4}\left(\tilde{m}^2_{\tau_L} - \tilde{m}^2_{\tau_R}\right)^2 + m_\tau^2\left(A_\tau - \mu\tan\beta\right)^2} \quad . \tag{3.29}$$

Higgs boson

In the MSSM at least two Higgs doublets with weak hypercharges $Y = +1/2$ and $Y = -1/2$ have to be introduced to give all particles masses, where the two complex Higgs doublets read as

$$H_u = \begin{pmatrix} H_u^0 \\ H_u^+ \end{pmatrix} = \begin{pmatrix} v_u + \frac{1}{\sqrt{2}}(\Phi_1 + i\Phi_2) \\ H_u^+ \end{pmatrix} \tag{3.30}$$

$$H_d = \begin{pmatrix} H_d^- \\ H_d^0 \end{pmatrix} = \begin{pmatrix} H_d^- \\ v_d + \frac{1}{\sqrt{2}}(\Phi_3 + i\Phi_4) \end{pmatrix} , \tag{3.31}$$

with the vacuum expectation values v_u and v_d of the neutral components. After setting $H_u^+ = H_d^- = 0$ ($H_d^- = 0$ follows from $\partial V/\partial H_u^+ = 0$ after setting $H_u^+ = 0$) gives the scalar potential

$$\begin{aligned} V =& (|\mu|^2 + m^2_{H_d})|H_u^0|^2 + (|\mu|^2 + m^2_{H_d})|H_d^0|^2 - B\mu(H_u^0 H_d^0 + c.c.) \\ &+ \frac{1}{8}(g^2 + g'^2)(|H_u^0|^2 - |H_d^0|^2)^2 \end{aligned} \tag{3.32}$$

Introducing the relations of the mass parameters

$$\begin{aligned} m_1^2 &= m^2_{H_u} + \mu^2 \\ m_2^2 &= m^2_{H_d} + \mu^2 \\ m_3^2 &= B m_0 \mu \qquad , \end{aligned} \tag{3.33}$$

a non trivial minimum of the potential in Eq. 3.32, and therefore electroweak symmetry breaking, can only be derived, if the following requirement on the mass parameters are fulfilled

$$\begin{aligned} m_1^2 m_2^2 &< m_3^4 \\ m_1^2 + m_2^2 &> 2m_3^2 \qquad . \end{aligned} \tag{3.34}$$

In total the two Higgs doublets have 8 degrees of freedom, where three of them correspond to the Goldstone bosons, which will become the longitudinal polarization of the $W^\pm$ and Z boson analogous to the SM, resulting into five physical Higgs bosons in the MSSM (h^0, H^0, A^0, $H^\pm$). The masses for those can be expressed as:

$$M^2_{A^0} = m_1^2 + m_2^2 \tag{3.35}$$

$$M^2_{H^0,h^0} = \frac{1}{2}\left(m^2_{A^0} + m_Z^2 \pm \sqrt{(m^2_{A^0} + m_Z^2)^2 - 4m^2_{A^0} m_Z^2 cos(2\beta)}\right) \tag{3.36}$$

$$M^2_{H^\pm} = m^2_{A^0} + m_W^2 \, . \tag{3.37}$$

In principle, the masses of A^0, H^0 and $H^{\pm}$ can be arbitrary high, whereas the lightest Higgs h^0 has an upper boundary:

$$m_h^2 \leq m_Z^2 cos^2(2\beta) \leq m_Z^2 \tag{3.38}$$

This mass range for the lightest MSSM Higgs is already excluded by former experiments [39] with the consequences that radiative corrections to the Higgs potential are important.

3.5 Constraints on cMSSM

Supersymmetry, if realized in nature, would affect many different fields of modern physics. Constraints on the supersymmetric models are coming from cosmological observations, direct/indirect WIMP searches, Higgs limits, precision measurements of SM properties and the motivation of the theory itself. In the following the dominant constraints and their effect on the cMSSM model will be shortly discussed.

Cosmology - Relic Density: Cosmological measurements of the Cosmic Microwave Background have shown, that about 23% of the energy of the universe consists of the cold dark matter (CDM) [40]. In R-Parity conserving SUSY models the lightest supersymmetric particle (LSP) is stable and in case of a neutralino-like, it would a perfect candidate for the CDM. The mass and the annihilation cross section of the LSP can be utilized to determine a model dependent expectation of the relic density in the universe. Out of the WMAP measurement (23% CDM) a constraint on the LSP anihilation cross section of SUSY models consistent with the relic density in our universe $\Omega_{\tilde{\chi}_1^0} h_0^2 \approx 0.11$ can be set, where the Hubble constant is $h_0 \approx 0.7$. For fixed $tan\beta$ this constraint leads to a narrow band in the cMSSM m_0-$m_{1/2}$ plane, but slight fine tuning of $tan\beta$ and therefore the mass of the pseudo scalar Higgs m_A and mostly the complete m_0-$m_{1/2}$ plane space is allowed [41].

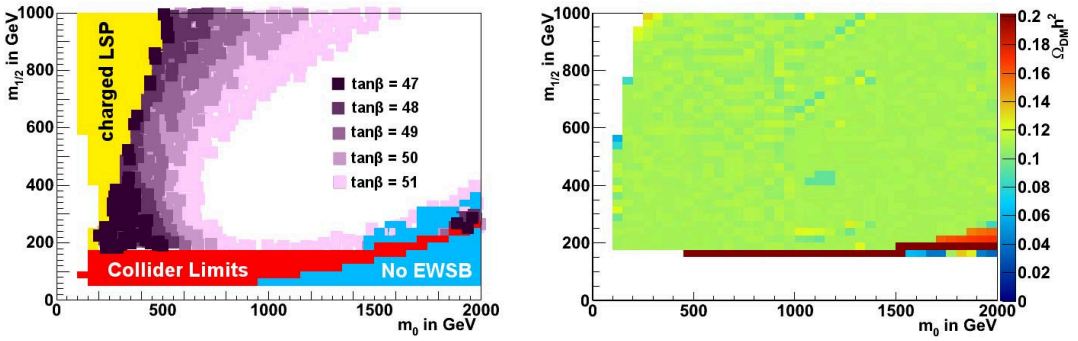

Figure 3.3: (Left) Allowed regions in the cMSSM m_0-$m_{1/2}$ plane for correct relic density in the universe for various values of $tan\beta$ and fixed trilinear coupling $A_0 = 0$ and $sign(\mu) = +1$. (Right) Relic density after tuning of $tan\beta$. Nearly the complete m_0-$m_{1/2}$ plane can be tuned to be consistent with the relic density in the universe. Plots are taken from [41].

Cosmology - Direct Dark Matter Searches: Several experiments designed to measure the nuclear recoils from weakly interacting massive particles (WIMP) of our galactic halo reported

interesting results over the last years. The experiments CDMS-II [42], Xenon100 [43] and EDELWEISS-II [44] have achieved the best sensitivities. Typically spin independent WIMP-nucleon elastic interaction cross section of about 10^{-9} pb are excluded at 90% confidence level over a wide range of WIMP masses [43].

B-Physics: Indirect measurements very sensitive to new physics beyond the Standard Model are the rare decay rates of B mesons. The constraints arising from the decay of a B_s meson into two muons $B_s \to \mu^+\mu^-$ will be exemplary discussed. $B_s \to \mu^+\mu^-$ processes are suppressed at tree level in the SM, since flavor changing neutral currents (FCNC) are not allowed, and so only higher order loop diagrams contribute. The branching fraction (BR) in the SM [45] is predicted to be

$$BR_{SM}(B_s \to \mu^+\mu^-) = (3.2 \pm 0.2) \cdot 10^{-9} \tag{3.39}$$

Recently, the CDF collaboration published an exciting results, where an excess in $B_s \to \mu^+\mu^-$ with a 1.9% probability of a combined background plus SM signal fluctuation was observed [46]. If one interprets the excess as signal, the corresponding branching fraction is of the order $BR_{CDF}(B_s \to \mu^+\mu^-) = 1.8^{+1.0}_{-0.9} \cdot 10^{-8}$. So far the excess could not be confirmed in a combined search reported by the LHCb and CMS collaboration [47], where an upper limit on the branching fraction was given as:

$$BR_{LHCb+CMS}(B_s \to \mu^+\mu^-) < 1.08(0.9) \cdot 10^{-8} \,@\, 95\%\,(90\%)\, C.L.\,. \tag{3.40}$$

The branching fraction can be significantly enhanced by SUSY models due to additional contributions from supersymmetric particles leading to a BR proportional to $tan^6\beta$. In principle one can expect strong constraints on the cMSSM model space from the measured upper limit on the branching fraction, but it was shown that a simultaneous fit of the trilinear coupling A_0 and $tan(\beta)$ in the combined data of $BR(B_s \to \mu^+\mu^-)$ and cosmological measurements of the relic density yields excluded ranges well below the constraints coming from the excluded Higgs masses [48].

Anomalous Magnetic Moment of the Muon:

The Muon G-2 collaboration has measured the anomalous magnetic moment of the muon [49] at the Brookhaven National Laboratory very precisely to be:

$$\alpha_\mu(Expt) = 11659208.0(63) \times 10^{-10}\,(0.54\,\text{ppm}) \quad , \tag{3.41}$$

which is about 2.2 to 2.7σ away from the SM expectation

$$\Delta\alpha_\mu(Expt - SM) = (22.4 \pm 10 \text{ to } 26.1 \pm 9.4) \times 10^{-10}\,(0.54\,\text{ppm}) \quad . \tag{3.42}$$

It turns out that the magnetic moment of the muon is very sensitive to radiative corrections from the SM, whereas additional contributions from SUSY particles can lead to the measured deviation. The sign of the shift in the magnetic moment, where leading SUSY contributions are proportional to $tan(\beta)sign(\mu)/{M^2_{SUSY}}^2$, fixes the sign of the Higgs mass parameter to positive values [50, 51].

[2] M_{SUSY}: a common mass for all superpartners is assumed

Collider Experiments: Several direct SUSY searches were already performed at former Collider experiments (LEP, Tevatron) and after two years of LHC running mostly already outdated. In Fig. 3.4 a summary of the actual exclusion limits of the various SUSY searches done within the CMS Collaboration in the context of the cMSSM are shown [52]. Additionally, the exclusion limit of a hadronic SUSY search performed by the ATLAS Collaboration with comparable performance is shown for comparison [53]. Both collaborations have quite similar analysis strategies: the analysis are split in different topologies defined by the number of physics objects (leptons, jets, E_T^{miss}). Translating the exclusion limits from the m_0-$m_{1/2}$ plane in excluded masses of SUSY particles both experiments gain a foothold at the TeV scale, where in case of CMS squark and gluino masses of about 1 TeV are already excluded over a wide range of m_0 (cMSSM).

Many more analysis not reported here are already published, where the results were also interpreted in different SUSY models and so called simplified models as well. A summary of all recent results can be found elsewhere for CMS [52] and ATLAS [53].

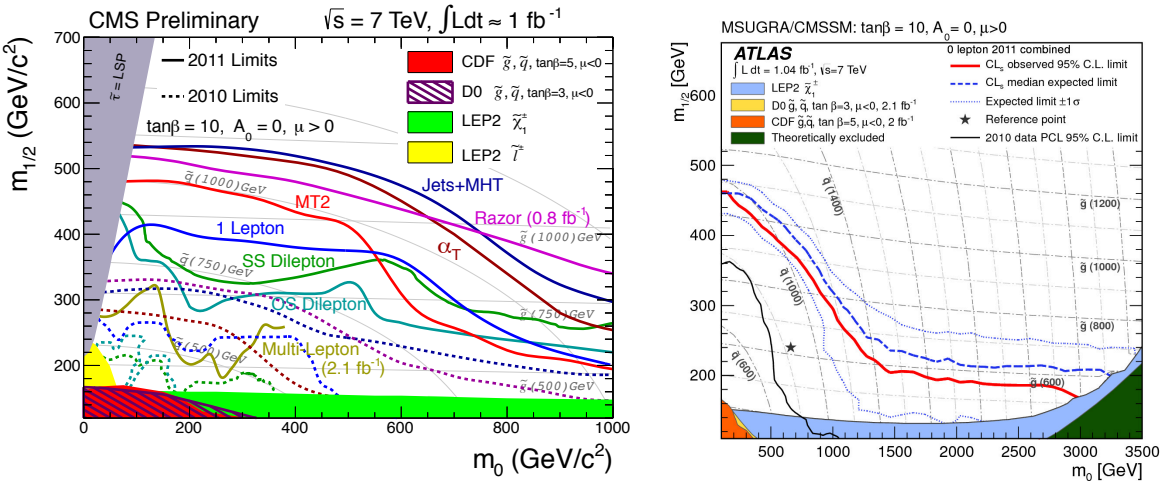

Figure 3.4: CMS (left) and ATLAS (right) exclusion limits in the context of the cMSSM model ($tan\beta = 10$, $A_0 = 0$, $sign(\mu) = +1$) corresponding to a data set of about $L_{\text{int}} \approx 1\,\text{fb}^{-1}$ recorded in 2011. In case of CMS all major results are incorporated in one plot, where hadronic searches (Jets+MHT, Razor) sets the most stringent limits. In case of ATLAS a similar hadronic analysis is shown with comparable limits. Plots are taken from [52, 53].

A complete consideration of all constraints[3] of precision measurements, SUSY searches at collider experiments and direct WIMP searches can be incorporated and the compatibility of different models with the measurements denoted by a χ^2 calculation was determined [54–56]. In Fig. 3.5 the 68% (95%) confidence level contours corresponding to $\Delta\chi^2 = 2.30(5.99)$ in respect to the best fit point are shown for the pre-LHC scenario and including recent LHC measurements and exclusion limits as well. In summary the LHC searches for physics beyond the SM just started to probe a new region of the cMSSM parameter space, which were not excluded by former constraints of precision measurements,

[3] Not all constraints incorporated in the analysis were discussed explicitly here but can be found in [54] .

cosmology and collider experiments and therefore its not surprising, that no significant hint on new, maybe supersymmetric, particles have been appeared so far.

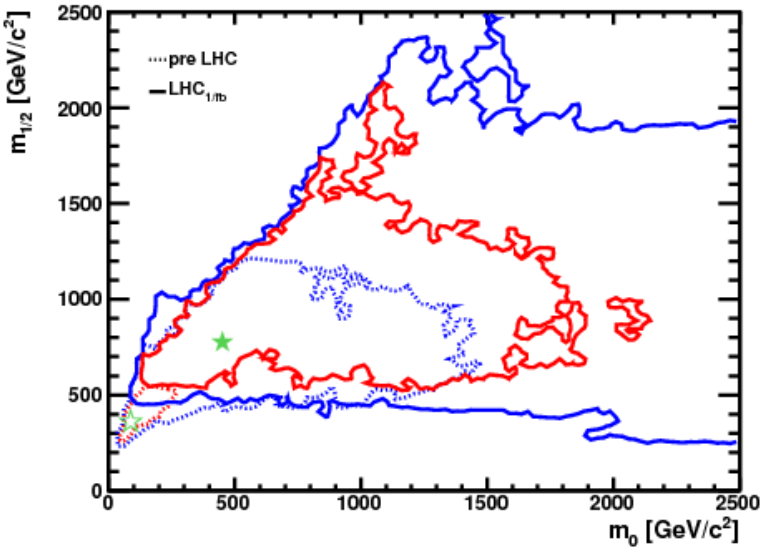

Figure 3.5: The m_0-$m_{1/2}$ plane in the cMSSM . The best-fit point after incorporation constraints including the LHC 1 fb^{-1} results is indicated by a filled green star, and the pre-LHC fit [56] by an open star. The $\Delta\chi^2 = 2.30$(red) and 5.99(blue) contours, commonly interpreted as the boundaries of the 68 and 95% CL regions. The solid line includes the LHC 1 fb^{-1} data and the dotted lines show the pre-LHC fits [54].

CHAPTER 4

The CMS Experiment at the Large Hadron Collider

In the last decades many discoveries and precision measurements performed in high energy particle physics were a big step up the ladder towards a better understanding of the universe. The Standard Model (SM) of particle physics is one of the most tested theories ever written down and describes numerous phenomena accessible up to now with an amazing precision. But as already discussed in the previous chapters, the Standard Model is an effective theory working at an energy scale of the order of 100 GeV and the natural question is: what is at energy scales of 1 TeV or even higher?

Another problem of the Standard Model comes the *Dark Matter* in the universe, which is presumably made of the so called *Weakly Interacting Massive Particle* (WIMP). This Dark Matter cannot be described within the Standard Model. Supersymmetric theories on the other hand provide a perfect candidate. Several experiments aimed to detect the WIMP's were built, but up to now no significant hints were measured. Those direct, and also indirect, dark matter search experiments are perfect to confirm the existence of WIMP's, but not suitable to reveal their nature.

For such purposes collider experiments are predestinated. The Large Hadron Collider (LHC) at the CERN near Genevea Switzerland, provides a perfect tool to jump into a new energy regime and hopefully in a time of many new discoveries, which could revolutionize our understanding of the universe.

CERN was founded in 1954 with 12 member states [57]. Two years later in 1959 the first proton accelerator *Proton-Synchroton* (PS) was built with the ability to accelerate protons up to an energy of 28 GeV; it is still operating nowadays. The proton-proton collider history starts also at CERN in 1971 as the first p-p collider *Intersecting Storage Rings* (ISR) with a diameter of 300 m starts operating. Parallel in the beginning of the 70ies the CERN success story starts accelerating, beginning with the discovery of neutral currents in the Gargamelle-bubble chamber in 1973 [58, 59]. New more energetic machines were built in the following years discovering for example the today well known W and Z boson(1983) [60, 61]: the *Super Proton Synchroton* (SPS) accelerating protons up to 300 GeV (400 GeV nowadays) built in 1976 and the *Large Electron Positron* (LEP) with a circumference of 27 km finalized in 1989. LEP ends its operation in November of 2000 clearing the way for the con-

struction of the LHC. Following the discoveries of the gauge bosons made at the various experiments at CERN, it is now the challenge (and duty) of the LHC to discover the last missing boson of the SM. In the next sections the LHC and in more detail the *Compact Muon Solenoid* experiment will be reviewed.

4.1 The Large Hadron Collider

The LHC [62] is today the world largest particle accelerator with a circumference of 26.7 km situated in average around 100 m beneath the surface in the tunnel of the former LEP[1] experiment near Geneva. With a present center of mass energy of $\sqrt{s} = 7$ TeV in proton-proton collisions it provides also the world most energetic collider as well. The overall conceptional design of the LHC is running with two 7 TeV proton beams at a luminosity of $\mathcal{L} = 10^{34}\,\mathrm{cm}^{-2}\mathrm{s}^{-1}$. Additional, dedicated periods with heavy ion runs are scheduled with an energy of 2.76 TeV per nucleon and $\mathcal{L} = 10^{27}\,\mathrm{cm}^{-2}\mathrm{s}^{-1}$. Four experiments are installed at the collision points: CMS, ATLAS[2] [63], LHCb[3] [64] and ALICE[4] [65]. LHCb and ALICE are experiments designed to study predefined physics, where LHCb is optimized for precision measurements of CP violation and decays of B mesons and ALICE focuses on physics of strongly interacting particles and the so called quark-gluon plasma, which is expected at extreme values of energy density and temperature. CMS and ATLAS are general purpose detectors with the primary aim to discover the Higgs boson and find evidence for new physics beyond the Standard Model.

A schematic layout of the CERN accelerator complex is presented in Fig. 4.2. The LHC is a particle-particle collider consisting of two rings with counter-rotating proton beams. Protons are pre-accelerated in the PS and SPS facilities up to an energy of 400 GeV and injected afterwards in the LHC ring. The beam is further accelerated via 16 high frequency cavity resonators and are crossed at four interactions points, where the main experiments are arranged. In order to bend both proton beams circulating in the LHC tunnel 1232 dipole magnets able to generate 8.3 T magnetic fields are installed across the ring. Quadrupole and sextupole magnets are used in order to focus and squeeze the beam. The advantage of using protons compared to electrons/positrons used in the former LEP experiment is the highly reduced beam energy loss due to synchroton radiation. Hence higher energies can be achieved only constrained by the magnetic fields available to bend the beams. A caveat in proton-proton collisions is the composite nature of protons and hence the a priori unknown center-of-mass energy of the involved partons, except the transverse energy is known to be zero and as a consequence mostly transverse components of particle observables are used in the analysis of hadron collisions.

Beside the importance of the beam energy another quantity, used several times already, is the luminosity, whcih is defined as:

$$\mathcal{L} = \frac{\gamma f k_B N_p^2}{4\pi\epsilon_n \beta^*} F\,, \tag{4.1}$$

where γ is the Lorentz factor, f is the revolution frequency, k_B is the number of bunches, N_P is the number of protons per bunch, ϵ_n is the normalized transverse emittance, β^* is the betatron function of

[1] LEP: Large Electron Positron Collider
[2] ATLAS: A Torodoil LHC ApparatuS
[3] LHCb Large Hadron Collider beauty experiment
[4] ALICE: A Large Ion Collider Experiment

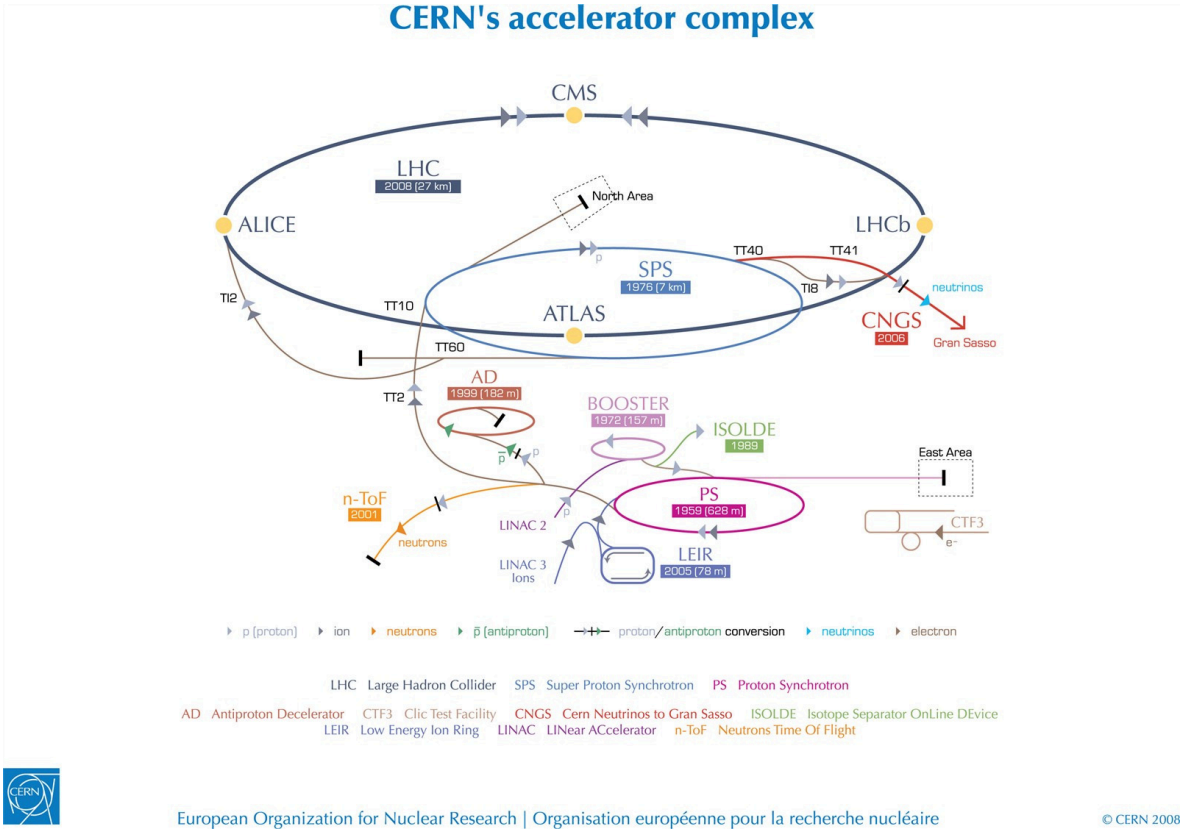

Figure 4.1: The CERN accelerator facility with the large LHC ring and the four main experiments. Protons getting pre-accelerated in the Proton-Synchroton (PS) and Super-Proton-Synchroton (SPS) up to 400 GeV before the injection into the main ring. Other experiments like the CERN-Neutrino to Gran Sasso (CNGS) beam, which was used by the OPERA [66] (Oscillation Project with Emulsion-tRacking Apparatus) collaboration for the exciting neutrino time of flight measurement [67], are shown as well.

the interaction point and F is a reduction factor induced by the crossing angle of the beams. In order to accumulate a large amount of events in a given time period, a high luminosity is required since it is directly related with the production rate:

$$\mathcal{N} = \sigma_{\text{prod}} \cdot \mathcal{L} \tag{4.2}$$

with σ_{prod} the production cross section for a specific process. Further the cross section is anti proportional to the energy $\sigma \propto E^{-2}$ and hence a high luminosity is required to compensate that effect. At the nominal intensity each beam will consist of 2808 bunches with about 10^{11} protons in a single bunch and a spacing of 25 ns between them colliding with a frequency of 40 MHz. A drawback of this high luminosity is the high average number of collision per bunch crossing, which is on the order of about 20 collisions. The integrated luminosity is defined as the integration of the luminosity over time and is mostly quoted as the amount of accumulated events.

$$N = \int \sigma \cdot \mathcal{L}\, dt = \sigma\, L_{\text{int}} \tag{4.3}$$

In Fig. 4.2 the instantaneous and integrated luminosity are shown for the 2011 data taking up to the technical stop in November. In total a data sample corresponding to an integrated luminosity of $L_{int} = 4.7\,fb^{-1}$ is recorded and will be used for this study. The luminosity can be measured by a so called *van der Meer scan* [68], which takes use of the advantage of direct correlation of the luminosity and the effective overlap area A_{eff} of the colliding beams. A_{eff} is measured by scanning in the transverse direction through the beams, where the relative interaction rate as a function of the transverse beam seperation is measured. The uncertainty on the integrated luminosity was determined to be 4.5% [69]. Additionally the luminosity can be measured in the hadron forward calorimeter by using the linear correlation of the occupancy of detector cells with the luminosity. Complementary to this online measurement the offline determination of primary vertices production in p-p collisions using zero-bias trigger streams can be used. The last two methods described are only relative measurements and the absolute normalization can be achieved by comparison with simulations resulting in large systematic uncertainties.

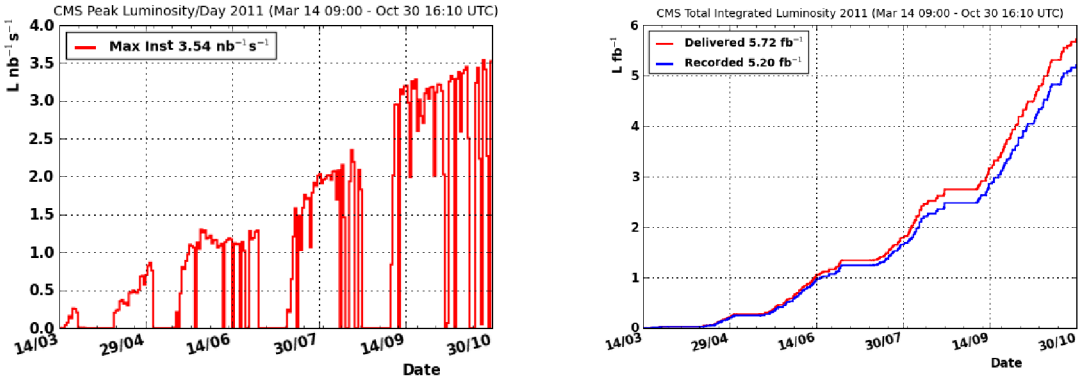

Figure 4.2: The daily peak instantaneous (left) and integrated (right) luminosity delivered by the LHC throughout the proton-proton run period in 2011. In total a data sample corresponding to an integrated luminosity of $L_{int} = 4.7\,fb^{-1}$ was recorded with a maximum peak luminosity of $\mathcal{L} = 3.54\,nb^{-1}s^{-1}$ reached at the end of the year. The right plot shows the integrated luminosity over time delivered by the LHC and actually recorded by CMS, where the recording efficiency is about 90%.

4.2 The Compact Muon Solenoid

In this section the *Compact Muon Solenoid* (CMS) detector and its components will be reviewed. A more detailed description can be found elsewhere [70]. The CMS detector is a general purpose detector designed and constructed by one of the largest worldwide operating collaboration of physicists, engineers and technicians up to now. As a result of this collaboration an excellent and compact detector with a length of 21.6 m, a diameter of 14.6 m with a total weight of 12500 tons is operational since the start of the LHC program in 2008. A schematic overview of the detector can be seen in Fig. 4.3. The detector is built approximately symmetric around the beam axis with a central barrel and two endcaps on both sides. A 13 m long, 5.9 m inner diameter and 3.8 T superconducting solenoid was chosen to design a compact detector with a good momentum resolution of charged particles. Within

the solenoid an inner tracking system and the calorimeters are installed. The still strong return field outside the solenoid, including a fully saturated 1.5 m thick iron yoke, harbors four layers of muon chambers inside this yoke. A more detailed review of the several subsystems will be discussed in the next sections by following the trajectory of particles emerging from the collision point.

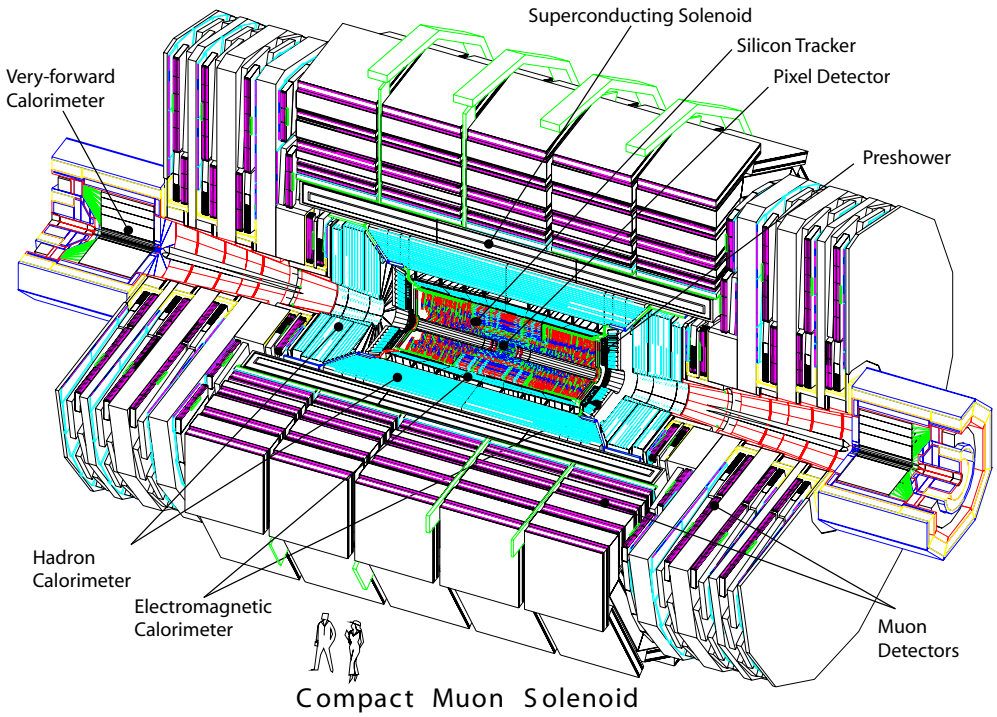

Figure 4.3: A schematic overview of the Compact Muon Solenoid detector with its various subsystems. The inner tracking system is installed closest to the beam line consisting of silicon pixel and strip detectors and is surrounded by the calorimeters. An electromagnetic and hadron calorimeter are placed within the superconducting solenoid. Outside the muon system is mounted within the iron return yokes of the solenoid. The picture is taken from [71].

4.2.1 The Coordinate System

The nominal collision point is the origin of the coordinate system used within the CMS collaboration. The z-axis is defined by the beam line and the perpendicular y and x axis are forming a right-handed coordinate system, where the y-axis is pointing vertically upwards and the azimuthal angle ϕ with respect to the positive x-axis is measured in the x-y plane. Similar the polar angle θ is defined with respect to the positive z-axis.
A quantity called pseudo rapidity η will be used in the following and is defined as

$$\eta = -\ln\left(\tan\left(\frac{\theta}{2}\right)\right) \ . \tag{4.4}$$

The pseudo rapidity depends only on the polar angle θ and is zero for any vector in the x-y plane and approaches infinity for the limit $\theta \to 0$. The sign of η indicates the hemisphere.

4.2.2 Inner Tracking System

The inner tracker system [70, 72–74] is designed to measure the trajectories of charged particles passing by with a high precision and efficiency. It should also be able to reconstruct primary and secondary vertices. Its scale is 5.8 m long with a diameter of 2.5 m and is built cylindrical around the beam pipe. A schematic overview of the inner tracking systems can be seen in Fig. 4.4.
If the LHC is running at the design luminosity of $\mathcal{L} = 10^{34}\text{cm}^{-2}\text{s}^{-1}$, there will be around 25 overlapping events per proton-proton collision leading to an average of 1000 particles to detect each 25 ns. A high granularity and fast response is required to ensure a proper trajectory identification with a long lifetime of the detector modules with respect to radiation damage of the high particle flux. Another important point is the material budget used in order to minimize multiple scattering, bremsstrahlung, photon conversions and nuclear interactions.
A tracker design using a combination of silicon pixel and strip detectors is chosen to meet the discussed requirements. Closest to the beam pipe, where the occupancy of the detector modules is highest, the silicon pixel elements are used. At higher radii lower occupancy allows to use silicon strip detectors.
In total the inner tracking systems is composed of 1440 silicon pixel and 15148 strip detector elements covering pseudo rapidities up to $|\eta| < 2.5$ with an total of 200m^2 active material.

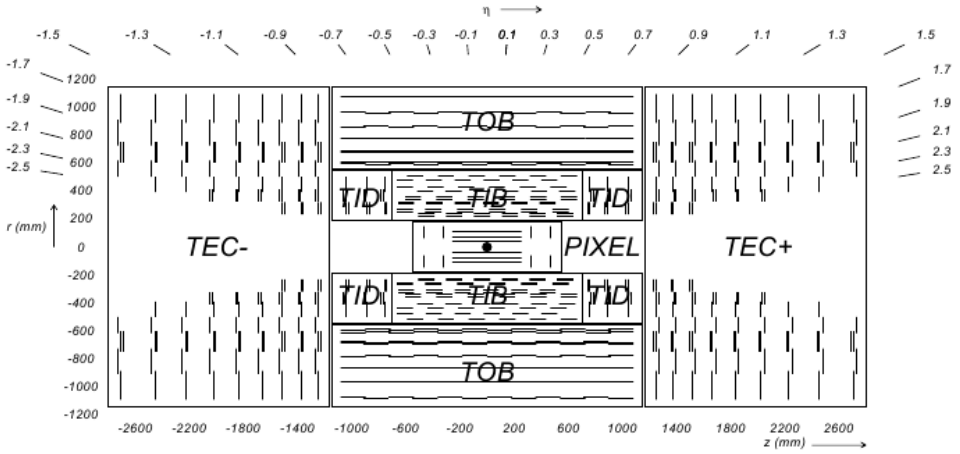

Figure 4.4: Schematic overview of the CMS inner tracking system [70]. Each line indicates a detector and double lines back-to-back elements. The inner tracking system consists of three layers pixel detectors in the barrel and two disks attached on each endcap. They are surrounded by ten layers of silicon strip detectors and twelve disks at each endcap. The picture is taken from [71].

Silicon Pixel Detector

The silicon pixel modules are the part of the tracker system closest to the beam pipe. A precise tracking in $r - \phi$ and $r - z$ is crucial for a small impact parameter resolution and identification of secondary vertices. Three layers of pixel detectors in the barrel region (BPix) at radii 4.4 cm, 7.3 cm and 10.2 cm and two disks on each endcap (FPix) at $z = \pm 34.5$ cm and $z = \pm 46.5$ cm with a total amount of 66

million pixels (48 million BPix + 18 million FPix) leading to 1m^2 of active pixel material covering pseudo rapidities up to $|\eta| < 2.5$, where the size of a single cell is $100 \times 150\,\mu m^2$.
Charged particles passing a silicon pixel detector induce electron-hole pairs perceiving a Lorentz drift in the crossed electricand magnetic fields in the barrel region. The angle between the Lorentz drift and the electric field is the so called *Lorentz angle*, which leads to a charge spreading over more than one pixel. This *charge sharing* of multiple pixels improves the spatial resolution. In order to also benefit in the FPix from the charge charring induced by the Lorentz effect, the pixel modules mounted on the endcap disks exhibits a turbine like geometry with blades rotated by $20°$.
This design of three layers in the barrel region and two disks on the endcaps yields three tracking points for each charged particle over almost the full η-range of the pixel detector with a spatial resolution of about $10\,\mu m$ for the $r-\phi$ and $20\,\mu m$ for the z-measurement.

Silicon Strip Detector

At higher radii the occupancy is getting lower and silicon strip detectors with a larger surface can be used, because the particle flux inducing radiation damage is decreasing with increasing radii. Ten layers of silicon strip- are surrounding the pixel-detectors in the barrel region between the radii 20 cm and 116 cm. The silicon strip detectors can be classified into three subsystems: (a) the *Tracker Inner Barrel* and *Disks* (TIB, TID) consist of four layers in the barrel (radii 20 cm-55 cm) and three disks in both endcap regions, (b) followed by six layers of *Tracker Outer Barrel* (TOB) up to a radii of 116 cm (c) and nine disks mounted with *Tracker EndCap* (TEC) elements. All silicon strip detector elements with 9.6 million strips have an active material area of $198\,\text{m}^2$.
The TIB/TID delivers four $r-\phi$ tracking points for each charged particles using $320\mu m$ thick silicon micro-strips mounted parallel to the beam axis. The first two layers of TIB consists of strips with a length of $80\,\mu m$ and layer three and four with a length of $120\,\mu m$, where the TID's strip length varies between 100 and $141\,\mu m$. The inner part of the tracker system is surrounded with $500\,\mu m$ thick silicon strip modules of the TOB, where the length of those strips are $183\,\mu m$ on the first four layers and $122\,\mu m$ on the last two layers. This structure allows six additional $r-\phi$ tracking points. The thickness of the TOB's can be increased with respect to TIB/D elements, because of another decrease in occupancy. At each endcap nine disks of TEC's carrying up to seven rings of silicon strip detectors with thicknesses of $320\,\mu m$ on the inner four rings and $500\,\mu m$ on the outer three rings are placed, which extending the z coverage to $|z| < 282$ cm. A second strip detector is mounted back-to-back with a stereo angle of 100 mrad on the modules of the first two layers of the TIB, TID, TOB's and as well of the first, second and fifth ring of the TEC's. Such an arrangement allows a measurement of the z-coordinate as well.
The single point resolution varies from $230-530\,\mu m$ in z and $23-52\,\mu m$ in the $r-\phi$ measurement and ensures at least nine tracking points in the η-range of $|\eta| < 2.4$.

4.2.3 Electromagnetic Calorimeter

The electromagnetic calorimeter (ECAL) [75] provides an energy measurement of photons, electrons and charged hadrons. Beside the common criteria like fine granularity, fast response and radiation resistance, it has to provide an excellent diphoton resolution in order to identify the Higgs decay

processes into two photons, whose discovery is one of the main goals of the CMS collaboration. A transverse overview of the ECAL can be seen in Fig. 4.5.

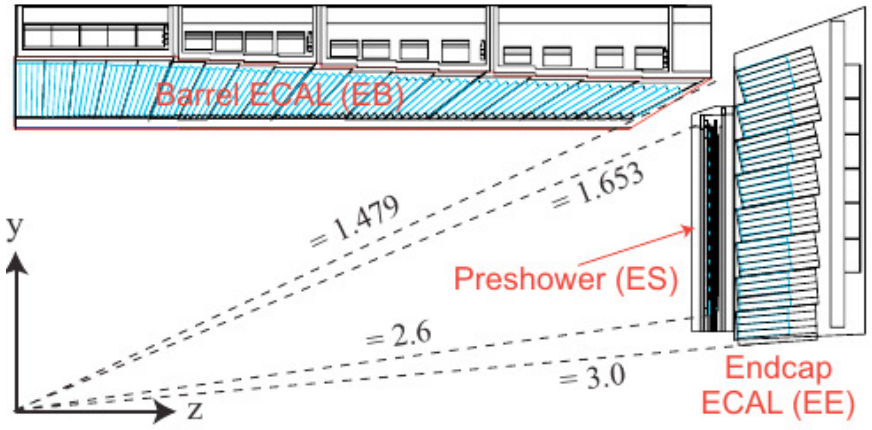

Figure 4.5: A slice through the CMS detector showing a schematic overview of the ECAL configuration. It consists of three subsystems: the ECAL barrel, the endcap and an electromagnetic preshower system in order to identify neutral pions in the forward region. The picture is taken from [71].

The ECAL is a hermetic homogeneous calorimeter built of lead tungstate ($PbWO_4$) crystals. $PbWO_4$ crystals have a high density of $\rho = 8.28\,\mathrm{g/cm^3}$, a short radiation length of $X_0 = 0.89\,\mathrm{cm}$ and a small Molière radius of $R_M = 2.2\,\mathrm{cm}$, which defines the radius of a cylinder containing on average 90% of the shower energy deposits. Those characteristics of $PbWO_4$ crystals allows to design a compact ECAL with fine granularity. Another advantage of those crystals is the fast scintillation decay time, which is in the same order as the LHC bunch crossing rate, namely about 80% of the total light emission within 25 ns.

Similar to the inner tracking system the ECAL is divided into a barrel region (EB) and endcaps (EE). The EB crystal volume is in total $8.14\,\mathrm{m^3}$ with an inner radius of 129 cm and a weight of 67.4 t. It covers pseudo rapidities up to $|\eta| < 1.479$ and the granularity is 360-fold in ϕ and 2×85-fold in η leading to a total amount of 61200 tapered shaped crystals mounted in a quasi-projective geometry to avoid cracks aligned with particle trajectories. The crystal have a front face cross section of 0.0174×0.0174 in η-ϕ ($22 \times 22\,\mathrm{mm^2}$) and $26 \times 26\,\mathrm{mm^2}$ at the rear face. The length of the crystals is 230mm, which corresponds to $25.8 X_0$.

The EE are extending the pseudo rapidity coverage of the ECAL to $1.479 < |\eta| < 3.0$ and are placed at $|z| = \pm 315.4\,\mathrm{cm}$, taking already the shift of 1.6cm towards the nominal interaction point into account once the magnetic field is switched on. It consists of another 14648 identically shaped crystals mounted in a rectangular x-y grid, where each crystal is pointing slightly off the interaction point. The front face cross section is $28.62 \times 28.62\,\mathrm{mm^2}$ and the rear face $30 \times 30\,\mathrm{mm^2}$ by a crystal length of 220 mm corresponding to $24.7\,X_0$.

The use of $PbWO_4$ crystals with its low light emittance, the high longitudinal magnetic field and radiation tolerance, especially in the endcap region of the ECAL leads to the choice of two types of photo detectors collecting the scintillation light of the crystals: *avalanche photodiodes* (APD) in the EB and *vaccum phototriodes* (VPT) in the endcaps. APD's are insensitive to high magnetic fields and

the high particle flux in the endcaps favored VPT's with lower quantum efficiency and internal gain, but larger surface coverage.
The last missing part of the ECAL is the preshower detector covering a range of $1.653 < |\eta| < 2.6$, which is installed in the endcap in order to identify pions. It is a sampling detector with two layers of lead radiators with silicon strip sensors attached and aligned orthogonal in the two planes, where the radiators working as initiators for electromagnetic showering and the silicon strip detectors measure the deposit energy and the transverse shower shape. The thickness of the first radiator layer corresponds to a material budget of $2X_0$ and the second to $1X_0$, hence 95% of single photons starts showering before the second sensor plane.
In 2004 the energy resolution of the ECAL was measured with electron beams having momenta between 20 and 250 GeV to be typically [70]

$$\left(\frac{\sigma}{E}\right)^2 = \left(\frac{2.8\%}{\sqrt{E}}\right)^2 + \left(\frac{0.12}{E}\right)^2 + (0.30\%)^2 \tag{4.5}$$

where E is the energy in GeV. The energy resolution consists of three parts: (1) the stochastic part proportional to $1/\sqrt{E}$, (2) a noise term including electronic, digitization and pileup noise and (3) constant term coming mainly from non-uniformity of the longitudinal light collection. For unconverted high energetic photons, $E \approx 100$ GeV, the dominant contribution to the resolution arises from the constant part and a good ECAL calibration is mandatory for a good performance.
The absolute energy calibration and the inter-calibration have been performed using electron test beams and *in situ* $\pi^0 \rightarrow \gamma\gamma$ physics events [76]. The inter-calibration is a channel-to-channel relative component, which originates from a crystal-to-crystal variation of the scintillation light yield. Using the first $250\,\mathrm{nb}^{-1}$ the channel-to-channel calibration precision is 0.6% for EB and 2.2% for the forward preshower. A similar performance was measured for the absolute energy calibration with a precision of 1% in the barrel and 3% in the endcap. An improvement will be achieved with a larger collection of data events including also Z and W decays into energetic electrons.

4.2.4 Hadron Calorimeter

A longitudinal view of the hadron calorimeter (HCAL) [77] is shown in Fig. 4.6. The HCAL is important for the measurements of hadronic jets and also missing transverse energy, due to undetected neutrinos or new exotic weakly interacting particles. It is splitted into four subsystems. The HCAL barrel (HB) and endcap (HE) are installed behind the ECAL system and the size is constrained to R=1.77 m for the inner radius and R=2.95 for the outer to be placed within the magnet coil. Due to this constrained size the amount of absorber material is limited and an additional *outer* component (HO) of the HCAL, outside the solenoid, used as a so called *tail catcher* is needed. The HB and HE have a coverage in pseudo rapidity up to $|\eta| < 3.0$, which is extended up to $|\eta| < 5.2$ by a *forward* calorimeter (HF) placed at $z \pm 11.2$ m, with respect to the nominal interaction point.
The HB is a sampling calorimeter based on steel and brass as absorber material and scintillators tiles as active material, which are divided in $\Delta\eta \times \Delta\Phi = 0.087 \times 0.087$. The inner- and outer most absorber plates are stainless steel absorber for structural strength and the rest are brass plates. Brass has a density of $\rho = 8.53\,\mathrm{g/cm}^3$ with a radiation length of $X_0 = 1.46$ cm and an interaction length of $\lambda_I = 16.42$ cm. At $\eta = 0$ the total absorber thickness corresponds to $5.82\lambda_I$, where at $|\eta| = 1.3$ it

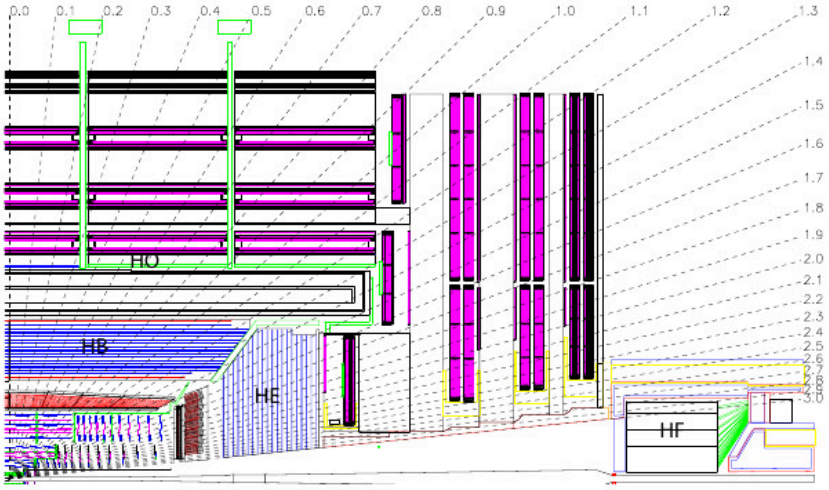

Figure 4.6: Schematic overview of the CMS hadron calorimeter [70] embedded within the superconducting solenoid. The HCAL is divided into four parts: the barrel hadron calorimeter (HB), the endcap calorimeter (HE) and an outer calorimeter (HO) outside the solenoid needed for the limited absorber material in the central region. An additional calorimeter is placed in the most forward region (HF). For comparison also the location of the inner tracking system, the ECAL and the muon system as well are shown. The picture is taken from [71].

is $10.6\lambda_I$, due to geometry reasons. The ECAL in front of the HCAL adds around $1.1\lambda_I$ of absorber material. Wavelength-shifting and clear fibers are employed to collect and transport optical signals emitted in the active material to hybrid photodiodes (HPD), that can operate in high axial magnetic fields.

Brass as absorber material was also chosen for the HE and the design is driven by minimizing the amount of cracks between HB and HE, rather than optimize the resolution of hadronic jets in the endcap region. In total the HE has a thickness of about $10\,\lambda_I$ including ECAL material and a granularity of the scintillator tiles of $\Delta\eta \times \Delta\Phi = 0.087 \times 0.087$ for $1.3 < |\eta| < 1.6$ and $\Delta\eta \times \Delta\Phi \approx 0.17 \times 0.17$ for $1.6 < |\eta| < 3.0$.

In the central region of the detector the EB and HB have together a thickness of about $7\lambda_I$, which is a not sufficient containment for hadron showers. Therefore an additional HO is mounted on top of the solenoid. The HO consists of scintillator with similar granularity as HB using the solenoid coil as an additional absorber material and covers ranges up $|\eta| < 1.26$. In the most central region, where the EB and HB absorber material budget is the lowest, two layers of scintillator are installed on either side of the first 19.5 cm thick iron yoke leading to a minimum of $11.8\,\lambda_I$ absorber thickness.

Very forward ranges $3.0 < |\eta| < 5.0$ are covered by the HF calorimeter. It is designed to survive the harsh environment with a high particle flux close to the beam pipe. Quartz fibers collecting the Cherenkov light of particles traversing through with a good radiation hardness were chosen for the active material and steel as absorber material.

The HCAL energy resolution has been measured in test beams with electrons, pions, protons and muons and complementary in cosmic muon data as well [78]. For the barrel and endcap calorimeters

(HB, HO, HE) the energy resolution has been measured to be [79]

$$\left(\frac{\sigma}{E}\right)^2 = \left(\frac{84.7\%}{\sqrt{E}}\right)^2 + (7.4\%)^2 \tag{4.6}$$

and analogeous for the forward calorimeter (HF) [80]

$$\left(\frac{\sigma}{E}\right)^2 = \left(\frac{198\%}{\sqrt{E}}\right)^2 + (9\%)^2\,, \tag{4.7}$$

including a stochastic and constant term. The hadronic energy resolution is largely determined by fluctuations in the neutral pion production in showers. In comparison the energy resolution of the HCAL is worse than as for the ECAL system.

4.2.5 Magnet

A large superconducting solenoid [81] is installed inside the CMS detector and encloses the inner tracker system, the ECAL and HCAL except the outer hadron calorimeter. It has a length of 12.9 m and an inner diameter of 5.9 m. A high magnetic field of 3.8 T inside the magnet is required to achieve a momentum resolution of $\Delta p/p \approx 10\%$ for energetic muons ($p = 1\,\text{TeV}$). The magnetic flux generated by the solenoid coil is returned via a 1.5m thick saturated iron yoke, which also hosts several layers of the muon system.

4.2.6 Muon System

The outermost part of the CMS detector [82] consists of the Muon system shown in Fig. 4.7. Muons are involved in many interesting physics processes, like Higgs decays and SUSY processes. In addition they are utilized for many SM precision measurements involving B physics and/or electroweak processes. The identification, reconstruction and momentum resolution of muons as well as triggering on muons is therefore of prior importance.
The muons system is splitted into two parts including three types of gaseous detectors to identify muon candidates and measure their momentum: (1) the central part *muon barrel* (MB) covering pseudo rapidities up to $|\eta| < 1.2$ and (2) forward parts with two *muon endcap*'s (ME) extending the coverage up to $|\eta| < 2.4$. In the barrel region drift tube chambers (DT) are used. Although slow because of the drift time and sensitive to the magnetic field because of the Lorentz force on the drifting electrons, they can be used in the barrel region with its low neutron background, low muon rate and low residual magentic field. In contrast the endcap faces a high neutron background, a high muon rate and also a high magnetic field as well. Hence so called cathode strip chambers (CSC) are used. In both muon subsystems also resistive plate chambers (RPC) are added with a fast response and good time resolution in order to assign correct bunch crossings. The spatial resolution of the RPC's is worse compared to the resolution of the DT's and CSC's and therefore a combination in both subsystem was chosen.
The DT are 1.2 mm thick and 9.6 mm long aluminium cathodes with stainless steel anodes wires at their center. A mixture of Ar and CO_2 is used as gas. The DT's have a maximal drift length of $2\,cm$ and a spatial resolution of about $200\,\mu m$. The precision in ϕ is $100\,\mu m$ and 1 mrad in the

direction of the muon vector with a time resolution of 5 ns. In comparison, the CSC's are $1m \times 2m$ trapezoidal chambers consisting of six gas gaps with each having a plane of radial cathodes and a plane of anode wires oriented perpendicular. As gas a mixture of Ar-CO_2-CF_4 is filled. The spatial resolution is typically on the order of 200 μm with an angular resolution of about 10 mrad in ϕ with a time resolution of 6 ns, which is a little bit higher compared to DT's. The last detector type used in the muon system are the RPC's. They consist of a double-gap chamber operating in avalanche mode with a gap width of 2 mm. The spatial resolution of the RPC is defined by the cell size.

The MB consists of 4 stations (MB1, MB2, MB3, MB4) at radii of 4.0, 4.9, 5.9 and 7.0 m including in total 250 drift tube chambers mounted cylindrical around the beam axis inside the iron yoke of the solenoid arranged in five wheels covering the barrel part. Each wheel is divided into twelve sectors, each covering 30° in azimuthal angle with the three inner stations consisting of 12 DT layers, whereas the outer stations consists of 14 DT layers. Two RPC's are attached on each of the first two stations and one RPC on each of the the two outermost stations. Hence a high p_T muon in the barrel region will pass six RPC's and four DT chambers leading up to 44 measured space points, which can be utilized to build a muon candidate.

Similarly the ME consists of 4 stations (ME1, ME2, ME3, ME4) of CSC's arranged in concentric rings around the beam axis. The first stations have three rings of CSC chambers and two rings for the RPCs, while the second ring of the fourth station has been staged out. In total 468 CSC chambers are installed in the two endcaps, where each ring consists of 36 chambers, except the first rings of the second, third and fourth station, where 18 chambers are installed. Each CSC measures up to six space coordinates (r, ϕ, z). RPC's are instrumented additionally in the first three stations.

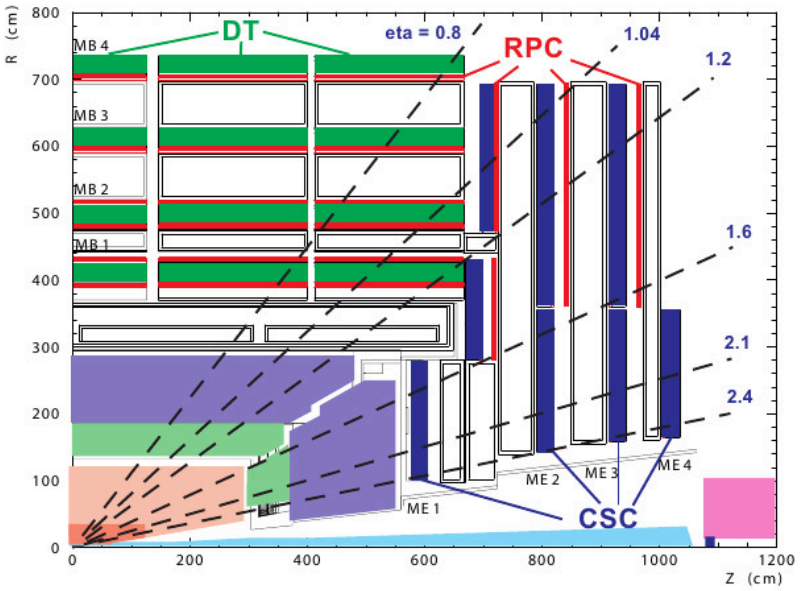

Figure 4.7: The muon system is the largest part of the CMS detector embedded in the iron return yoke of the solenoid. In the barrel region four stations including several layers of DTs and RPCs are installed, whereas in the endcap region four disks mounted with CSCs and RPCs are in usage. The picture is taken from [71].

4.3 Trigger and Data Acquisition System

At the design luminosity of the LHC with a bunch crossing rate of 40 MHz there will be around 10^9 collisions per second in the detector. Assuming an event size of 1.5 MB leads to tens of TB/s to record, which is impossible to handle with the limited computing resources available. Therefore a two level trigger and data acquisition system were designed in order to reduce the amount of recorded collisions by six orders of magnitude (see Fig. 4.8). The trigger selects interesting events out of millions of uninteresting ones, so the trigger is of exceptional importance and needs a very careful consideration reviewed in the following.

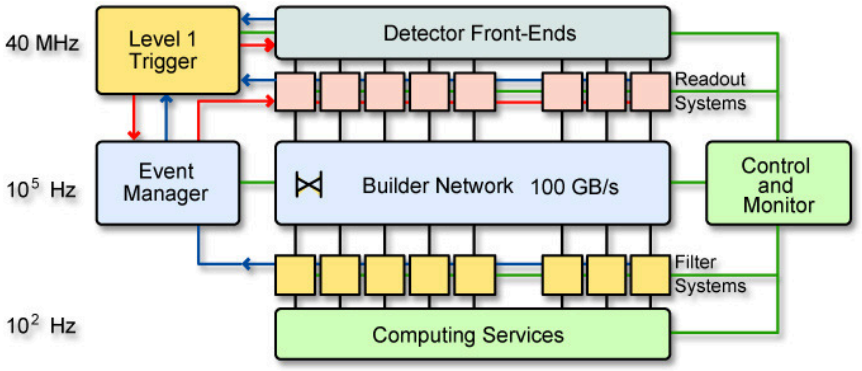

Figure 4.8: The data acquisition and trigger systems consists of the front-end readout electronics, a L1 hardware trigger system and a software based HLT system running on a computer farm. This system allows to reduce the event rate of about 40 MHz at the design luminosity of the LHC to a manageable level of about 100 Hz. The picture is taken from [71].

Level-1 trigger

The Level-1 (L1) trigger system [83] is built of hardware processors and reduces the event rate from 40 MHz to 100 kHz. In total 3.2 μs are allocated for the transition from the front-end electronics to and back from the L1 trigger system including the decision making time. The detector informations are stored meanwhile in memory buffers of the front-end electronics.
The L1 decision is based on informations of the calorimeters and muon systems with a reduced granularity and resolution of the detector. Also correlations of both detector subsystem are taken into account by so called global L1 triggers. In a first step trigger objects are formed from the information provided by the calorimeter and muon system including photons, electrons, muons and jets. Subsequently those objects and additional the total and missing transverse energy and the jet multiplicity are passed to the global triggers, which take a decision based on the presence of several objects passing predefined thresholds.

High-Level trigger

If an event is accepted by the L1 trigger system the high resolution detector data is passed to the high-level trigger software running on a CPU farm. The High-Level trigger (HLT) system [84] is a software

based routine reducing the event rate of 100 kHz after the L1 decision to finally about 150 Hz at high luminosity runs. A more sophisticated detailed event reconstruction is used to provide all needed objects and topologies in order to select events according to the physics goals. Since the HLT's are software triggers, the operation is very flexible and due to changing environments or physics goals the individual trigger rates can easily be adjusted in terms of selection algorithm and/or object thresholds. The final event rate of about 150 Hz corresponds to the data stream of 225 MB/s (event size ≈ 1.5 MB) is transferred to a central storage system based at CERN.

CHAPTER 5

Software Tools and Event Reconstruction

Each event recorded by the CMS detector is stored including the raw electronic responses of the detector. The information has to be translated into physics objects and processes, which have took place within the detector, commonly called *reconstruction*. In order to compare the measurements with theoretical predictions, a huge amount Monte Calo events have to be processed and the detector response simulated. The CMS software (CMSSW) framework, developed to meet these requirements, will be reviewed in the following as well as the Monte Carlo event generation, detector simulation and physics object reconstruction. Finally the CMS computing model will be discussed.

5.1 CMSSW: CMS Software Framework

The CMSSW (**CMS S**oft**W**are) framework is a modular package built based on the Event Data Model (EDM). Several services taking for example care of simulation, calibration and reconstuction are included. It runs with a single executable *cmsRun*, both for MC and data samples, where the specific declaration of plugin modules to carried out are specified in a configuration file written in Python [85]. For each event the chain of modules listed in the configuration file with its given parameters are executed.
The event in the CMS EDM concept is a C++ object container for all raw and reconstructed data for a single collision. All objects in the event can be written into ROOT [86] files offering a simple tree structure.
The CMSSW framework uses six different types of loadable modules with different functionalities:

- **Source:** Generates the event by reading the EventSetup from the ROOT files, or simply an empty event in case of MC generation.
- **EDProducer:** Writes new objects to the event.
- **EDFilter:** Studies the properties of the events and returns a boolean value, which can be used to stop the execution of further modules, i.e. skip the event.

- **EDAnalyzer:** Analyzes the event and writes some output, e.g. a set of histograms.
- **EDLooper:** Controlling of the multi-pass looping.
- **OutputModule:** After execution of all desired modules, the event information is read and stored.

A typical processing chain used within cmsRun is illustrated in Fig. 5.1.

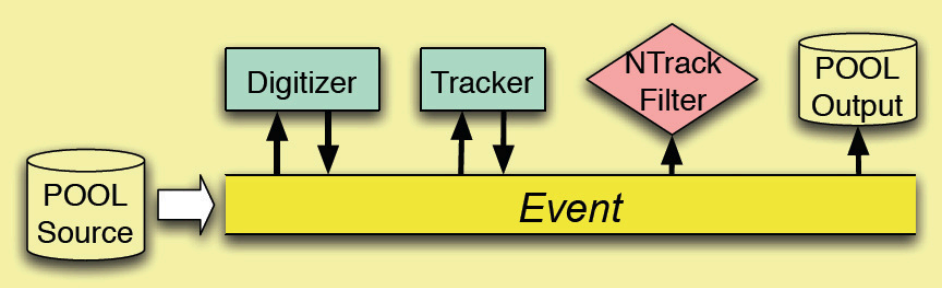

Figure 5.1: A sample module chain containing a *Source* which creates the event, various *EDProducers* (Digitizer, Tracker) adding additional data to the event and an *EDFilter* (NTrack filter) filtering only interesting events. Once all modules have been executed the *OuptutModule* stores the output. The plot is taken from [87].

5.2 Monte Carlo Event Generation

Monte Carlo (MC) event generators are tools to help studying the complex particle interactions in high energy physics. Modern generators split the entire event modeling, including QCD/QED radiation, secondery interactions, hadronization of partons and hadron decays, in several steps. Starting from the lagrangian structure of the physics model the hard interaction is calculated, which is provided by so called matrix element generators. The hadronization and fragmentation processes of colored final state partons from the matrix element or parton shower transforms them into colorless hadrons, which will finally decay. Matrix element generation and parton shower evolution are complementary and the combination is necessary for studying multi-jet processes. But the combination can lead to double counting. Therefore so called matching schemes are developed in order to match jets from the matrix element with jets from parton showers.
Interfaces implemented in the CMSSW framework are realized for many event generators (Pythia6 [88] (Pythia8 [89]), Herwig++ [90], Alpgen [91], Sherpa [92], Madgrah [93]). In this study the MC events used were generated with Madgraph5 interfaced to Pythia6 for hadronization and fragmentation. SUSY mass spectra and branching ratios were calculated with SOFTSUSY [94] and SUSY-HIT [95] packages. The actual event generation is done with Pythia6.

- **Pythia6:** is a general purpose event generator offering leading order $2 \rightarrow 2$ matrix element calculations and parton shower evolution, describing many physics aspects. The hard interaction describing the initial high energetic interaction is implemented in Pythia for more than 300

processes including the SM and beyond SM models as well. Higher order corrections and radiative effects are described by the concept of parton showers. Coloured particles which might results from the hard process or parton shower are hadronized via the so called Lund string fragmentation model [96].

- **Madgraph/MadEvent:** MadEvent is a multi-purpose tree-level event generator, which uses the matrix element calculations from Madgraph in order to calculate the cross section and events. Madgraph can handle processes up $2 \rightarrow 6$ including SM and also beyond SM processes. The event produced by MadEvent can be passed to a shower MC program, which is in case of CMSSW framework Pythia6. In order to match the multi parton matrix elements with the partons added by the concept of parton shower the so called MLM [97] matching scheme is applied.

- **Softsusy:** calculates the mass spectras of sparticles in the MSSM with the full flavor mixing structure by solving the renormalization group equations including theoretical constraints on soft supersymmetry breaking terms, specified by the user.

- **SUSYHIT:** is a package for the computation of supersymmetric particle decays in the MSSM. It is based on HDECAY [98] and SDECAY [99], which calculate the decay widths and branching ratios of the MSSM higgs boson and SUSY particles, respectivley.

5.3 Detector Simulation

The detector simulation can be split into three components: the simulation of the particles traversing through and interacting with the detector material, the simulation of the signals coming from the CMS readout structure and the simulation of the L1 trigger system.
Generated particles emerging from the collision have to pass several detector components and interact with the material. For this purpose the simulation package Geant4 [100] is implemented within the CMSSW framework. This package includes tracking, geometry, physics models and hits. The physics models contain the description of electromagnetic and nuclear interactions in presence of a magnetic field over an energy range of 250 eV up to the TeV scale.
The simulation of the electronics readout response leading to digital signals in presence of different energy deposits is called *digitization*.

5.4 Event Reconstruction

Particles emerging from the collision point deposit energy in the calorimeter systems or signal points in the active material of the inner tracking or muon system respectively. Out of those signals the reconstruction and identification of different physics objects is necessary, where the signatures in the detector vary from object to object. Table 5.1 summarizes the physics objects and the detector subsystems used to reconstruct and identify them.
Muons for example are minimum ionizing particles and deposit only a small amount of energy in the calorimeter and can be identified by several hits in the tracker and muon system. Electrons on the

other hand will deposit most of its energy in the electromagnetic calorimeter, due to bremsstrahlung and pair conversion. Hadronically decaying taus and hadronic jets can be reconstructed by energy clusters in the calorimeters, but a more sophisticated algorithm with improved accuracy is available. The so called Particle Flow (PF) algorithm [101] combines the information from the various CMS sub-detectors to identify all charged and neutral particles in an event. Tracks reconstructed in the inner tracking system are extrapolated and linked to energy clusters in the electromagnetic and hadron calorimeter. Those reconstructed particles are used to determine hadronic jets, hadronic decaying taus and missing transverse energy.
The following sections summarize the reconstruction and identification algorithm used within this study. A more detailed description can be found in the corresponding publications given in each part.

Table 5.1: Summary of the information of the CMS sub-detectors used in the reconstruction of physics objects. The partilce flow (PF) algorithm combines the information of all sub-detectors in order to reconstruct all physics objects.

Object	Tracker	ECAL	HCAL	Muon System
Electron/Photon	✓	✓	-	-
Muon	✓	-	-	✓
Particle Flow Taus	✓	✓	✓	✓
Calorimeter Jets	-	✓	✓	-
Particle Flow Jets	✓	✓	✓	✓
Particle Flow E_T^{miss}	✓	✓	✓	✓

5.4.1 Track Reconstruction

Most object algorithms are using reconstructed tracks in the inner tracker system for identification. Charged particles passing through the tracker system leave several signal points in the detector modules. The algorithm to find and reconstruct track candidates in the CMS collaboration is the combinatorial track finder (CTF) [102, 103]. The starting point in the CTF algorithm are pairs or triplets of hits, which form, with the additional assumption that the track originates from either a known vertex or beam spot, the seed for the propagation. The parameters of the seed are first estimated at the beam spot using a perfect helix as fit through the hit points and then propagated to the outer hit, while updating the parameters at each reconstructed point.
Based on the seed parameters a Kalman filter [104] proceeds iteratively through all layers of the tracker system updating successively the track parameters with each new measurement and finally yields a track trajectory. The layers compatible with the initial trajectory are determined according to the equations of motion of a charged particle in a constant magnetic field including energy losses.If several hits in the new layer are compatible with the predicted trajectory, a new track candidate is created for each hit and an additional one without any hit to account for cases were the charged track did not leave a hit.
To avoid ambiguities in the track finding, like the same track candidate is reconstructed starting from different seeds or more than one track candidate originates from the same seed resulting in double

counting, the fraction of shared hits of two track candidates should not exceed a predefined value. If two track candidates do so the candidate with the least number of hits or with the highest χ^2 is discarded.
The last step is a refitting of the track candidate using the identified hits, because the trajectory parameters are finally determined with the last hit and can be biased by the constraints used before. This refitting is done in multiple iterations yielding an optimal estimate of the parameters.

5.4.2 Vertex Reconstruction

Another very important task is the correct reconstruction of the interaction vertex. The location and the uncertainty of the so called *primary vertex* is computed from a given set of reconstructed tracks [103, 105]. Tracks emerging from the primary collision point are selected by their transverse impact parameter significance with respect to the beam line ($S_{d_{xy}} = d_{xy}(BL)/\sigma_{d_{xy}}$), number of hits in silicon pixel and strip detectors and the normalized track χ^2, where no transverse momentum p_T requirements on the tracks were set to ensure also high reconstruction efficiency in minimum bias events. Vertex candidates are then defined by grouping tracks within $\Delta z_{sep} \leq 1\,\text{cm}$ with respect to their nearest neighbors, where z is the longitudinal coordinate of the extrapolated point of closest approach to the beam line. Candidates containing at least two tracks are then parsed to an *adaptive vertex filter* (AVF) [106] to compute the vertex parameters.
The AVF algorithm is an iterative re-weighted least squares fit and does not reject outlying tracks rather it down-weights them, where the weight depends on the track compatibility via its χ^2 with the vertex. A track consistent with the vertex will get a weight close to one $w \approx 1$. The weights for an initial vertex candidate will be computed and a updated vertex is estimated. More iterations are done until convergence is reached. For the vertex fitting in each iteration a Kalman filter is used, which takes also the weights of the tracks into account. The number of degrees of freedom in this procedure is defined as $n_{dof} = 2\sum_{i=0}^{nTracks} w_i - 3$ with w_i is the weight of the ith track. It can be easily seen, that the n_{dof} is directly correlated with the number of compatible tracks with the primary vertex and hence can be used to select the p-p collisions, where the vertex resolution depends strongly on the number of tracks belonging to the vertex and their transverse momentum p_T. In Fig. 5.2 the vertex resolutions measured in minimum bias events are shown in comparison with Pythia simulations [103]. The resolution in x(y) and z is typically about $25\mu m$ and $20\mu m$ for primary vertices reconstructed with more than 30 tracks with a reconstruction efficiency close to 1 if there are two or more tracks with transverse momenta greater than 0.5 GeV emerging from the vertex.

5.4.3 Electron and Photon Reconstruction

Electrons and photons have characteristic signatures which can be used in order to reconstruct and identify the corresponding energy deposits. Both particles interact with the detector material and loose a significant amount of energy due to bremsstrahlung and pair conversion in form of an electromagnetic (EM) shower. In order to determine the initial energy of the electrons or photons the sum of all energy deposits including the characteristic EM shower has to be taken into account. Due to the tracker material more than 50% of the photons are converted into electron positron pairs and around 35% of the electrons have radiated about 70% of their initial energy already before reaching

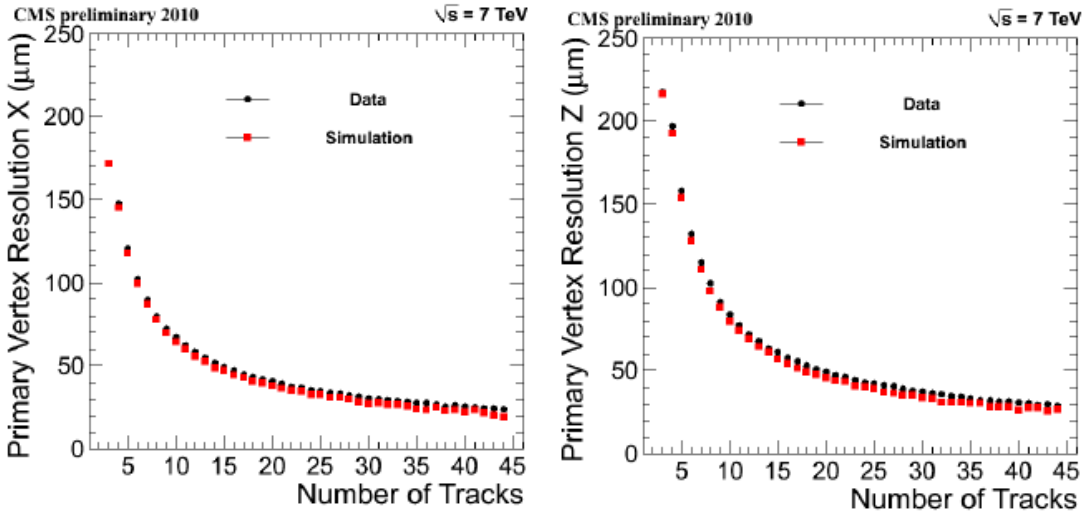

Figure 5.2: Vertex resolution in x (left) and z (right) as a function of the number of tracks used within the reconstruction algorithm. For comparison also prediction from simulations (Pythia8) are shown. The plots are taken from [103].

the ECAL with a shower spread in ϕ due to the Lorentz drift induced by the magnetic field. The use of $PbWO_4$ crystals with a Molière radius of $R_M = 2.2\,\text{cm}$ results in a typical energy spread of unconverted photons within 5×5 crystals.

Different algorithms for the barrel and endcap region are used to form superclusters out of the ECAL energy deposits [71, 107], where superclusters are aimed to recover the energy of emitted photons due to bremsstrahlung. In the barrel region the so called hybrid algorithm is performed. This algorithm starts with the highest E_T crystal and forms dominoes of a narrow width in η corresponding to 3 or 5 crystals. Collecting all dominoes along the ϕ direction up to an extension of 0.3 rad with respect to the initial seed forms the supercluster. In the endcap the multi5x5 or often also quoted as island algorithm is used for creating the superclusters, which are the sum of all matrix clusters along the ϕ direction with respect to the initial seed, where matrix clusters are energy deposits inside 5×5 matrices of crystals. Similar to the hybrid algorithm the maximum radial extension is also 0.3 rad for superclusters in the endcap.

The definition of superclusters is similar for electron and photon reconstruction, but the final trajectory is done differently, due to the fact that the electron track can be reconstructed by its hits in the tracker system, whereas photons do not leave any hits. We start with the electron reconstruction, which is based on the so called ECAL driven seeding. The ECAL driven seeding uses superclusters with $E_T > 4\,\text{GeV}$ and tries to match hits in the tracker system to those superclusters. The characteristic narrow width in η and the spread in ϕ, due to bremsstrahlung in the tracker material and the electron bending in the magnetic field, is taken into account in the prediction of hit pairs in the innermost pixel detector layers. If two pixel hits consistent with the propagation are found they will serve as a seed for the electron track reconstruction. The propagation through the tracker material is done with a Gaussian Sum Filter (GSF) [108] using a specific Bethe Heitler modeling [109] of the energy loss due to bremsstrahlung, which describes the electron propagation better in comparison with the standard

Kalman Filter procedure used within the track reconstruction.
The photon reconstruction uses the same supercluster algorithm as a starting point. In contrast to electrons no track reconstructed with the GSF procedure should coincide with the ECAL superclusters. Photons reaching the ECAL system can be unconverted and converted photons as well. In order to distinguish them the $R9$ observable can be utilized, which is defined as:

$$R9 = \frac{E_{3\times3}}{E_{SC}}\,, \tag{5.1}$$

where $E_{3\times3}$ is the energy deposit in a 3×3 array of crystals around the supercluster crystal with the highest E_T and E_{SC} is the total supercluster energy. Unconverted or close to the ECAL system converted photons are populating $R9$ values around unity.
An impression how well the electron/photon reconstruction and identification works can be seen from Fig. 5.3 where the dielectron invariant mass spectrum in the upsilon region $m_{ee} = [6, 12]\mathrm{GeV/c^2}$ and the diphoton invariant mass spectrum for $\pi^0 \to \gamma\gamma$ decays are shown.

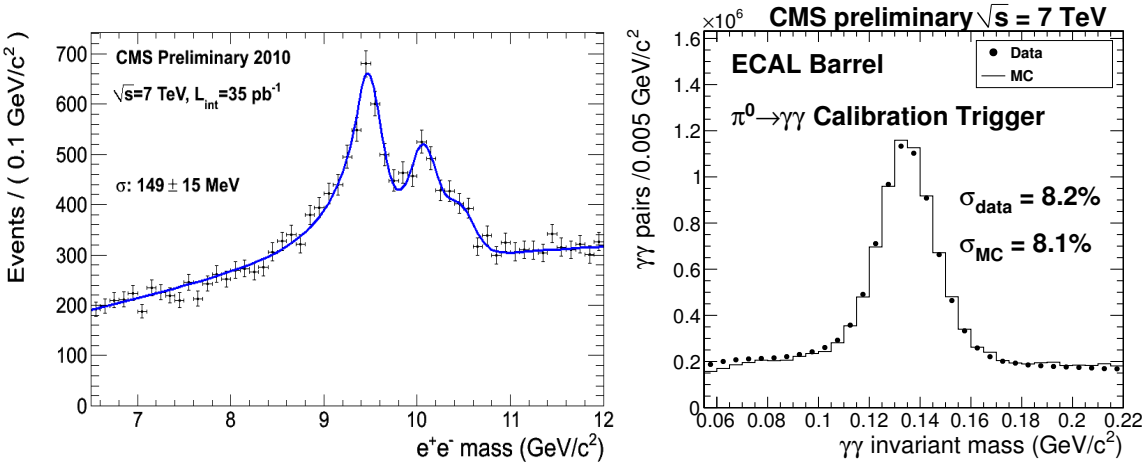

Figure 5.3: Dielectron (left) -photon (right) invariant mass spectrum measured in data corresponding to an integrated luminosity of $L = 35\mathrm{pb}^{-1}$ and $L = 18\mathrm{nb}^{-1}$, respectively. The dielectron invariant mass spectrum is zoomed into the upsilon region $m_{ee} = [6, 12]\mathrm{GeV/c^2}$ and the $\Upsilon(1s)$ and $\Upsilon(2s)$ resonances can be observed, whit a hint for the $\Upsilon(3s)$ resonance. Similar the diphoton invariant mass spectrum recorded with an on-line π^0 trigger stream shows nicely the π^0 peak. The plots are taken from [76, 110, 111].

5.4.4 Muon Reconstruction

The muon reconstruction algorithm combines information of the muon system and the inner tracker. Two reconstruction approaches are used, where one starts from track candidates and tries to match them to hits in the muon system (*inside-out*), whereas the other approach starts from the so called standalone muons reconstructed using only the information in the muon system and tries to match them with track candidates (*outside-in*).
Standalone muon candidate reconstruction starts with local track segments based on measured drift times in the various muon chambers. The segments in the first muon station (see Section 4.2.6) are

used as the candidates seed. In a similar fashion to the track candidate reconstruction using the hits in the inner tracker system, a muon parameter estimate using the seed is determined and a Kalman filter procedure adds successively segments of the outer stations until the end is reached. Once the outermost segments are reached a backward Kalman filter is applied refitting from outside in and the candidate parameters are determined at the innermost muon segment, which yields a standalone muon candidate. Throughout the propagation to the outer muon station and backwards the energy losses and scattering in the material between the stations and also the inhomogeneous magnetic field are taken into account.
The outside-in algorithm, commonly referred as the global muon reconstruction, uses the standalone muon candidate collection and matches it to track candidates by propagating the muon trajectory to the outermost layer of the tracker system including energy loss and multiple scattering in the detector material, especially in the dense material of the calorimeter and the solenoid. Around the propagated impact in the outermost layer of the tracker system a region of interest is defined and local seeds are built using two hits from different layers and the track algorithm described before (section 5.4.1) is performed creating trajectories out of each seed. Finally a global fit is performed using the track and the standalone muon candidates leading to the global muon candidate collection.
In contrast to the outside-in algorithm the inside-out algorithm, commonly referred as the tracker muon reconstruction, uses all track candidates reconstructed in the tracker system and propagates analogously their trajectories from the outermost tracker layer to the muon system. If at least one segment in the muon system matches the propagated trajectory, the corresponding track candidates get classified as a tracker muon.
The majority of muons with a sufficient momentum emerging from the collision point are either reconstructed as global- or tracker muons, or mostly as both. In about 1% of the cases muons from collisions are failing both reconstruction algorithms and are flagged as standalone muons. Those standalone muons have a much higher cosmic muon acceptance and hence the global and tracker requirement on muon candidates is preferred over standalone muons.
The excellent performance of the muon reconstruction is beautifully demonstrated in Fig. 5.4, where the dimuon spectrum with different dimuon triggers is shown . Without any quality cuts on the reconstructed muons well-known resonances can be easily identified by their peak in the spectrum, even the ω and ϕ resonances can be observed.

5.4.5 Tauon Reconstruction

Taus can either decay into leptons or hadrons with associated neutrinos, where the leptonic decay modes can not directly be related to a τ-decay. Two hadronic tau reconstruction and identification approaches can be utilized. Hadronic decaying taus have a branching fraction into hadronic single-prong decays of about 50% and into three prong of about 15%. The single prong taus can even be further spitted into single-prong with associated π^0s ($BR \approx 36\%$) and without ($BR \approx 14\%$) [16]. The efficient identification of those signatures inspite of a large soft QCD background is done with the *hadron plus strips* (HPS) and *tau neural classifier* (TaNC) algorithms [113]. As a basis all particle flow particles (charged hadrons, photons, neutral hadrons, muons, electrons) are used in both algorithms in order to reconstruct the three different hadronic tau topologies separately.
The tau reconstruction starts with the PF jet reconstruction (Section 5.4.6) using the anti-k_T clustering

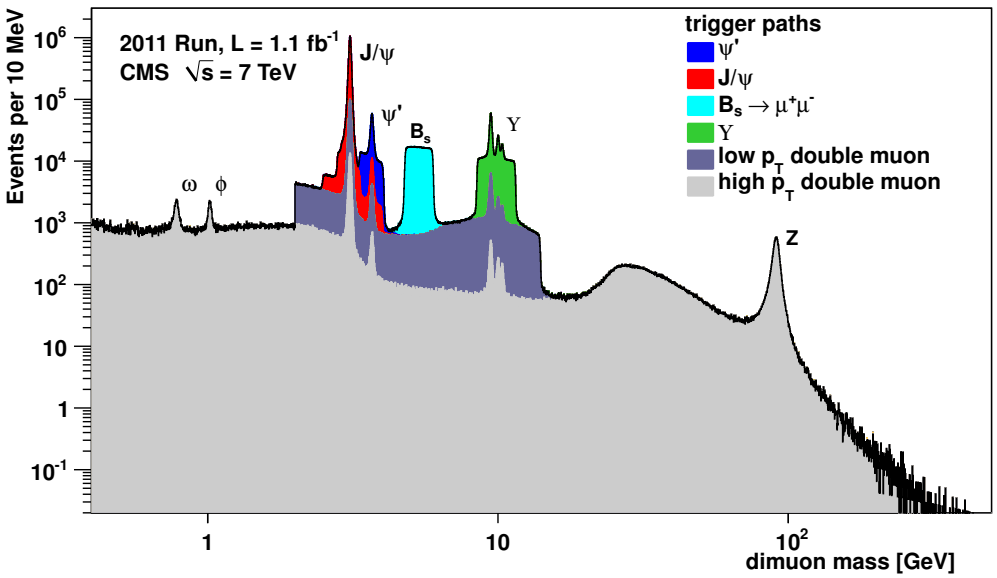

Figure 5.4: Invariant mass spectrum for pairs of muon. Datasets recorded by different dimuon trigger paths in 2011 corresponding to an integrated luminosity of $1.1\,\text{fb}^{-1}$ are superpositioned. The plot is taken from [112].

algorithm with a distance parameter of R=0.5 [114]. Afterwards the used algorithm reconstructs the π^0 candidates components of the τ_hs and combines them with charged hadron candidates in order to identify the tau decay mode and yields finally the four momentum vector and isolation quantities. The details of defining τ_h candidates differs between the algorithms and will be shortly reviewed.

TaNC Algorithm: The TaNC algorithm uses neural networks as classifiers, where for each decay mode a specific neural network was trained. But first a τ_h candidate is built out of the PF jet collection. The four momenta of the τ_h candidate is reconstructed as a sum of all particles with $p_T > 0.5\,\text{GeV}$ in a signal cone $\Delta R < 0.15$ ($\Delta R < 0.15$ for photons and $0.07 < \Delta R_{charged} < 0.15$ for charged hadrons with $\Delta R_{charged} = 5\,\text{GeV}/E_T^{\tau_h}$) around the direction of the leading particle with $p_T > 5\,\text{GeV}$. π^0 candidates are reconstructed by merging two photons with an invariant mass less than $0.2\,\text{GeV/c}^2$ and unpaired photons with $p_T > 0.1 \times p_T^{\tau_h}$. By just counting the tracks and π^0 candidates inside the signal cone the considered decay modes can be identified and the corresponding neural networks yields to a continuous discriminant, which can be used to define different working points. The neural networks are optimized for each decay mode and the input variables are typically the p_T spectrum of the nearby particles, angular correlations, invariant masses and number of charged particles in the signal and isolation cone, where the neural networks were trained beforehand to discriminate τ_h from Z decays ($Z \to \tau\tau$) versus QCD multi-jet events.

HPS Algorithm: The HPS algorithm gives special attention to the photon conversion, where the bending of electrons/positrons of converted photons emerging from neutral pions, which broadens the calorimeter signatures in the azimuth direction, is taken into account by reconstructing photons

in strips. It collects electromagnetic particles in a η-ϕ strip ($\Delta\eta = 0.05$, $\Delta\phi = 0.20$) iterative, recalculating the four momentum vector after each new added particle, until no further particle can be associated. Pions can produce several strip-signatures: (1) low energetic pions will lead to no strips, (2) emerging photons close together will be reconstruct within one strip (3) and if they are well separated two strips. Finally combining all strips with $p_T > 1\,\text{GeV}$ and charged hadrons inside a cone $\Delta R = 2.8\,\text{GeV}/p_T^{\tau_h}$ the individual decay modes can be reconstructed, where the four-vector sum of strips and charged hadrons have to be consistent with intermediate resonances (π^0, ρ, a_1). Apart from the τ_h decay products there should be no other charged hadrons or photons inside of an isolation cone $\Delta R = 0.5$ around the direction of the τ_h. Adjusting the transverse momentum p_T thresholds for those particles, different isolation working points can be defined (loose, medium, tight).

The performance of the τ_h reconstruction and identification algorithm has been measured using $Z \to \tau\tau$ events [113] summarized in Table 5.2 for the pre-defined working points. Commonly the HPS algorithm is used and the TaNC serves as a cross check. The HPS τ_h identification efficiencies are about 70%, 50% and 30% for the three working points (loose, medium, tight) with a miss-identification rate of about 1%, 0.4% and 0.2% respectively. The miss-identification rate is defined as the rate of QCD jets faking hadronic tau candidates.

Table 5.2: Efficiency for τ_h to pass the HPS and TaNC identification criteria measured in $Z \to \tau\tau$ events. Table is taken from [113].

Algorithm	Fit data	Expected MC	Data/MC
HPS "loose"	0.70 ± 0.15	0.70	1.00 ± 0.24
HPS "medium"	0.53 ± 0.13	0.53	1.01 ± 0.26
HPS "tight"	0.33 ± 0.08	0.36	0.93 ± 0.25
TaNC "loose"	0.76 ± 0.20	0.72	1.06 ± 0.30
TaNC "medium"	0.63 ± 0.17	0.66	0.96 ± 0.27
TaNC "tight"	0.55 ± 0.15	0.55	1.00 ± 0.28

5.4.6 Jet Reconstruction

At hadron colliders one of the main tools to analyze recorded events are jet clustering algorithms. Quarks and gluons produced in the hard scattering process will undergo fragmentation and hadronization processes into collimated streams of color neutral hadrons, due to QCD confinement, which does not allow free colored particles. A jet is defined as the sum of hadrons within a pre-defined cone or clustering algorithm. A robust jet algorithm has to be stable towards small variations of the input, namely the particle activity within the jet. Two common aspects have to be fulfilled by modern algorithms: (1) infrared safe and (2) collinear safe. Infrared safety is the robustness of the algorithm by facing additional soft partons between two jets, which should not have any influence on the stability of the jets candidates. Collinear safety ensures on the other hand, that additional collinear gluon radiated by the hadronic jets do not alter the jet reconstruction algorithm. Collinear and infrared safety is especially important for obtaining meaningful comparison with theoretical models.

The jet reconstruction algorithms are starting usually by clustering objects within some cone and a recombination scheme which defines the method to combine all clustered objects into a jet four-vector. Several jet finding algorithms were developed over the last years, where cone algorithms are the easier ones and are based on the idea of defining a jet by an angular cone around some seed direction. Since all cone algorithms were replaced in the CMS reconstruction process by so called clustering algorithms, a detailed description will be skipped at this point.
Common jet clustering algorithms define two distances: d_{ij} between the particles i and j and d_{iB} between particle i and the beam line. Objects with a minimum distance d_{ij} getting iterative combined until only particles with $d_{ij} > d_{iB}$ remain. The resulting object is called a jet. Those jets are then removed from the list of particles. This procedure is redone until no particles are left. The algorithms differ in the definition of the distance parameter:

$$\begin{aligned} d_{ij} &= min(k_{ti}^{2p}, k_{tj}^{2p}) \frac{\Delta_{ij}^2}{R^2} \\ d_{iB} &= k_{ti}^{2p} \, , \end{aligned} \tag{5.2}$$

here $\Delta_{ij}^2 = (y_i - y_j)^2 + (\phi_i - \phi_j)^2$ and k_{ti}, y_i and ϕ_i are the transverse momentum, rapidity and azimuth of the particle i, respectively and R is the radius parameter. This radius parameter R serves to rescale the distance d_{ij} such that any pair of jets is separated by at least $\Delta_{ij} = R$. The value $p = 1$ corresponds to the k_t algorithm [115, 116], $p = 0$ to the Cambridge/Aachen [117] and $p = -1$ to the anti-k_t algorithm [114]. All three algorithms are infrared and collinear safe and just differ in the actual distance definition. In CMS the k_T and anti-k_T algorithm are implemented.
Another crucial ingredient for the jet reconstruction algorithms is the input collection of objects used for the clustering. The most basic jet input collection are energy deposits in the ECAL and HCAL cells combined together into calorimeter towers forming the class of so called *caloJets*. In order to improve the p_T response and resolution of caloJets, information of the tracker system can be added. Charged particle tracks measured in the tracker system associated with each jets can be used to improve the jet transverse momentum and direction (*Jet Plus Tracks* (JPT)) [118]. The last jet input collection used is the list of all reconstructed particle flow objects, where the PF algorithm combines the information of all sub-detectors [101]. Fig. 5.5 shows the jet transverse momentum p_T resolution for central jets ($|\eta| < 0.5$) measured in data using the dijet-asymmetry method for the different jet definitions clustered with the anti-k_T clustering (radius parameter $R = 0.5$) [119].
Several corrections are applied on top of the raw jet transverse momentum to relate the average energy measured for the detector jets to the energy corresponding to the true particle. The correction factor C^{tot} is applied as a multiplicative factor on the raw jet four-momentum components

$$p_\mu^{corr-jet} = C^{tot} p_\mu^{raw} \tag{5.3}$$

and is composed of various correction-levels

$$C^{tot} = C^{offset}(p_T^{raw}) C^{MC}(p_T', \eta) C^{rel}(\eta) C^{abs}(p_T'') \tag{5.4}$$

with p_T' is the transverse momentum p_T of the jet after the C^{offset} correction and p_T'' after all previous corrections applied [120]. The offset correction C^{offset} subtracts the energy contributions not associated with the hard scattering process (electronic noise, PileUp). MC correction C^{MC} are applied

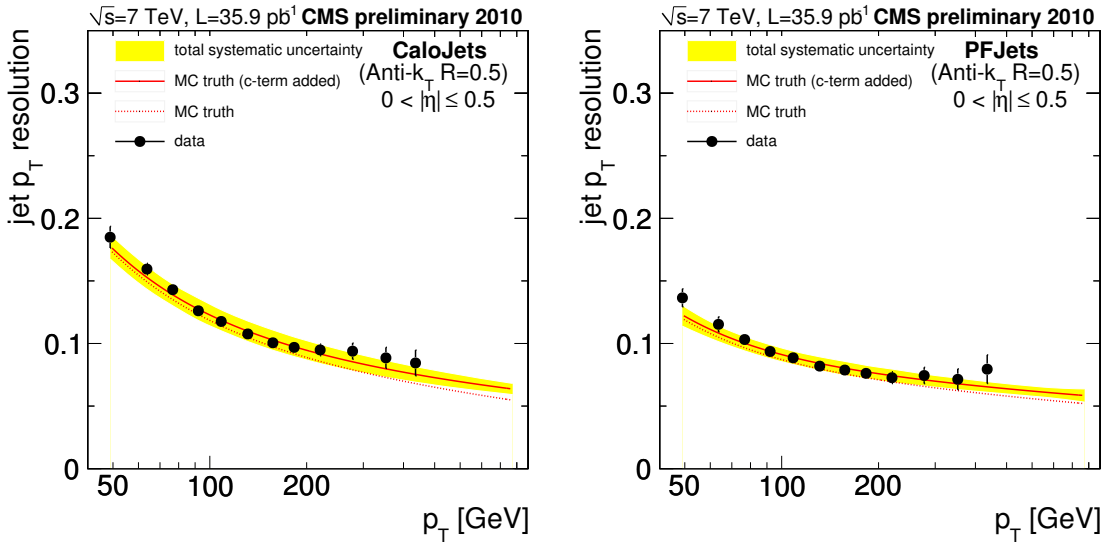

Figure 5.5: Central Jet ($|\eta| < 0.5$) p_T resolution measured in data compared to MC predictions for caloJets (left) and PFJets (right). JPTs have comparable p_T resolution as PFJets and are not shown explicitly. The plots are taken from [119].

to correct the reconstructed jet energy to be equal to the generated jet energy determined in simulations. Non-uniform calorimeter responses in η are corrected with the relative correction C^{rel} and the absolute correction C^{abs} accounts for the p_T dependent calorimeter response.

5.4.7 Missing transverse Energy Reconstruction

The CMS detector covers nearly 4π solid angle with pseudo rapidities up to $|\eta| < 5$, enable to detect most particles emerging from the collision, except exclusive weakly interacting particles like neutrinos which escape undetected. Since the initial particles exhibit no transverse momentum, the vectorial sum of all particles should vanish and hence an indirect indication for the presence of neutrinos is the so called *missing transverse energy* (E_T^{miss}). It is commonly calculated as the magnitude of the negative vectorial sum of all reconstructed final state particles.

$$\vec{E}_T^{\text{miss}} = -\sum_{i=0}^{N} \vec{E}_T^{i}\,, \text{ with } i = \text{ith particle} \tag{5.5}$$

Implemented in the CMS reconstruction process are four different algorithms to calculate E_T^{miss} , varying in the reconstructed objects used for the calculations.

(1) $caloE_T^{\text{miss}}$: Calorimeter based E_T^{miss} using the energy deposits in the calorimeter towers up to $|\eta| < 5$ above a noise thresholds and angles defined by a vector pointing from the primary vertex to the tower. Minimum ionizing muons reconstructed in the inner tracker and outer muon system have to be added, while subtracting their energy deposits in the calorimeter [121].

(2) tcE_T^{miss}: The track-corrected E_T^{miss} starts from the $caloE_T^{\text{miss}}$ and adds subsequently all p_T of reconstructed tracks matched to calorimeter tower, while subtracting the corresponding energy

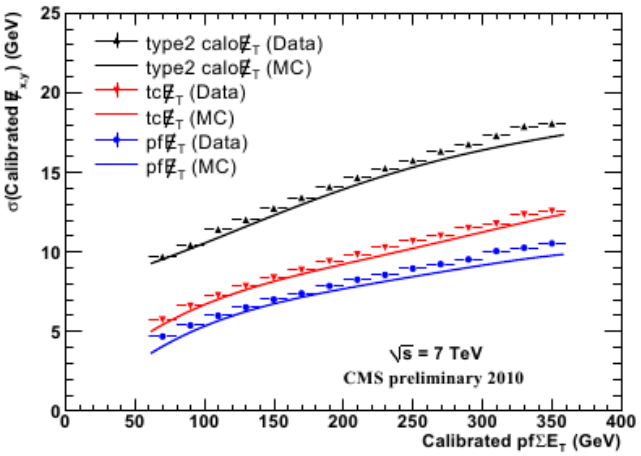

Figure 5.6: Resolution of $caloE_T^{\text{miss}}$, tcE_T^{miss} and pfE_T^{miss} measured in minimum bias events and MC. The plot is taken from [124].

deposits in the towers [122].

(3) pfE_T^{miss}: The particle flow E_T^{miss} is calculated by the negative vectorial sum of all objects reconstructed with the PF algorithm [101].

(4) MH_T: Another often used missing transverse energy measurement is MH_T (missing H_T) for which only reconstructed jets are used.

In order to account for the non-compensating and non-linear response of the calorimeter several corrections have to be applied for an adequate reconstruction of $caloE_T^{\text{miss}}$. For this purpose the jet energy corrections are used for calorimeter towers within jets and an additional set of corrections for towers outside any jet. The E_T^{miss} resolution for the $caloE_T^{\text{miss}}$, tcE_T^{miss} and pfE_T^{miss} algorithm measured in minimum bias events is shown in Fig. 5.6. tcE_T^{miss} and especially pfE_T^{miss} improve the E_T^{miss} resolution compared to the traditional $caloE_T^{\text{miss}}$ [123, 124].

5.5 CMS Computing Model

In order to manage the huge amount of data recorded with the CMS detector and MC event production, the Worldwide LHC Computing Grid Project (WLCG) has been developed [125, 126]. It is based on a multitier structure with decentralized computing and mass storage resources. One Tier-0 centre located at CERN performs a first prompt reconstruction on the raw data streams coming from the HLT and Data Acquisition System. The processed data is distributed to dedicated Tier-1 centers located in the various CMS Collaboration member states. At the Tier-1 centres a further processing like rereconstruction or calibration is performed and massive data archiving services are provided. A larger amount of Tier-2 centres offer substantial CPU ressources for analysis, calibration and MC sample production. Typically the Tier-2 centers rely upon Tier-1 centers for fast access to large data sets. Finally the Tier-3 centers provide interactive resources for local groups.

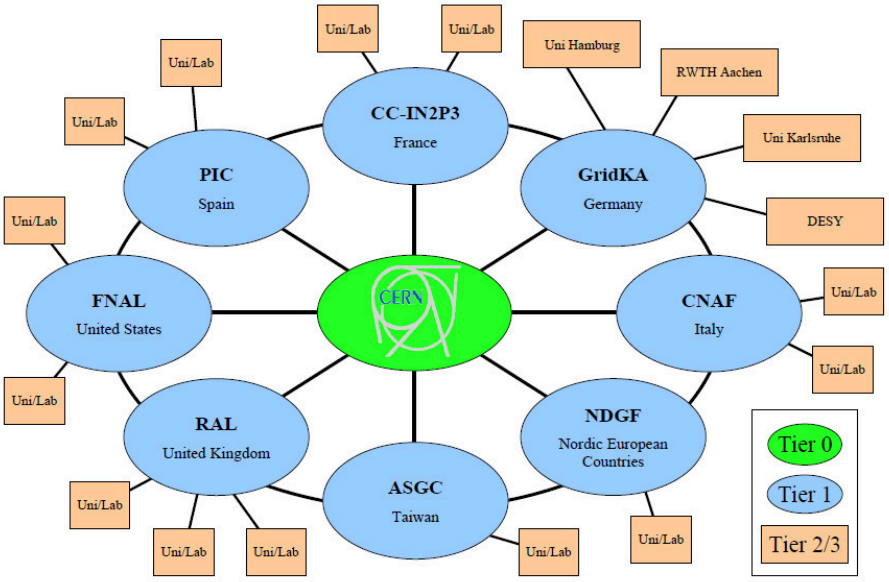

Figure 5.7: Schematic view of the WLCG tier structure of CMS. The plot is taken from [127].

5.6 Statistical Procedure

The statistical model used for the determination of the 95% confidence level (C.L.) exclusion limit within the CLs [128] method is based on the Likelihood formalism and has two main components: statistical (Poisson) and systematics [129,130]. In the absence of systematics the combination of Nch search channels can be written as:

$$L(n|H) = \prod_{k}^{Nch} Poiss(n_k|\nu_k \cdot s + b_k), \tag{5.6}$$

where s is the expected signal yield, ν_k is a signal strength modifier that multiplies the expected SUSY yield such that $s' = \nu_k \cdot s$ and b_k is the expected background yield. The systematics complicate the picture, each source of systematics introduces a nuisance parameter distributed according to some probability density function (pdf). The shape of this pdf is unknown, usually a log-normal distributed pdf is assumed but also gaussian or gamma distributions have been proposed for uncertainties. The log-normal distribution is given by

$$f_X(x;\mu,\sigma) = \frac{1}{x\sigma\sqrt{2\pi}} e^{-\frac{(lnx-\mu)^2}{2\sigma^2}}, x > 0 \tag{5.7}$$

with μ and σ are commonly called location and shape parameter. For simplicity only log-normal pdfs are used. The log-normal distribution has two important differences in comparison with a simple truncated gaussian:

- The log-normal distribution has longer tails leading to more conservative results
- The probability density of the log-Normal distribution at b=0 is always zero.

Each channel may have some search specific systematics resulting in Nch nuisance parameters plus some common systematics. The treatment of large number of nuisance parameters is a challenge in statistics. On the other hand, as we will see later in Chapter 8, the number of objects in signal topologies is limited to 3 lepton flavors, Jets and E_T^{miss} , and the number of major backgrounds is limited to WZ, ZZ (incl. DY(llγ)), DY+Jets, $t\bar{t}$ and more rare processes (WW, $WW\gamma$, TTZ, TTW combined). For simplicity the systematics are factorized into 10 nuisance parameters δ^i.

1-2 . Combined systematics in SM backgrounds : $\delta^{WZ+ZZ+Rare}$ and $\delta^{DY+t\bar{t}}$. The background nuisance parameters are split into one data-driven estimated for DY+Jets and $t\bar{t}$, and one MC simulation based for WZ, ZZ and rare processes assuming 100% correlation for the individual elements of the single nuisance parameters for simplicity.

3. MC uncertainties on signal efficiency. Here we assume single nuisance for all channels: δ^{MC}.
4. Uncertainties in JES related to the H_T and E_T^{miss} selection: δ^{JES}.
5. Uncertainties in muon selection efficiency: δ^{μ}.
6. Uncertainties in electron selection efficiency: δ^{e}.
7. Uncertainties in tau selection efficiency: δ^{τ} .

8. A common systematic uncertainty affecting signal and MC estimated backgrounds from luminosity measurements: δ^{lumi}.

9. Uncertainties in trigger efficiencies: δ^{trig}.

10. Combined PDF and SCALE uncertainties: δ^{pdf}.

Such a factorization also takes care about correlations of systematic uncertainties in different channels. The model with systematics can be presented as:

$$L(n|H) = \prod_{k}^{Nch} Poiss(n_k|\mu_k) \prod_{i}^{Nnuis} N(\delta_i|0,\sigma_i) \tag{5.8}$$

where the expectation $\mu_k = \nu_k \cdot S + B_k$ depends on all nuisance parameters and $N(\delta|0,\sigma)$ are the pdf for the $Nnuis$=10 nuisance parameters. The contribution of each correlated nuisance parameter δ_i in the particular search channel k is defined by the scaling factor f_k^i, that is, the sensitivity of the signal efficiency or the background to the variation of the nuisance. The maximum deviations among all search channels determines the σ of the systematics pdf. The factors f are obtained from MC simulations using the so called Δ method: by varying the systematics within the expected uncertainties the variation of the number of selected events is determined. The signal part is:

$$\begin{aligned} S_k =& s_k \cdot \nu \cdot \prod_l (1 + f_l^s \cdot \delta_l) \cdot (1 + f_k^{MC} \cdot \delta^{MC}) \cdot (1 + f_k^{JES} \delta^{JES}) \\ & \cdot (1 + f_k^{trig} \delta^{trig}) \cdot (1 + \delta^{pdf}) \cdot (1 + \delta^{lumi}) \end{aligned}$$

where $\prod_l^{Nl=3,4}(1+f_l^s \cdot \delta_l)$ is defined by the lepton combination in the final state ($\mu\mu\mu\mu$, $\mu\mu\mu e$, $\mu\mu\mu$, $\mu\mu ee$, etc) and ν is the signal strength parameter. The background part reads like $B_k = B_k^{WZ+ZZ+Rare} + B_k^{DY+t\bar{t}}$ where the individual parts can be expressed as:

$$B_k^X = b_K^X \cdot (1 + f_k^X \cdot \delta^X)$$

where X is the corresponding background channel.
All statistical modeling is done within the landS package [131], which was extensively cross checked with implemented methods in RooStats [132].
In order to set exclusion limits on a SUSY hypothesis, a test statistic Q has to be defined, which depends on the hypothesised signal rate ν_k. The test statistic uses a Likelihood Ratio [133, 134] after performing a maximization with respect to the nuisance and the signal strength parameter:

$$Q = \frac{max(L(n|\nu \cdot s, b, \hat{\delta}^b)}{max(L(n|\hat{\nu} \cdot s, b, \hat{\delta}^b)} ,$$

where quantities indicated with a hat are used for maximization. The test-statistic Q is then converted into $-2ln(Q)$. This definition of the test statistics is referred to as the *LHC-Style*, since it differs slightly from the one used in searches at LEP and the Tevatron, where a background-only hypothesis was used in the denominator of Q. In the limit of large number of background events, the expected distributions of Q are known analytically [1, 135].

The 95% exclusion limit calculation uses the CL_s [128, 136] method implemented in the landS code. CLs is often referred as the modified frequentist analysis and is defined as

$$CL_s = CL_{s+b}/CL_b$$

where CL_{s+b} and CL_b are given by the probability that the test-statistic Q is less or equal than the observed value Q_{obs}:

$$CL_{s+b} = P_{s+b}(-2lnQ \geq -2lnQ_{obs}) \qquad \text{or} \qquad CL_b = P_b(-2lnQ \geq -2lnQ_{obs})$$

where CL_{s+b} corresponds to the signal + background and CL_b to the background only hypothesis. This normalization of the observed confidence level for CL_{s+b} to the observed confidence level for CL_b avoids so called "unphysical" exclusions of zero signal expectations in context of possible downward fluctuations of the background[1].
If $CL_S \leq \alpha$ for $\nu = 1$ one can determine that the SUSY model is excluded at the $1 - \alpha$ confidence level. To quote the upper limit on ν at the 95% confidence level, ν is adjusted until the desired value of $CL_s = 0.05$ within a predefined tolerance is obtained.

[1] More details on this subject can be found in [128]

CHAPTER 6

Search for Supersymmetry using Multileptonic Signatures

The search strategy for physics beyond the standard model within the CMS SUSY group is split into different analysis, in the following called *reference analysis* (RA). They focus each on various topologies arising from possible supersymmetric extensions of the SM including leptons, a certain jet activity and/or missing transverse energy. Several hadronic analysis [137, 138], vetoing events containing leptons, and leptonic analysis requiring one [139], two [140–142] or more leptons [12–15] in the final state were performed in the first two years of data taking at the LHC. Up to now no evidence for any supersymmetric model has been observed and the physicists were able to exceed the limits on new physics of former collider experiments [8–11]. The hadronic analysis set the most striking limits for the commonly referred SUSY model, the cMSSM introduced in Chapter 3.

The following chapter describes the analysis done using multileptonic events, with at least three leptons (e, μ or τ) in the final state based on an integrated luminosity of $L_{int} = 4.7\,fb^{-1}$. This study is embedded in the RA7 activity. Multileptonic signatures are commonly called *"Golden Channels"* for SUSY searches, because of the clean signature. Clean in the sense that the SM processes leading to multileptonic final states are quite rare, whereas in many SUSY models those signatures can be enhanced.

The analysis is organized as follows: in the first part the production of SUSY particles and their decay signatures at the LHC will be summarized. After defining the object and event selection the analysis will be discussed and the results shown and interpreted in the context of cMSSM and the so called simplified model spectra which will be introduced at the given time. Many channels, signal and control channels, are examined and combined in one statistical model. The focus will be placed on the various SM background predictions, which are data driven or rely on MC simulations but are cross checked in various control regions, and the discussion of the results.

6.1 Multilepton Production in SUSY Models

In this section the production of sparticles and their possible decay chains leading to leptons in the final states at the LHC is presented. Since we focus on the R-parity conserving cMSSM, sparticles can be produced only in pairs. The superpartners of the quarks and leptons are the squarks ($\tilde{q}$) and sleptons ($\tilde{l}$). Gauginos ($\tilde{\chi}^{\pm}$,$\tilde{\chi}^{0}$) and higgsinos are paired with the gauge and higgs particles. The sparticle production can be split into the production of colored squarks and gluinos, and the direct weak production of neutralinos ($\tilde{\chi}^{0}$), charginos ($\tilde{\chi}^{\pm}$) or sleptons.
Typical squark and gluino production processes at leading order (LO) with different combinations in the final state ($\tilde{q}\bar{\tilde{q}}$, $\tilde{q}\tilde{q}$, $\bar{\tilde{q}}\bar{\tilde{q}}$, $\tilde{g}\tilde{g}$, $\tilde{g}\tilde{q}$, $\tilde{g}\bar{\tilde{q}}$) [143], where the chiralities of the squarks ($\tilde{q}_R$, $\tilde{q}_L$) and the flavor indices are not given for simplicity, are shown in Fig. 6.1. In order to produce squark-antisquark final states ($\tilde{q}\bar{\tilde{q}}$), quark-antiquark or gluon-gluon initial states are required, whereas squark pair final states ($\tilde{q}\tilde{q}$) can only be produced from quark pair initial states. Gluino pair production ($\tilde{g}\tilde{g}$) needs a gluon-gluon or quark-antiquark initial state and only quark-gluon interactions lead to squark-gluino final states ($\tilde{q}\tilde{g}$).

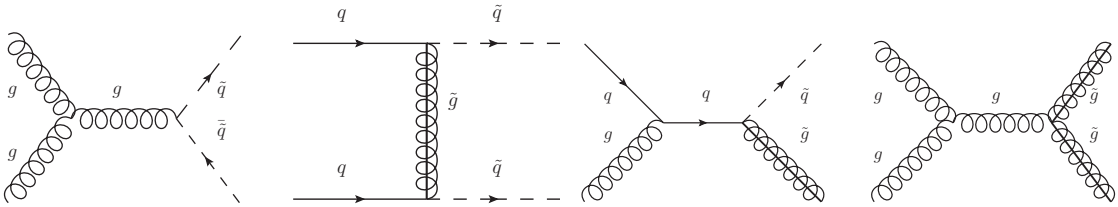

Figure 6.1: Typical LO diagrams for $\tilde{q}\bar{\tilde{q}}$, $\tilde{q}\tilde{q}$, $\tilde{g}\tilde{q}$ and $\tilde{g}\tilde{g}$ (from left to right) production at hadron colliders. These diagrams represent only a subset of all possibilities, which can be found elsewhere [143].

The non-colored neutralinos and charginos can not only be produced in cascade decays of squarks/ gluinos, but also in direct production [144] as shown in Fig. 6.2. Since neutralinos are mixtures of the neutral wino, the bino and the higgsinos and the charginos are mixtures of the charged winos and higgsinos, the vector bosons (γ, Z, W) couple to the gaugino and higgsino components, whereas in the t-channel diagram, with an virtual squark exchange, only the gaugino components are involved.

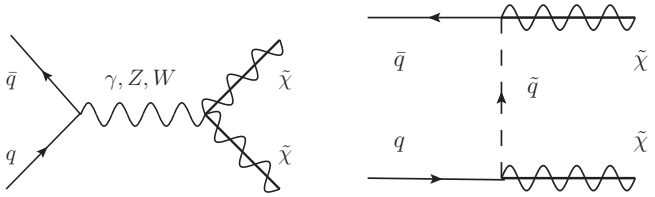

Figure 6.2: Typical LO diagrams for direct gaugino production involving vector bosons (left) or squark exchange (right).

The cross section for squark/gluino and gaugino production depends, as a good approximation, mainly on the masses of the sparticles, i.e. $m_{1/2}$, shown in the m_0 - $m_{1/2}$ parameter space for fixed $tan\beta = 10$, $A_0 = 0$ and $sign(\mu) = +1$ (cMSSM). The total sparticle production cross section is calculated with Prospino [145] (Fig. 6.3) at next-to-leading order (NLO) for p-p collisions at a center of mass

energy $\sqrt{s} = 7\,\text{TeV}$. The cross section shows a strong dependence on varying $m_{1/2}$ and only a moderate dependence on the unified scalar mass parameter m_0. In regions, where the squark/gluino masses are kinematically accessible, their production channels play a dominant role (Fig. 6.4 bottom panel). The direct production of charginos and neutralinos nevertheless can have also a significant contribution, due to typically lower masses compared to squarks/gluinos. With increasing m_0 the squarks get heavier and the electroweak sparticle production takes over as the dominant processes (Fig. 6.4 (top)). Assuming a signal selection efficiency for a typically SUSY search of $\epsilon = 0.1\%$ with a complete background suppression ($N_{Bkg} = 0$), the lowest cross section, where the search would be sensitive for in the sense of a 95% confidence level exclusion limit for an integrated luminosity of $\text{L}_{\text{int}} = 4.7\,\text{fb}^{-1}$ is

$$N_{95\%C.L.} = \sigma_{Prod,95\%C.L.} \times \epsilon_{sel} \times L_{int} \approx 3 \quad \rightarrow \quad \sigma_{Prod,95\%C.L.} \approx 0.6\,\text{pb}\,,$$

which is indicated by the line (constant cross section) added to Figures 6.3 and 6.4. Here a constant selection efficiency over the full parameter space is assumed. Those lines indicate the maximum sensitivity with the quoted signal selection efficiency of the LHC in context of the cMSSM predictions with the data set collected so far.

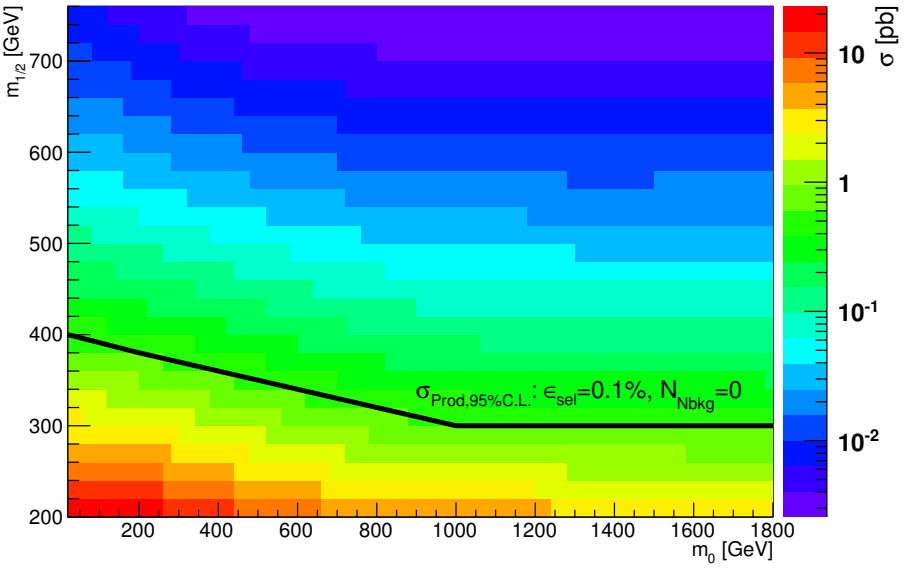

Figure 6.3: Sparticle production cross section for p-p collisions at a center of mass energy $\sqrt{s} = 7$ TeV in the cMSSM $m_0 - m_{1/2}$ parameter space for fixed $tan\beta = 10$, $A_0 = 0$ and $sign(\mu) = +1$.

A selection efficiency of 100% with a negligible background rate of $Nbkg << 1$ is typically not achievable. But nevertheless in order to define a selection as sensitive as possible to new physics signals one has to set thresholds on common objects or kinematic/event properties modifying the signal selection efficiency ϵ_{sel} and simultaneous reducing the SM background rate. Hence the detailed knowledge of the possible decay chains of the initial produced sparticles and their properties are important.

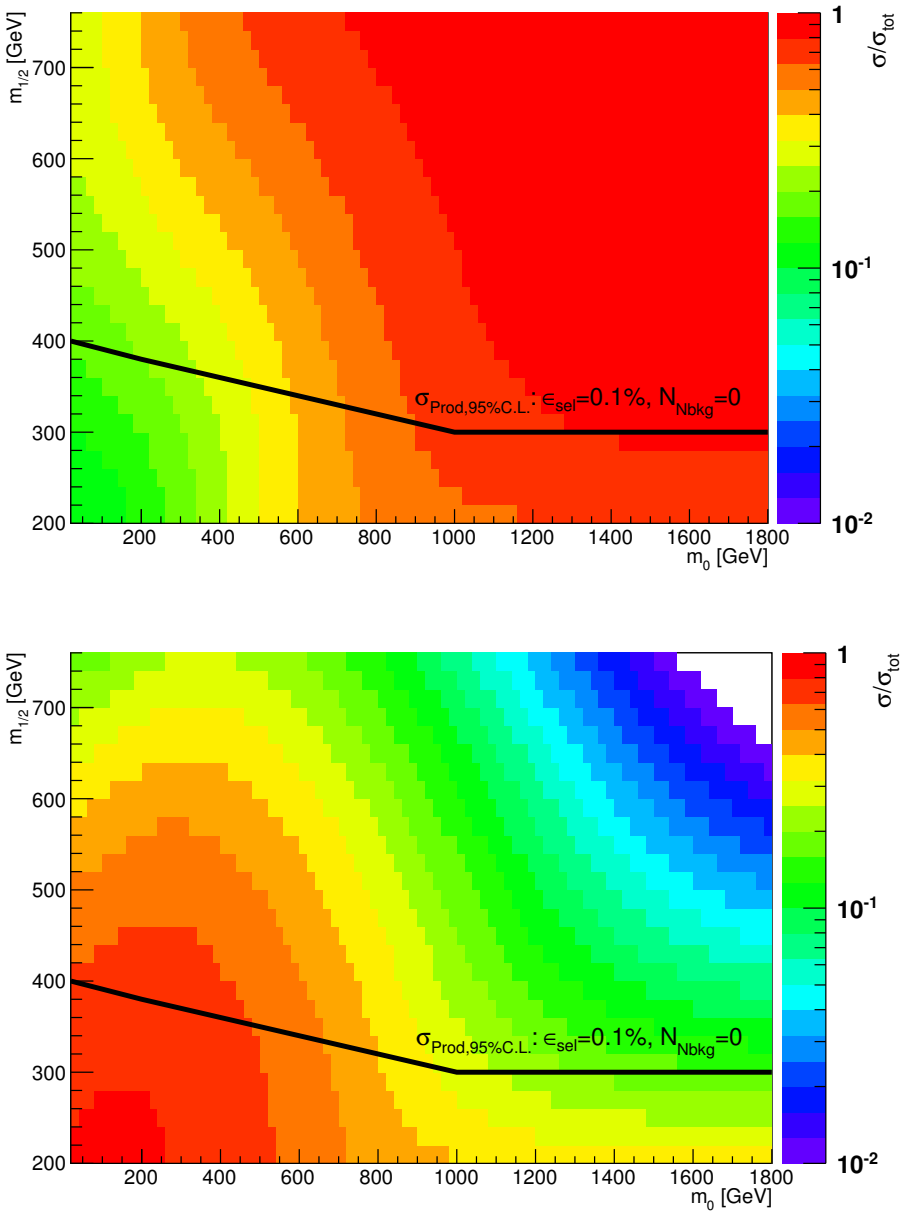

Figure 6.4: Relative fraction of chargino/neutralino $pp \to \chi^0\chi^0, \chi^0\chi^\pm, \chi^\pm\chi^\pm$ (top) and squark/gluino $pp \to \tilde{g}\tilde{g}, \tilde{g}\tilde{q}, \tilde{q}q$ (bottom) production to the total SUSY particle production cross section. At low m_0 values the colored squark/gluino production is dominant, whereas at higher values the electroweak production of charginos/neutralinos is overtaking.

The fact that we concentrate on R-parity conserving models implies the existence of a lightest stable supersymmetric particle (LSP) and we assume it to be the lightest neutralino ($\tilde{\chi}_1^0$).
Gluinos can only decay through a squark and, if kinematically allowed, the two body decays $\tilde{g} \to q\tilde{q}$ are dominant. In the case where all squarks are heavier, the gluino have to decay through a virtual squark into $\tilde{g} \to q\bar{q}\tilde{\chi}^0$ or $qq'\tilde{\chi}^{\pm}$. Similar to gluinos, squarks will decay to quark-gluino $\tilde{q} \to q\tilde{g}$ dominantly, if this process is kinematically allowed and elsewhere into neutralino or charginos $\tilde{q} \to q\tilde{\chi}^0$,$q'\tilde{\chi}^{\pm}$.
Leptons are produced mainly in the decay of the next-to-lightest neutralino ($\tilde{\chi}_2^0$) and lightest chargino ($\tilde{\chi}_1^{\pm}$), which can be produced either directly in the hard interactions, or in cascade decays of squarks/gluinos. Following the couplings of the weak interaction, neutralinos and charginos can decay through a two body decay into a lepton-slepton or quark-squark pair, where squarks are often heavier and lepton-slepton final states are enhanced. The sleptons then decay into the $\tilde{\chi}_1^0$ and a lepton.

$$\tilde{\chi}_2^0 \to \tilde{l}l \to \tilde{\chi}_1^0 ll \ , \ \tilde{\chi}_2^0 \to \tilde{\nu}\nu \to \tilde{\chi}_1^0 \nu\nu$$
$$\tilde{\chi}_1^{\pm} \to \tilde{l}\nu \to \tilde{\chi}_1^0 l\nu \ , \ \tilde{\chi}_1^{\pm} \to \tilde{\nu}l \to \tilde{\chi}_1^0 \nu l$$

Neutralinos and charginos can on the other hand also decay into lighter neutralinos or charginos with an associated vector or Higgs boson:

$$\tilde{\chi}_2^0 \to \tilde{\chi}_1^0 Z \ , \ \tilde{\chi}_2^0 \to \tilde{\chi}_1^0 h^0 \ , \ \tilde{\chi}_2^0 \to \tilde{\chi}_1^{\pm} W^{\pm}$$
$$\tilde{\chi}_1^{\pm} \to \tilde{\chi}_1^0 W^{\pm} \to \tilde{\chi}_1^0 l\nu$$

If those two-body decays are kinematically not allowed, they will decay in a three body decay into the same final states, but through off-shell gauge bosons

$$\tilde{\chi}_2^0 \to \tilde{\chi}_1^0 ll \quad \text{and} \quad \tilde{\chi}_1^{\pm} \to \tilde{\chi}_1^0 l\nu$$

Similar decays with quark final states can arise from neutralino and chargino decays [4], but not listed here, since we will focus in the following on signatures including multiple leptons in the final state. Fig. 6.5 shows the dominant branchings of the lightest chargino and next-to-lightest neutralino in the corresponding regions in the m_0-$m_{1/2}$ plane for fixed $tan\beta = 10$, $A_0 = 0$ and $sign(\mu) = +1$. One has to note that the various regions can vary for different values of $tan\beta$ and A_0. In most cMSSM (mSUGRA) parameter points the neutralinos and charginos tend to decay into the lightest higgs or W boson accompanied by the LSP. At low $m_{1/2}$ the mass splitting between the next-to-lightest neutralino/chargino and the lightest neutralino gets small, which results in solely three body decays. In case of the next-to-lightest neutralino there exists a narrow band around $m_{1/2} \approx 300\,\text{GeV}$, where the mass difference is well below the lightest higgs mass suppressing this branching, but large enough for an on-shell Z boson. For low m_0 and midrange $m_{1/2}$ masses, where the sleptons are relative light and the neutralino/charginos are heavier, the two body decays $\tilde{\chi}_2^0 \to \tilde{l}l$ and $\tilde{\chi}_1^{\pm} \to \tilde{l}\nu$ get dominant.

Multileptonic Final States

In Fig. 6.6 two diagrams for possible SUSY processes leading to tri-leptons in the final state are presented. The gluino-gluino pair production leads to a cascade decay of each gluino down to the LSP,

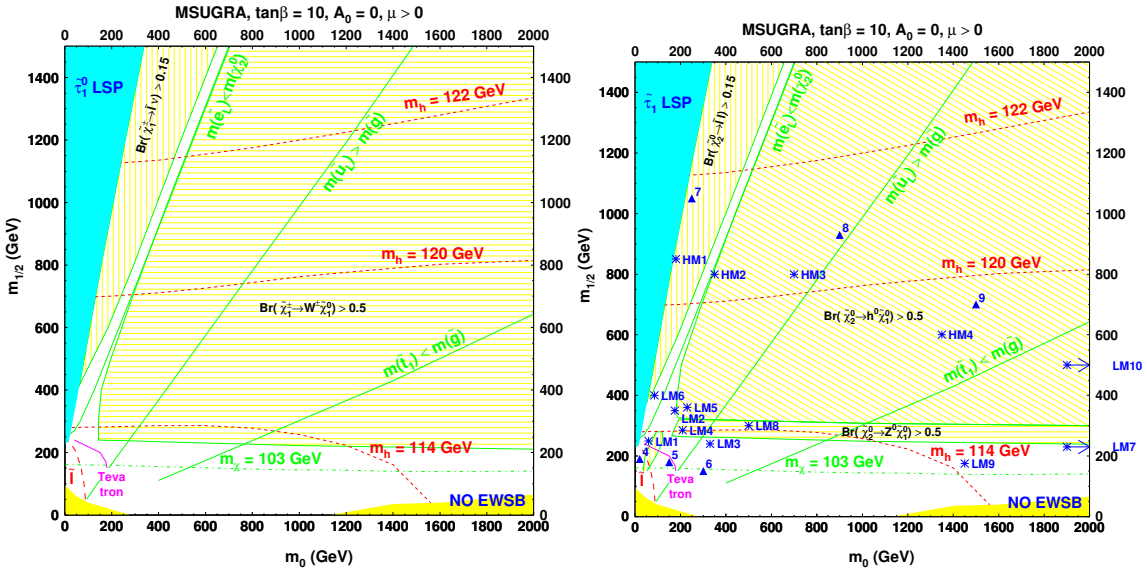

Figure 6.5: Regions in the m_0-$m_{1/2}$ plane for fixed $tan\beta = 10$, $A_0 = 0$ and $sign(\mu) = +1$ corresponding the dominant decay modes of the lightest charginos $\tilde{\chi}_1^{\pm}$ (left) and next-to-lightest neutralinos $\tilde{\chi}_2^0$ (right), where additional several benchmark points are indicated. Plots are taken from [146]

where in one leg an intermediate neutralino and in the second leg an intermediate chargino is produced, each decaying through a vector boson into leptons. Additionally, several quarks hadronizing to jets are produced simulating a three lepton plus four jets and large missing energy signature. In contrast the direct neutralino-chargino production leads to a signature with three leptons and missing energy without any jet activity.

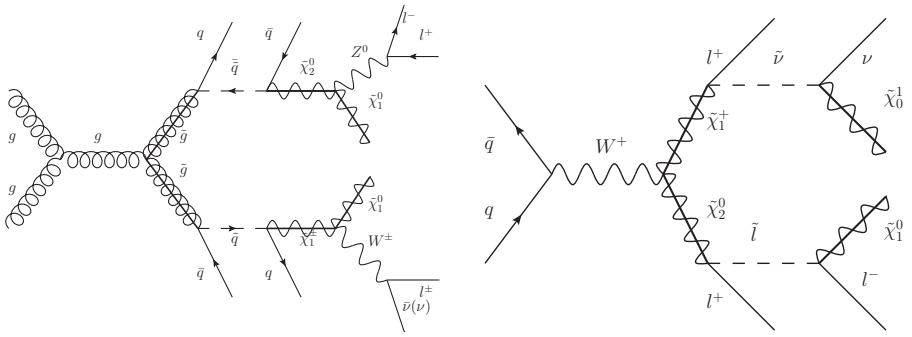

Figure 6.6: Gluino-gluino (left) and direct neutralino-chargino (right) production leading to tri-lepton final states. Gluino are decaying down to the LSP via a cascade. A number of jets and leptons are produced, where in case of electroweak neutralino-chargino production leptons and LSPs without accompanied jets are produced.

The decay branchings of all intermediate sparticles, and so the cascade length of the gluino decays shown in Fig. 6.6 (left), and the momentum spectra of final state particles depend on the underlying mass spectra and mass differences Δm. A larger mass difference for gluinos and squarks $\Delta m = (m_{\tilde{g}} - m_{\tilde{q}})$ results in longer tails in the associated jet momentum spectra. The mass spectrum

of two specific models in the cMSSM parameter space LM6[1] ($m_0 = 85$, $m_{1/2} = 400$, $tan\beta = 10$, $A_0 = 0$, $sign(\mu) = +1$) and LM9 ($m_0 = 1450$, $m_{1/2} = 175$, $tan\beta = 50$, $A_0 = 0$, $sign(\mu) = +1$) are displayed in Fig. 6.7 and Fig. 6.8, respectively. The mass spectra are generated with SoftSusy 3.2 [94] and the decay widths and branching ratios calculated with SUSY-Hit 1.5 [95]. In case of the LM6 point the left handed sleptons ($\tilde{l}_L$, $\tilde{\tau}_1$) and neutralinos/charginos ($\tilde{\chi}_2^0$, $\tilde{\chi}_1^\pm$) are nearly mass degenerated $\Delta m \approx 11 - 13\,\mathrm{GeV/c^2}$ ($m_{\tilde{l}_L} \approx 286\,\mathrm{GeV/c^2}$, $m_{\tilde{\tau}_2} \approx 288\,\mathrm{GeV/c^2}$, $m_{\tilde{\chi}_2^0} \approx m_{\tilde{\chi}_1^\pm} \approx 302.8\,\mathrm{GeV/c^2}$) and the decay $\tilde{\chi}_2^0 \rightarrow \tilde{l}l$ will lead to relative soft leptons, whereas the lepton produced in the subsequent decay of the slepton $\tilde{l} \rightarrow l\tilde{\chi}_1^0$ can have larger momentum due to a higher mass difference $\Delta m = (m_{\tilde{l}} - m_{\tilde{\chi}_2^0}) \approx 126\,\mathrm{GeV/c^2}$. This results in events with a hard lepton and an associated soft lepton. On the other hand gluinos/squarks can produce a long cascade with hard jets, due to large mass splittings in the squark sector. Comparing LM6 with the mass spectrum of LM9 one observes, that the sleptons are much heavier than the gauginos, and the gluino is the lightest colored sparticle. The next-to-lightest neutralino and lightest chargino will decay through a three body decay into the LSP and leptons or quarks via virtual gauge bosons. The fact that the gluino is the lightest colored sparticle has an interesting effect, because it can only decay via a virtual squark, e.g. a sbottom ($\tilde{b}$) or stop ($\tilde{t}$) into quark pairs and a chargino or neutralino. Those quarks occur to have lower transverse momentum p_T due to the three-body decay of the gluino. The kinematic distributions $E_T^{textmiss}$, $H_T = \sum_i E_T^{jet,i}(E_T > 30\,\mathrm{GeV}, |\eta| < 3)$, $L_T = \sum_i p_T^{lepton,i}(p_T > 3\,\mathrm{GeV}, |\eta| < 3)$ and $S_T = E_T^{\mathrm{miss}} + H_T + L_T$ are shown in Fig. 6.9 for both models. The leptons used for the calculation of the L_T observable are well reconstructed and isolated electrons and muons. Details of the individual selection criteria will be discussed later in Section 7.3. As expected the jet activity is significantly lower for LM9 compared to LM6. Also the E_T^{miss} spectrum is softer, due to lighter LSPs.

In summary the kinematically accessible parameter space for sparticle production at the LHC of the cMSSM is still dominated by gluino/squark pair production. In the decay chains of the initially produced sparticles a number of jets and leptons can appear and the LSP, which is assumed to be the lightest neutralino $\tilde{\chi}_1^0$, will escape undetected resulting in missing energy. Depending on the underlying model and especially the mass spectrum, the jet, lepton and missing energy spectra in SUSY processes vary. Models with degenerated slepton and next to lightest chargino/neutralino masses result in softer leptons, which can fail the lepton selection thresholds and hence searches based on multileptonic signatures will not be sensitive.

Since no evidence of any direct SUSY particle production process is observed at the LHC, and other experiments as well, a search strategy should be as model independent as possible. A split into lepton topologies as it is conventional in the CMS SUSY group covers most of the possible signatures. Thus an individual optimization to increase the sensitivity for a special phase space of the SUSY parameter space with simultaneous reduction of the SM background rate can be achieved.

[1] LM points: Low Mass benchmark models used by the CMS Collaboration

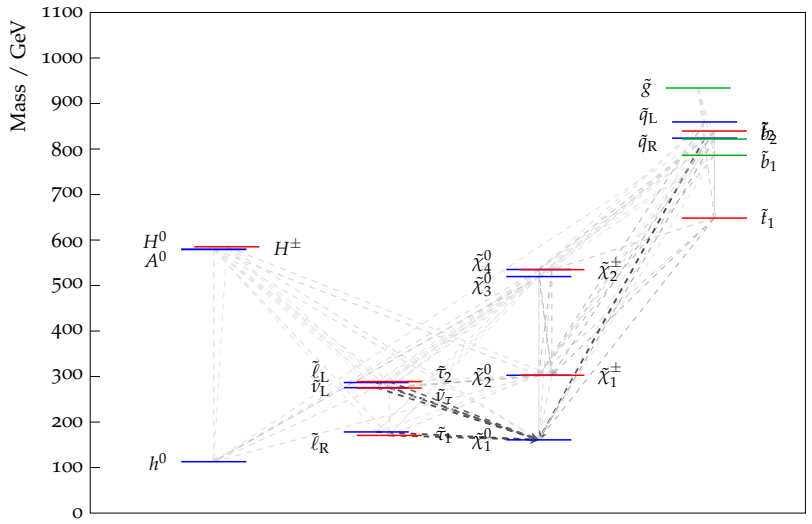

Figure 6.7: Mass spectrum for the cMSSM model LM6 ($m_0 = 85$, $m_{1/2} = 400$, $tan\beta = 10$, $A_0 = 0$, $sign(\mu) = +1$) generated with SoftSusy 3.2 + SUSY-HIT 1.3 and visualized with pyslha-1.2.8 [147]. The dashed lines and their widths indicates the branching ratios of the sparticles.

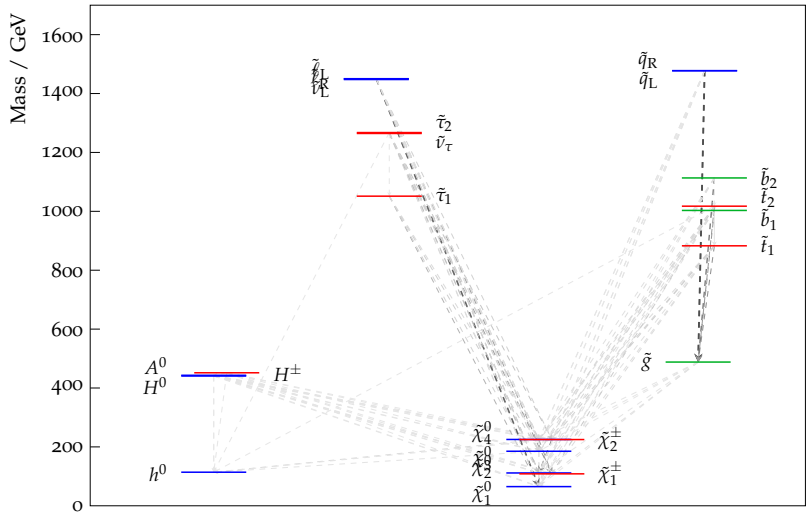

Figure 6.8: Mass spectrum for the cMSSM model LM9 ($m_0 = 1450$, $m_{1/2} = 175$, $tan\beta = 50$, $A_0 = 0$, $sign(\mu) = +1$), generated with SoftSusy 3.2 + SUSY-HIT 1.3 and visualized with pyslha-1.2.8 [147]. The dashed lines and their widths indicate the branching ratios of the sparticles.

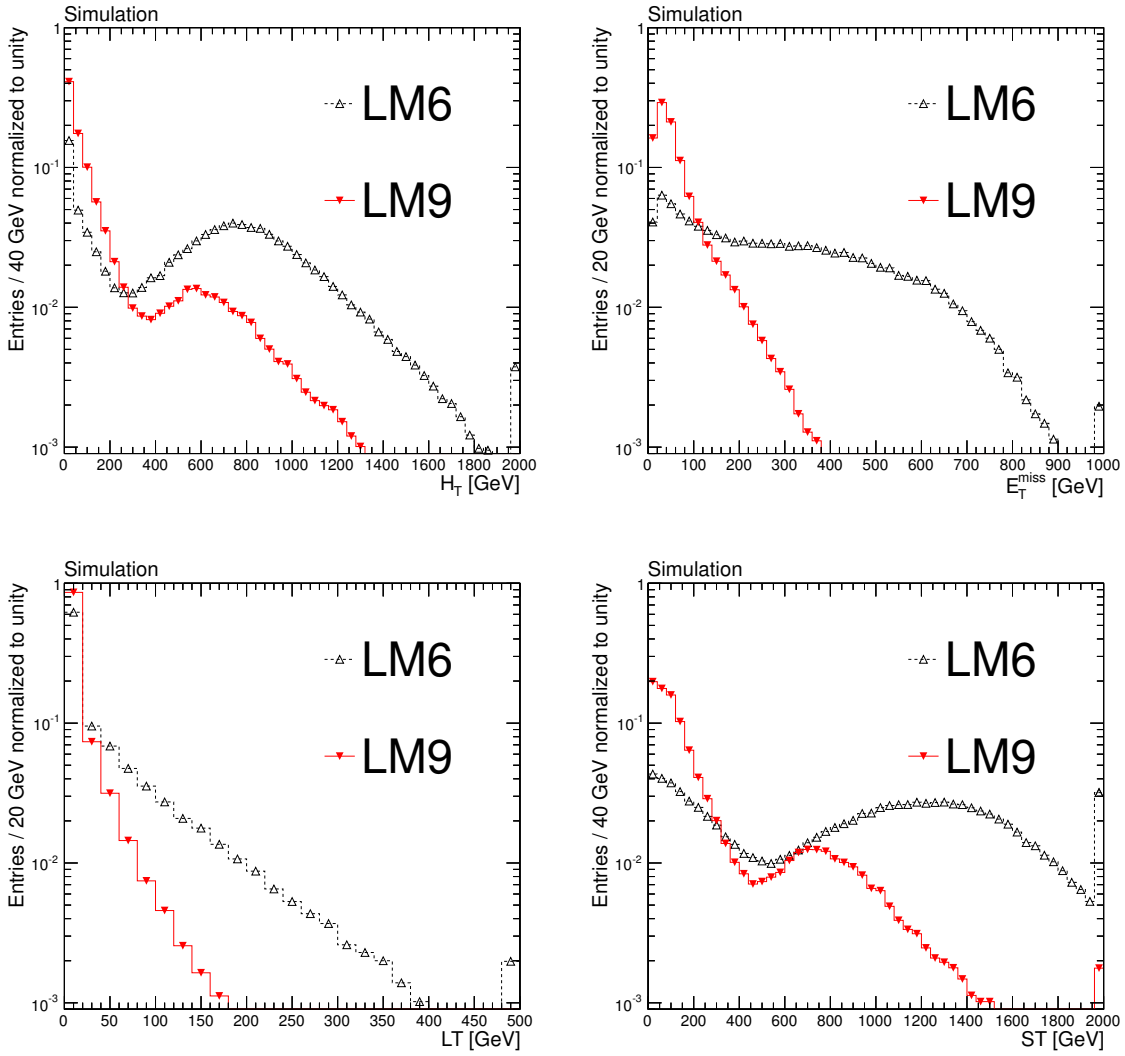

Figure 6.9: Kinematic distribution for the benchmark points LM6 and LM9. Shown are $H_T = \sum_i E_T^{jet,i}$ (top left) and E_T^{miss} (top right), $L_T = \sum_i p_T^{lepton,i}$ (bottom left) and $S_T = E_T^{\text{miss}} + H_T + L_T$ (bottom right). See also Fig. 6.5 (right) for the definition of the benchmark points.

6.2 Standard Model Backgrounds

Prompt leptons appear from neutralino/charginos ($\tilde{\chi}^0$,$\tilde{\chi}^{\pm}$) decays in common SUSY models and from short living bosons (Z,W,H) in the SM . Those leptons are characterized by a small impact parameter (d_{xy}) in the xy-plane with respect to the primary vertex or beam spot and small energy deposits in a cone $\Delta R = \sqrt{\Delta\Phi^2 + \Delta\eta^2} < 0.3$ around the lepton trajectory (*isolation*). To keep the efficiency for prompt leptons in SUSY processes high, the requirements on d_{xy} and isolation could not be to strong and thus one obtains, apart from the irreducible background including prompt leptons, a background including so called fake leptons. The sources of such fake leptons differ for each lepton flavor.
Muon fakes are mainly produced in jets, predominantly from heavy flavor decays $b/c \rightarrow \mu + jet$ [148]. Additional false association of tracks with accidental hits from hadronic shower leakage in the muon system (*punch through*) may also lead to fake muons. Cosmic ray muons are negligible at the underground CMS cavern [149].
Electron fakes are mainly caused by an electromagnetic shower overlapping with a charged track, by leptons from heavy flavor decays or by electrons from asymmetric photon conversion in the material before the calorimeter [150] .
Taus decay 34% purely leptonically ($\tau \rightarrow \mu\nu_\mu\nu_\tau$ and $\tau \rightarrow e\nu_e\nu_\tau$), 50% into hadronic one-prongs ($\tau \rightarrow \pi\nu$, etc.) and with 15% into hadronic three-prongs ($\tau \rightarrow K^-\pi^+\pi^-\nu_\tau$, etc.) signatures [16]. The one-prong tau decays are clearly the most important, but have the highest background. Leptonically tau decays have similar background like muons or electrons, but due to the three-body decays lower transverse momentum p_T. The background for one-prong tau decays are mainly soft jets/pions faking those processes [151].
In Fig. 6.10 the production mechanism of fake leptons from heavy flavor decays and asymmetric photon conversions are shown.

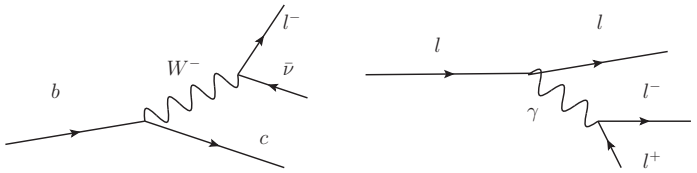

Figure 6.10: Production mechanism of fake leptons from heavy flavor decays (left) and asymmetric photon conversions (right). The asymmetric photon conversion is indicated by the different length of the outgoing fermion lines.

Following the prompt and fake lepton definition, the SM background for multileptonic signatures can be split into fake and prompt SM background. The irreducible prompt background consists dominantly of double boson production (ZZ inclusive $\gamma*$, Z/γ^*W) decaying into leptons. The ZZ production with subsequent Z decays into two leptons can contribute to the 4 lepton (4L) channels, but also to 3L channels, where one lepton is missed, due to detector acceptance or failing object selection. The LO diagrams for double boson production are shown in Fig. 6.11. Rare processes like $t\bar{t}W$, $t\bar{t}Z$ and WWW with three prompt leptons will also be taken into account.
The other important backgrounds are single- or di-lepton processes with additional isolated fake leptons mimicking tri-lepton processes. Di-lepton processes include leptonic Drell-Yan+Jets, $t\bar{t}$ and WW

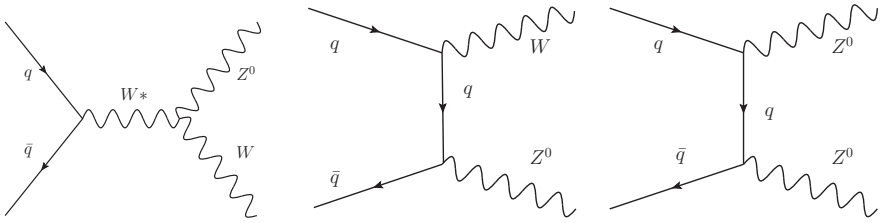

Figure 6.11: LO order diagrams for double boson production.

processes. Typical diagrams for the dominant DY+Jets and $t\bar{t}$ processes are presented in Fig. 6.12. To get contributions in the 3L channels (or 4L as well) from those di-lepton processes, one or more fake lepton have to be produced and selected. The production cross section of fake leptons can have huge uncertainties [148] and a careful considerations is appropriate.
With decreasing number of prompt leptons in the final state, the involved number of fake leptons have to increase to simulate a three lepton signature. Since it has been shown [152] that the fake lepton rate, e.g the rate of fake leptons to be selected and isolated in simulated QCD events, are in the order of 0.1% (fake muons) and the probability for having two ore more isolated fake leptons decreases exponentially, the contributions of leptonic decaying W+Jets with two or QCD processes including three isolated fake leptons are negligible.

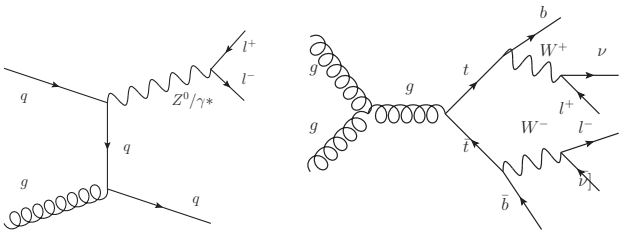

Figure 6.12: Typical Feynman diagrams for Drell-Yan+Jets (left) and $t\bar{t}$ (right).

Kinematic distributions like E_T^{miss}, H_T, L_T, S_T, the invariant mass of all opposite sign same flavor lepton pairs m_{ll}, jet multiplicity, loose lepton transverse momentum, relative isolation and transverse impact parameter are shown in Fig. 6.13 and 6.14 for events with at least three leptons ($p_T > 8\,\text{GeV}$, $|\eta| < 2.1$). At least two of them should pass the tight selection criteria. The detailed lepton selection criteria will be discussed in Section 7.3. For comparison also the LM9 point is added. One can easily see the general problem of SUSY searches, which have to handle huge SM backgrounds by typically small signal expectations. SM processes including at least one fake lepton in the event can be suppressed by requirements on the relative isolation and transverse impact parameter. The irreducible backgrounds from double boson production in contrast have similar kinematic properties compared to the LM9 predictions and are hard to suppress without loosing signal sensitivity. It is clear that one can find suitable models with specific kinematic properties sitting in the tails of the SM distributions, which allow a more simple treatment, but this is not subject of this study.

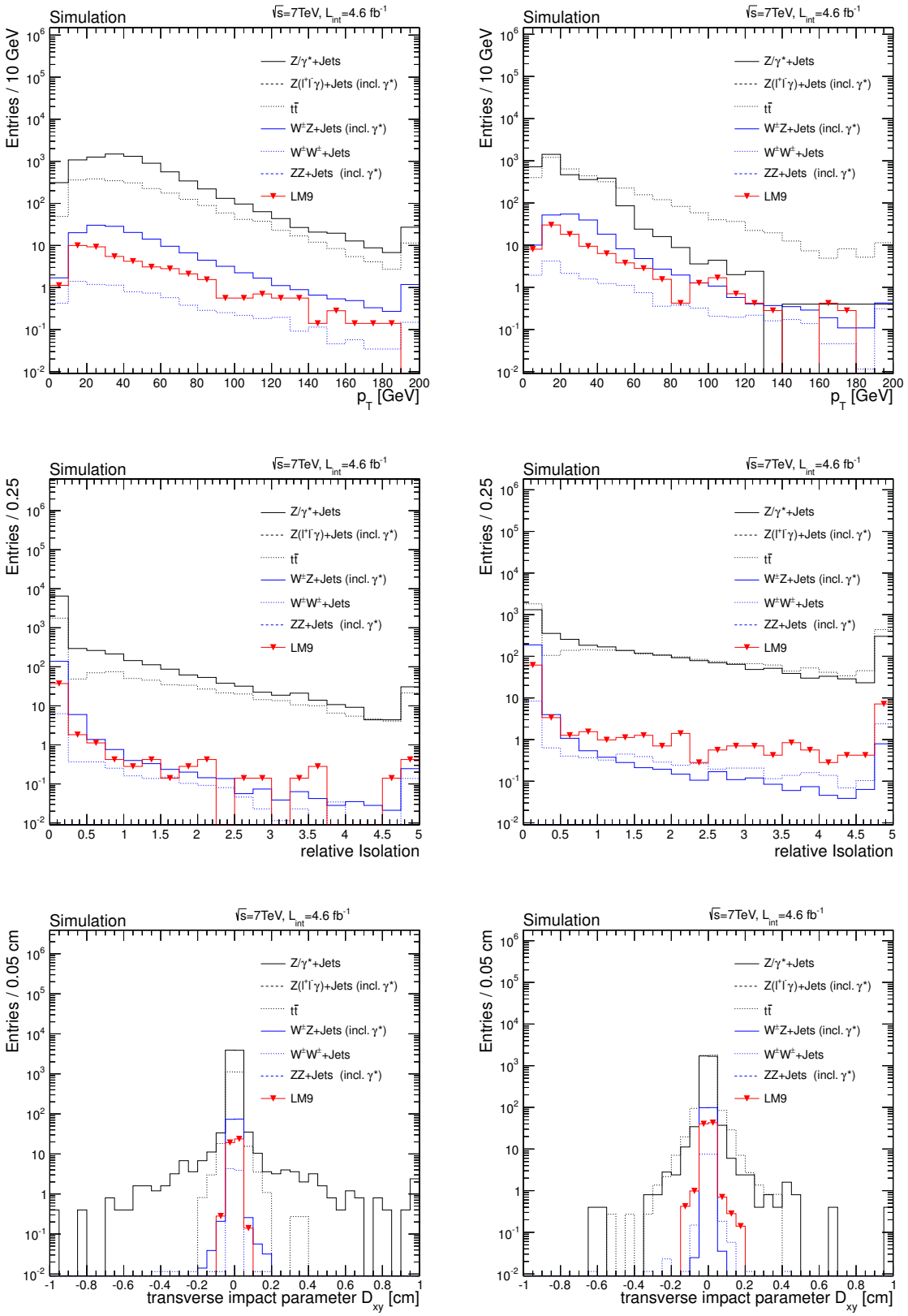

Figure 6.13: Third loose lepton (e left column, μ right column) transverse momentum p_T (top), relative isolation Riso (middle) and transverse impact parameter dxy with respect to the beam spot (bottom) for the SUSY benchmark point LM9 and dominant SM processes selected with three leptons ($p_T > 8\,\text{GeV}$, $|\eta| < 2.1$), where at least two of them pass the tight selection criteria.

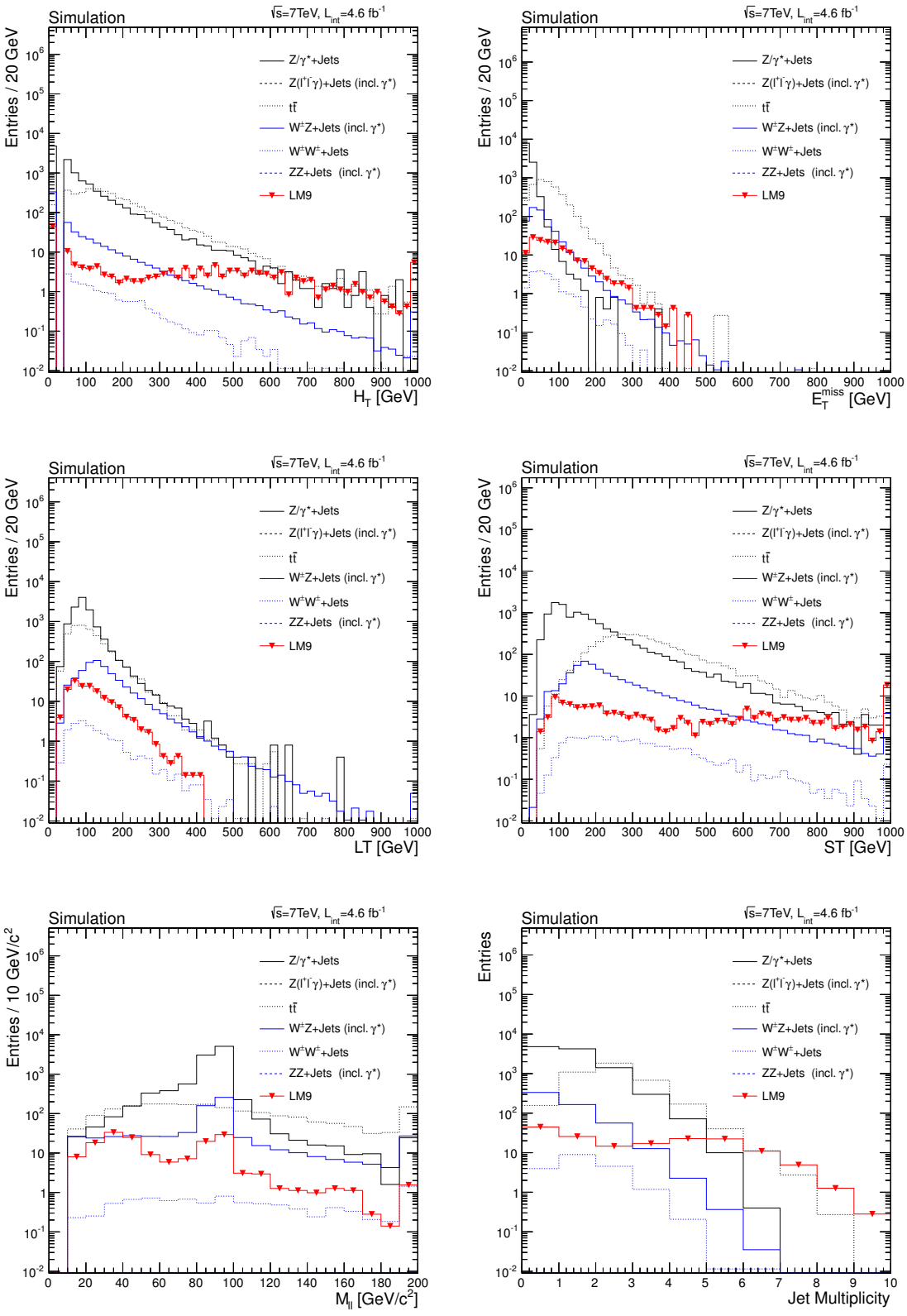

Figure 6.14: H_T (top left), E_T^{miss} (top right), L_T (middle left), S_T (middle right), m_{ll} (bottom left) and jet multiplicity (bottom right) for the SUSY benchmark point LM9 and dominant SM processes selected with three leptons ($p_T > 8\,\text{GeV}$, $|\eta| < 2.1$), where at least two of them pass the tight selection criteria.

CHAPTER 7

Prerequisites

Before discussing the core analysis some prerequisites have to be defined and discussed. The starting point of all analysis is, after defining the topology, to simulate the corresponding SM backgrounds and define the object and event selection. Efficiency of the object selection requirements have to be measured in data, if possible, and applied to MC to minimize the reliance on simulations of detector inefficiencies.
The chapter is organized as following: In the first part the used data and MC samples are summarized and the individual cross sections and integrated luminosities are given. Afterwards the issue of pile up events is discussed before going into the individual object selections and their efficiency measurements. Finally the trigger path selection and trigger efficiency and as well the event selection is discussed.

7.1 Data and MC Samples

The raw data sets are skimmed into different trigger streams, e.g. in the data set *DoubleMu* events are stored, where at least one double μ HLT trigger has fired. The used data sets in this study correspond to the chosen trigger paths Single+Double Muon, Single+Double Electron, Muon+Electron and are listed in Table A.2 in Appendix A, where in addition the integrated luminosity is given. Two runs throughout the year 2011 were recorded, where RunA corresponds to a data set recorded up to a technical stop of the LHC in August 2011 and RunB includes the part of the data recorded afterwards. A run gets certified by the *data certification* or *Data Quality Monitoring* (DQM) team. Lumisections[1], where all detector subsystems are working properly, are flagged as good and summarized in so called *JSON* (Java Script Object Notation) file. The released JSON files

Cert_160404-163869_7TeV_May10ReReco_Collisions11_JSON_v3.txt

Cert_170249-172619_7TeV_ReReco5Aug_Collisions11_JSON_v3.txt

[1]Lumisection: a lumi section consists of several beam orbits

Cert_160404-180252_7TeV_PromptReco_Collisions11_JSON.txt

are used and correspond to an accumulated integrated luminosity of $L_{int} = 4.7\,fb^{-1}$.
In Section 6.2 all SM backgrounds contributing to multileptonic signatures were reviewed. There are several MC LO generators on the market and the commonly used generators within the CMS collaboration are Pythia6 [88] (Pythia8 [89]) and Madgraph5 [93]. Most of the MC samples used in this study are produced with Madgraph and are summarized in Table A.1 in Appendix A, where also the total number of simulated events and the cross sections are given. For most of the SM processes the NLO cross section is calculated with MCFM [153] or the measured cross sections in case of availability is used [154, 155]. The official produced sample ZZJetsTo4L_TuneZ2_7TeV-madgraph-tauola has an internal generator cut on the invariant mass of all opposite sign same flavor lepton pairs of $m_{ll} > 50\,GeV/c^2$, which suppresses a major part of possible backgrounds and is hence not usable. A private production with reduced generator cuts ($m_{ll} > 5\,GeV/c^2$) is used instead but cross checked with the official sample. Similar, so called internal conversions (see Section 8.2) are not generated as well and a MC sample was produced privately with Madgraph5. The data and production cards, generator distributions and comparisons with the official sample can be found in Appendix B.
Additionally, the SUSY benchmark points LM6 and LM9 are used as a reference point in the following. The NLO cross sections for the SUSY points were calculated with Prospino [145].

7.2 Pile Up Events

The excellent performance and the high luminosity during the various LHC data taking runs throughout the year 2011 results in a fast data taking. A side effect of the high luminosity in the data taking periods in 2011 is a not negligible probability for recording more than one interaction per bunch crossing. Those events are commonly called pile up events (PU) and require a careful consideration. The number of interactions n per bunch crossing is poisson distributed around the mean μ value

$$p(n,\mu) = \mu^n \frac{e^{-\mu}}{n!}\,, \tag{7.1}$$

where the mean is defined by the total cross section σ, the instantaneous luminosity L and the bunch crossing rate f_{BX}. Given the values for the run conditions of the used data set at a center of mass energy $\sqrt{s} = 7\,TeV$ ($\sigma_{ie} = 68\,mb$ - total inelastic cross section [71], peak luminosity $L = 3.54\,nb^{-1}s^{-1}$, $f_{BX} = 1380/3564 \cdot 40\,MHz$), results in an average number of interactions per bunch crossing

$$\mu = \frac{\sigma_{ie+d} L}{f_{BX}} \simeq 15 \tag{7.2}$$

reached at the end of the 2011 LHC run. 1380 out of 3564 possible bunch slots were filled, where at maximum 2808 bunches are colliding with a rate of 40 MHz. For comparison, the mean value μ at the design luminosity of $L = 10^{34}\,cm^{-1}s^{-1}$, assuming a cross section $\sigma_{ie} = 80\,mb$ (at $\sqrt{s} = 14\,TeV$) and a bunch crossing rate $f_{BX} = 2808/3564 \cdot 40\,MHz$ of the LHC [71] would be $\mu \simeq 25$, a factor of ~ 1.6 higher.
Charged particles with a well reconstructed track in the tracker system produced in PU events can be associated to different primary vertices, which can be distinguished by the longitudinal distance to the vertex of the hard interaction. Nevertheless neutral particles can deposit additional energy in

both calorimeters (ECal,HCal) without any signals in the tracker system. The angular resolution of the calorimeters does not allow to associate those energy deposits to particles produced in a PU event and thus can harm objects of the hard interaction, which are reconstructed using various calorimeter informations, like the missing transverse energy or jets. Fig. 7.1 shows the E_T^{miss} and H_T distributions for different PU scenarios of data events selected with two isolated muons with opposite sign and an invariant mass comparable with the Z boson mass, where indeed a dependency is observed. The missing transverse energy is smeared to a broader distribution for a larger number of PU events, whereas it has no or only a small effect on the H_T distribution, because only quite hard jets with a transverse energy of at least $E_T > 40\,\text{GeV}$ are taken into account and small additional energy deposits has little effect on the reconstruction of hard jets. If the jet threshold is lowered the H_T distribution becomes also sensitive to PU, see right panel of Fig. 7.1.

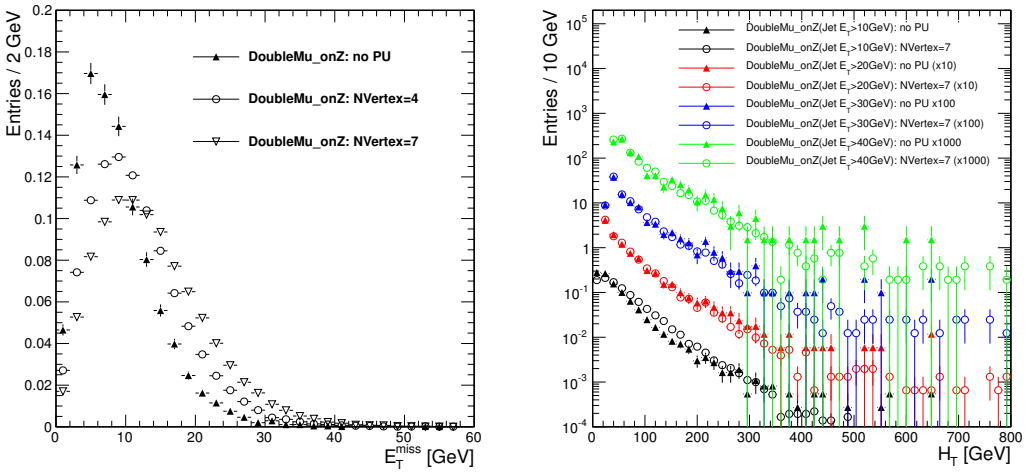

Figure 7.1: E_T^{miss} (left) and H_T (right) distribution for different PU scenarios (number of primary vertices=1, 4, 7) of data events selected with two isolated muons building an invariant mass consistent with the Z boson mass. Also various jet E_T thresholds (10, 20, 30, 40 GeV) are selected for the H_T distribution. Soft jets and the E_T^{miss} distributions are modified by an additional contribution of pile up events.

MC PU scenarios differ from the measured ones. Therefore the MC events are reweighted to reproduce the same number of primary vertices in data. This procedure is shown in Fig. 7.2, where the vertex distribution for MC without and with reweighting is plotted, both compared to data for intermediate instantaneous luminosity settings. As shown the distribution of the number of vertices has a sharp peak at zero in MC simulation, whereas in data this distribution peaks at 6 in this scenario. In order to account for the observed difference a weighting factor per number of primary vertices ($nVtx$) is calculated as $w = N_{MC}(nVtx)/N_{Data}(nVtx)$, with the normalized vertex distribution N_{Data} for data and N_{MC} for MC, respectively. The vertex distribution needs to be normalized in order to guarantee that the total number of predicted events after and before the reweighting agrees, and only shapes are modified.

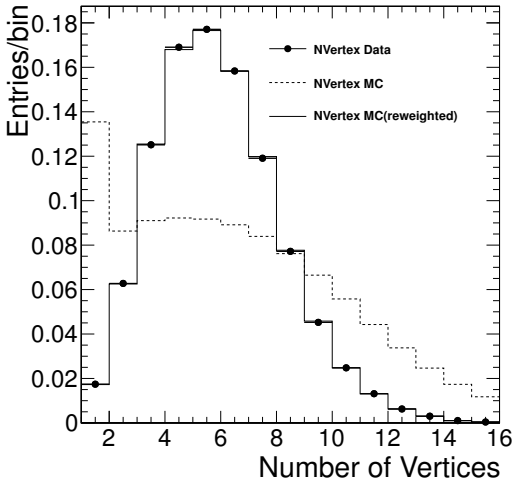

Figure 7.2: Number of primary vertices in data and MC events normalized to unity. The primary vertex multiplicity differences are correct by applying event by event weights on the MC sample.

7.3 Object Definition and Selection

The interplay between the different components of the CMS detector (see Section 4.2) allows to reconstruct most of the physics objects (see Section 5.4). Charged particles can be identified by a track in the tracker and energy deposits in the calorimeters or signals in the muon system, respectively. Solely weak interacting particles like neutrinos or the neutral LSP in many SUSY models do not deposit energy in any detector subsystem, but an indirect indication for the presence in the event is the missing transverse energy due to energy conservation.
In this study leptons (e,μ,τ), jets and missing transverse energy E_T^{miss} are used. The individual definitions and selections are presented in this section. Leptons passing all selection criteria are called *tight leptons* in the following.

Muon selection

Muons are selected by a simple set of cuts to have a reasonable efficient reduction of fake muons in the signal region. Starting from global muons (see Section.5.4.4) a set of requirements on the muon track are applied to select only well reconstructed muons: number of hits in the tracker *NTrackHits* and the quality of the global fit χ^2.
To suppress fake leptons from jets a cut on the relative isolation *Riso*, which is the sum of all energy deposits around the muon in the cone $\Delta R < 0.3$ relative to the transverse momentum of the muon, and the impact parameter in the xy-plane with respect to the beam spot d_{xy}(BS) is applied. The longitudinal impact parameter with respect to the primary vertex $|dz|$ allows to distinguish muons from pile up (see Section 7.2) events.
All selection requirements are listed in Table 7.1. The optimization for muons from SUSY processes can be found in [156, 157], where the selection criteria were optimized in a prompt muon enriched sample versus a fake enriched sample.

Table 7.1: Summary of the muon selection requirements. Several requirements are applied on the muon track quality. In order to suppress fake muons from jets a small transverse impact parameter $d_{xy}(BS)$ and low activity in a cone $\Delta R = 0.3$ around the muon trajectory reflected by a small relative isolation value is required.

Muon Observable	Selection
Transverse momentum p_T	$p_T > 8\,\text{GeV}$
Pseudo rapidity $\|\eta\|$	$\|\eta\| < 2.1$
Identification	isGlobalMuonPromptTight
Number of hits in the tracker	NTrackHits > 10
Global χ^2_{ndof} of the fit	$\chi^2_{ndof} < 10$
Longitudinal impact parameter $\|d_z\|$	$\|dz\| < 1.0$
Transverse impact parameter d_{xy} with respect to the beam spot	$\|dxy(BS)\| < 0.02$
Relative isolation $Riso = \frac{TrackIso+CaloIso}{p_T}$	$Riso < 0.15$

Electron Selection

Similar to muons the electron selection is based on a set of simple cuts. The identification requirements follow the VBTF90[2] recommendation, which corresponds to a 90% selection efficiency for prompt electrons ($p_T > 20\,\text{GeV}$) from Z decays [150].
Fake electrons are dominated by fakes from jets and fakes from asymmetric photon conversion. To suppress fake electrons from jets, requirements similar to the muon selection on the relative isolation *Riso* and transverse impact parameter d_{xy} are applied.
Electrons from asymmetric photon conversion have a displaced secondary vertex due to the fact, that a conversion occurs in the detector material (beam pipe or tracker layers), and the d_{xy} requirement is quite sufficient ($\sim 50\%$) [150]. Further suppression can be achieved by using the conversion partner track. Typically photon conversion results in two tracks, which can be identified by the parameter *ConvDist*, the two dimensional distance between the electron track (GSFTrack) and a surrounding track (CTFTrack), and by the angle θ relation *ConverDCotTheta*:

$$\Delta cot(\Theta) = cot(\Theta_{CTFTrack}) - cot(\Theta_{GSFTrack})$$

of the tracks [150].
For electrons in the barrel region we subtract an additional 1 GeV of the ECalIsolation[3] to account for accumulated noise. To avoid electrons radiated from muons at least a $\delta R = \sqrt{\Delta\eta^2 + \Delta\Phi^2} > 0.1$ of the electron with respect to the nearest tight muon is required.
Table 7.2 summarizes all selection requirements for electrons.

Tau selection

Leptonically decaying taus are already covered by the muon/electron selections. The hadronic decay modes are reconstructed with the HPS algorithm (see Section 5.4.5). This algorithm allows to distinguish between different hadronic tau topologies: single-prong, single-prong with neutral pions (π^0)

[2] https://twiki.cern.ch/twiki/bin/view/CMS/SimpleCutBasedEleID
[3] ECalIsolation: sum of all energy deposits in the ECal around the lepton track in a cone $\Delta R < 0.3$

Table 7.2: Summary of the electron selection requirements. Several electron ID criteria are different for the barrel ($|\eta| < 1.44$) and endcap ($1.56 < |\eta| < 2.1$) region. The latter are given in brackets. The requirements corresponds to the VBTF90 working point. .

Electron observable	Selection
Transverse momentum p_T	$p_T > 8$ GeV
Pseudo rapidity $\|\eta\|$	$\|\eta\| < 2.1$
Transverse shape of the electromagnetic cluster	$\sigma_{i\eta i\eta} < 0.01\,(< 0.03)$
Spatial (Φ) matching between track and supercluster	$\Delta\Phi < 0.8\,(< 0.7)$
Spatial (η) matching between track and supercluster	$\Delta\eta < 0.0007\,(< 0.009)$
Hadronic leakage variable	HoE $< 0.12\,(< 0.05)$
Impact parameter z-axis $\|dz\|$	$\|dz\| < 1.0$
Impact parameter $\|dxy(BS)\|$	$\|dxy(BS)\| < 0.02$
$Riso = \frac{TrackIso+max(0,ECalIso-1.0(Barrel))+HCalIso}{p_T}$	$Riso < 0.15$
Conversion rejection	ConverDist< 0.02 & ConverDCotTheta< 0.02
Number of missing hits in the tracker	NumberOfLostHits< 2
δR to nearest muon	$\delta R > 0.1$
Veto electrons in gap region	Veto: $1.44 < \|\eta\| < 1.56$

and three-prong tau decays. An internal transverse momentum p_T threshold classifies the HPS tau candidates.
Single prong, single prong + π^0 and three prong HPS tau candidates are required to be isolated, i.e. no charged hadrons or photons apart from the tau decay products to be in a cone $\Delta R < 0.5$. In this sense different working points are defined *vloose*, *loose*, *medium* and *tight* by adjusting the p_T thresholds for charged hadron candidates considered within the isolation cone. The selection efficiency over a broad range of the tau transverse momentum for the different isolation working points are $\sim 50\%$ (loose),$\sim 37\%$ (medium) and $\sim 25\%$ (tight), respectively for hadronic taus from Z decays ($Z \to \tau_h\tau_h$) [151].
The transverse momentum threshold of the tau candidates is $p_T > 15$ GeV, due to internal thresholds of the HPS algorithm. Table 7.3 summarizes the selection criteria.

Photon Selection

Photon candidates are not used for the final results, but used for the prediction of asymmetric photon conversions into isolated leptons (see Section 8.2). The selection is summarized in Table 7.4 and corresponds to the recommended *PhotonCutBasedIDTight* photon identification criteria [158].

Jet and E_T^{miss} Selection

Jets reconstructed using particle flow objects clustered with the anti-k$_t$ algorithm [114], with a distance parameter of $\delta = 0.5$, are used for the $H_T = \Sigma_{jets} p_T^{jet}$ calculation, where only jets with a transverse momentum $p_T > 40\,GeV$ and pseudo rapidity $|\eta| < 2.5$ are taken into account. The distance between

Table 7.3: Summary of the tau selection requirements. HPS τ_h candidates are used to reconstruct the single-prong, single prong + π^0 and three prong tau decay modes. The isolation criteria are pre-defined discriminators and only boolean values are accessible.

Tau observable	Selection
Transverse momentum p_T	$p_T > 15\,\text{GeV}$
Pseudo rapidity $\|\eta\|$	$\|\eta\| < 2.1$
Tau decay mode finder	*decayModeFinding*=True
Discriminator against muon misidentification	*againstMuonTight*=True
Discriminator against electron misidentification	*againstElectronTight*=True
HPS Isolation Discriminators	
HPS vloose isolation	*byHPSvloose*=True
or HPS loose isolation	*byHPSloose*=True
δR to nearest muon/electron	$\delta R > 0.1$

Table 7.4: Summary of the photon selection criteria used for prediction of asymmetric photon conversions.

Photon observable	selection
Transverse momentum p_T	$p_T > 8GeV$
Pseudo rapidity $\|\eta\|$	$\|\eta\| < 2.1$
Transverse shape of the electromagnetic cluster	$\sigma_{i\eta i\eta} < 0.01 (< 0.03)$
Hadronic leakage variable	HoE< 0.05
ECal Isolation ($\Delta R < 0.4$)	$ISO_{ECal} < 4.2 + 0.0006 \cdot p_T$
HCal Isolation ($\Delta R < 0.4$)	$ISO_{HCal} < 2.2 + 0.0025 \cdot p_T$
Track Isolation ($\Delta R < 0.4$)	$ISO_{HCal} < 2 + 0.001 \cdot p_T$
Pixel Seed	*hasPixelSeed*=false
δR to nearest muon/electron	$\delta R > 0.1$

jets and selected electrons, muons and taus is required to be above $\Delta R > 0.3$. The missing transverse energy is calculated by the PF algorithm [101]. Jets and E_T^{miss} are corrected according the latest correction factors [120].

7.3.1 Lepton Selection Efficiency

The selection efficiency (e, μ) is measured in data using the so called tag&probe method. A detailed description can be found in [152].

In this study the efficiency of the lepton identification is measured using $Z \to l^+l^-$ events. Events are selected with tight selection requirements on one lepton, the so called *tag-lepton*, and a looser selection on the other *probe-lepton*. The fraction of probe-leptons passing also the tight selection criteria gives an estimate of the selection efficiency.

As a tag lepton we define a lepton passing all selection criteria discussed before, except increased p_T threshold of $p_T^{\mu(e)} > 35(85)$ GeV, to ensure the lepton to be triggered by the single muon (electron) HLT trigger.

The selection efficiency is factorized into two sequential steps: lepton identification (ID) and isolation (ISO). To measure the lepton ID (ISO) efficiency the probe lepton is required to pass all selection criteria except the ID (ISO) cuts and to form a invariant mass with the tagged lepton to be comparable with the Z mass. The ID (ISO) efficiency is determined by counting probe leptons passing/failing the ID (ISO) criteria on the Z peak.

$$\epsilon = \frac{N_{\text{passing}}}{N_{\text{passing}} + N_{\text{failing}}}$$

Fig. 7.3 and 7.4 show the measured efficiency in comparison to $Z \to ll$ MC predictions in bins of the probe lepton p_T and number of primary vertices, i.e. pileup, for muons and electrons, summarized in addition in Table 7.5.

Table 7.5: Summary of the measured ID and ISO efficiency for muons and electrons determined in MC and data using the tag&probe method. The efficiency for electrons/muons are listed for leptons integrated over the full phase space ($p_T > 30\,\text{GeV}$, $|\eta| < 2.1$) as a function of the pimary vertex multiplicity (nVtx). The tag and probe leptons are required to form an invariant mass comparable with the Z mass and the efficiency is estimated by the fraction of probe leptons passing/failing the tight selection criteria. The errors correspond to rounding errors. Statistical errors are an order of magnitude lower.

Lepton flavor	T&P Data			T&P MC		
nVtx	0-4	5-8	9-20	0-4	5-8	9-20
Identification efficiency						
Muon	97.0 ± 0.1	96.7 ± 0.1	96.0 ± 0.1	96.6 ± 0.1	96.5 ± 0.1	96.4 ± 0.1
Electron	96.7 ± 0.1	96.7 ± 0.1	93.9 ± 0.1	95.3 ± 0.1	94.7 ± 0.1	96.4 ± 0.1
Isolation efficiency						
Muon	99.0 ± 0.1	98.6 ± 0.1	97.8 ± 0.1	99.2 ± 0.1	98.7 ± 0.1	$97.8 - 0.1$
Electron	98.7 ± 0.1	98.4 ± 0.1	97.7 ± 0.1	99.0 ± 0.1	98.3 ± 0.1	96.7 ± 0.1

One observes a good agreement between the measured selection efficiency for muons and electrons in data and MC simulated $Z \to l^+l^-$ events. Differences, especially for soft leptons, and the uncertainties of the tag&probe method are taken as an additional systematic uncertainties on the final background predictions (see Section 9.1). The tag&probe method can be used for hadronic taus as well. The fact that neutrinos are involved in all decay modes of τ_h complicates the efficiency determination, since only the visible transverse momentum p_T^{vis} can be reconstructed and the $Z \to \tau\tau$ mass peak is shifted to lower values, which has to be taken into account. A complementary approach takes advantage of the fact, that the decays of the two τs are uncorrelated and by requiring one tau to decay leptonically (muon) and the other hadronically, the identification efficiency can be checked. Since this splitting further decreases the statistics of the sample a p_T and η binned evolution of the efficiency is not in the scope so far. The $Z \to \mu\nu_\tau\nu_\mu\tau_h$ control sample can be selected by requiring one tight muon with $p_T > 20\,\text{GeV}$ (trigger), a τ_h candidate (HPS τ_h candidates), $E_T^{\text{miss}} < 30\,\text{GeV}$ and the transverse mass of the muon with $m_T < 15\,\text{GeV/c}^2$. In Fig. 7.5 the invariant mass of the tight muon and the HPS τ_h candidates are shown. Since in the Run2011B data set the single muon trigger threshold was increased and the number of selected events is not sufficient. Thus it is assumed that the accuracy of

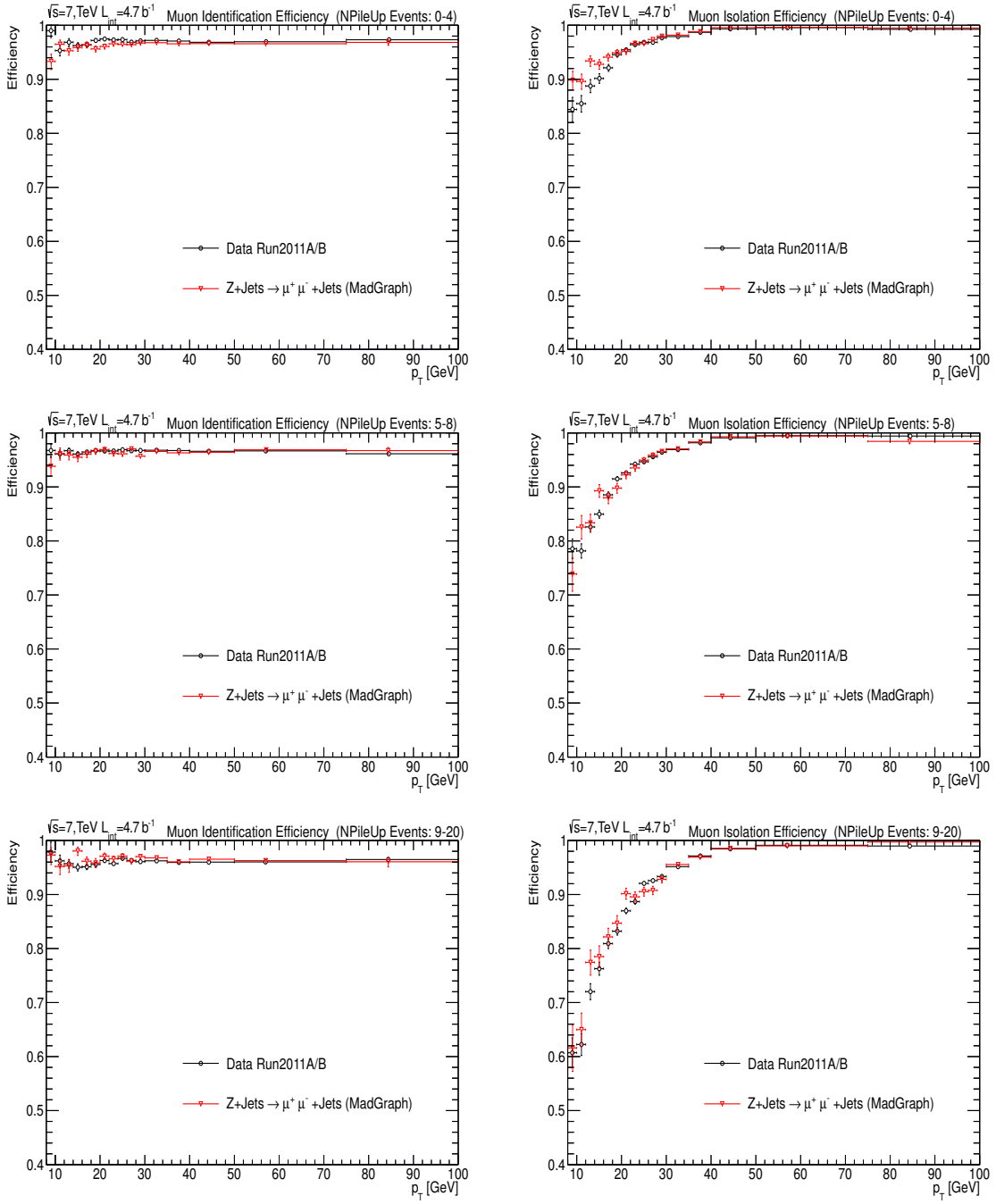

Figure 7.3: Muon ID (left) and ISO (right) efficiency in bins of the probe muon p_T and number of PileUp events (0-4 (top), 5-8 (middle), 9-20 (bottom)) measured in data using the tag&probe method. For comparison the muon ID/ISO efficiency is also shown for a $Z \to \mu\mu$ MC sample

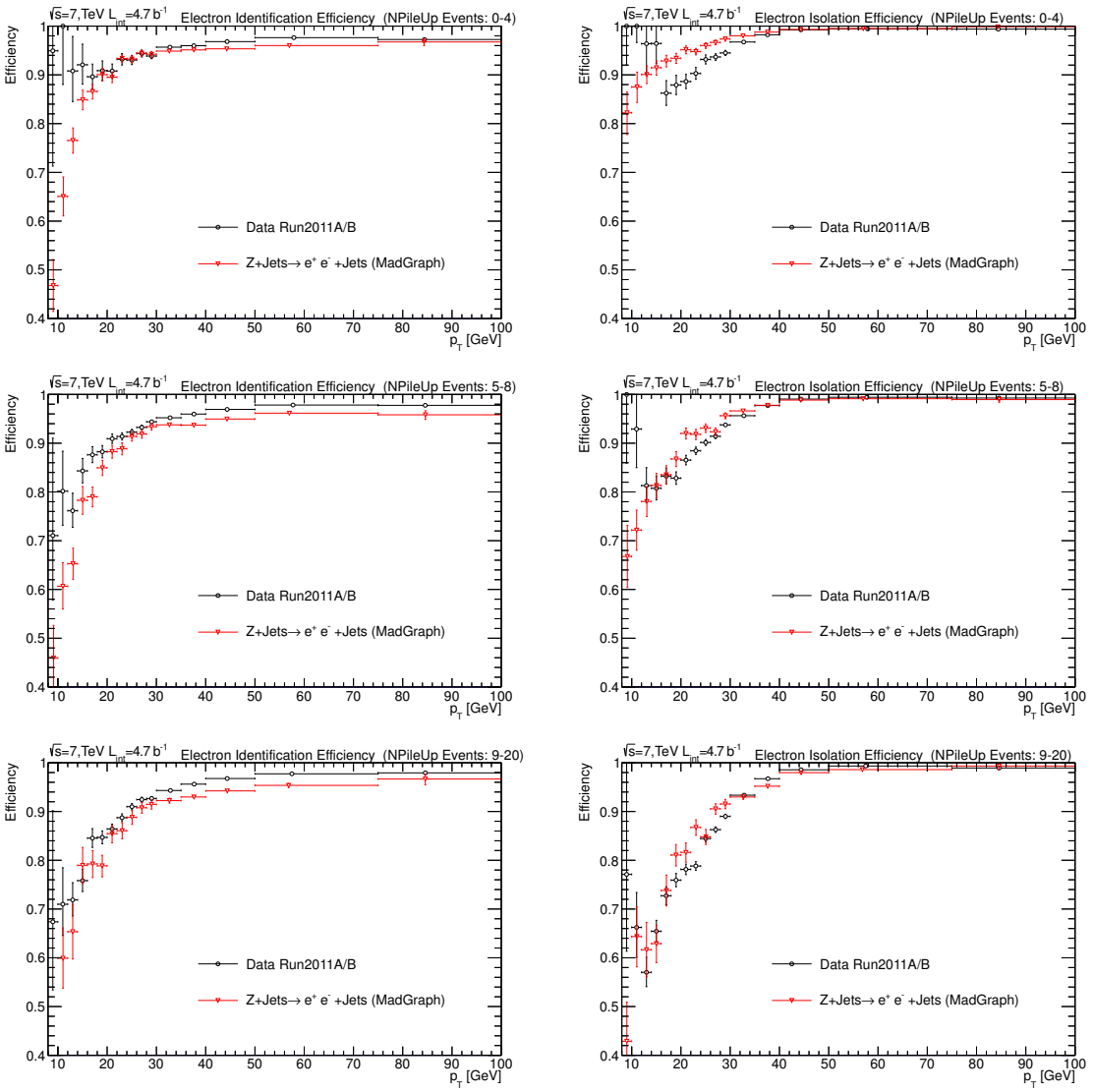

Figure 7.4: Electron ID (left) and ISO (right) efficiency in bins of the probe electron p_T and number of PileUp events (0-4 (top), 5-8 (middle), 9-20 (bottom)) measured in data using the tag&probe method. For comparison the electron ID/ISO efficiency is also shown for a $Z \rightarrow ee$ MC sample

the MC predictions did not change. The statistical uncertainty of the τ_h control sample determines the uncertainty of the tau selection efficiency, which is determined to be $\approx 6\%$ for all decay modes (HPS single prong, single prong + π^0 and three prong τ_h decay candidates).

7.4 Trigger Selection and Efficiency

In this study only un-prescaled muon and electron based triggers are considered. Tau triggers are excluded for simplicity, but could be included in future studies. To maximize the trigger efficiency, i.e. the efficiency of the trigger system to fire for a given lepton multiplicity, all chosen single-, double- and cross-lepton (μ, e) triggers are combined. A summary of all trigger paths is listed in Table C.1 in Appendix C.

The trigger efficiency is an important issue, which should be measured in data to minimize the reliance on simulations of inefficiencies of the detector, due to dead cells, material structure and or fast changing recording environments, e.g. luminosity. From the combined trigger efficiency of an event triggered by the two triggers i and j with efficiency ϵ_{ij} the efficiency of the single trigger ϵ_i can be obtained

$$\epsilon_{\mathrm{i}} = \frac{\mathrm{N}_{\mathrm{Events}}^{\text{selected+trigger i + trigger j}}}{\mathrm{N}_{\mathrm{Events}}^{\text{selected + trigger j}}} \,, \tag{7.3}$$

where *i* is the signal trigger and *j* the orthogonal trigger used. The trigger efficiency integrated over the full phase space ($|\eta^{e,\mu}| < 2.1$) varies between 77% and 99% dependend on the trigger. The measured trigger efficiencies using H_T triggered data samples have been summarized in Table C.1 in Appendix C. The lepton transverse momentum thresholds are set according to the trigger thresholds, but shifted slightly to higher values ($+[2, 5]$ GeV) depending on the individual trigger to ensure, that the selected lepton phase space is on the efficiency plateaus. The actual values will be discussed in Section 7.5. This special consideration is in principle not needed, but would require a careful consideration in the transition regions.

Since the luminosity has been increased throughout the data taking in 2011, the trigger thresholds and the requirements on the trigger objects have been adjusted according to the maximum bandwidth pre-defined for each trigger stream. This results in various trigger paths used to select interesting events. The trigger efficiency for Double-Muon, Double-Electron and Muon-Electron cross triggers as a function of the data taking runs are shown in Fig. 7.6. The trigger efficiency as a function of the leading or next-to-leading leptons pseudo rapidity η are shown in Appendix C.

SM MC predictions are corrected to the measured trigger efficiency in the following and the uncertainties will be treated as a systematic uncertainty in final predictions (see Section 9). Since multiple triggers can fire for a single event, the combination of all trigger possibilities lead to mostly 100% efficiency for events with three and more leptons.

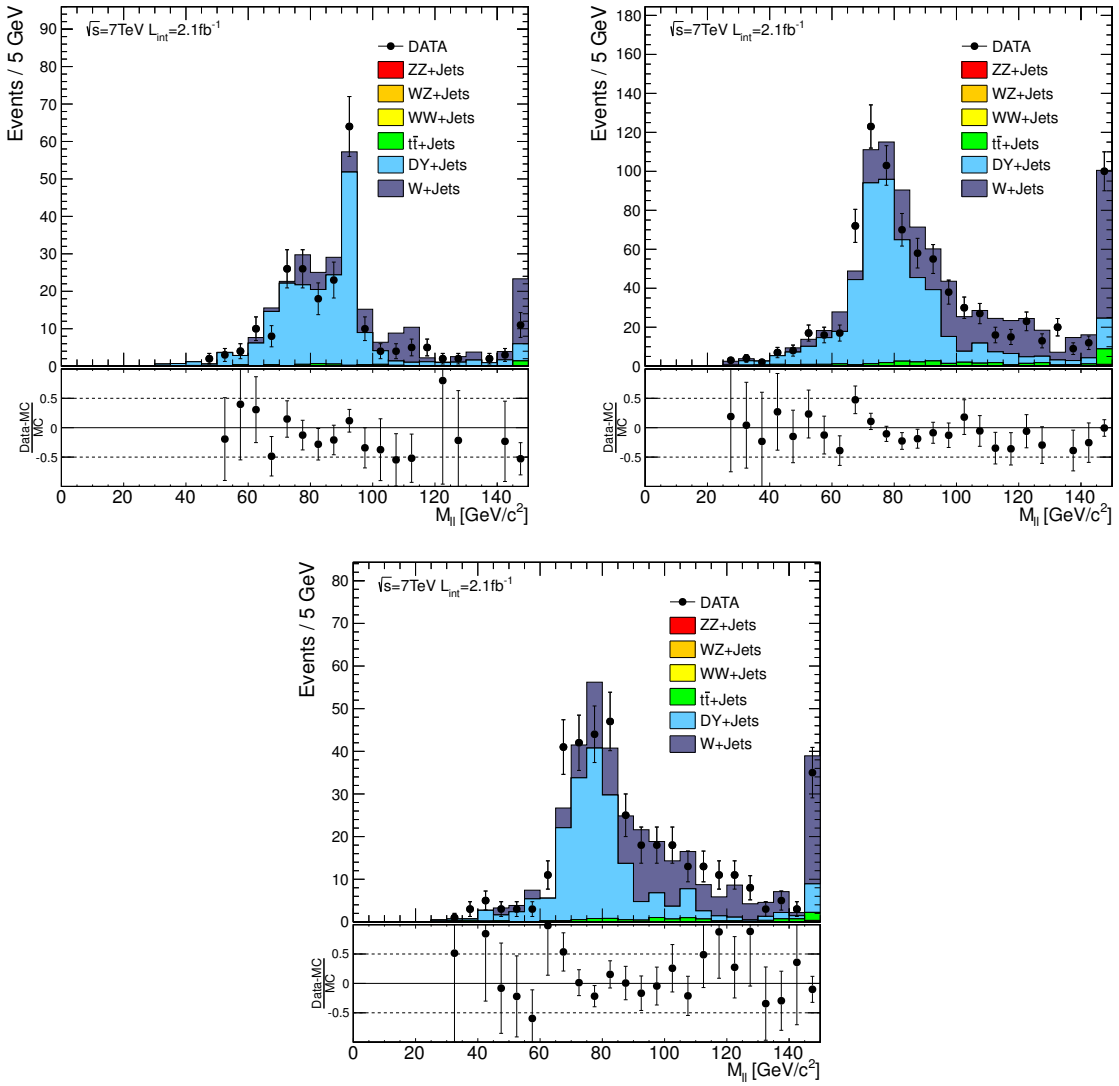

Figure 7.5: Invariant mass distribution m_{ll} of a tight muon and HPS single prong (top left), single prong + π^0 (top right) and three prong τ_h decay candidates (bottom) in the τ_h isolation and identification efficiency control sample. An overall good agreement is observed. Electrons and/or muons failing their identification criteria can be catched by single prong τ_h candidate reconstruction indicated by the peak around the Z mass (top left). The peak at $m_{ll} \approx 150\,\text{GeV/c}^2$ originates from the fact, that all entries above 150 are added to this overflow bin.

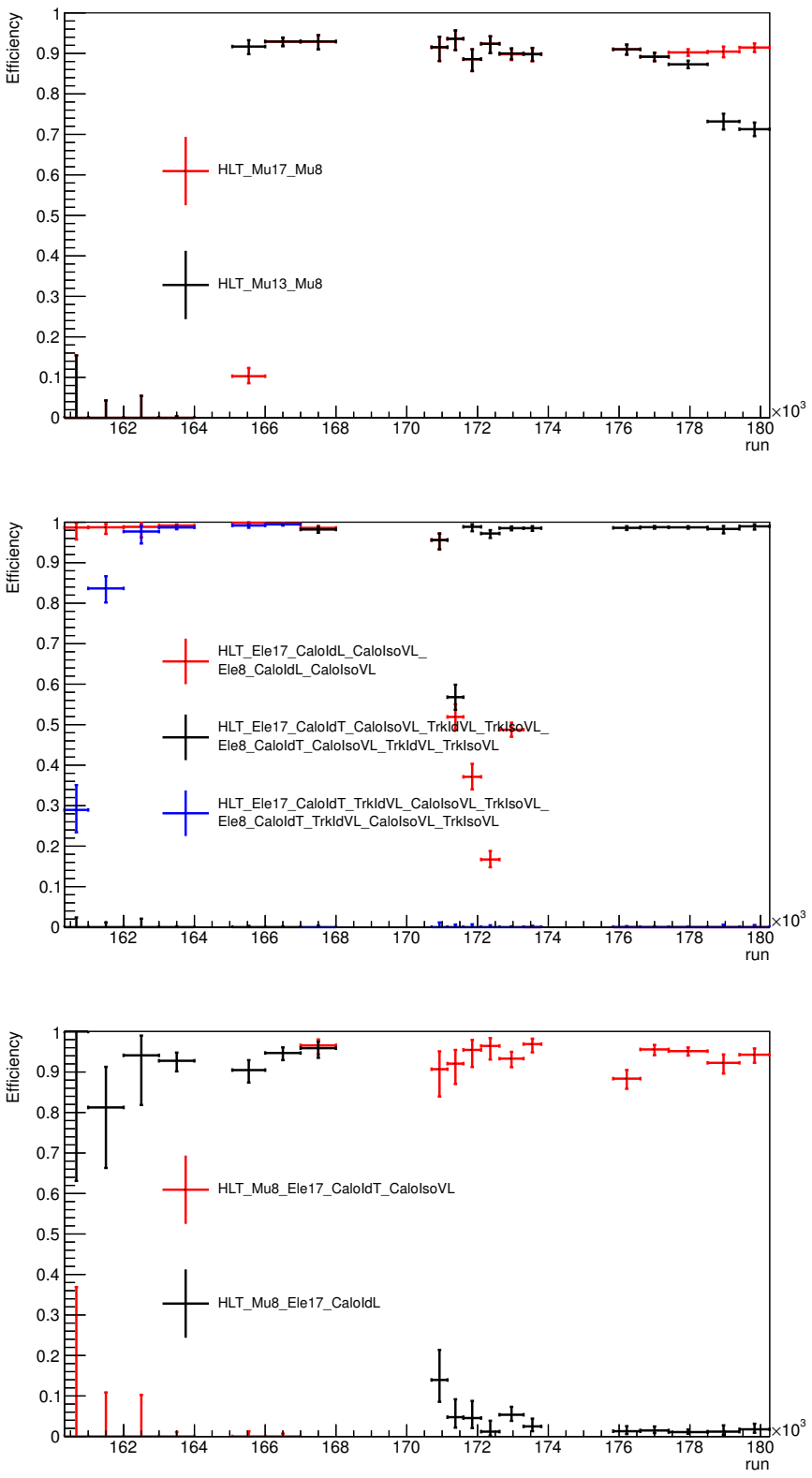

Figure 7.6: Average trigger efficiency of Double-Muon (top), Double-Electron (middle) and Electron-Muon cross trigger paths (bottom) as a function of the recorded runs. Gaps correspond to technical stops and test beam phases were no certified runs were recorded. With increasing luminosity the trigger paths were pre-scaled and/or thresholds increased resulting in changed trigger paths. The trigger thresholds on the trigger primitives are indicated in the path name, e.g. Ele17 correspond to the trigger requirement on an electron to be above $p_T > 17\,\text{GeV}$.

7.5 Event Selection

In this analysis we select events triggered by single or double lepton (μ, e) triggers including cross triggers (μ+e). The threshold of these triggers define the lower p_T cuts for the leading leptons and so each event has to pass at least one of the following requirements:

- leading muon with $p_T^{\mu_1} > 35\,\text{GeV}$
- leading muon with $p_T^{\mu_1} > 20\,\text{GeV}$ and next to leading muon with $p_T^{\mu_2} > 10\,\text{GeV}$
- leading electron with $p_T^{e_1} > 85\,\text{GeV}$
- leading electron with $p_T^{e_1} > 20\text{GeV}$ and next to leading electron with $p_T^{e_2} > 10\,\text{GeV}$
- leading muon with $p_T^{\mu_1} > 10\,\text{GeV}$ and leading electron with $p_T^{e_1} > 20\,\text{GeV}$
- leading muon with $p_T^{\mu_1} > 20\,\text{GeV}$ and leading electron with $p_T^{e_1} > 10\,\text{GeV}$,

where the individual thresholds were set slightly above the actual trigger thresholds to ensure a selection on the efficiency plateaus. For simplicity the thresholds on the transverse momentum p_T are set constant for the full run range and are defined by the last un-prescaled trigger paths with the highest thresholds. Runs recorded in the beginning of 2011 are characterized by low luminosity and thus lower thresholds. Hence one could increase the statistics by run dependent p_T thresholds, which is for the time being not applied.
Default cuts to select good events, like a good primary vertex ($ndof > 4$, $|z| < 15\,\text{cm}$, $r < 2.0\,\text{cm}$) [159] and reject beam scraping events, were applied. Protons in the beam halo can hit detector or accelerator components and form a rich source of secondary particles called beam scraping events. Proton-proton interactions are distinguished by the number of tracks satisfying basic kinematic requirements; if more than ten tracks are present at least 25% should be high quality [159].
The amount of background decreases with increasing number of prompt leptons per event, but so does the signal cross section. Hence, the cuts to suppress the SM background, like missing transverse energy and transverse energy can change with the number of prompt leptons. In Fig. 7.7 the E_T^{miss} and H_T distributions are shown for SM backgrounds and a SUSY benchmark model (TeV3[4]) selected with a basic three lepton selection. With a H_T cut of 200 GeV or similar a E_T^{miss} cut of 50 GeV the SM background can be strongly suppressed with comparable background rejections.
The signal efficiency of the selection cuts are model dependend, e.g. an E_T^{miss} based analysis is more sensitive for models, where the direct chargino neutralino production is dominant and H_T is more sensitive for squark/gluino production, which results in cascade decays leading to higher jet multiplicities and so higher H_T. The model dependency of the average $<E_T^{\text{miss}}>$ and $< H_T >$ in the cMSSM parameter space (m_0, $m_{1/2}$) for fixed $tan\beta = 3$ and $A_0 = 0$ is shown in Fig. 7.8. There are regions in the cMSSM model space, where the H_T cut has a worse signal efficiency as E_T^{miss}, and vice versa for other regions.
In order to be as model independent as possible the measurement is binnend in H_T and E_T^{miss}. The basic measurement strategy is shown in Fig. 7.9. An event gets classified in terms of *low*-H_T ($H_T \leq$

[4]TeV3: $m_0 = 60$, $m_{1/2} = 230$, $tan\beta = 3$, $A_0 = 0$ and $sign(\mu) = +1$ benchmark model is already excluded and used only for visualization.

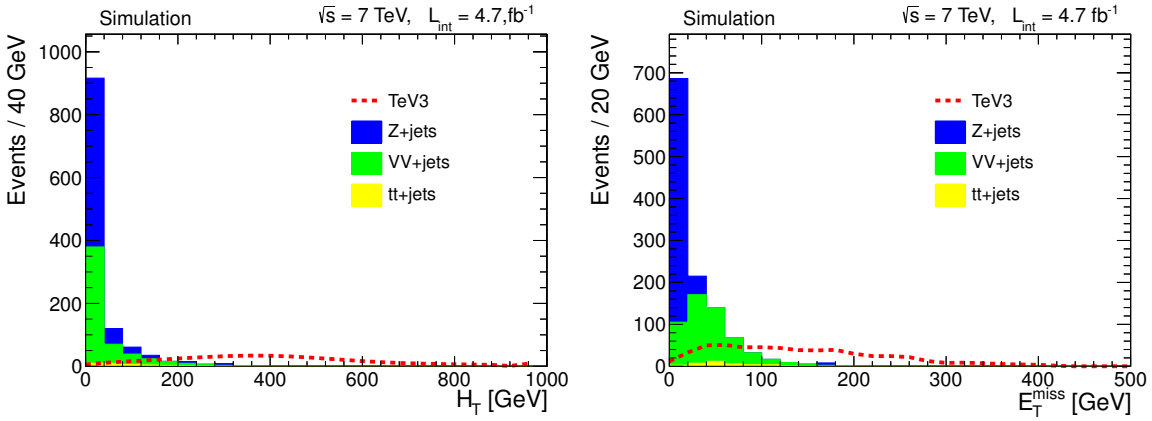

Figure 7.7: H_T (left) and E_T^{miss} (right) distribution for SM backgrounds and a SUSY benchmark model (TeV3). A H_T cut of 200 GeV or similar a E_T^{miss} cut of 50 GeV the SM background can be strongly suppressed with comparable background rejections and similar signal sensitivity.

200 GeV), *high-*H_T ($H_T > 200$ GeV), *low-*E_T^{miss} ($E_T^{\text{miss}} \leq 50$ GeV) and *high-*E_T^{miss} ($E_T^{\text{miss}} > 50$ GeV). Furthermore events are classified by the kind of lepton pairs with opposite sign (OS) or same sign (SS), opposite flavor (OF) or same flavor (SS) and if there exists at least one opposite sign same flavor (OS-SF) lepton pair with an invariant mass comparable with the Z-mass $|m_{\text{ll}} - Z_{\text{mass}}| < 15$ GeV (*on-Z*) or not (*off-Z*). If no OS-SF lepton is present the event gets classified as no-OSSF. The selection strategy does not cut out phase space were no specific SUSY contributions are expected, but rather considers simultaneously bins of signal and background dominated region, which allows a simultaneous control over the background. In the different search regions *low-*H_T *high-*E_T^{miss}, *high-*H_T *low-*E_T^{miss} and *high-*H_T *high-*E_T^{miss} counting experiments are performed.
To summarize: we select events with at least three tight leptons (μ, e, τ) with $N(\tau_h) \leq 2$, which are classified by their jet activity (H_T), missing energy (E_T^{miss}) and lepton pairs (on-Z, off-Z, no-OSSF). Two additional requirements will be applied to suppress leptons from low mass resonances and initial or final state radiation. Low mass resonances like J/Ψ or Ypsilon (Υ) are suppressed by requiring all OS-SF lepton pairs to have an invariant mass above 12 GeV ($m_{\Upsilon(1S)} \approx 9.5$ GeV). FSR processes can be suppressed by requiring the invariant mass of all leptons m_{lll} to be $|m_{\text{lll}} - Z_{\text{mass}}| > 15$ GeV. The $|m_{\text{lll}} - Z_{\text{mass}}| > 15$ GeV veto is applied only in the SM dominated control region "low-E_T^{miss} low-H_T off-Z". Details are given in Section 8.2.

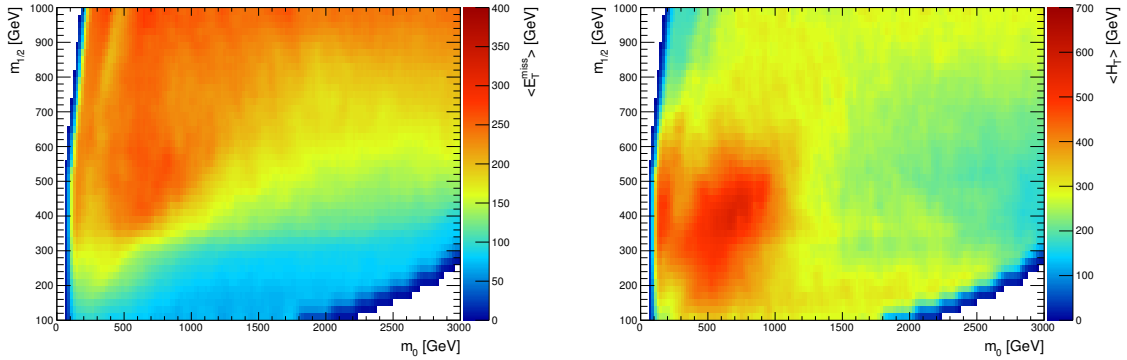

Figure 7.8: Average $<E_T^{\text{miss}}>$ (left) and $< H_T >$ (right) in the cMSSM parameter space (m_0, $m_{1/2}$) for fixed $tan\beta = 10$ and $A_0 = 0$. Events are preselected with three tight leptons (e, μ). The selection efficiency for E_T^{miss} and H_T requirements have strong model dependence.

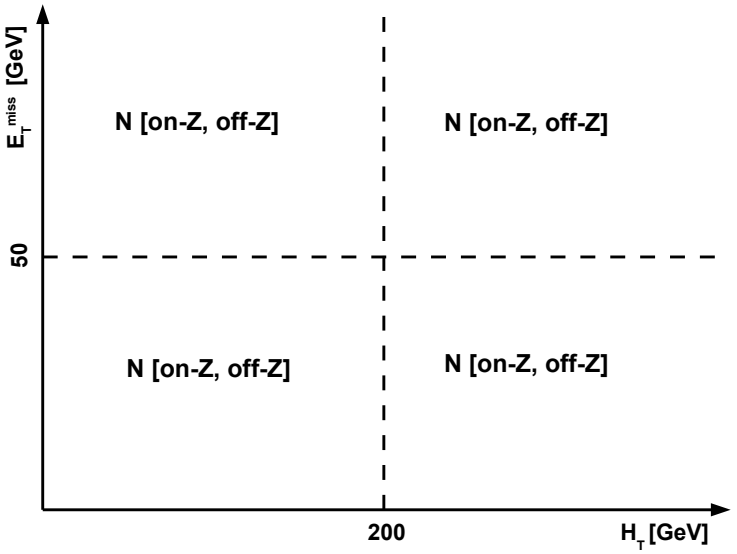

Figure 7.9: Event selection strategy displayed in the H_T-E_T^{miss} plane. The measurement is binnend in H_T,E_T^{miss} and separated additionally in on-Z and off-Z bins, which are distiguished by the presence of an OS-SF lepton pair inside or outside the Z-mass window of 75-105 GeV/c^2.

CHAPTER 8

SM Background Prediction

Supersymmetric signals are expected to increase smooth over time, and not to pop up immediately with the first bunch of integrated luminosity. Also many SUSY models predict contributions in the very tails of the kinematic distributions (like E_T^{miss}) of SM processes. Those both assumptions requires a very good knowledge of the background processes in not yet well tested phase spaces, to be able to establish funded presumptions on the measurement about possible signals of new physics.

In Section 6.2 the dominant SM processes leading to multileptonic signatures were reviewed. Several processes are expected to contribute: (1) dilepton processes ($Z/\gamma*$, $t\bar{t}$, WW) with an additional fake lepton, (2) backgrounds with a lepton from pair conversion of initial/final state radiated photons, (3) prompt backgrounds ($WZ/\gamma*$, $t\bar{t}W$, $t\bar{t}Z$, WWW) and (4) backgrounds with missed leptons (ZZ, $t\bar{t}Z$), where leptons can be missed due to detector acceptance or failing object selections.

Since the measurement is split in various search regions in E_T^{miss}, H_T and on/off-Z, each SM process contribution is distributed over the search channels differently. The challenge is to control all SM backgrounds simultaneously with a high accuracy.

The easiest way would be to trust the SM MC generation and simulation of generated particle propagation through and their interactions with the detector material. A good description of the data is in such cases not guaranteed, due to uncertainties in prescription of underlying events, parton density functions, detector inefficiencies and alignment, and many more sources, which can harm the predictions. Recording further data, MC simulation can be tuned to well known standard model processes and improve their predictions over time. Nevertheless backgrounds derived from MC simulations require as many as possible control regions, to reveal any inconsistencies. The definitions of such control regions should be close enough to the signal regions, to test almost similar phase spaces, but also be SM dominated, i.e. the expected signal contributions has to be negligible. Otherwise difference in those control regions can be misinterpreted as poorly data describing MC simulations and signal excess can drop away.

More sophisticated methods are so called *Data Driven Methods*, which derive their predictions directly from data ideally without using MC informations. The advantage is that the reliance on MC is

minimized. Despite that the data driven methods can be rather complicated and are commonly defined for single phase space regions or special kinematic properties of the processes.
In this chapter the SM backgrounds will be discussed one by one. For each source of background a prediction method, or at least a control region, is defined and cross checked in closure tests. A hybrid method, data driven with shapes taken from MC, for dileptons plus an additional fake lepton is utilized. A data driven calibration is performed in the fake lepton isolation side-band and propagated to the isolation signal region. This measurement is done for $Z/\gamma * (ll) + l^{\text{fake}}$, and $t\bar{t}(ll) + l^{\text{fake}}$ processes separately, because the fake lepton composition in those processes can diver, simply due to the fact, that in $t\bar{t}$ two hard b-jets occur in every event and Drell-Yan is dominated by light (udsg) jets. Dileptons and a lepton from photon pair conversion mimicking a three lepton signature need a special consideration and a dedicated simulation for electrons/muons from pair conversion is generated and extensivly cross checked to predict those backgrounds. The residual prompt backgrounds (ZW, ZZ) are taken from MC and are checked in well defined control regions. Only the very rare processes $t\bar{t}W$, $t\bar{t}Z$ and WWW are taken completely from MC without any cross checks, because no suitable control region can be defined with the accumulated integrated luminosity so far.

8.1 Dilepton - Data Driven Fake Background Calibration

Fake leptons, i.e. leptons mainly produced in light (udsg) and heavy flavor decays ($b/c \to \mu, e$), are a dominant background sources beside the prompt double boson production. The cross sections of the $Z/\gamma * + Jets$ and $t\bar{t}$ production with subsequent branching into two prompt leptons in the final states are high. Hence the contribution including a third fake lepton from jets can be significant and has to be controlled. Leptons produced in jets can be identified by their isolation values (Riso), and in case of heavy flavor decays with a longer lifetime, by their transverse impact parameter (d_{xy}). Typically the multiplicity around the fake lepton is high in jets and the isolation variable tends to be significant higher in comparison with prompt leptons produced in Z or W decays.
The basic idea of the *Data Driven Fake Background Determination* is the extrapolation of the side-band of the isolation distribution to the signal region using the shape from Monte Carlo simulation.
Since the data driven background determination is applied on the relative isolation side-bands, where the shape depends on the fake composition, i.e. the heavy flavor content in the events, the side-band technique has to be performed for light jets dominated backgrounds like $Z/\gamma*$ and the heavy flavor enriched $t\bar{t}$ processes separately.
In case of fake electrons and muons the dominant sources are light/heavy flavor decays within jets in the event. Heavy flavor decays can be identified by a large transverse impact parameter d_{xy}. This can be used as a closure test of the data driven determination for the fake lepton subset from heavy flavor decays by repeating the side-band technique from the isolation variable for large transverse impact parameter values.
In contrast, fake hadronic tau decays are dominated by soft jets misidentified by the tau reconstruction and identification algorithm. The signatures of taus used in this study are (1) single prong, (2) single prong with accompanied photons and (3) three prong τ_h decay candidates. The decay branching ratios for these channels are 14%, 36% and 15%, respectively. An isolation including information of the decay properties of the taus can be defined (Section.7.3) and used as signal and side-band region.

Here a closure test with large d_{xy} values cannot be done because of absence of the d_{xy} variable in the τ_h candidate selection. Instead a closure test with a complementary $t\bar{t}$ sample ($t\bar{t}$ events with one prompt lepton) will be performed.

8.1.1 Drell-Yan

The first fake background to be discussed is $Z/\gamma*$+Jets. Before looking into the fake lepton production in such processes control plots for the prompt part has to be defined in order to ensure a proper description of the underlying process $Z/\gamma* \to l^+l^-$ in MC simulation.

Control Plots

The Z boson has the useful property that it decays with a branching ratio of $\sim 10\%$ into an opposite sign (OS) same flavor (SF) lepton pair ($\sim 3.3\%$ for each lepton flavor) with an invariant mass

$$m_{l^+l^-} = \sqrt{(E_{l^+} + E_{l^-})^2 - (p_{l+} + p_{l^-})^2} \tag{8.1}$$

consistent with the Z mass. A relatively pure Z sample can be selected by requiring two tight opposite sign same flavor leptons on top of the common criteria like a good primary vertex, beam scraping veto and trigger requirements for single and dilepton triggers (see Section 7.5). The invariant mass is shown in Fig. 8.1 for e^+e^-, $\mu^+\mu^-$ events with $E_T^{\text{miss}} < 50$ GeV and $H_T < 200$ GeV. The E_T^{miss} and H_T requirement ensure a negligible signal contamination. One observes good agreement between measurement and MC and a good description of the Z peak in the invariant mass distribution.

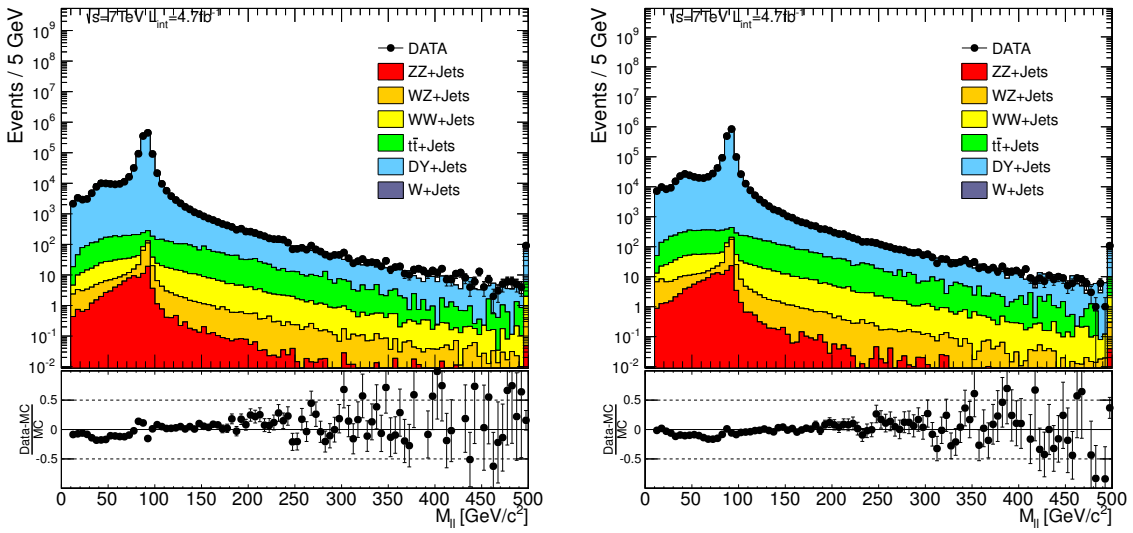

Figure 8.1: Invariant mass distributions of two tight leptons with opposite sign same flavor e^+e^- (left) and $\mu^+\mu^-$ (right). An overall good description of the MC simulation in comparison with the observation is observed, also the long tails in the invariant mass distribution are described well. The peak at $m_{ll} \approx 500\,\text{GeV/c}^2$ originates from the fact that all entries above 500 are added to this overflow bin.

In order to have an additional fake lepton produced within Drell-Yan events associated jets have to be present. The production mechanism for additional jets in Z events are similar to $\gamma*$ events, where at tree level the following processes contribute to $pp \rightarrow Z/\gamma* + 1$Jet:

$$(1)\ q\bar{q} \rightarrow Z/\gamma* + g \qquad (2)\ qg \rightarrow Z/\gamma* + q \qquad (3)\ \bar{q}g \rightarrow Z/\gamma* + \bar{q}\ .$$

Processes decaying to two leptons do not have associated neutrinos in the event, which implies no intrinsic missing transverse energy and so any measured E_T^{miss} corresponds to miss measurements of the involved physics objects, accumulated noise in the detector or pile up events.
Nevertheless the source of E_T^{miss} and the production mechanism for accompanied jets are similar for processes involving Z or $\gamma*$ and a determination of the fake lepton production for one process is suitable for conclusions on the other.

Data Driven Determination of Fake Electrons/Muons

After cross checking the $Z/\gamma* +$Jets production with the subsequent decay into two tight leptons $Z/\gamma* \rightarrow l^+l^-$, the data driven side-band technique discussed before can be applied. In order to select a fake lepton enriched Z data sample the following set of cuts can be applied:

- one OS-SF tight lepton pair
- invariant mass $|m_{ll} - Z_{\text{mass}}| < 10$ GeV/c^2
- third loose lepton (Riso side-band: Riso$= [0.15, 5]$)
- $H_T < 200$ GeV
- $E_T^{\text{miss}} < 50$ GeV

The third loose lepton has the same requirements as the tight selection criteria except an inverted relative isolation requirement $Riso > 0.15$ with the restriction on the upper boundary $Riso < 5.0$. Fake leptons with an relative isolation above 5 are not taken into account, because the fake leptons close to the signal region $Riso < 0.15$ allow for a more reliable extrapolation to the signal region.
The transverse momentum p_T and pseudo rapidity η of the third loose lepton are presented in Fig. 8.2. One observes that indeed such a selected sample is dominated by $Z +$ Jets $\rightarrow l^+l^- + l^{\pm}_{\text{fake}}$ events and the transverse momentum p_T spectrum is dominated by soft fake leptons ($p_T < 20$ GeV). Using the full phase space ($p_T > 8$ GeV, $|\eta| < 2.1$) any side-band measurement will be defined by soft fake leptons. In order to account for high p_T leptons the data driven determination has to be performed as a function of the transverse momentum. Due to limited statistics three bins in p_T are selected $p_T = [8, 12]$ GeV, $p_T = [12, 20]$ GeV and $p_T = [20, \text{inf}]$ GeV.
The side-bands Riso$= [0.15, 5]$ are presented in Fig. 8.3 for electrons and muons in the various transverse momentum p_T bins. The MC prediction (including other SM processes than Drell-Yan events as well) for the isolation signal region are added to get a feeling for the final contribution. The data in the signal region (Riso<0.15) is left out on purpose, since other SM backgrounds contributing have to be discussed first and also not to open the signal box at this stage in order to be unbiased with respect to any interpretation. In Section 9 the corresponding search channels will be discussed, where the

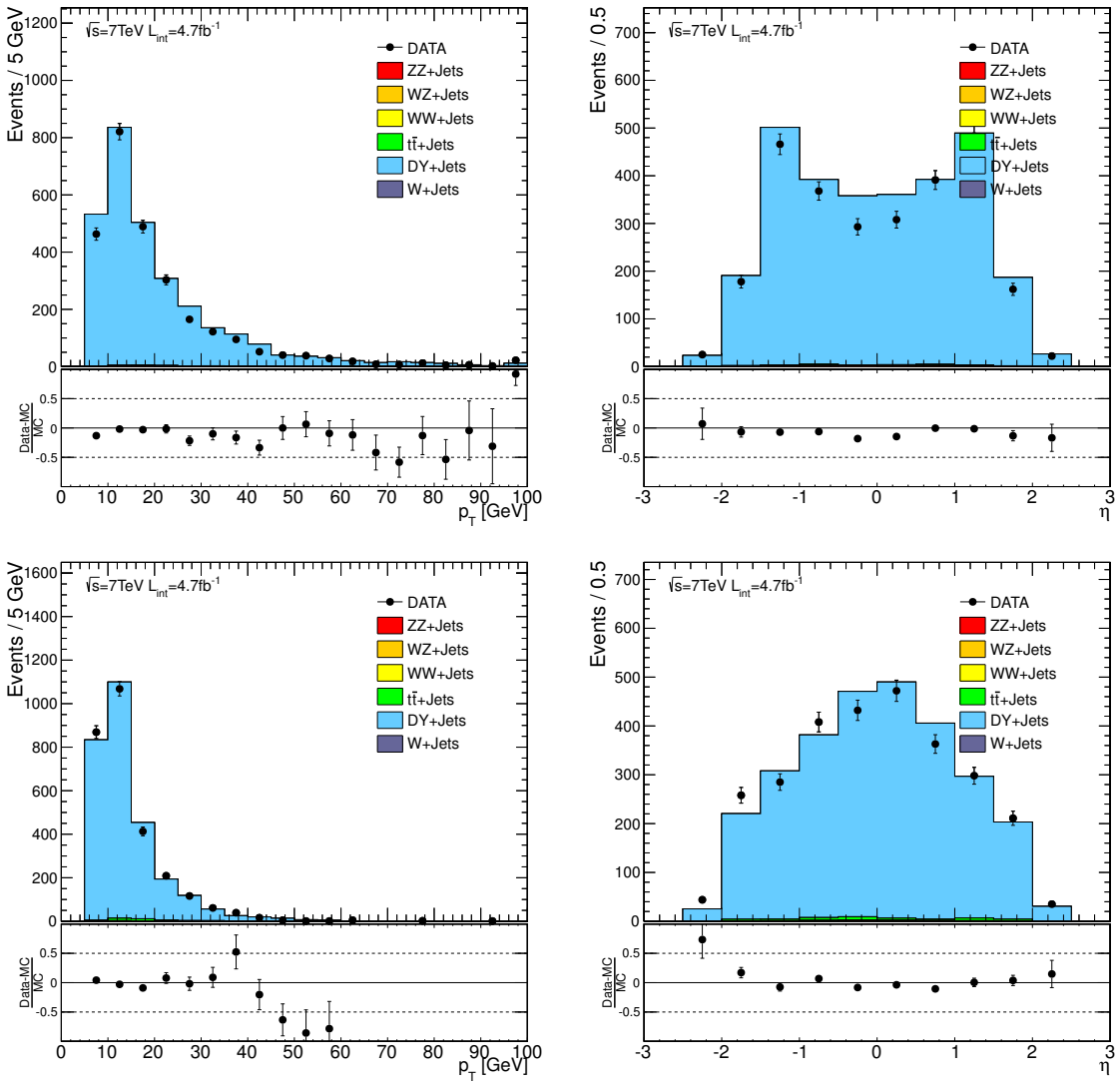

Figure 8.2: Transverse momentum p_T and pseudo rapidity η distributions of the third loose lepton for e (top) and μ (bottom) in $Z \rightarrow l^+l^- +$ Jets events selected with $H_T < 200$ GeV, $E_T^{\text{miss}} < 50$ GeV and the invariant mass of the opposite sign same flavor lepton pair in the mass range $|m_{ll} - Z_{\text{mass}}| < 10\ \text{GeV}/\text{c}^2$.

isolation signal regions discussed above corresponds to the "low-H_T, low-E_T^{miss}, on-Z" 3L channel. An overall good description of fake leptons in Drell-Yan events is observed.
The discussion of the uncertainty on this data driven fake background determination is postponed to Section 8.1.4.

Data Driven Fake Rate of τ_h

HPS τ_h candidates are used for the reconstruction of the single prong, single prong + π^0 and three prong decay modes. To determine the fake τ_h prediction using the isolation side-band measurement requires a slight modification compared to fake electrons and muons. The reason for this is simply the fact, that the tau identification for HPS τ_h candidates used within the CMS collaboration is a boolean member function of the tau candidate collection. As discussed previously in Section 7.3, four different working points corresponding to different efficiencies can be used, where the loose is chosen as the isolation signal region in this study. The isolation side-band is defined as a tau candidate passing the vloose (very loose) identification criteria, but failing the loose criteria. This procedure selects a complementary data set.
The p_T and η distribution of a third "very loose" τ_h decays in events selected with an OS-SF tight lepton pair (e^+e^-,$\mu^+\mu^-$) with an invariant mass comparable with the Z mass $|m_{ll} - Z_{\text{mass}}| < 10$ GeV/c^2 are presented in Fig. 8.4 for the three different τ_h decay modes, data and MC predictions are in good agreement.
Again the discussion of the uncertainty on this measurement is postponed to Section 8.1.4.

Closure test

The side-bands for fake leptons from jets in Drell-Yan events are in good agreement with MC predictions, so we take the MC shape to predict the number of fake leptons in the signal region.
In order to cross check the results for fake leptons in Drell-Yan+Jets events, one can select a complementary fake enriched data set by requiring additionally the transverse impact parameter of the third loose lepton within a dedicated side-band $|dxy| > 0.02$. The advantage of this cross check is the possibility to look into the isolation signal region without opening the signal box and a direct comparison can be done. The dxy side-band selection induces a different fake composition of the fake lepton enriched sample (and hence only an effective subset of the actual fake contribution are cross checked by this test), i.e. the heavy flavor contribution is enhanced. The relative isolation distributions of a third loose lepton (Riso < 5.0, $|d_{xy}| > 0.02$ cm), where the lepton flavor is either e or μ in events with an OS-SF tight lepton (e^+e^-, $\mu^+\mu^-$) pair forming an invariant mass consistent with the Z mass are shown in Fig. 8.5.
An important fact to note is that in case for electron fakes the isolation signal and close by regions are also populated with fake electrons from initial/final state radiated photons, which convert (either in the detector or at matrix element level) into a pair of leptons and if this conversion appears to be asymmetric one lepton can be mistakenly be identified as a prompt (detailed discussion of those backgrounds is postponed to Section 8.2). This contamination can harm the conclusion, since if any discrepancies are observed, both sources can be accounted for. Also in cases like here where the prediction and the measurement agrees well, the conclusion derived has to be carefully discussed,

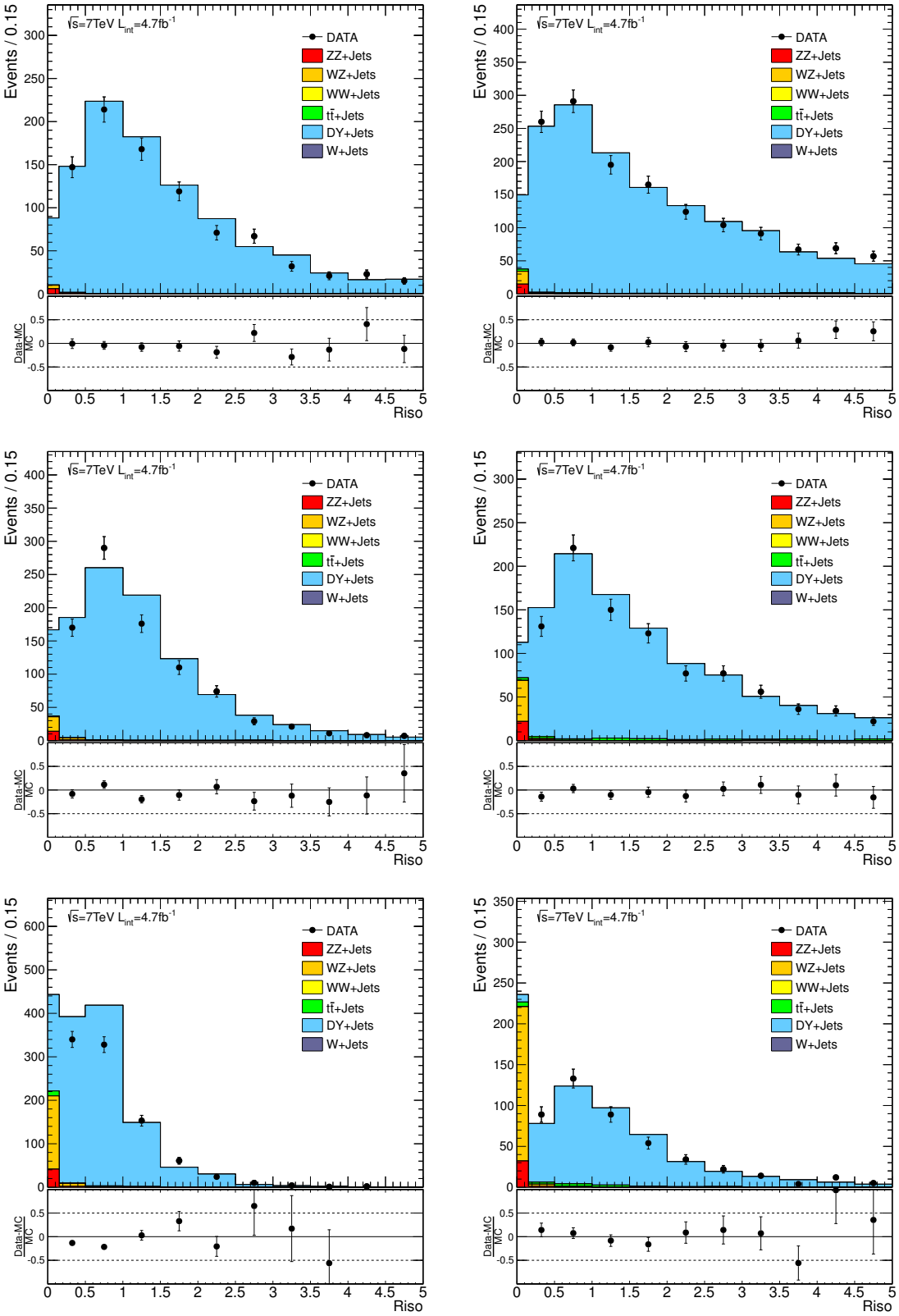

Figure 8.3: Relative isolation Riso distribution of the third loose lepton for e (left column) and μ (right column) split in various p_T bins ($p_T = [8, 12]$ GeV (top), $p_T = [12, 20]$ GeV (middle), $p_T = [20, \text{inf}]$ GeV (bottom)) in $Z \rightarrow l^+l^- +$ Jets events selected with $H_T < 200$ GeV, $E_T^{\text{miss}} < 200$ GeV and the invariant mass of the opposite sign same flavor lepton pair in the range $|m_{ll} - Z_{\text{mass}}| < 10$ GeV/c^2. An overall good description of the Riso distribution is observed. The measurement in the signal region (Riso) is excluded on purpose.

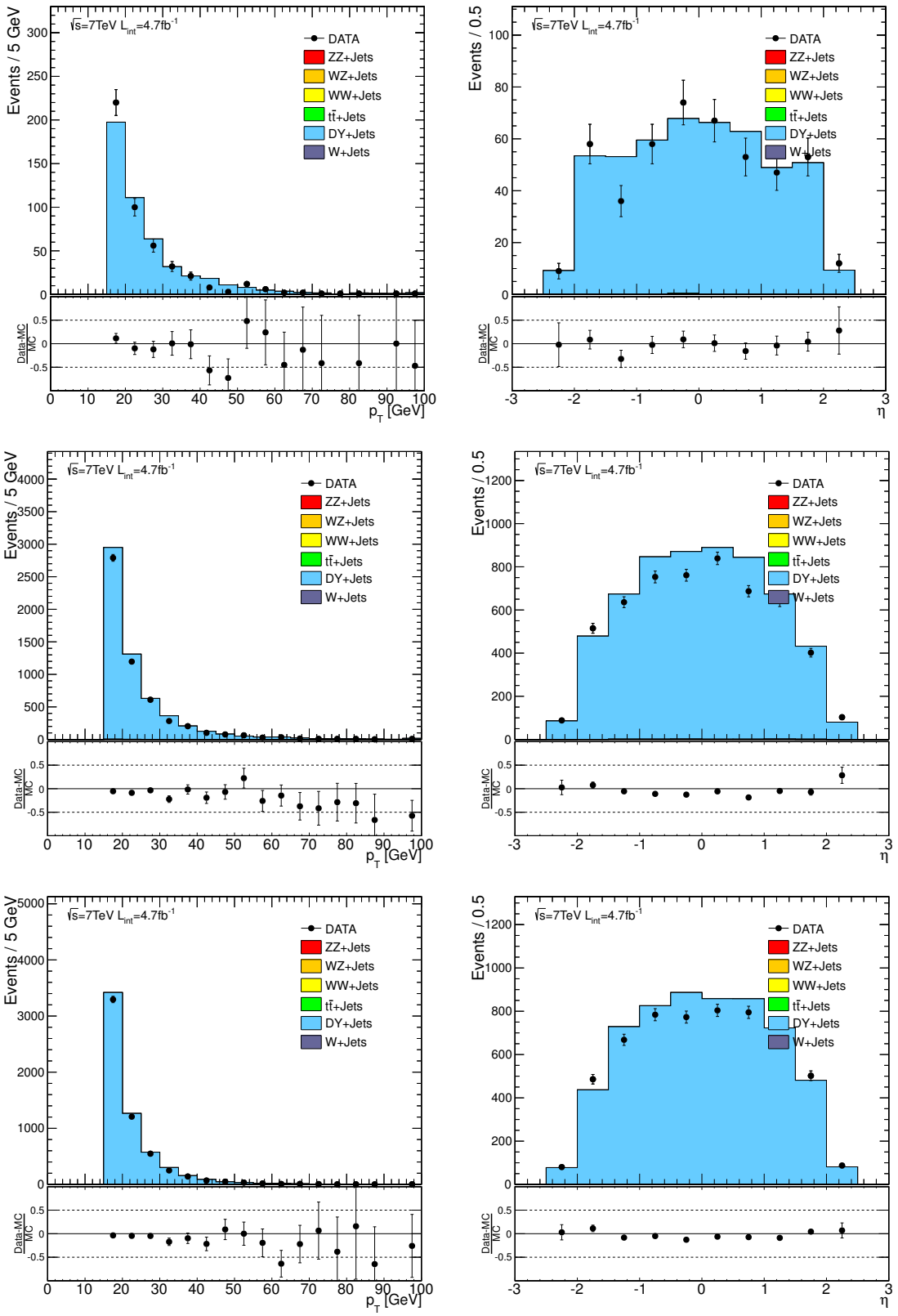

Figure 8.4: Transverse momentum p_T (left) and pseudo rapidity η (right) distribution of a third vloose HPS single prong (top), single prong $+\pi^0$ (middle) and three prong (bottom) HPS τ_h candidate in $Z \rightarrow l^+l^- +$ Jets events selected with $H_T < 200$ GeV, $E_T^{\text{miss}} < 200$ GeV and the invariant mass of the opposite sign same flavor lepton pair in the mass range $|m_{ll} - Z_{\text{mass}}| < 10\,\text{GeV/c}^2$. An overall good agreement is observed.

since both can be effected by a systematic error in opposite directions resulting in a cancellation.
Nevertheless, if one takes the isolation side-bands in both fake lepton flavor Riso distributions with an overall good description of the shape into account, a similar conclusion like in the previous measurement can be stated, i.e. the fake lepton description determined in the isolation side-band, can be used for the extrapolation to the signal region.
τ_h candidates are not cross checked here, because of the absence of a transverse impact parameter requirement within the selection. In case of $t\bar{t}$ events with two prompt leptons discussed in the next sections an additional closure test including cross checks for fake τ_h candidates is performed. The impact on Drell-Yan events is discussed later in Section 8.1.4.

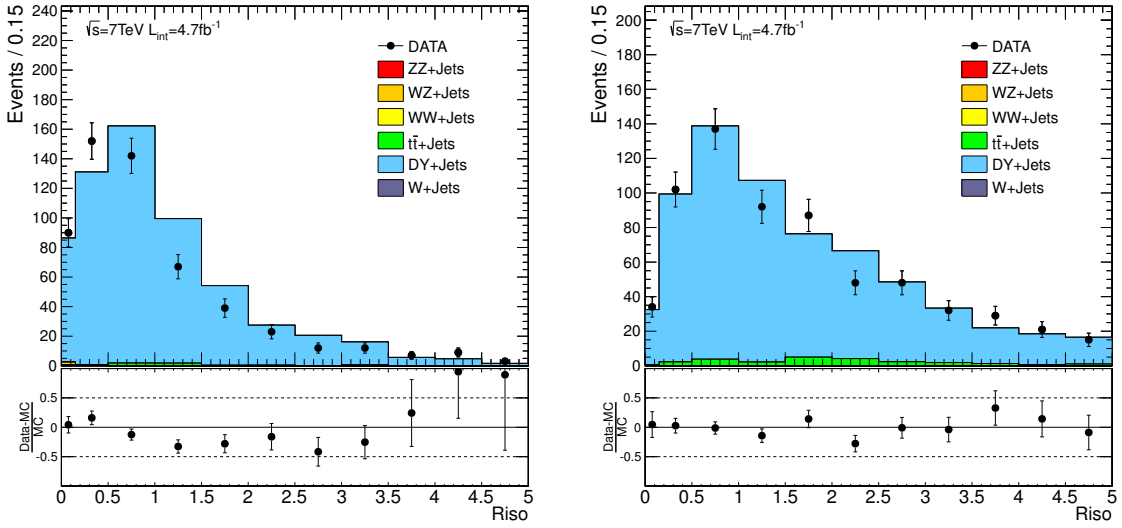

Figure 8.5: Relative isolation Riso distribution for loose leptons for e (left) and μ (right) in Z events, where also the transverse impact parameter is inverted $|dxy| > 0.02$. The underlying event selection is an opposite sign same flavor tight lepton pair with an invariant mass consistent with the Z mass and a third loose lepton in events with $H_T < 200$ GeV and $E_T^{\text{miss}} < 50$ GeV. A similar good agreement is measured for fake leptons in the transverse impact parameter side-band, despite a contamination of fake electron from initial/final state radiated photons in the isolation signal region, included in the Drell-Yan sample (DY).

8.1.2 $t\bar{t}$

In this section the background from $t\bar{t}$ events with two prompt leptons and an additional fake lepton from jets will be discussed. A similar procedure to $Z/\gamma*$+Jets will be followed.
$t\bar{t}$ processes are the next important dilepton process, which can contribute to the signal region with an additional fake lepton. Top quarks decay instantaneously into a b-quark and a W boson with a branching ratio of $BR(t \to bW) \sim 100\%$. Other top decays are suppressed by their corresponding CKM matrix elements. The subsequent decays of the W bosons to leptons and neutrinos ($BR(W \to l\nu) \sim 33\%$) lead to a dilepton signature.

$$t\bar{t} \rightarrow bW^+\bar{b}W^- \rightarrow bl^+\nu\bar{b}l^-\bar{\nu}$$

In contrast to $Z/\gamma*$+Jets processes $t\bar{t}$ events with two prompt leptons contain two associated neutrinos in the final state leading to intrinsic missing transverse energy and two b-jets. This interplay of intrinsic missing transverse energy and heavy flavor jets in each leptonic $t\bar{t}$ event raises the importance of this background in prospect of SUSY signals, which are expected to have comparable properties.
The contribution to the trilepton signatures requires an additional fake lepton in the event. In principal the production mechanism for fake leptons in $t\bar{t}$ is similar to $Z/\gamma*$+Jets , but the jet composition can be different, due to fact, that the b-jet density varies in both processes. In that sense the background determination performed for $Z/\gamma*$+Jets events can not be consulted for $t\bar{t}$ and have to be done separately.

Control Region

The fake lepton data driven background determination requires a pure seed, populated mainly with the processes which should be tested. $t\bar{t}$ events with two prompt leptons can be split according to same flavor (SF) or opposite flavor (OF) leptons pairs in the event :

$$(1)\ t\bar{t} \rightarrow b\bar{b}\nu\bar{\nu}l^+l^- \qquad (2)\ t\bar{t} \rightarrow b\bar{b}\nu\bar{\nu}l^+l'^-$$

with $l = e, \mu$ and ll' indicates OF leptons. W decays to τ's are not taken into account here for simplicity. Since the lepton flavors in both W decays are uncorrelated the rate of OF and SF leptons pairs in $t\bar{t}$ processes are similar, except small correction due to different reconstruction and selection efficiency for electrons and muons.
The dominant process, which has to be suppressed in order to select a relative pure $t\bar{t}$ sample using same flavor lepton signatures is $Z/\gamma*$+Jets with the subsequent decay into a SF-lepton pair, which can be suppressed to an acceptable level by requirements on E_T^{miss} , H_T , number of b-jets and the invariant mass of the lepton pair.
On the other hand the advantage of OF signatures is the lack of crucial SM backgrounds contributing and so additional requirements can be soften. Selecting $t\bar{t}$ sample with OF leptons, one has to suppress the dominant process $Z/\gamma* \rightarrow \tau\tau$, where each tau decays leptonically $\tau \rightarrow l\nu_l\nu_\tau$. The E_T^{miss} and H_T distribution in events selected with two tight leptons OF and opposite sign on top standard good event and trigger requirements (see Section 7.5) are shown in Fig. 8.6 with $H_T > 150\,\text{GeV}$ applied for the E_T^{miss} distribution suppressing $Z/\gamma* \rightarrow \tau\tau$ processes. Additional backgrounds with smaller contributions like W+Jets, WW and WZ are shown as well. Requiring additionally $H_T > 150\,\text{GeV}$ selects a $t\bar{t}$ dominated sample with a purity of $> 90\%$.
The number of $t\bar{t}$ events with two prompt leptons in such a selected data sample can be further increased by combining OF and SF lepton signatures. The increase in $t\bar{t}$ events is roughly a factor two, but as discussed before additional requirements to suppress $Z/\gamma* \rightarrow l^+l^-$ ($l = e, \mu$) have to be applied. As it can be seen in the next section, where fake leptons in $t\bar{t}$ will be discussed, the final increase in statistical accuracy of the background determination by combining both signatures, is expected to be low and is disregarded for now.

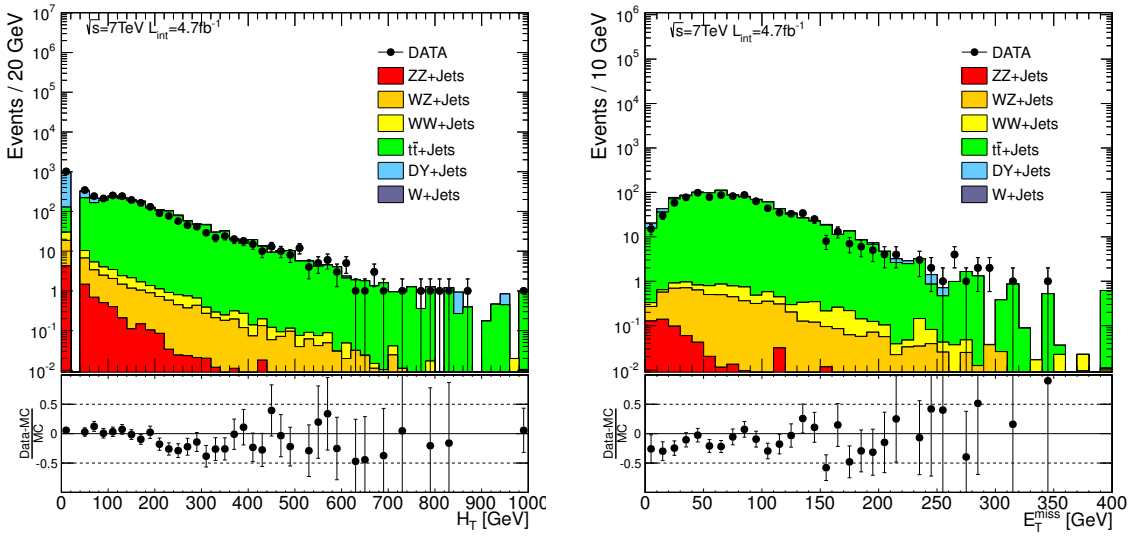

Figure 8.6: H_T (left) and E_T^{miss} (right) distribution for two tight leptons opposite sign opposite flavor ($e^{\pm}, \mu^{\mp}$). In case of the E_T^{miss} distribution an additional requirement on $H_T > 150\,\text{GeV}$ was applied to suppress $Z/\gamma* \rightarrow \tau\tau$ and thus selecting a pure $t\bar{t}$ events with two prompt leptons sample. The H_T and E_T^{miss} distributions are well described by the MC simulations. The peak at $E_T^{\text{miss}} \approx 400\,\text{GeV}$ and $H_T \approx 1000\,\text{GeV}$ originates from the fact, that all entries above 400 (1000) are added to this "overflow bin".

Data Driven Fake Background Determinaton

The data driven determination of fake leptons was discussed before extensively in case of Drell-Yan processes and will be applied also to $t\bar{t}$ processes. As a seed a relative pure $t\bar{t}$ sample with two prompt leptons and an additional fake lepton sample can be selected by the following requirements:

- two tight lepton OS-OF ($l = e, \mu$),
- $H_T > 150\,\text{GeV}$,
- third loose lepton ($l = e, \mu, \tau$),

where the loose leptons have again the same selection criteria compared to the tight lepton selection, but inverted isolation. The definitions of the relative isolation side-bands are similar as discussed already in Section 8.1.1 for $Z/\gamma*$+Jets . The transverse momentum p_T and pseudo rapidity η distribution of the third loose lepton are presented in Fig. 8.7 for fake electrons/muons and in Fig. 8.8 for vloose HPS τ_h candidates, respectively. The τ_h candidates are not split into the different reconstructed decay modes due to lack of required number of events.
The data driven fake background determination is again performed in the relative isolation side-bands ($Riso = [0.15, 5]$) of electrons and muons or simply in the isolation side-band (ID=vloose) for fake τ_h candidates. Despite the fact that the isolation side-band is dominated by soft leptons, no p_T binning is applied because the number of events is too low to have a reasonable binning. The relative isolation distributions for loose electrons and muons are presented in Fig. 8.9.

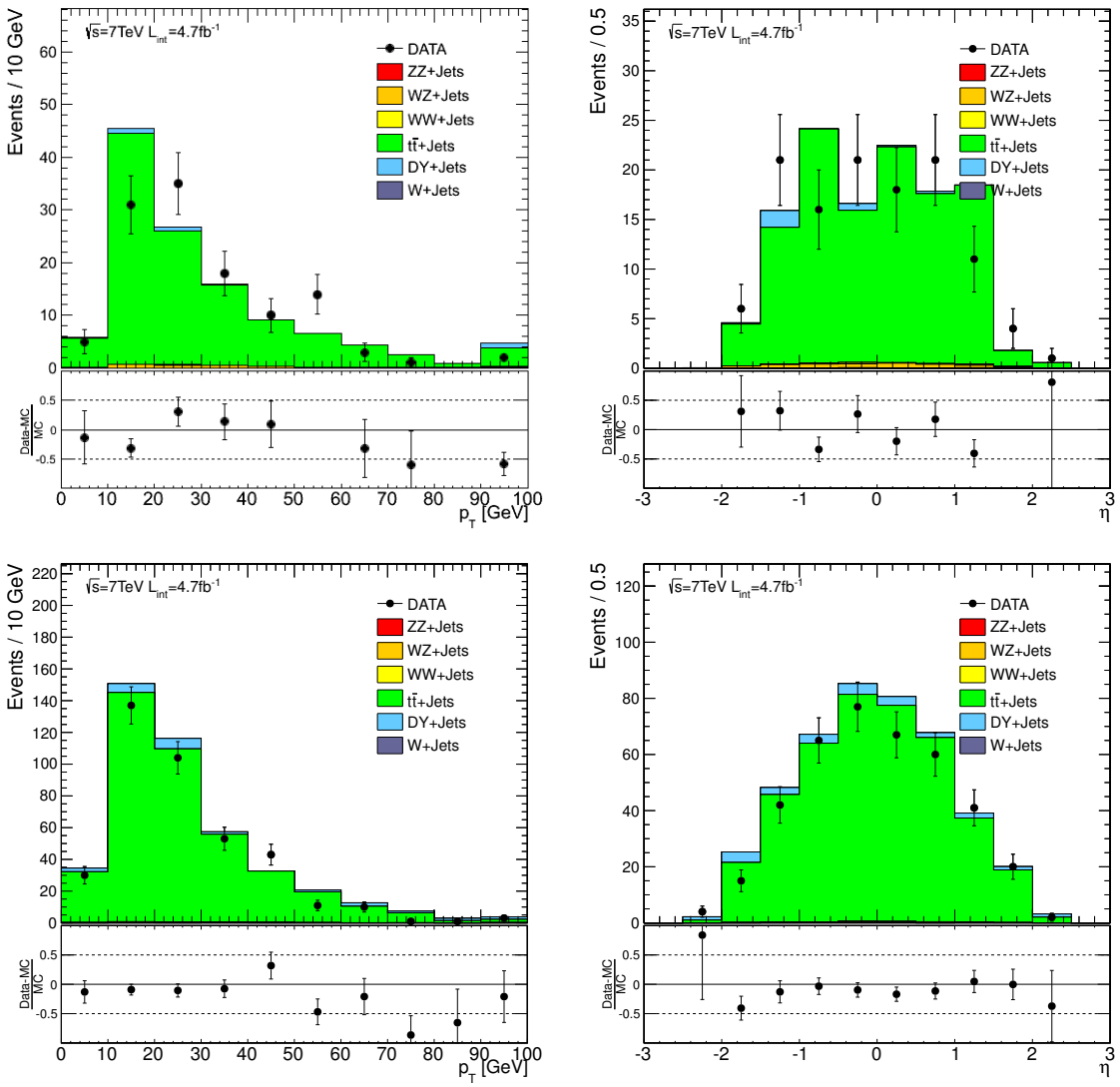

Figure 8.7: Transverse momentum p_T (left) and pseudo rapidity η (right) distributions of fake leptons for e (top) and μ (bottom) in the $t\bar{t}$ fake enriched data sample selected with two tight opposite sign opposite flavor leptons (e, μ) and $H_T > 150\,\text{GeV}$.

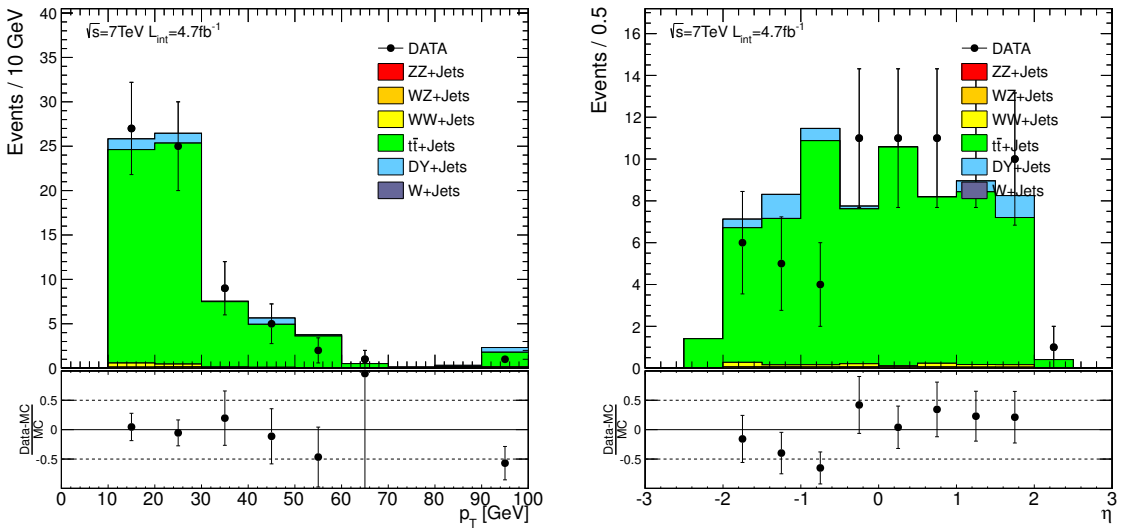

Figure 8.8: Transverse momentum p_T (left) and pseudo rapidity η (right) distributions for fake τ_h candidates (single prong, single prong + π^0 and three prong combined) with vloose ID in the $t\bar{t}$ fake enriched data sample selected with two tight opposite sign opposite flavor leptons (e, μ) and $H_T > 150$ GeV.

Similar reasons as discussed before in case of the fake background predictions for Drell-Yan processes demands to exclude the observation in the isolation signal region (Riso < 0.15), where only the MC prediction is shown. Again an overall good description of the isolation side-bands is observed. The discussion of the uncertainties is postponed to Section 8.1.4.

Closure Test

Following the same procedure as in case of Drell-Yan events the side-band technique for fake electrons and muons the selected $t\bar{t}$ fake enriched sample with two prompt leptons can be cross checked in a complementary data set selected in the fake lepton transverse impact parameter side-band $|dxy| > 0.02$ cm. With this side-band the same fake background determination can be performed. The results are presented in Fig. 8.10, where the relative isolation side-bands for the fake electrons and muons with inverted $|d_{xy}| > 0.02$ cm requirement are shown. This procedure with an inverted d_{xy} requierement allows for a direct comparison of the side-band determination in the isolation signal region.
In case of loose muons the observations are in good agreement with the predictions in the side-band and the signal region as well. For electrons a deviation for low relative isolation values is measured within Riso$= [0.15, 1.5]$ to be $\approx 50\%$. Despite this deviation at the lower border of the isolation side-band, the signal region (Riso < 0.15) prediction and observation are consistent within errors.

Additional Closure Test

The data driven background determination shows consistent results, which implies that the description of the fake lepton production is well modeled in MC simulations. In principle the scaling factors are equal to one as has been cross checked in a closure test repeating the side-band technique with the

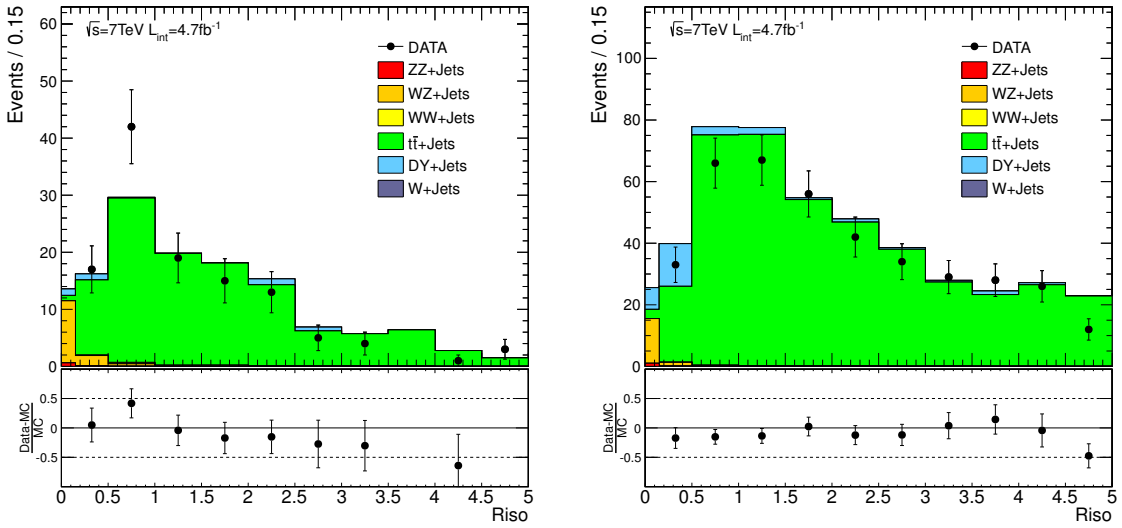

Figure 8.9: Relative isolation Riso distribution for fake leptons (e (left), μ (right)) in the leptonic $t\bar{t}$ fake enriched data sample selected with two tight opposite sign opposite flavor leptons(e, μ) and $H_T > 150\,\text{GeV}$.

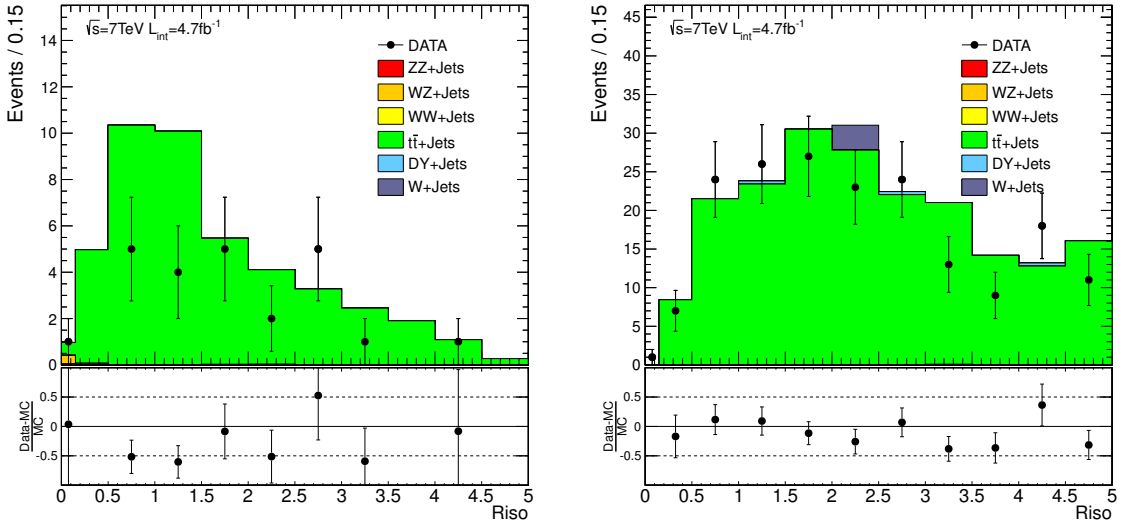

Figure 8.10: Relative isolation Riso distribution for fake leptons (e (left), μ (right)) with the inverted transverse impact parameter requirement $|d_{xy}| > 0.02\,\text{cm}$ in the leptonic $t\bar{t}$ fake enriched data sample selected with two tight opposite sign opposite flavor (OS-OF) leptons(e, μ) and $H_T > 150\,\text{GeV}$.

orthogonal observable d_{xy}.
Nevertheless $t\bar{t}$ events with its various decay branchings allows to define several control regions, where complementary side-band measurements can be performed and the predictions can be verified once more. An option is to use $t\bar{t}$ events with no or one prompt lepton, i.e. one semileptonic and one hadronic or both hadronic top decay. Those branchings allows for an independent cross check of the fake lepton prediction. $t\bar{t}$ events with no or one prompt lepton have the following signatures:

$$t\bar{t} \rightarrow bW^+\bar{b}W^- \rightarrow b\bar{b}q\bar{q}l^{\pm}\nu$$
$$t\bar{t} \rightarrow bW^+\bar{b}W^- \rightarrow b\bar{b}q\bar{q}q\bar{q}\,.$$

The dominant background of the hadronic $t\bar{t}$ production are QCD multijet events [160]. QCD events are hard to control and to suppress. The detailed study of a hadronic $t\bar{t}$ enriched data sample as a closure test for the actual measurement of dilepton $t\bar{t}$ is not worth the effort, because $t\bar{t}$ events with one prompt lepton are more easily to use as a closure test. The dominant backgrounds are leptonically decaying W+Jets and Z+Jets processes [161]. The starting point is one tight lepton in the event. Here only tight muons are considered, because the trigger threshold for the single electron trigger is $p_T > 85\,\text{GeV}$ in the last runs recorded, which is a far too strong requirement. In principle cross triggers with electron and jets can be used instead, but also not used for simplicity. W/Z+Jets processes can be suppressed by requiring high jet activity with at least one b-tagged jet. As a b-tagger the so called TrackCountingHighPurity [162] tagger at the working point TCHPT> 3.41 is used.
The *Track Counting* (TC) algorithm relies on tracks with large impact parameter (IP). All tracks get ranked by decreasing the three dimensional impact parameter significance $S_{IP} = IP/\sigma_{IP}$ and the discriminator is the S_{IP} value of the Nth track, where the *High Purity* (HP) discriminator is based on three associated tracks. For several working points (*loose, medium, tight*) the efficiency for light jets (udsg) to be tagged are determined on a simulated QCD sample to be $\sim 10\%$ (*loose*), $\sim 1\%$ (*medium*) and $\sim 0.1\%$ (*tight*). The miss tag rate for light jets measured in data for jets with a transverse momentum $p_T = [50, 80]\,\text{GeV}$ for the *Track Counting High Purity Tight* (TCHPT) algorithm is $0.0017 \pm 0.0001 \pm 0.0004$ with an b-tag efficiency for b-jets with similar p_T of 0.37 ± 0.01 [163].
The H_T and E_T^{miss} distribution for events selected with a tight muon ($p_T > 45\,\text{GeV}$, $|\eta| < 2.1$), more than two jets ($p_T > 40$ GeV, $|\eta| < 2.5$) with at least one b-tagged jet (TCHPT:$S_{IP} > 3.41$) on top of the common event selection criteria are shown in Fig. 8.11, where one can observe a good agreement between data and MC prediction.
With requirements of $E_T^{\text{miss}} > 35\,\text{GeV}$ and $H_T > 150\,\text{GeV}$ a pure $t\bar{t}$ sample with one prompt lepton can be selected. A second loose lepton ($l = e, \mu, \tau$) allows to cross check the findings derived for leptonic $t\bar{t}$ events with additional fake leptons from jets. The Riso distributions of the second loose lepton (e, μ) are presented in Fig. 8.12, where in a similar fashion the relative isolation requirement is loosened to $Riso < 5.0$. Two things to note here: (1) the tails of the Riso distribution are dominated by $t\bar{t}$ events with one prompt lepton and an additional fake lepton, whereas in the signal region $Riso < 0.15$ di-prompt lepton $t\bar{t}$ processes dominate, (2) the overall description of the fake lepton relative isolation MC prediction are consitent with the observation within erros. Since the contribution of dilepton $t\bar{t}$ events is by far the dominant contribution and the uncertainty on the probability of leptons failing the tight selection criteria is unknown, i.e. it is taken from MC simulation, no direct conclusion on the fake background in the Riso signal region can be stated. To suppress the di-prompt lepton

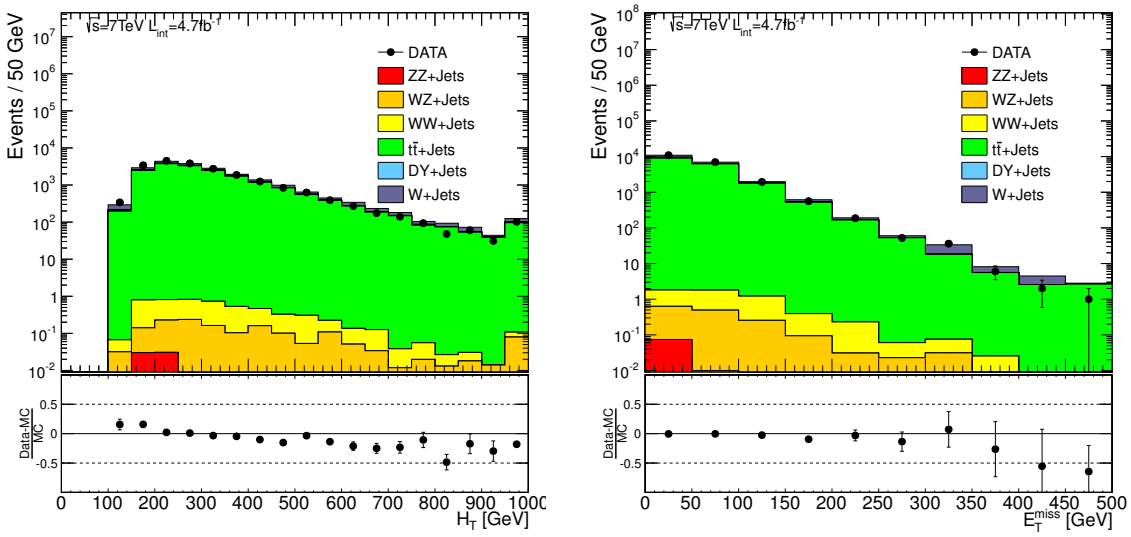

Figure 8.11: H_T (left)and E_T^{miss} (right) distribution in $t\bar{t}$ events with one prompt lepton selected with a tight muon ($p_T > 45\,\text{GeV}$, $|\eta| < 2.1$) and more than two jets ($p_T > 40\,\text{GeV}$, $|\eta| < 2.5$) with at least one b-tagged jet. The H_T and E_T^{miss} distribution are in good agreement. The peak at $E_T^{\text{miss}} \approx 500\,\text{GeV}$ and $H_T \approx 1000\,\text{GeV}$ originates from the fact, that all entries above 500 (1000) GeV are added to this overflow bin.

$t\bar{t}$ background the impact parameter requirement on the second loose lepton can be inverted. The corresponding relative isolation Riso distributions are presented in Fig. 8.13, where the $t\bar{t}$ events with one prompt lepton and an additional fake lepton dominate in the side-band region and an overall good agreement can be observed again, especially in the Riso signal region the MC prediction is consistent with the measurement.
The $t\bar{t}$ fake enriched data sample with one prompt lepton can be utilized to perform the fake τ_h background determination in the isolation side-band and to cross check the findings in the dedicated signal region. The result of both measurements are presented in Fig. 8.14.

8.1.3 $WW \to l\nu l\nu$

Finally, the last prompt dilepton SM process which can contribute to multileptonic signatures via an additional fake lepton is $WW \to l\nu l\nu$. The dilepton WW cross section is measured by the CMS collaboration to be $\sigma_{WW} = 55.5 \pm 3.3(\text{stats.}) \pm 6.9(\text{syst.}) \pm 3.3(\text{lumi.})$ [155], which is in good agreement with the SM NLO calculations $\sigma_{WW} = 43.0 \pm 2.0pb$ [153]. This cross section measurement can be used as a cross check of $WW \to l\nu l\nu$, but since an additional fake lepton is required to contribute, the interesting processes are WW+Jets processes, which are not directly covered by the cross section measurement listed above [155].
Partonic processes involved in $pp \to WW + 1$ jet are

$$(1)\ q\bar{q} \to W^+W^-g \qquad (2)\ qg \to W^+W^-q \qquad (3)\ \bar{q}g \to W^+W^-\bar{q}.$$

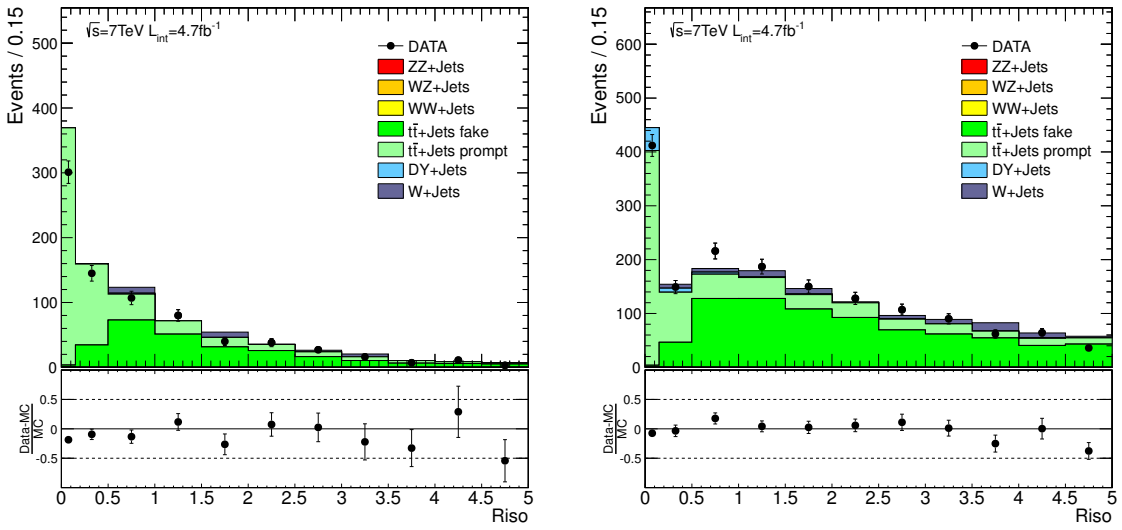

Figure 8.12: Relative isolation distribution of loose electrons (left) and muons (right)) in $t\bar{t}$ events with one prompt lepton selected with a tight muon ($p_T > 45\,\text{GeV}$, $|\eta| < 2.1$) and more than two jets ($p_T > 40$ GeV, $|\eta| < 2.5$) with at least one b-tagged jet. The isolation signal region is dominated by leptonic $t\bar{t}$ processes and only the tail of the Riso distribution is dominated by loose fake electrons/muons.

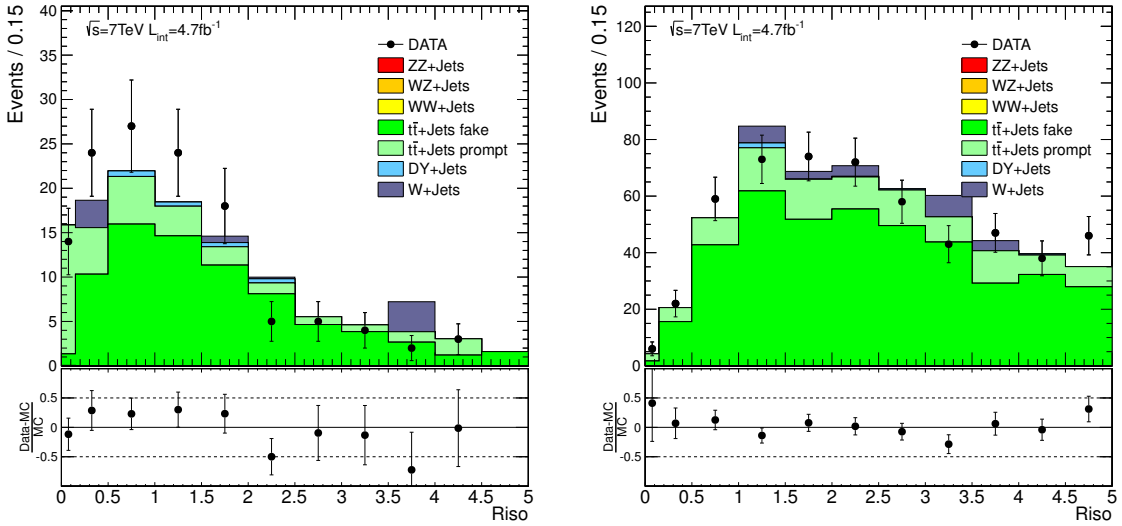

Figure 8.13: Relative isolation distribution of loose electron (left) and muons (right) with an inverted $|d_{xy}| > 0.02$ requirement in $t\bar{t}$ events with one prompt lepton selected with a tight muon ($p_T > 45\,\text{GeV}$, $|\eta| < 2.1$) and more than two jets ($p_T > 40$ GeV, $|\eta| < 2.5$) with at least one b-tagged jet. In contrast to the transverse impact parameter signal region $|d_{xy}| < 0.02$ the complementary data set is dominated by $t\bar{t}$ events with one prompt lepton and additional loose fake electrons/muons.

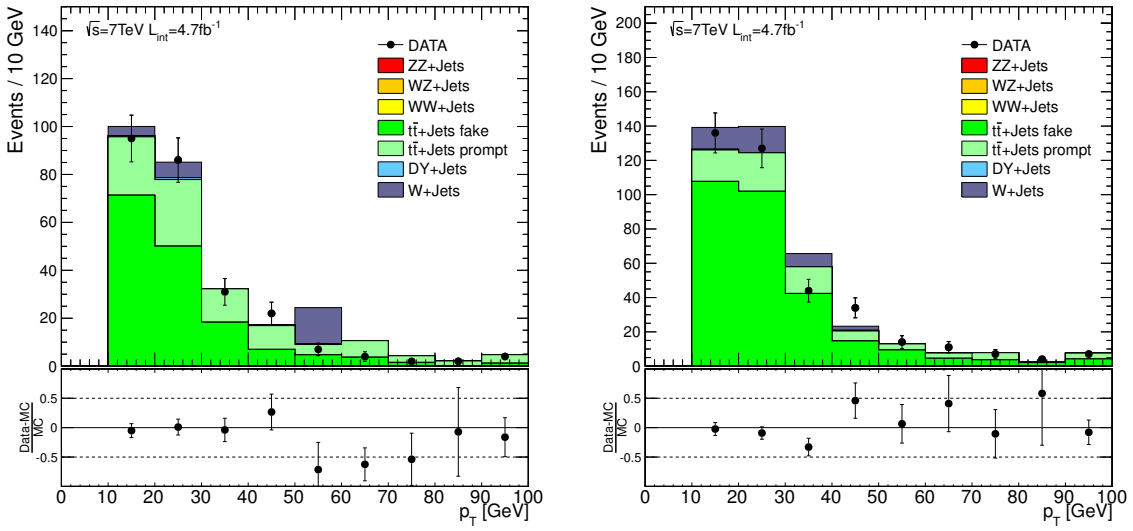

Figure 8.14: Transverse momentum p_T distributions for HPS τ_h decay mode candidates (single prong, single prong $+\pi^0$ and three prong combined) in the isolation side-band (left) and isolation signal region (right) in $t\bar{t}$ events with one prompt lepton selected with a tight muon ($p_T > 30\,\text{GeV}$, $|\eta| < 2.1$) and more than two jets ($p_T > 40$ GeV, $|\eta| < 2.5$) with at least one b-tagged jet. Note: the simulated number of event of the used W+Jets MC sample is not sufficient and has huge statistical uncertainties.

The WW cross section is a factor of ~ 4 smaller compared to the dilepton $t\bar{t}$ cross section and adding additional jets to the matrix element calculation reduces it further by a factor ~ 2, as estimated with Madgraph[1] [93]. Requiring in addition a fake lepton to be selected the contributions from WW+Jets are small and a data driven prediction cannot be performed with enough events so far. Hence MC simulations will be taken for the predictions of $W \to l\nu l\nu$ and an adequate uncertainty defined by the data driven fake background determinations done for Drell-Yan+Jets and $t\bar{t}$ processes will be added to the cross section uncertainties.

8.1.4 Systematic Uncertainties & Summary

In the last sections a set of data driven background determinations were performed in order to predict the fake lepton contributions in dilepton processes like Drell-Yan+Jets and $t\bar{t}$. The fake lepton contribution was measured in the isolation side-band and propagated to the signal region using shape informations from MC simulation. For fake electrons and muons closure tests using the transverse impact parameter side-band d_{xy} for validation were defined and consistent results were obtained. Additionally the $t\bar{t}$ events with one prompt lepton including additional fake leptons were utilized for further closure tests including a cross check for fake τ_h candidates.
An important issue not discussed up to now are the systematic uncertainties in the data driven background determination. Lets first discuss the fake electron and fake muon measurements in Drell-Yan

[1] Leading Order cross sections: $\sigma_{pp\to W^+W^-} = 29.51 \pm 0.09$ pb and $\sigma_{pp\to W^+W^-j} = 14.74 \pm 0.05$ pb calculated with Madgraph.

and $t\bar{t}$ processes simultaneously. The statistical uncertainty of the side-band measurements varies for Drell-Yan between 6% and 70% in the tails, where the most important are the Riso bins close to the signal region, where the uncertainty is determined to be $\approx 6-10\%$ for electrons and $\approx 6-11\%$ for muons. One has to note that the statistical uncertainties are rather arbitrary since the bin wise uncertainty depends on the actual bin sizes and only the total statistical uncertainty is fixed. Additionally the maximum deviation in all side-band measurements and closure tests are $\approx 20\%(20\%)$ for fake electron (muons). Similar considerations can be applied for $t\bar{t}$ processes which have higher statistical uncertainties $\approx 14(10)\%$ for electrons (muons) in the isolation region close to the signal region and a maximum deviation of $\approx 50(20)\%$. To be conservative in the uncertainty estimation the maximum of $50\%(20\%)$ is taken as systematic uncertainty for fake electrons (muons) in $t\bar{t}$, $20\%(20\%)$ for fake electrons (muons) in $Z/\gamma*+$Jets and as well WW, which is assumed to have a comparable performance.

An overall combined systematic uncertainty on the fake HPS τ_h candidates is determined by the side-band measurement with a statistical uncertainty of $\approx 6\%$ and a maximum deviation in the closure test in $t\bar{t}$ events with one prompt lepton of $\approx 50\%$. Again these systematic uncertainties are conservative and are applied on Drell-Yan, $t\bar{t}$ and WW predictions.

To summarize the findings derived for dilepton processes in well defined control regions the E_T^{miss} and H_T distribution in fake enriched events selected with two tight OS-SF leptons and one loose lepton ($Riso = [0.15, 5.0]$, $|d_{xy}| < 0.02\,\text{cm}$), where the lepton flavor of the two tight leptons are restricted to e and μ and the loose can be a τ_h candidate, are presented in Fig. 8.15. Those data samples are dominated by Drell-Yan+Jets and at higher H_T and/or E_T^{miss} values by $t\bar{t}$ events. The E_T^{miss} and H_T MC simulation are consistent with the observation.

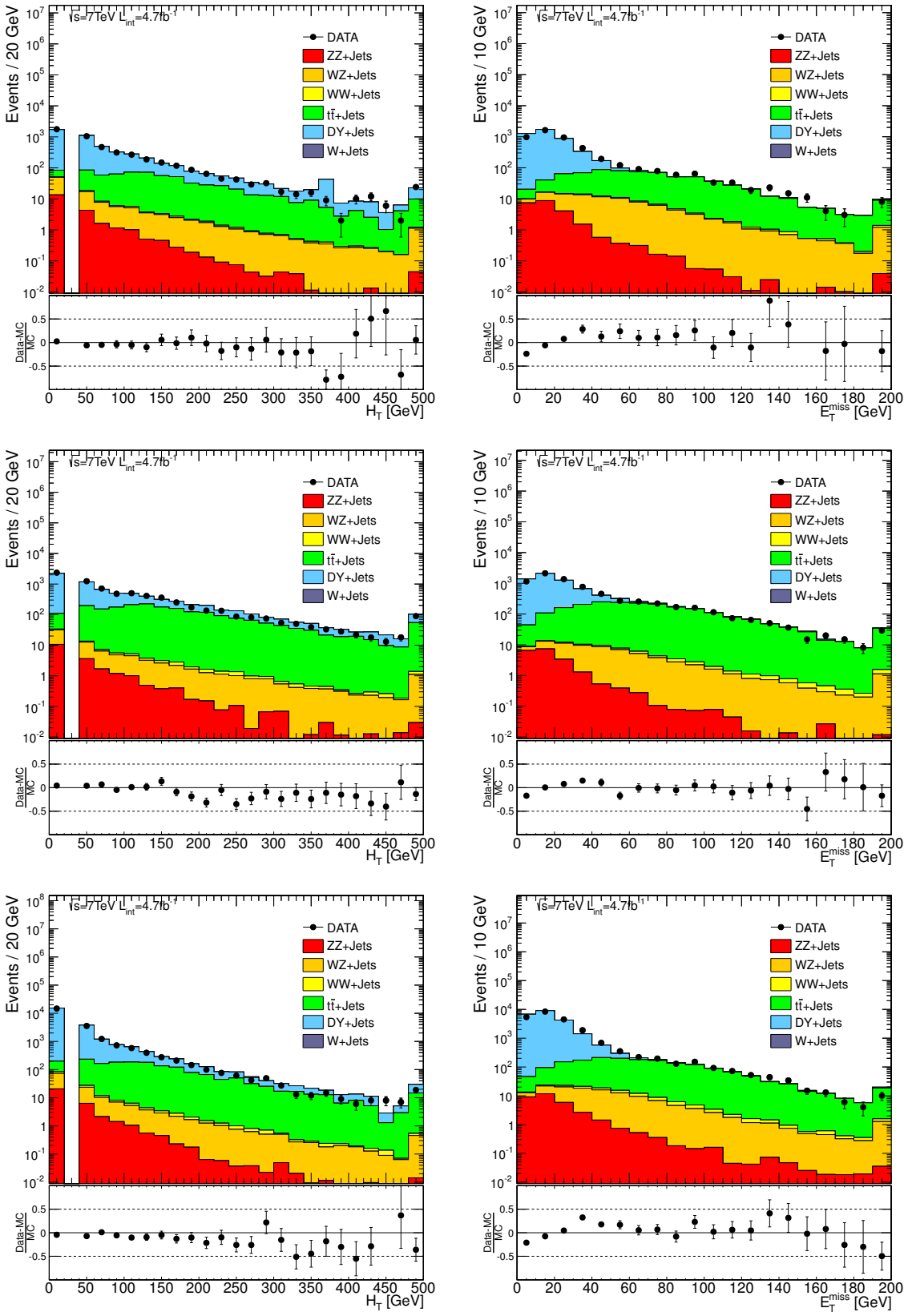

Figure 8.15: H_T (left) and E_T^{miss} (right) distribution for three lepton events including two tight (e, μ) and one loose lepton, where the loose lepton flavor is either an electron (top), a muon (middle) or a τ_h (bottom). The peaks at $E_T^{\text{miss}} \approx 200\,\text{GeV}$ and $H_T \approx 500\,\text{GeV}$ originate from the fact that all entries above 200 (500) GeV are added to this overflow bin.

8.2 Initial/Final State Radiation

Another background, which has to be discussed, is the so called *Initial/Final State Radiation* (I/FSR) background. Prompt dilepton processes with a radiated photon converting into an OS-SF lepton pair can mimic a multileptonic event. The requirement $m_{l^+l^-} > 12\,\text{GeV/c}^2$ on all OS-SF lepton pairs suppresses processes from Υ, J/Ψ and low mass Drell-Yan. Only asymmetric photon decay, where one lepton is soft and failing the selection criteria and the other takes most of the photon momentum, can contribute. The schematic mechanism of a $Z/\gamma*$ decaying into a OS-SF lepton pair, where one lepton radiates a photon, is shown in Fig. 8.16. The asymmetric decay of the radiated photon is indicated by the different length of the fermion lines.

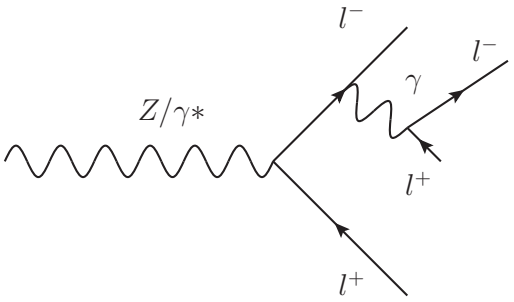

Figure 8.16: Asymmetric photon conversion in Drell-Yan events. The asymmetry of the photon decay is indicated by the length of the outgoing fermion lines, where most of the photon energy is taken by one lepton.

The tight photon selection efficiency can be checked in a control region presented in Fig. 8.17, where the three body mass $m_{ll\gamma}$ of $Z \to l^+l^- + \gamma$ events is shown.

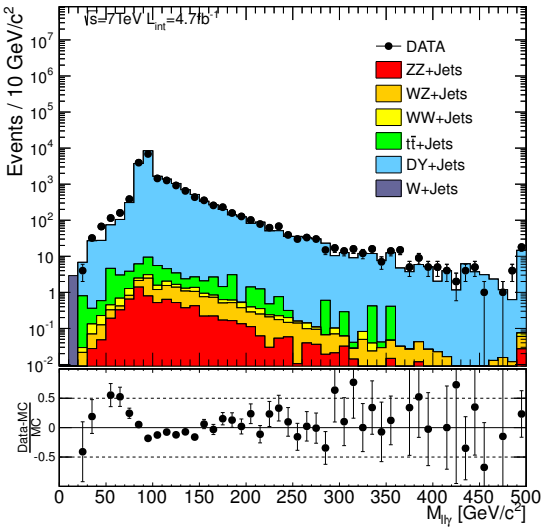

Figure 8.17: Three body mass $m_{ll\gamma}$ distribution of $Z \to l^+l^- + \gamma$ events. The peak at $m_{ll\gamma} \approx 500\,\text{GeV/c}^2$ originates from the fact that all entries above $500\,\text{GeV/c}^2$ are added to this overflow bin.

Two kinds of photon conversion are possible: (1) *external* and (2) *internal* photon conversion. External conversion are on-shell photons interacting with the detector material and converting into a lepton pair. In such processes the decay into two muons is suppressed by a factor $f \approx (m_e/m_\mu)^2 \approx 10^{-4} - 10^{-5}$ compared to the decay into two electrons. Hence no contributions of an additional muon produced via external conversion is expected. The picture changes for internal conversion, where a photon decays asymmetric into a lepton pair. Here the branching ratios are nearly $BR(e^+e^-)/BR(\mu^+\mu^-) \approx 1$.

The most important background for multileptonic searches including asymmetric photon conversion is $Z/\gamma*+$Jets due to the high prompt dilepton production cross section. A FSR photon causes the invariant mass of the opposite sign same flavor lepton pair of the Z decays to be shifted to lower values corresponding to the radiated photon momentum. This effect can be nicely seen in Fig. 8.18, where data events with two tight leptons with opposite sign and same flavor (e^+e^-, $\mu^+\mu^-$) with an associated tight photon are distributed in the invariant mass of the leptons $m_{l^+l^-}$ versus the three body mass of the leptons and the photon $m_{l^+l^-\gamma}$ plane is shown for low $H_T < 200\,\text{GeV}$ and low $E_T^{\text{miss}} < 50\,\text{GeV}$. FSR photon events are populating the band in three body mass $m_{l^+l^-\gamma}$ (y-axis) around the Z mass, whereas initial state radiated photons in Z events do not effect the two body mass of the lepton pair, but pushes the three body mass to higher values, which results in the band around the Z mass of the two body mass $m_{l^+l^-}$ (x-axis). Similar the three body mass of OS-SF lepton pair with an additional lepton ($l^+l^-e^\pm$ and $\mu^+\mu^-\mu^\pm$) for low H_T and low E_T^{miss} is presented in Fig. 8.19. The peak around $90\,\text{GeV}$ corresponds to Drell-Yan with internal asymmetric photon conversion and the other peak to double boson (WZ) production or Drell-Yan with an additional fake lepton from jets, which pushes the invariant mass to higher values. The gap between both peaks is a result of the transverse momentum thresholds $p_T > 8\,\text{GeV}$ of the third lepton, which is visible only for $\mu^+\mu^-\mu^\pm$. In Fig. 8.19 predictions from MC simulations are added for comparison. External conversion are already included in the corresponding MC simulation. Internal photon conversions are not included in the official Madgraph samples available, because of p_T thresholds on leptons at the matrix element level, which suppresses asymmetric photon conversion, if one lepton is soft. For this purpose a private MC sample is produced including those processes[2]. The private sample including internal photon conversion besides other double boson production with the subsequent decay to four leptons processes are labeled with *ZZ+Jets*.

Internal and external photon conversion can be suppressed by an invariant mass cut on the three body mass distribution of the selected tight leptons, where at least one OS-SF lepton pair should be present, but with an two-body mass inconsistent with the Z mass to account for the shift of the reconstructed like-Z mass. The underlying process of the dominant FSR contribution is the Drell-Yan production and the E_T^{miss} and H_T shape should not be affected by the FSR. These are presented in Fig. 8.20 for events including $l^+l^-e^\pm$ and $\mu^+\mu^-\mu^\pm$ with $m_{l^+l^-} \neq [75, 105]\,\text{GeV/c}^2$. Steeply falling distributions can be observed and expectations in the high-H_T or high-E_T^{miss} region are negligible. As already mentioned in Section 7.5 the three body invariant mass veto in three lepton channels with no opposite sign same flavor lepton pair forming an invariant mass consistent with the Z mass (off-Z), is only needed in the low-H_T and low-E_T^{miss} region.

In Fig. 8.19 the prediction for internal photon conversions are shown and corrected, because they

[2] Asymmetric photon Madgraph sample: detailed informations in Appendix B

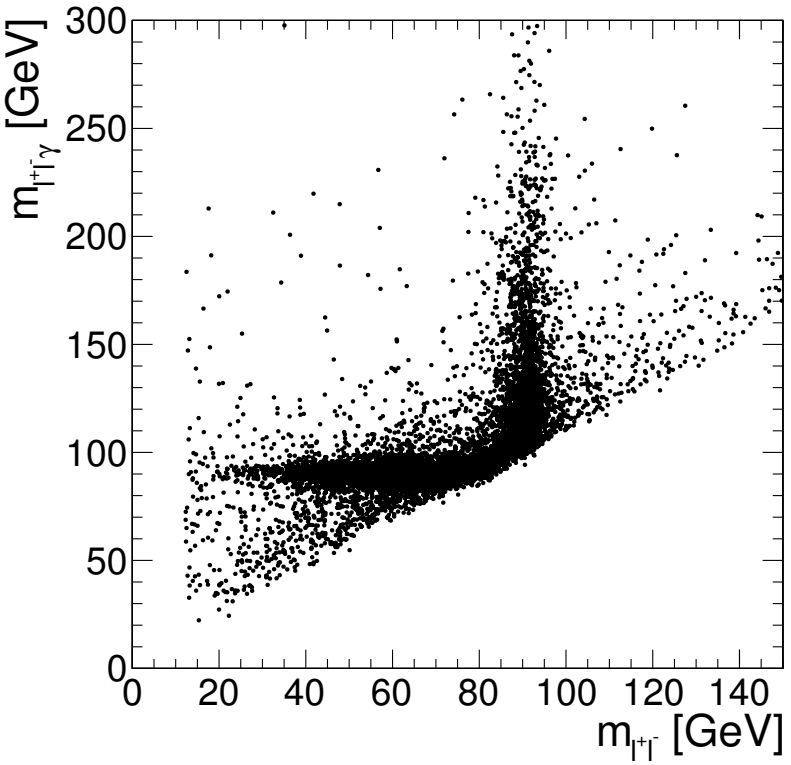

Figure 8.18: Events selected with two tight opposite sign same flavor (OF-SF) leptons and an additional tight photon distributed in the $m_{l^+l^-}$-$m_{l^+l^-\gamma}$ plane for low H_T and low E_T^{miss} , where on the y-axis the three body mass of the leptons and the photon and on the x-axis the two-body mass of the leptons is plotted . Leptonic Z decays, where one lepton radiated a photon are populating the band around the Z mass on the y-axis.

appear to be underestimated, especially in the case of $\mu^+\mu^-\mu^\pm$, where essentially no external conversions are contributing. The reason for this underestimation of the Z peak by a factor ~ 3 can have several sources: (1) next to leading cross section corrections can be important (Madgraph used LO calculation) and (2) the generator threshold on the invariant mass distribution for OS-SF lepton pairs in the final state is $m_{l^+l^-} > 5\,\text{GeV/c}^2$ shown in Fig. B.1 in Appendix B. The first effect is expected to be of the order of DY+Jets NLO corrections (k-factor ≈ 1.3), where the prediction are sensitive to the generator $m_{l^+l^-}$ cut and a correction factor is estimated from the invariant mass distribution of the two leptons produced in the internal photon conversion. This factor is already included in Fig. 8.19 for the predictions of the internal photon conversion included in the MC sample labeled with "ZZ+Jets".

In addition to asymmetric decays one expects internal photon conversion, where both lepton are selected and mimick four lepton processes. To cross check the internal conversion prediction of the privatly produced Madgraph sample a data sample selected with four leptons (e, μ) is selected. The transverse momentum of the leptons is reduced to $p_T > 3\,\text{GeV}$ to increase the numnber of selected events[3]. In Section 7.3.1 the lepton identification and isolation efficiency are measured and a signifi-

[3]Note: the trigger requirements with essential higher thresholds on two of the four lepton transverse momentum are still

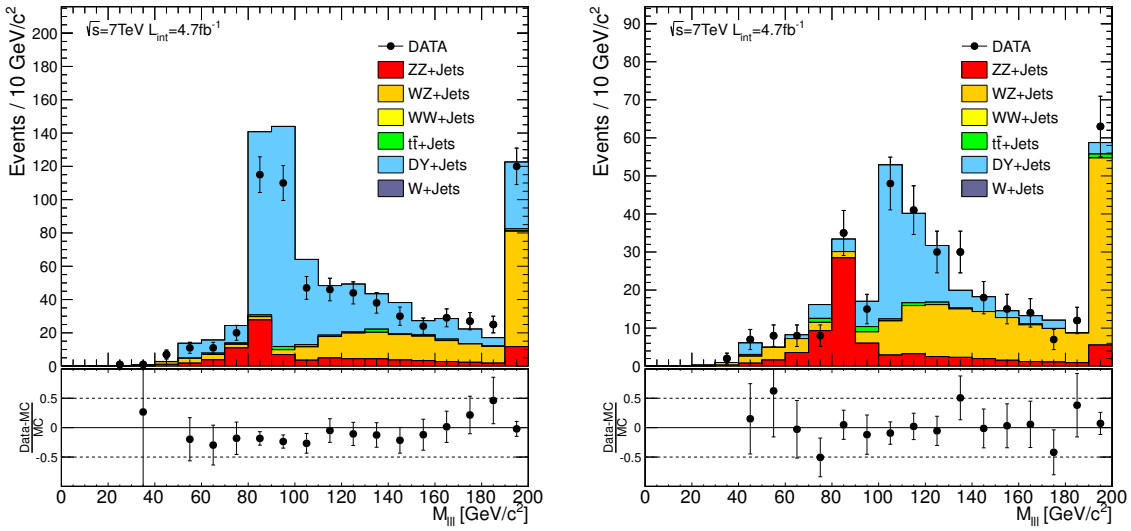

Figure 8.19: Three body mass distribution for $l^+l^-e^\pm$ (left) and $\mu^+\mu^-\mu^\pm$ (right) events with low H_T and low E_T^{miss} . The peak around 90 GeV/c^2 corresponds to Drell-Yan processes with final state radiated photons, which decayed asymmetrical. A third (fake) lepton from jets or W decay pushes the invariant mass distribution to higher values, which corresponds to the other peak around 100 GeV/c^2, which is visible only for $\mu^+\mu^-\mu^\pm$, due negligible contributions from external conversions. The peak at $m_{ll} \approx 200$ GeV/c^2 originates from the fact, that all entries above 200 GeV/c^2 are added to this overflow bin.

cant deviation between MC and data for low momentum leptons has been observed which is corrected for in this case. Additionally, the invariant mass of two opposite sign same flavor leptons is decreased to 0 GeV/c^2, since in four lepton events the contamination from low mass resonances is negligible. To account for the momentum shift of one lepton due to the radiated photon and a corresponding shift of the two body invariant mass to lower values, any OS-SF lepton pair is required to be out of the Z peak region. The signature of Drell-Yan+Jets with a FSR photon converting to two lepton is a four body mass consistent with the Z mass, which can be seen in Fig. 8.21, where a clean Z peak can be observed. The ratio of internal photon conversion to be asymmetric (failing selection criteria) with respect to symmetric appears to be $R(C_{ASY}/C_{SY}) \approx 7.0$. This large ratio is expected from the decay kinematics: one obtains the highest energy of one lepton if the decay is along the flight direction, but the other lepton decays in the direction opposite to the photon direction, so it will obtain the minimum energy and is prone to be lost. In order to estimate the contribution from internal photon conversion the invariant mass threshold on all OS-SF lepton pairs was successively increased. The result of this procedure is presented in Fig. 8.21 (R), where the integrated observation and MC prediction for events including four leptons with a four-body-mass consistent with the Z mass ($|m_{llll} - m_Z| < 15$ GeV/c^2) as a function of the two body invariant mass threshold is shown. An overall good agreement can be observed.

To summarize: an additional requirement on the three body mass $m_{l^+l^-l^\pm}$ in cases where no opposite sign same flavor dilepton pair with a mass comparable with the Z mass occurs in the event can suppress

required.

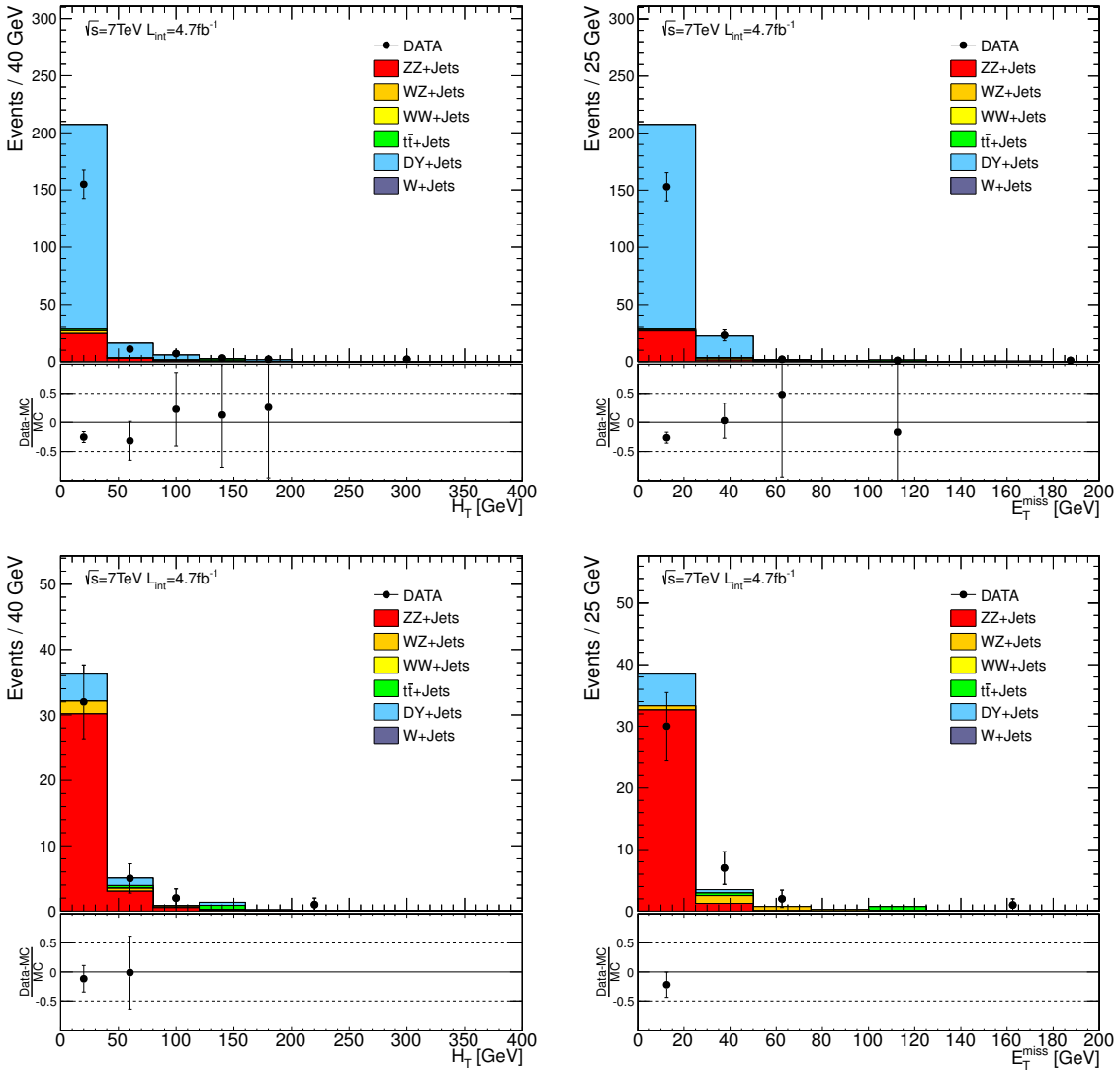

Figure 8.20: H_T (left) and E_T^{miss} (right) distribution for events including $l^+l^-e^\pm$ (top) and and $\mu^+\mu^-\mu^\pm$ (bottom), where the opposite sign same flavor (OS-SF) lepton pair should be off-Z. Internal conversion are corrected by a factor 3 to account for generator cuts. Prediction of FSR SM background in high-H_T or high-E_T^{miss} regions are negligible and the three body FSR-veto is applied only in low-H_T and low-E_T^{miss} search channels.

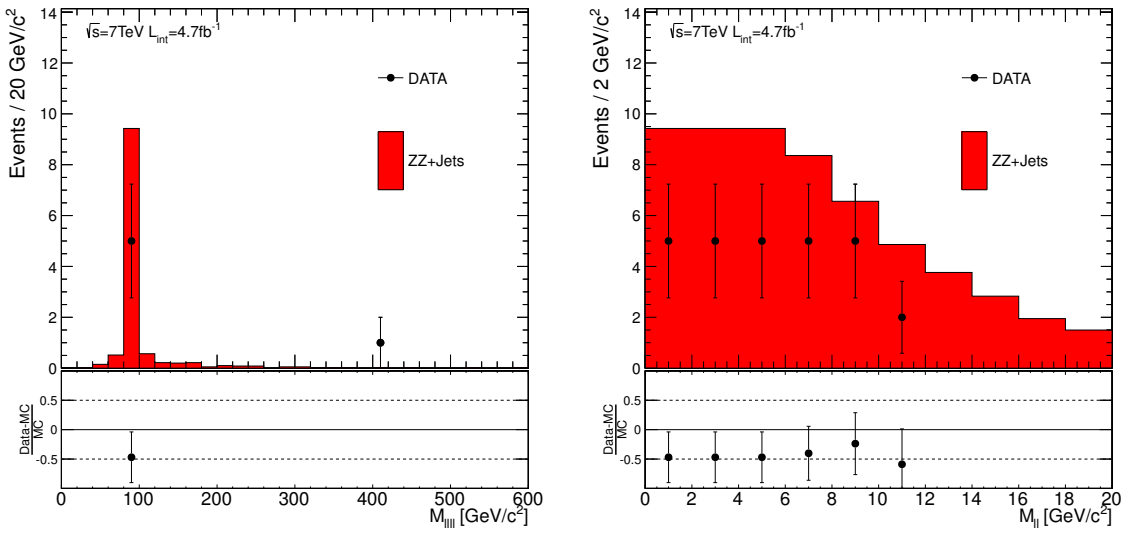

Figure 8.21: Four-body-mass of events with four leptons with decreased transverse momentum ($p_T > 3\,\text{GeV}$) and two body mass thresholds ($m_{l^+l^-} > 0\,\text{GeV/c}^2$) (left). In addition no opposite sign same flavor (OS-SF) lepton pair should form an invariant mass within the Z mass to account for the shift due to FSR photon. (Right) The integrated observation and MC prediction for event including four leptons with a four-body-mass consistent with the Z mass as a function of the two body invariant mass threshold.

the FSR background contributing to 3L channels sufficiently. The E_T^{miss} and H_T distribution are similar to the ones of the $Z/\gamma * +$Jets processes, where no intrinsic missing transverse energy is present except for a small contribution from the second missing soft lepton in the photon conversion. The contributions from FSR are negligible in the high H_T and/or high E_T^{miss} signal regions. Hence the additional three body mass cut is applied only in events wit low H_T , low E_T^{miss} and no OS-SF lepton pair building a Z boson. Due to lack the large correction (factor 3) for I/FSR asymmetric internal conversion background a conservative 100% uncertainty is applied on this and on the symmetric internal conversion background as well. The description of the external photon conversion is well modeled by MC simulations (left panel of Fig. 8.19). Since the major part of this background is vetoed the maximum deviation in the off-Z tight photon three body mass distribution shown in Fig. 8.17 of $\approx 50\%$ is taken as an uncertainty on the remaining external photon conversion background. This uncertainty is extrapolated to the high-E_T^{miss} and high-H_T by a linear fit of the uncertainties given in Fig. 8.20 (top panel) for low-E_T^{miss} (H_T) and are determined to be $\approx 100\%$ (H_T) and $\approx 50\%$ (E_T^{miss}).

This first measurement of internal photon conversions in collaboration with a group at Rutgers University[4] in the CMS collaboration has also implication to recent Higgs searches [164]. An additional background in case of for example $H \to WW$ [165,166] searches can arise from internal photon conversion in leptonic W+Jets processes. Also the symmetric conversion leading to four lepton processes can contribute to recent Higgs searches like $H \to ZZ$ [167].

[4]Richard C. Gray et.al.

8.3 Prompt Lepton Background

Up to now only SM backgrounds with additional non prompt leptons, i.e. leptons not coming from Z/W (including $t \to W$) decays, were discussed. The double boson production with the subsequent decays to leptons are an irreducible background. Fake leptons can be suppressed by requiring strong isolation and impact parameter boundaries, whereas the multiple prompt leptons in double boson processes have similar properties as prompt leptons in SUSY decays. Hence WZ and ZZ processes have to be controlled and will be discussed in the following. Both production cross sections were measured by the CMS Collaboration [155], which are in good agreement with NLO calculations.

8.3.1 WZ/γ^*

With higher luminosity the irreducible prompt SM background WZ/γ^* is getting one of the dominant backgrounds and the MC predictions are going to be statistical testable. In case of simultaneous leptonic branching of the Z/γ^* and W boson, three prompt leptons appear in the final state with an associated neutrino:

$$WZ/\gamma* \to l^{\pm}\nu l^{+}l^{-}.$$

Those events can be reconstructed by selecting three tight leptons (e, μ) including at least one opposite sign same flavor lepton pair with a mass consistent with the Z mass. The W decay can be selected by requiring a transverse missing energy of $E_T^{\text{miss}} > 20\,\text{GeV}$ from the undetected neutrino and the transverse mass $M_T(l_3, E_T^{\text{miss}}) > 15\,\text{GeV}$, where M_T is defined as:

$$M_T = \sqrt{(\Sigma E_T^i)^2 - (\Sigma p_T^i)^2}\,.$$

The invariant mass m_{ll} of all opposite sign same flavor lepton pairs in such a selected data sample is shown in Fig. 8.22. All combinations ($\mu^+\mu^-\mu^{\pm}$, $\mu^+\mu^-e^{\pm}$, $e^+e^-\mu^{\pm}$, $e^+e^-e^{\pm}$) are combined and in case of three leptons with the same flavors, i.e. $\mu\mu\mu$ and eee, the opposite sign same flavor lepton pair with a two body mass closest to the Z mass is taken and the remaining lepton is used to calculate the transverse mass M_T.

This control sample can be used to check processes with an on-shell Z produced. Processes including an off-shell Z or W can not be well modeled, especially in the context of higher order QCD. The available Madgraph sample is produced with up to 2 Jets at the matrix element. Fig. 8.23 shows example Feynman diagrams for $WZ + X$ Jets with $X = 0, 1, 2$ used within the Madgraph production. For WZ+1Jet a typical initial state radiation gluon is added to the diagram, whereas for WZ+2Jets also new diagrams with higher order QCD and off-shell W and/or Z have to be added to the calculations (see Fig. 8.23). Including WZ+2Jets to the production the LO cross section calculated with Madgraph is increased by $\sim 40\%$ compared to WZ+0,1 Jets, which is consistent with the NLO cross section within errors. The large amount (~ 2000) of additional diagrams including intermediate off-shell bosons changes the off-Z/on-Z ratio of those events by $\sim 30\%$, i.e. the ratio changed from $f(WZ + 0, 1Jets) = \frac{\text{off-Z}}{\text{on-Z}} \approx 14\%$ to $f(WZ + 0, 1, 2Jets) \approx 18\%$ [5].

[5] Comparison of Spring11 VV+Jets Madgraph (pp>llllj) and Summer11 WZ+Jets Madgraph sample (pp>llljj) performed in low-E_T^{miss} , low-H_T , off-Z/on-Z 3l channels.

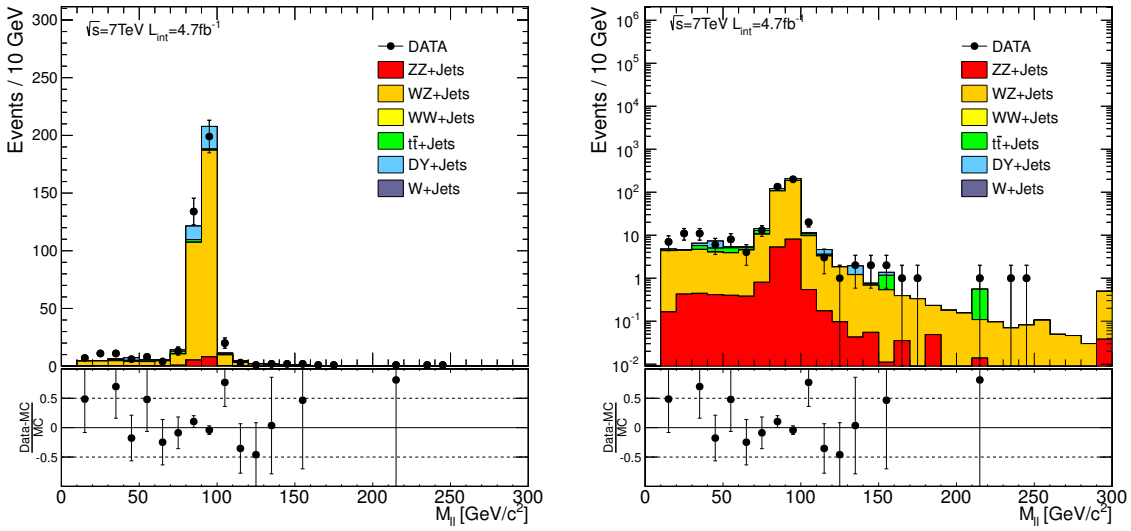

Figure 8.22: Invariant mass distribution m_{ll} of all opposite sign same flavor lepton pairs in the $WZ/\gamma*$ control sample with three tight leptons, at least one OS-SF pair with $m_{l^+l^-} = [80, 100]\,\text{GeV/c}^2$, $E_T^{\text{miss}} > 20\,\text{GeV}$ and $M_T(l_3, E_T^{\text{miss}}) > 15\,\text{GeV/c}^2$. The MC prediction of the invariant mass distribution of all OS-SF lepton pairs (left) and same but logarithmic (right) are in good agreement with measurement.

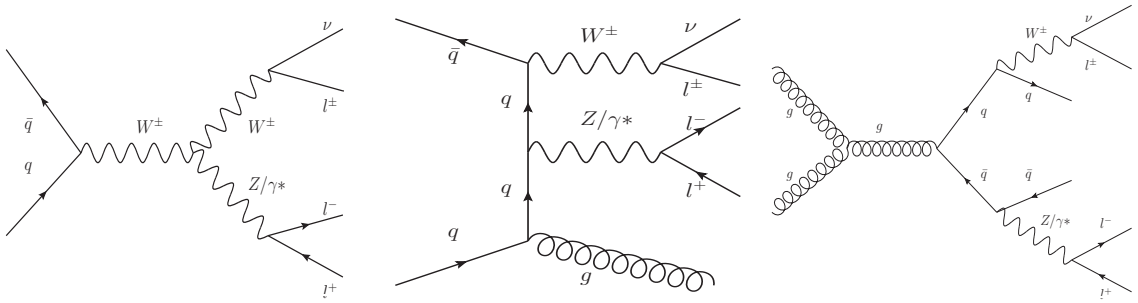

Figure 8.23: Example diagrams for WZ + 0 (left), 1 (middle) and 2 (right) Jets in the final state used within the Madgraph MC production. A new type of diagrams are included for higher order QCD processes, where intermediate off-shell bosons are playing a crucial role.

Since NLO calculations for WZ+0,1,2,X Jets in the corners of the phase space - off-shell and high-H_T , high-E_T^{miss} as well - are not available and control regions to cross check the predictions are not feasible, a reasonable and motivated uncertainty has to be assigned. To do so the control region selected above are binned in H_T ($\Delta H_T = 20\,\text{GeV}$) and E_T^{miss} ($\Delta E_T^{\text{miss}} = 10\,\text{GeV}$) and a k-like-factor value is determined in each bin assuming to be the source of possible differences between the measurement and MC prediction. The uncertainties on those factors are extrapolated to the different phase space by linear propagation. The resulting uncertainties in the k-like-factors are used as an estimate of the systematic uncertainty on the MC prediction, which reads as $\pm 50\%$ and $\pm 15\%$ for high-H_T and high-E_T^{miss}. For low-H_T and low-E_T^{miss} the uncertainty for on-Z WZ events is determined

by the statistical uncertainty in the control regions discussed above to be $\approx 6\%$. Since the ratio of off-Z/on-Z is sensitive and cannot be controlled in data a conservative 50% uncertainty is applied to the WZ prediction classified as off-Z.

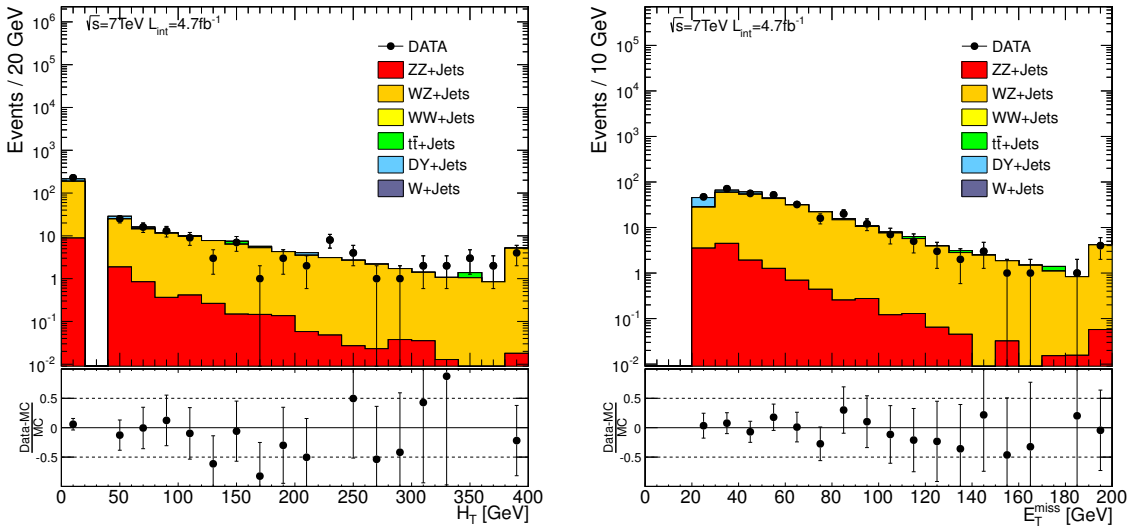

Figure 8.24: H_T and E_T^{miss} distribution of WZ events including three tight leptons (e, μ) with at least one opposite sign same flavor lepton pair forming an invariant mass consistent with the Z mass and the remaining lepton a transverse mass with E_T^{miss} to be above 20 GeV. Those distributions are used to estimate the systematic uncertainty on the MC predictions in the high-H_T and/or high-E_T^{miss} regions. The peak at $E_T^{\text{miss}} \approx 200$ GeV and $H_T \approx 400$ GeV originates from the fact, that all entries above 200 (400) GeV are added to this overflow bin.

8.3.2 ZZ, $Z\gamma*$, $\gamma*\gamma*$

The next prompt background is the ZZ, $Z\gamma^*$ and $\gamma^*\gamma^*$ background, where the leptonic decay modes lead to four leptons in the final state. A non-negligible probability that one lepton out of four is out of the acceptance and/or failing the selection requirements yields a contribution to the 3L channels. Their probability is taken from MC.

The ZZ production can be checked by selecting four tight leptons with at least two OS-SF pairs each building a Z candidate, again on top of the common event and trigger selections. In Fig. 8.25 the invariant mass of OS-SF lepton pairs are shown, where the combinatorial multiplicity due to four leptons can be high, so the tails are populated as well. A good agreement between observation and MC prediction is observed and the statistical error of the data sample is taken as an uncertainty on the ZZ (incl.$\gamma*$) MC predictions, i.e. an uncertainty on the k-factor of the production cross section, determined to be $\approx 21\%$.

The k-factor on the ZZ production is assumed to be flat over the full phase space, which is not necessarily true, following the discussion for WZ+Jets production, especially in cases with intermediate off-shell Z bosons. In order to estimate a reliable uncertainty on the prediction in the phase space regions $H_T > 200$ GeV and/or $E_T^{\text{miss}} > 50$ GeV the ZZ control sample is binned in various ΔH_T

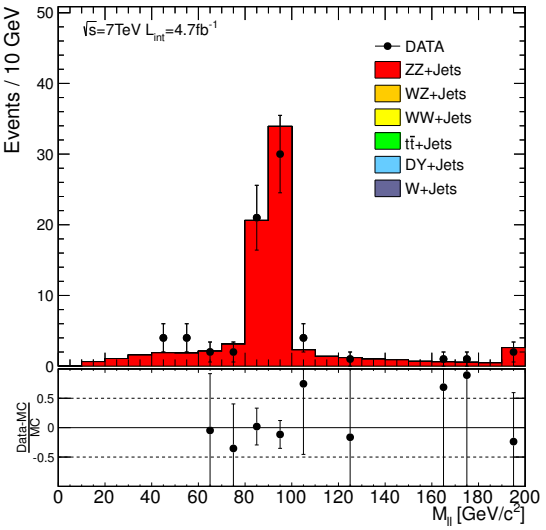

Figure 8.25: ZZ control sample with four tight leptons including two opposite sign same flavor lepton pairs with each forming an invariant mass consistent with the Z mass.

$= 100\,\text{GeV}/\ \Delta E_T^{\text{miss}} = 25\,\text{GeV}$ bins, as shown in Fig. 8.26. The uncertainty is estimated by defining in a similar fashion k-like-factors in the two bins below the channel thresholds and propagate the uncertainties to the signal region. Those k-like-factors lead to uncertainties in the high-H_T and high-E_T^{miss} region of $^{+140}_{-100}\%$ and $\pm 75\%$, respectively.

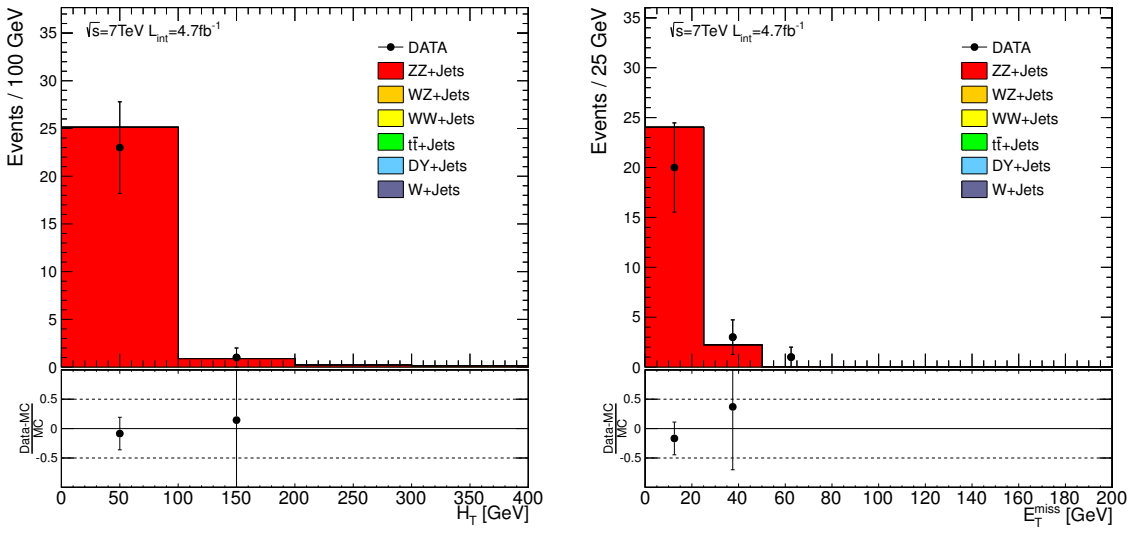

Figure 8.26: H_T (left) and E_T^{miss} (right) distribution of ZZ events including four tight leptons (e, μ) with at least two opposite sign same flavor lepton pairs forming an invariant mass consistent with the Z mass. Those distributions are used to estimate the systematic uncertainty on the MC predictions in the high-H_T and high-E_T^{miss} region.

8.4 Summary

After discussing the SM background processes a short summary follows before looking into results: dilepton processes with additional fake leptons from light and heavy flavor decays are determined in dedicated side-band measurements, where the relative isolation side band was utilized and cross checked in the transverse impact parameter side-bands. For the dominant dilepton processes $Z/\gamma* \rightarrow l^+l^-$ and $t\bar{t} \rightarrow b\bar{b}l^+l^-\nu\bar{\nu}$ a good agreement between the measurement and prediction is observed. One has to keep in mind that Drell-Yan+Jets processes are playing only a minor role in the signal regions (high-E_T^{miss} or high-H_T), whereas $t\bar{t} + Jets$ is one of the dominant background contribution. The second type of fake leptons discussed in the last sections is coming from photon conversions. Two kinds of photon conversion were observed: (1) external where an on-shell photon interacts with the detector material and converts into two leptons and (2) internal where a virtual photon converts into leptons at the matrix element level. A dedicated MC sample to account for this background was produced and cross checked for asymmetric and symmetric photon conversion as well.
Double boson processes with three or more prompt leptons in the final state are an irreducible background for multileptonic signatures, since the lepton properties are similar to typical SUSY processes, and are checked in several control regions. All control regions show consistent MC predictions with observations. Due to lack of recorded events so far a data driven method for predictions in the signal regions cannot be made, but the uncertainty on the k-factor for off-shell productions were estimated from extrapolation in H_T and E_T^{miss} bins.
More rare processes like WWγ, TTW, and TTZ are taken completely from MC simulations without cross checking in control regions, since they are not accessible in the near future.
In Fig. 8.27, 8.28 and 8.29 diagrams with the relative background composition for three lepton (e, μ, no-τ_h) channels in the various search regions are presented. Similar to the defined binning the channels were split into off-Z and on-Z, i.e. if there is an opposite sign same flavor lepton pair with mass consistent with the Z mass or not. In total only a subset of 12 channels out of the 48 search channels are shown for reasons of clarity. The evolution of the SM backgrounds between low- and high-H_T (E_T^{miss}) signal regions can be nicely seen. Especially in low-E_T^{miss} and low-H_T the dominant SM process is DY+Jets, which is overtaken by the irreducible WZ background in other channels. Also $t\bar{t}$ is one of the primary backgrounds in high-H_T (E_T^{miss}) regions, especially in off-Z and no-OSSF channels.

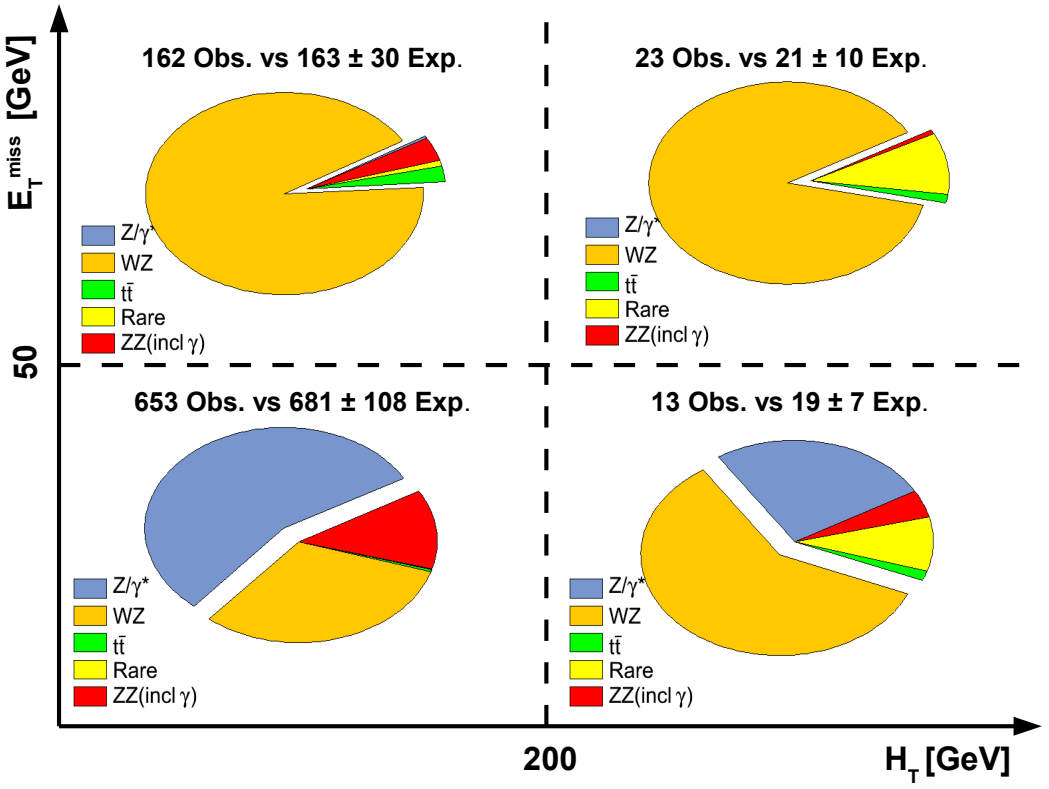

Figure 8.27: Relative background composition of different SM processes contributing to the three lepton (e, μ) channels with one opposite sign same flavor pair on-Z. Rare processes include WW, TTZ, TTW and WWγ. The given observations (Obs.) and expectations (Exp.) will be discussed in Chapter 9 in more detail.

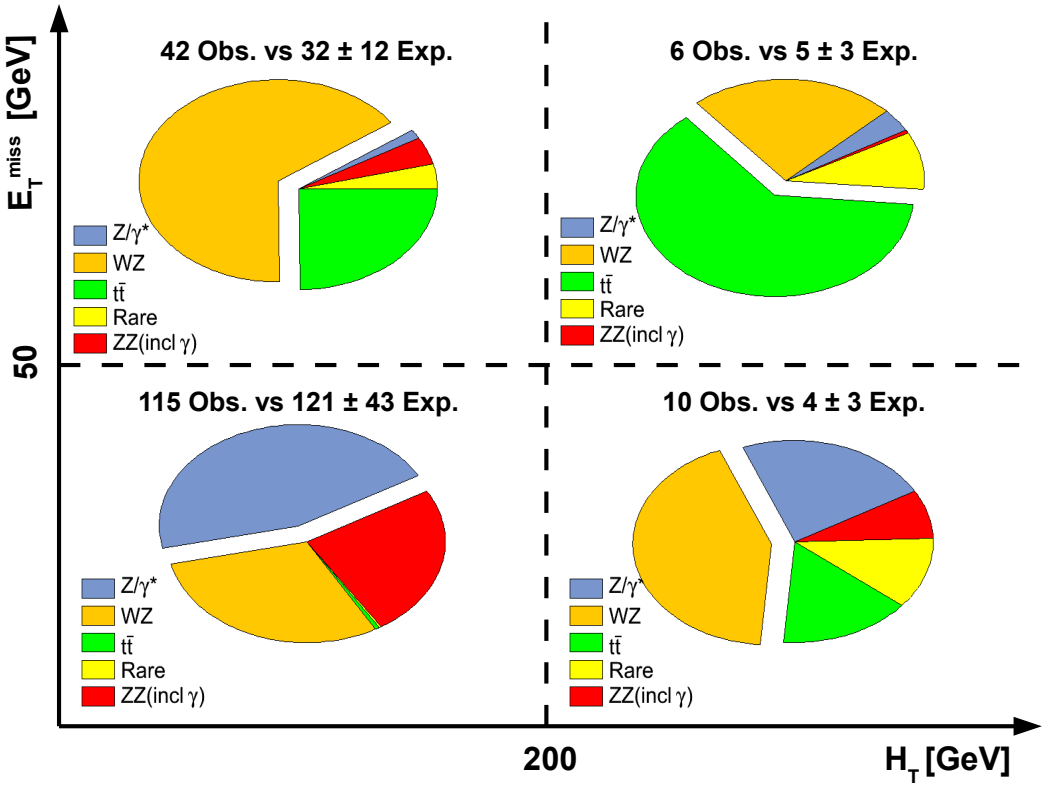

Figure 8.28: Relative background composition of different SM processes contributing to the three lepton (e, μ) channels with one opposite sign same flavor lepton pair off-Z. Rare processes include WW, TTZ, TTW and WWγ. The given observations (Obs.) and expectations (Exp.) will be discussed in Chapter 9 in more detail.

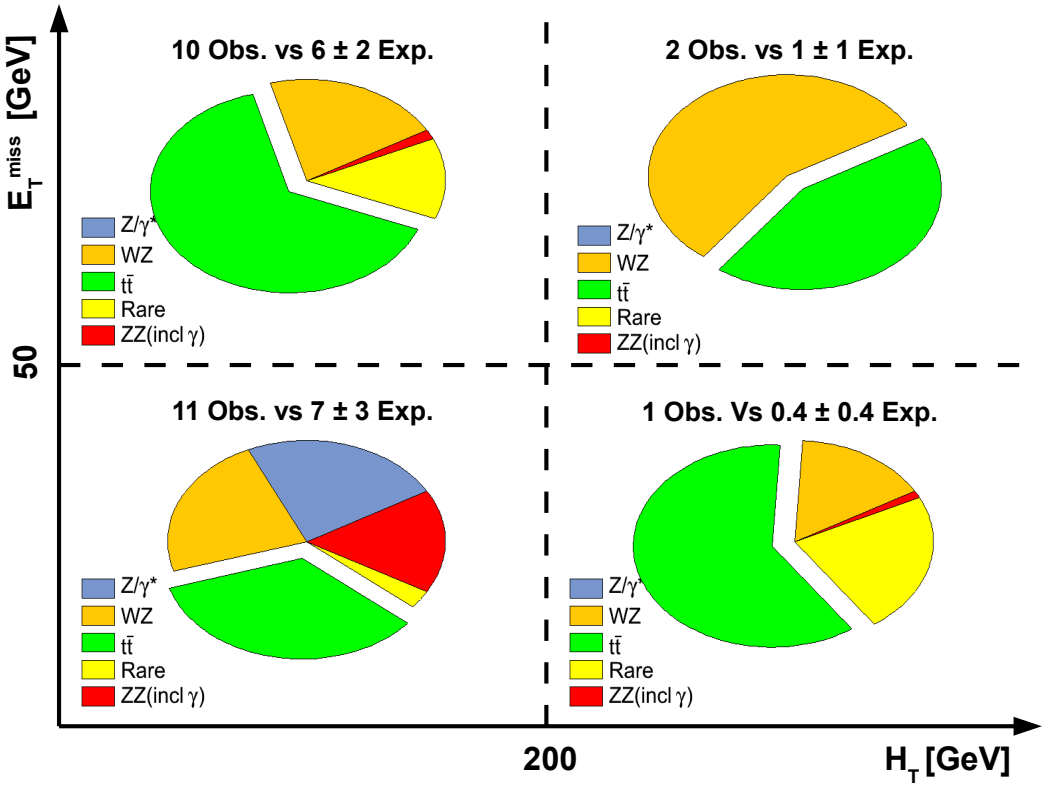

Figure 8.29: Relative background composition of different SM processes contributing to the various three lepton (e, μ) channels without opposite sign same flavor lepton pairs . Rare processes include WW, TTZ, TTW and WWγ. The given observations (Obs.) and expectations (Exp.) will be discussed in Chapter 9 in more detail.

CHAPTER 9

Results

Finally, after defining the event and object selection, measuring the selection and trigger efficiencies, cross checking SM backgrounds in control regions and applying methods to predict the most dangerous backgrounds in a data driven fashion, the signal regions can be investigated. Table 9.1 summarizes the observed number of three and four lepton events summed over electron and muon flavors. They are classified according to the number of tight τ_h's involved ($N(\tau) = 0, 1, 2$). The sum of all SM predictions are shown as well. Different selections are indicated by the labels going down, where the H_T and E_T^{miss} requirements are given. Furthermore, the selection is separated in events with and without an opposite sign same flavor (OSSF) lepton pair. If an OSSF pair is present, the sample is divided in on-Z and off-Z events. Non-signal regions with low-E_T^{miss} and low-H_T are combined in order to present the whole picture. This presentation allows for a direct comparison of channels next to the signal regions ($H_T > 200\,\text{GeV}$ and/or $E_T^{\text{miss}} > 50\,\text{GeV}$).
One observes a slight excess in the following three channels:

1. 3L $N(\tau = 0)$ off-Z $E_T^{\text{miss}} > 50\,\text{GeV}$ and $H_T < 200\,\text{GeV}$ **(42 obs. and 31.57$\pm$ 11.98 exp.)**,

2. 3L $N(\tau = 0)$ off-Z $E_T^{\text{miss}} < 50\,\text{GeV}$ and $H_T > 200\,\text{GeV}$ **(10 obs. and 4.47$\pm$ 3.01 exp.)** and

3. 3L $N(\tau = 1)$ no-OSSF $E_T^{\text{miss}} > 50\,\text{GeV}$ and $H_T < 200\,\text{GeV}$ **(14 obs. and 5.89$\pm$ 3.04 exp.)**.

The H_T and E_T^{miss} distributions for the 3L (N(τ)=0) channels (on-Z, off-Z) are presented in Fig. 9.1, where the off-Z distributions corresponds to the first minor deviation listed above. For comparison the on-Z distributions are presented in the same figure. Additionally the invariant mass distributions of all OS-SF lepton pairs (e^+e^-, $\mu^+\mu^-$) are shown as well. One observes a good agreement between data and SM background expectation for the on-Z distributions, whereas for off-Z a slight excess occurs starting from $E_T^{\text{miss}} > 30\,\text{GeV}$. This excess, shown also in the invariant mass distribution of all OS muon pairs, appears to be at low invariant masses $m_{\mu^+\mu^-} = [20, 50]\,\text{GeV/c}^2$. The dominant background in this phase space arises from W$\gamma*$ processes. Comparing also the H_T distribution for

Table 9.1: Results summed over electron and muon flavors corresponding to an integrated luminosity $L_{int} = 4.7\,fb^{-1}$ recorded in 2011. The selection labels refer to whether there is an opposite sign same flavor (OS-SF) lepton pair with a mass (in)consistent with the Z mass (off/on-Z) or not (no-OSSF), and the H_T and E_T^{miss} requirements. Additionally the results are split into τ candidate multiplicity ($N(\tau) = 0, 1, 2$). All channels listed are exclusive.

Selection	N(τ)=0		N(τ)=1		N(τ)=2	
	obs	expect	obs	expect	obs	expect
4 Leptons						
OFF Z, HT>200, MET>50,	0	0.04 ± 0.04	0	0.03 ± 0.02	0	0.01 ± 0.02
ON Z, HT>200, MET>50,	0	0.19 ± 0.18	0	0.17 ± 0.08	1	0.01 ± 0.02
OFF Z, HT<200, MET>50,	1	0.09 ± 0.07	1	0.37 ± 0.20	3	2.03 ± 2.82
ON Z, HT<200, MET>50,	2	0.84 ± 0.63	0	1.85 ± 0.77	0	0.67 ± 0.56
OFF Z, HT>200, MET<50,	0	0.028 ± 0.03	0	0.02 ± 0.02	1	0.40 ± 0.68
ON Z, HT>200, MET<50,	1	0.43 ± 0.38	0	0.12 ± 0.06	1	1.21 ± 1.84
OFF Z, HT<200, MET<50,	1	3.19 ± 1.68	3	1.13 ± 0.45	11	12.06 ± 13.49
ON Z, HT<200, MET<50,	32	36.84 ± 7.53	6	5.33 ± 1.61	34	33.60 ± 30.68
3 Leptons						
no-OSSF, HT>200, MET>50,	2	0.95 ± 0.56	23	25.51 ± 12.13	-	-
no-OSSF, HT<200, MET>50,	10	6.35 ± 2.15	127	110.69 ± 48.07	-	-
no-OSSF, HT>200, MET<50,	1	0.43 ± 0.43	14	5.89 ± 3.04	-	-
no-OSSF, HT<200, MET<50,	11	6.92 ± 2.59	210	207.27 ± 77.32	-	-
OFF Z, HT>200, MET>50,	6	4.86 ± 2.61	14	18.51 ± 9.10	-	-
ON Z, HT>200, MET>50,	23	21.39 ± 10.31	9	11.19 ± 4.10	-	-
OFF Z, HT<200, MET>50,	42	31.57 ± 11.98	117	89.70 ± 37.99	-	-
ON Z, HT<200, MET>50,	162	162.66 ± 29.86	110	83.56 ± 26.93	-	-
OFF Z, HT>200, MET<50,	10	4.47 ± 3.01	19	19.15 ± 10.41	-	-
ON Z, HT>200, MET<50,	13	18.62 ± 7.33	101	94.43 ± 49.35	-	-
OFF Z, HT<200, MET<50,	115	120.91 ± 43.40	3254	3480 ± 1718	-	-
ON Z, HT<200, MET<50,	653	681 ± 108	12242	12770 ± 6301	-	-
Total 4 Leptons:	37	41.65 ± 10.23	10	9.02 ± 2.52	51	49.98 ± 45.23
Total 3 Leptons:	1048	1060 ± 168	16240	16917 ± 8182	-	-

the SM expectations and observation the excess in this channel has a similar shape as the W$\gamma*$ prediction, just a factor ≈ 1.5 to high. One has to note, as shown in Section 8.3.1, that the description of $W\gamma*$+Jets processes is sensitive to the production mechanism and a large uncertainty has been assigned for this channel. Thus, the actual deviation of the observation with respect to the expectation is less than $\Delta \leq 1\sigma$. The estimate of the deviation is calculated as $\Delta = (N_{obs} - N_{exp})/\sqrt{\sigma^2_{obs} + \sigma^2_{exp}}$. More details on the expectations split into individual processes, observations and SUSY signal expectations for the LM9 benchmark[1] can be found in Table 9.2. Additionally the flavor decomposition (eee, $ee\mu$,...) is presented. A complete set of detailed Tables for all channels presented can be found in Appendix E.

The second excess listed above appears in the channel (3L, $N(\tau = 0)$, off-Z, $E_T^{\text{miss}} < 50\,\text{GeV}$ and $H_T > 200\,\text{GeV}$) channel, where 10 events are observed and 4.47$\pm$3.01 expected with a deviation of 1.27σ. Again, more details on the expectations and observations can be found in Table 9.2. The main deviation is in the subchannel $\mu^+\mu^- e^\pm$, where 7 events are observed and 2.07 $\pm$ 2.05 are expected. Taking into account also the corresponding on-Z subchannel ($\mu^+\mu^- e^\pm$, on-Z, $E_T^{\text{miss}} < 50\,\text{GeV}$ and $H_T > 200\,\text{GeV}$), where 1 event is observed and 6.80 $\pm$ 3.26 are expected, it occurs that 3 of the 7 events measured in the off-Z region have an invariant mass of the OS-SF pair close to the Z-Veto window $\Delta m \leq 8\,\text{GeV/c}^2$ ($m_{\mu\mu} = 67.46\,\text{GeV/c}^2$, $m_{\mu\mu} = 68.62\,\text{GeV/c}^2$, $m_{\mu\mu} = 113.66\,\text{GeV/c}^2$) and the interpretation as a statistical fluctuation is appropriate.

A deviation in the order of 1.68σ is observed in the channel (3L, $N(\tau = 1)$, no-OSSF, $E_T^{\text{miss}} > 50\,\text{GeV}$ and $H_T < 200\,\text{GeV}$), where 14 events were observed and 5.89 $\pm$ 3.04 are expected. Again, detailed information about the expectations split into individual processes and observations can be found in Table E.8 of Appendix E. The excess appears to be only in the subchannel ($e^\pm\mu^\pm\tau$, $E_T^{\text{miss}} > 50\,\text{GeV}$, $H_T < 200\,\text{GeV}$), where 13 events are observed with an expectation of 5.27 $\pm$ 2.93. The dominant SM process occurs to be $t\bar{t}$ (4.79 $\pm$ 2.89). The E_T^{miss} distributions for $H_T < 200\,\text{GeV}$ and $H_T > 200\,\text{GeV}$ are both presented in Fig. 9.2 for direct comparison. In the low H_T and low E_T^{miss} region the dominant background is $Z/\gamma* \to \tau\tau \to \mu^\pm\nu_\mu\nu_\tau e^\pm\nu_e\nu_\tau$ plus an additional fake tau. For $H_T > 200\,\text{GeV}$ those contributions are highly suppressed and the remaining background is $t\bar{t}$. The overall description of the shape is in good agreement between data and background prediction and the deviation in the low E_T^{miss} region may be a threshold effect induced by the low statistics in the $t\bar{t}$ (WJets) MC samples.

Another two interesting 4L events are observed with vanishing background predictions. The first event contains three electron- and one muon candidate, where the invariant masses of the OS electron pairs are $m_{e_1e_3} \approx 322\,\text{GeV/c}^2$ and $m_{e_2e_3} \approx 54\,\text{GeV/c}^2$. The jet activity in the event is low ($H_T \approx 84\,\text{GeV}$) with $E_T^{\text{miss}} \approx 231\,\text{GeV}$ and the total background expectation is 0.09$\pm$0.07 with a probability of 8% to fluctuate to 1 or more events[2].

The second interesting 4L events consist of two muon and two tau candidates with an invariant mass of the OS muon pair $m_{\mu_1\mu_2} \approx 84\,\text{GeV/c}^2$ consistent with a Z decay. The event is accompanied by one hard jet with $E_T \approx 231\,\text{GeV}$ and the missing transverse energy in the event is $E_T^{\text{miss}} \approx 81\,\text{GeV}$. In total a SM background expectation of 0.01$\pm$0.02 is estimated, which correspond to a probability of 1.2% to fluctuate to one or more events[3].

[1] LM9: $m_0 = 1450$, $m_{1/2} = 175$, $tan\beta$=50, $A_0 = 0$, $sign(\mu) = +1$

[2] Poisson probability for μ=0.09: $P(0.09) \geq 1$

[3] Poisson probability for μ=0.01: $P(0.01) \geq 1$

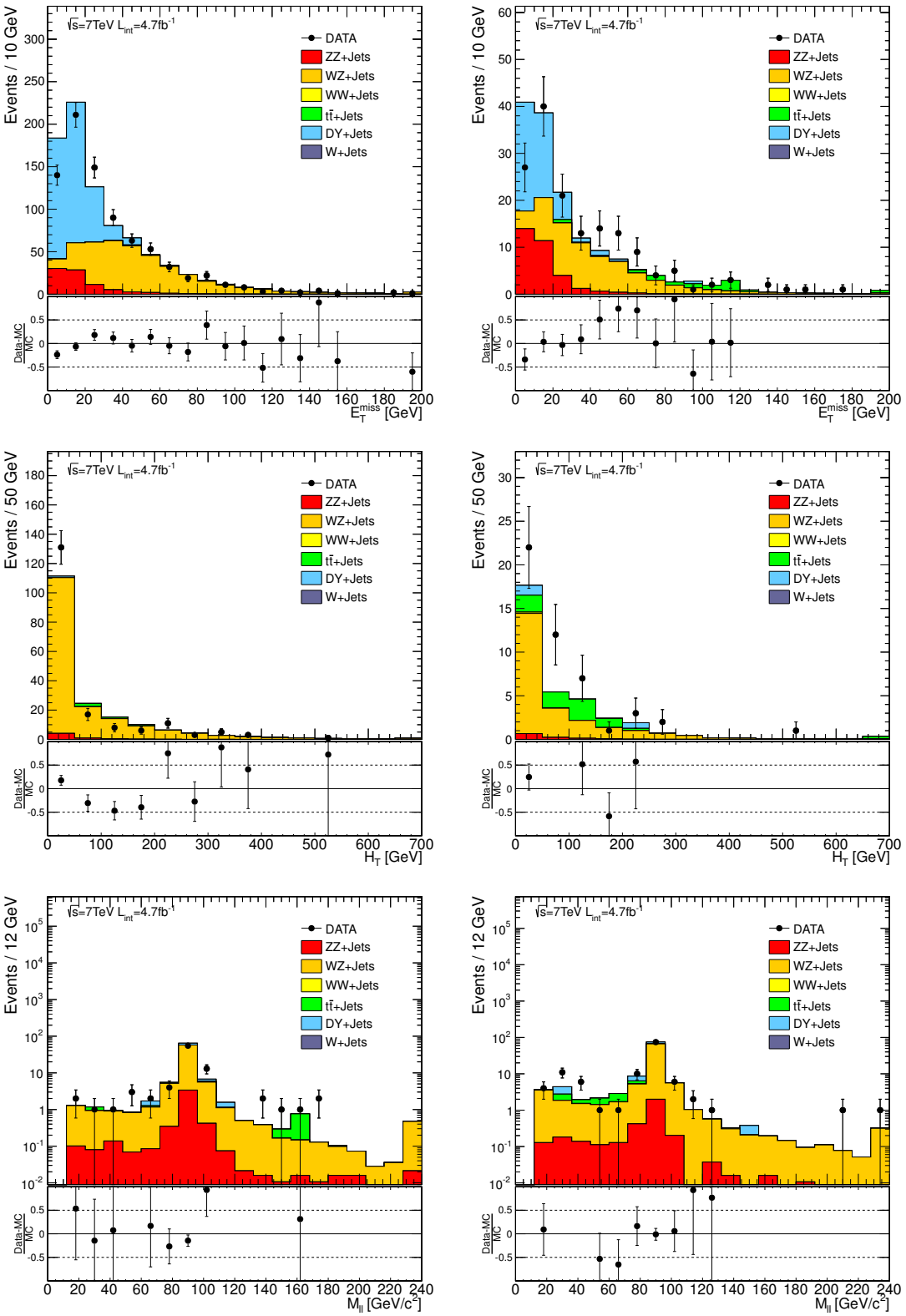

Figure 9.1: E_T^{miss} (top) and H_T (middle) distribution for three lepton events passing all selection criteria, except H_T or E_T^{miss} for the top and middle rows, respectively. Plots on the right have the Z-veto applied, while plots on the left include leptons from Z. The invariant mass distributions of opposite sign same flavor lepton pairs e^+e^- (bottom left) and $\mu^+\mu^-$ (bottom right), where $E_T^{\text{miss}} > 30\,GeV$ is required, are presented as well. Note: The DY_M-10-50 MC sample has only 7 unweighted events (around 32 weighted) left for the off-Z E_T^{miss} distribution (top right) and thus no pile up reweighting is applied.

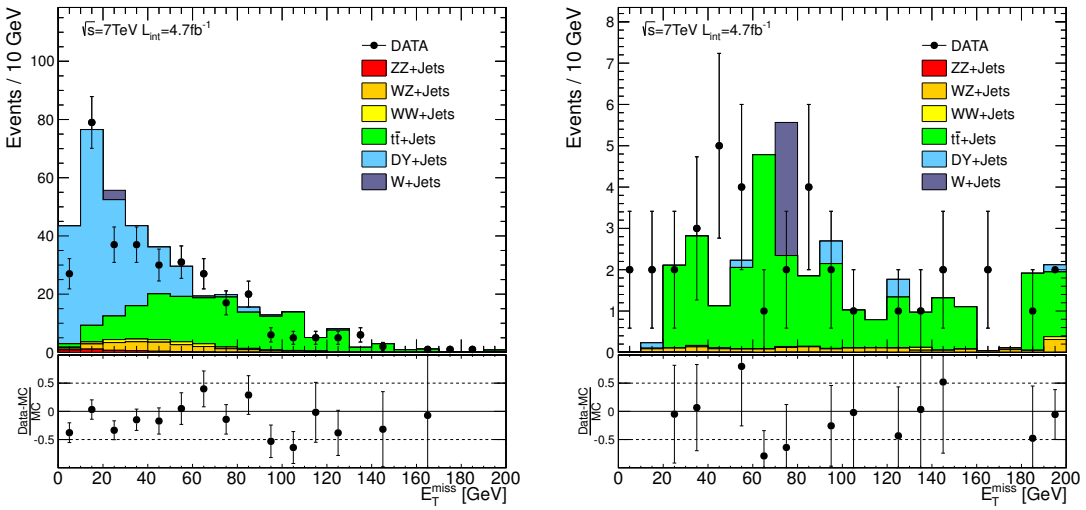

Figure 9.2: E_T^{miss} distribution for three lepton events including one τ_h candidate and no opposite sign same flavor lepton pair for low-H_T (left) and high-H_T (right).

A detailed event display for both events are presented in Fig. H.1-H.2 ($eee\mu$) and Fig. H.3-H.4 ($\mu\mu\tau\tau$), respectively (Appendix H). The values shown can differ from the actual values used due to jet energy corrections applied afterwards.

However given the probability for a statistical 2σ fluctuation in the measured cross sections in as many as 48 exclusive channels, the observation of the measured deviations discussed above is expected. This effect is called the look-elsewhere-effect.

Nevertheless, one can check how typical SUSY models would contribute to the individual channels. Taking a closer look into the kinematic distributions shown in Fig. 9.1 one observes a small excess at midrange E_T^{miss} ($E_T^{\text{miss}} = [40, 80]\,\text{GeV}$) and low H_T ($H_T < 200\,\text{GeV}$) dominated by WZ/γ^* background processes (disregarding $N(\tau) = 1$ channels for now). Assuming the excess arising from new physics models and taken into account the fact that the dominant SM background model is electroweak double boson production, a SUSY model with dominant electroweak production (SUSY benchmark point: LM9) is added. It can be seen that this specific SUSY model just fills the small excess. However, the statistical significance of this particular channel is small because of the high systematic uncertainties on the SM background prediction. The added SUSY prediction is only an example for the sensitivity to SUSY models in those particular channels. In Appendix E all 48 channels examined are presented including flavor decomposition, individual process contributions and SUSY signal expectations for the LM9 benchmark point.

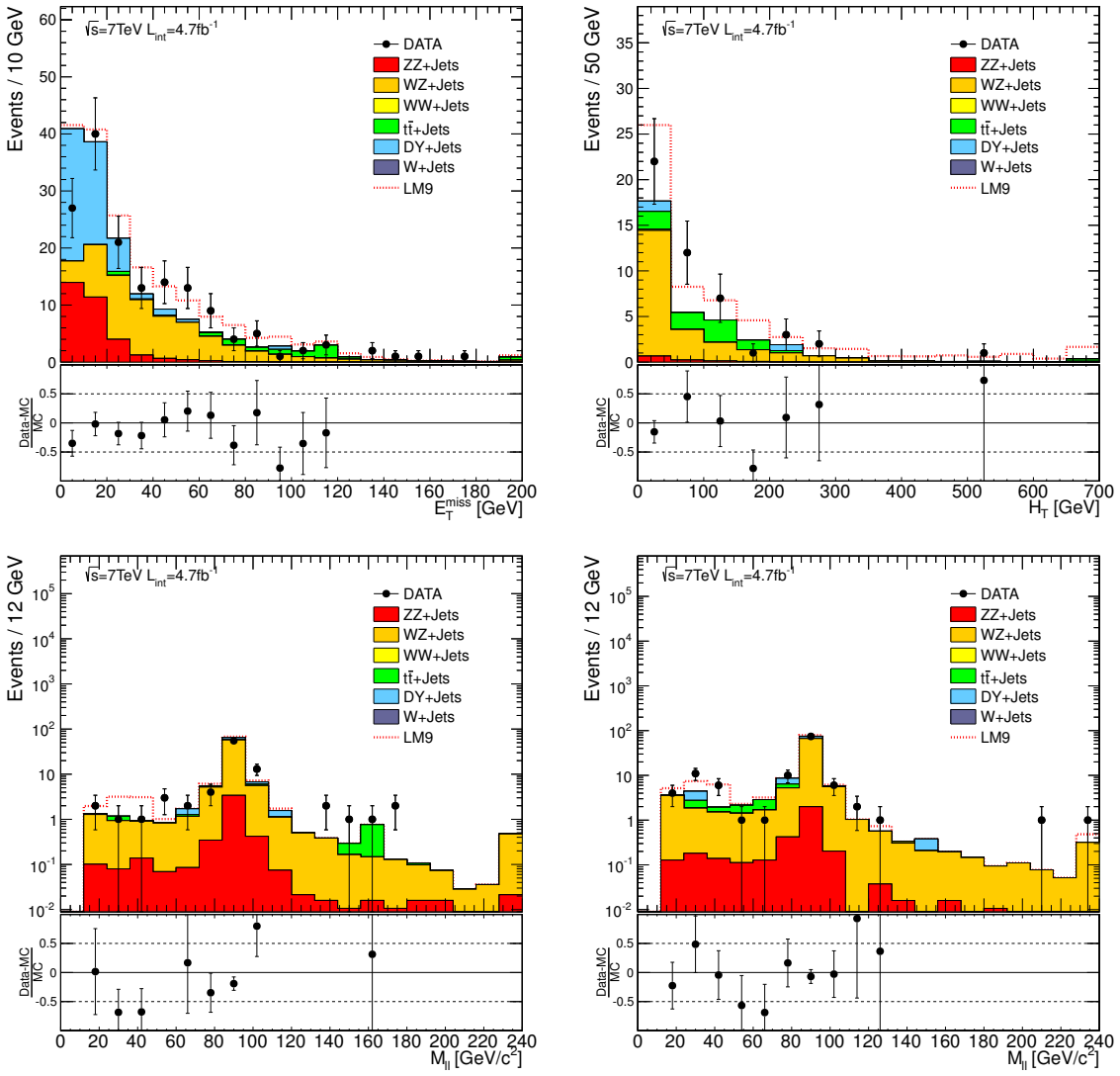

Figure 9.3: E_T^{miss} (top left) and H_T (top right) distribution for three lepton events passing all selection criteria. The invariant mass distributions of OS-SF pairs e^+e^- (bottom left) and $\mu^+\mu^-$ (bottom right), where $E_T^{\text{miss}} > 30\,\text{GeV}$ is required, are shown in the bottom row. Included are also signal prediction for the SUSY benchmark model LM9. Note: The DY_M-10-50 MC sample has only 7 unweighted events (around 32 weighted) left for the off-Z E_T^{miss} distribution (top left) and thus no pile up reweighting is applied.

Table 9.2: Results split in electron and muon flavors corresponding to an integrated luminosity $L_{int} = 4.7\,fb^{-1}$ recorded in 2011. The selection labels refer to whether there is an opposite sign same flavor lepton pair with a mass (in)consistent with the Z mass (off/on-Z), and the H_T and E_T^{miss} requirements. Four 3l N(τ)=0 channels of Table 9.1 are shown: (top block) off-Z, HT $<$ 200, MET $>$ 50; (second block) on-Z, HT $<$ 200, MET $>$ 50; (third block) off-Z, HT $>$ 200 MET $<$ 50 and (bottom block) on-Z HT$>$200 MET$<$50. The SM expectation is split into single processes (second to fifths columns). The total SM expectations and observation are given in the six and seventh columns and the signal expectations for the SUSY LM9 benchmark point in the last column. If given value is "$-$" no expectation for the process are given due to limited simulated MC events.

Channel	DYJets	WZJets	TTJets	Rare	ZZ(incG)	SumSM	Data	LM9
N(τ)=0; 3 Leptons; OFF Z; HT$<$200; MET$>$50;								
eee	-	2.695 ± 1.438	0.363 ± 0.324	0.162 ± 0.129	0.111 ± 0.130	3.331 ± 1.512	4	2.405 ± 0.660
$ee\mu$	0.442 ± 0.498	4.526 ± 2.412	1.356 ± 1.031	0.527 ± 0.354	0.379 ± 0.454	7.230 ± 2.845	9	2.172 ± 0.663
$e\mu\mu$	-	6.433 ± 3.427	3.045 ± 1.697	0.530 ± 0.390	0.966 ± 0.984	10.974 ± 4.150	15	6.340 ± 1.464
$\mu\mu\mu$	0.192 ± 0.189	6.728 ± 3.583	2.461 ± 1.255	0.279 ± 0.200	0.372 ± 0.431	10.483 ± 3.962	14	3.656 ± 1.056
Sum:	0.634 ± 0.532	20.383 ± 10.845	7.226 ± 3.204	1.499 ± 1.057	1.827 ± 1.708	31.569 ± 11.977	42	14.573 ± 2.100
N(τ)=0; 3 Leptons; ON Z; HT$<$200; MET$>$50;								
eee	0.332 ± 0.398	26.406 ± 4.884	0.073 ± 0.104	0.299 ± 0.248	0.861 ± 0.886	27.971 ± 5.167	32	1.797 ± 0.817
$ee\mu$	-	34.618 ± 6.399	0.392 ± 0.356	0.399 ± 0.344	1.895 ± 1.944	37.303 ± 7.005	35	0.910 ± 0.408
$e\mu\mu$	0.541 ± 0.630	37.594 ± 6.948	1.667 ± 0.918	0.520 ± 0.415	0.856 ± 0.880	41.178 ± 7.516	40	3.084 ± 0.971
$\mu\mu\mu$	-	51.754 ± 9.560	1.867 ± 1.055	0.501 ± 0.428	2.081 ± 2.134	56.203 ± 10.367	55	3.454 ± 0.989
Sum:	0.873 ± 0.842	150.372 ± 27.751	3.999 ± 1.706	1.719 ± 1.427	5.693 ± 5.833	162.656 ± 29.864	162	9.246 ± 1.684
N(τ)=0; 3 Leptons; OFF Z; HT$>$200; MET$<$50;								
eee	0.534 ± 0.849	0.193 ± 0.145	0.272 ± 0.411	0.043 ± 0.038	0.030 ± 0.039	1.073 ± 1.105	0	-
$ee\mu$	-	0.387 ± 0.287	-	0.121 ± 0.091	0.058 ± 0.075	0.566 ± 0.318	1	0.050 ± 0.051
$e\mu\mu$	0.534 ± 0.849	0.454 ± 0.336	0.271 ± 0.390	0.115 ± 0.087	0.698 ± 1.098	2.072 ± 2.052	7	-
$\mu\mu\mu$	-	0.543 ± 0.401	-	0.104 ± 0.090	0.110 ± 0.156	0.757 ± 0.450	2	0.406 ± 0.249
Sum:	1.069 ± 1.316	1.577 ± 1.158	0.543 ± 0.699	0.383 ± 0.293	0.896 ± 1.154	4.467 ± 3.009	10	0.457 ± 0.254
N(τ)=0; 3 Leptons; ON Z; HT$>$200; MET$<$50;								
eee	0.743 ± 0.739	2.011 ± 1.082	-	0.273 ± 0.274	0.196 ± 0.207	3.223 ± 1.425	2	-
$ee\mu$	1.442 ± 1.083	2.139 ± 1.150	0.272 ± 0.411	0.323 ± 0.312	0.140 ± 0.147	4.316 ± 1.786	5	0.128 ± 0.128
$e\mu\mu$	2.385 ± 1.856	3.228 ± 1.734	-	0.348 ± 0.347	0.836 ± 1.120	6.797 ± 3.256	1	0.006 ± 0.006
$\mu\mu\mu$	-	3.586 ± 1.925	-	0.449 ± 0.446	0.249 ± 0.261	4.285 ± 2.038	5	0.006 ± 0.006
Sum:	4.570 ± 2.479	10.964 ± 5.877	0.272 ± 0.411	1.393 ± 1.373	1.422 ± 1.387	18.621 ± 7.330	13	0.140 ± 0.129

9.1 Systematic Uncertainties

In this section the various systematic uncertainties for each investigated channel will be reviewed and the correlations discussed. In Table 9.1 the systematic uncertainties on the total SM background were already given but the individual components not yet explicitly discussed. They have been summarized in Table 9.3. We distinguish between systematic uncertainties affecting both signal and background processes, background only and signal only. Background only uncertainties are systematic induced by the prediction methods or statistical uncertainties in the control regions and uncertainties in the propagation to different phase spaces. Since for most SM backgrounds a data driven method or at least control regions are defined, all systematic uncertainties are included and only some residuals on the signal processes are evaluated.

Systematic uncertainties affecting signal and SM background processes:

- **Luminosity uncertainty**: For the systematic uncertainty on the luminosity measurement the CMS Collaboration uses a value of 4.5%, induced by the van der Meer scan method used to measure the luminosity of the colliding beams.

- **Trigger efficiency**: the trigger efficiency uncertainty is measured directly in data for each trigger separately. It is dominated by the statistical error of the data sample used for evaluation, especially for the high lepton multiplicity triggers the statistics is low. The final combined trigger efficiency in case of more than one possible trigger to be fired is determined event by event. The uncertainties on the combined efficiency is calculated via the error propagation: $\sigma_{\text{comb}} = \sqrt{\sum_i (\partial/\partial_{\epsilon_i}(1 - \Pi_j(1 - \epsilon_j)) \cdot \sigma_{\epsilon_i})^2}$ with ϵ_i the efficiency and σ_{ϵ_i} the uncertainty of the trigger i (see Section 7.4).

- **Lepton identification and isolation efficiency**: The uncertainty on the lepton identification / isolation efficiency associated with the tag&probe method for e, μ and the statistics for the τ ID control sample, respectively, depends on the transverse momentum p_T of the lepton. This is due to the usage of $Z \to l^+l^-$ events to determine the efficiency, where the rate of soft leptons is quite low. In principle the uncertainty for soft leptons can be reduced by using low resonances ($J/\Psi \to l^+l^-$), but since the overall uncertainty is dominated by other systematics a further study is postponed for now. The uncertainties vary between 1% - 11% for e, μ and 6% for tau lepton (see Section 7.3.1).

- **Jet energy scale:** The jet energy scale uncertainty is assumed to be 5%. The effect on the final selection is approximated by varying the H_T and E_T^{miss} cut by 5% up and down and taking the difference in the event yield as an uncertainty, which vary between 1-14% for E_T^{miss} and 1-18% for H_T , depending on the channel.

- **MC sample size:** The MC statistical uncertainty corresponds to the size of the used MC samples.

- **Vertex reweighting:** In Section 7.2 the pile up reweighting technique used in this study was discussed. Let's consider the impact of the vertex reweighting on the final result table. Since

the final table is inclusive in E_T^{miss} , i.e. E_T^{miss} >50 GeV and E_T^{miss} <50 GeV is considered both, the total number of predicted events should not depend on the number of vertices in simulation, because the difference in vertex multiplicity only affects the shape of the E_T^{miss} distribution. The same holds for the prediction in subchannels which are split in E_T^{miss} , e.g. on-Z, H_T >200 GeV, E_T^{miss} <50 GeV and E_T^{miss} >50 GeV. In order to guarantee that the total number of events in each channel is conserved for each MC sample and subchannel a weighting factor has to be calculated. Since the statistics in some subchannels is too small (<10 events) to allow for a meaningful calculation of the weighting factors, the MC prediction in such channels is instead assigned an extra 75% uncertainty accounting for the observed difference, as shown in Fig. D.1 in Appendix D.

Systematic Uncertainties affecting SM background processes only:

- **DY+Jets:** The systematic uncertainties in the DY+Jets processes are defined by the data driven side-band technique applied. The uncertainties are conservatively estimated to be 20% for electrons, muons and 50% for taus (see Section 8.1.1).

- $t\bar{t}$**:** The systematic uncertainty for the $t\bar{t}$ processes are defined by the data driven side-band technique applied. The uncertainties are conservatively estimated to be 20% for muons and 50% for electrons and taus (see Section 8.1.2).

- **WZ:** The uncertainty of 6% is defined by the statistical uncertainty in the control sample and cross section uncertainties. A propagation of the uncertainties from low E_T^{miss} (H_T) to the high E_T^{miss} (H_T) regions allows for a more reliable systematic uncertainty assigned in the corners of phase space. The latter vary between 15% and 50% for high-E_T^{miss} and/or high-H_T, respectively. Since the ratio on-Z/off-Z is sensitive to higher order corrections a conservative 50% uncertainty is applied to the off-Z predictions (see Section 8.3.1).

- **ZZ:** Similar considerations as for WZ are applied for ZZ events, where the uncertainties on the MC predictions vary between 75% and 100% for high-H_T and/or high-E_T^{miss} , respectively (see Section 8.3.2).

- **Z(**$ll\gamma$**):** For internal photon conversion a systematic uncertainty of 100% is assigned based on the large correction factor (~ 3) needed for the MC to agree with the data. For external photon conversions a systematic uncertainty of 50% for low-H_T and low-E_T^{miss} was assigned and the propagation to signal regions high-H_T (E_T^{miss}) leads to an additional 100%(50%) uncertainty (see Section 8.2).

Residual systematic uncertainties affecting signal processes:

- **Parton Density Function (PDF)**: A theoretical systematic uncertainty arising from variation of the parton density functions is determined to be 14% on MC signal simulation.

- **Renormalization and factorization scale**: This theoretical systematic uncertainty is determined by varying the factorization and renormalization scale ($\times 2$, $\times 0.5$) to be 10% on MC signal simulation.

All sources of systematic uncertainties discussed above have been summarized in Table 9.3. The correlations between different sources have to be taken into account. Common event and object uncertainties like luminosity, trigger efficiency and lepton identification and isolation efficiency are correlated for all channels and background sources. Similarly, the jet energy scale is correlated for the various signatures. The MC statistical uncertainties are uncorrelated. The uncertainties on dedicated SM background predictions are assumed to be correlated, which is not necessarily true.The $t\bar{t}$ and Drell-Yan+Jets prediction are based on the same method and are assumed to be correlated. Similar the backgrounds predicted completely from MC simulation, namely WZ and ZZ inclusive $\gamma*$ (and the other rare processes), are combined corresponding to 100% correlation. A more ideal correlation model could improve the final results, but for simplicitly in the statistical model this more conservative approach is used. The PDF and SCALE uncertainties on the signal processes are correlated for all channels.
The total uncertainty given in Table 9.1 is the linear sum of all correlated and squared sum of all uncorrelated systematic uncertainties given in Table 9.3.

Table 9.3: The sources and values of systematic uncertainties associated with this analysis. Uncertainties vary for different phase space of the leptons and/or search channels.

Source of Uncertainty	Uncertainty
Luminosity	4.5%
Single Muon Trigger efficiency	1-9%
Single Electron Trigger efficiency	1-6%
Double Muon Trigger efficiency	3-4%
Double Electron Trigger efficiency	1-2%
Electron Muon Cross Trigger efficiency	6-8%
Muon ID/Iso at 8 GeV ($>$30 GeV)	7%(1%)
Electron ID/Iso at 8 GeV ($>$30 GeV)	10% (1%)
Jet Energy Scale	1-18%
τ (HPS τ_h candidates)ID/ISO	6%
Parton Density Function	14%
Renormalization and Factorization Scale	10%
MC Statistics	3%-100%
Vertex Reweighting	0%-100%
SM Background Uncertainties	
DY+Jets	20-50%
DY($ll\gamma$) - (external) FSR	50-122%
DY($ll\gamma$) - (internal) FSR	100%
$t\bar{t}$	20-50%
WZ	6-71%
ZZ	75%-125%

9.2 Interpretation of the Results

The results of this study can be interpreted in terms of different SUSY models, like the common cMSSM. In addition the interpretation in terms of so called simplified models is presented: *TChiSlepSlep* and *TChiWZ* driven by direct neutralino-chargino production, and *TChiZZ* driven by direct neutralino-neutralino production. A detailed description can be found in [168] and will be given at the point needed.

9.2.1 cMSSM ($tan\beta = 10$)

In the cMSSM model one assumes the masses and gauge couplings to be unified at the GUT scale, i.e. one has a common mass m_0 ($m_{1/2}$) for all spin 0 (1/2) particles at the GUT scale. The real masses at a low scale are obtained from the renormalization group equations. Most limits have been given in the $m_0 - m_{1/2}$ plane. However, the masses depend also on the other parameters, notably $\tan\beta$, since the latter causes a mixing between left and right handed particles which depends on the Higgs sector and hence on $\tan\beta$. This mixing is especially important for the third generation, which has large Yukawa couplings. One observes that for larger values of $\tan\beta$ the stau becomes lighter than the other sleptons and in this case the squarks will decay preferentially into staus in the regions of small m_0, where the sleptons are lighter than the squarks, thus reducing the number of final states with muons and electrons. This will reduce the efficiency.

The observed 95% C.L. exclusion limit for the combination of all channels given in Table 9.1 interpreted as an excluded region in cMSSM is shown in Fig. 9.4 for $\tan\beta = 10$ and in Fig. 9.7 for $\tan\beta = 40$. The excluded regions are derived by dividing the cMSSM m_0-$m_{1/2}$ plane for fixed $tan\beta = 10(40)$, $A_0 = 0(-500)$ and $sign(\mu) = +1$ into $\sim$ 7K($\sim$ 6K) points, corresponding to $\Delta m_{0,1/2} = 20\,\text{GeV}$ and simulating 20k events per point. The SUSY signal prediction for the various search channels are determined using the NLO cross section calculated with Prospino [145] for each point. The observed exclusion region is calculated with the statistical procedure discussed in Section 5.6 using the observations and background predictions given in Table 9.1. Additionally, the expected exclusion region and the 1σ and 2σ bands are added.

Several independent constraints are added to the figures. At low m_0 and high $m_{1/2}$ masses (colored with dark gray) the LSP is the charged stau ($\tilde{\tau}$), which is ruled out by cosmological measurements and is not considered in this study. Previous searches performed with the LEP experiment are displayed at low $m_{1/2}$ masses colored with dark green (direct chargino production) and yellow (direct slepton production). Another constrain is the requirement of electroweak symmetry breaking (EWSB), which can not be achieved at high values of m_0 colored with light gray and indicated as *NO EWSB*. Adjacent to the *NO EWSB* region is a small band colored with light blue indicated as *Non-Convergent RGE's*. Here the solution of the renormalization group equations (RGE) do not converge and thus the calculated mass spectrum is not reliable. A more detailed description of the incorporated constraints can be found in [169].

$m_{1/2}$ values below $\sim 200\,\text{GeV}$ are excluded over a wide range of m_0 except at low m_0, where values of $m_{1/2} < 300\,\text{GeV}$ for $m_0 \approx [200, 300]\,\text{GeV}$ and $m_{1/2} < 350\,\text{GeV}$ for m_0 around 150 GeV are excluded. The spiky structure of the limit curve is due to statistical fluctuations of the dedicated signal MC samples. The two more fundamental steps in the limit at low values of m_0, namely at around

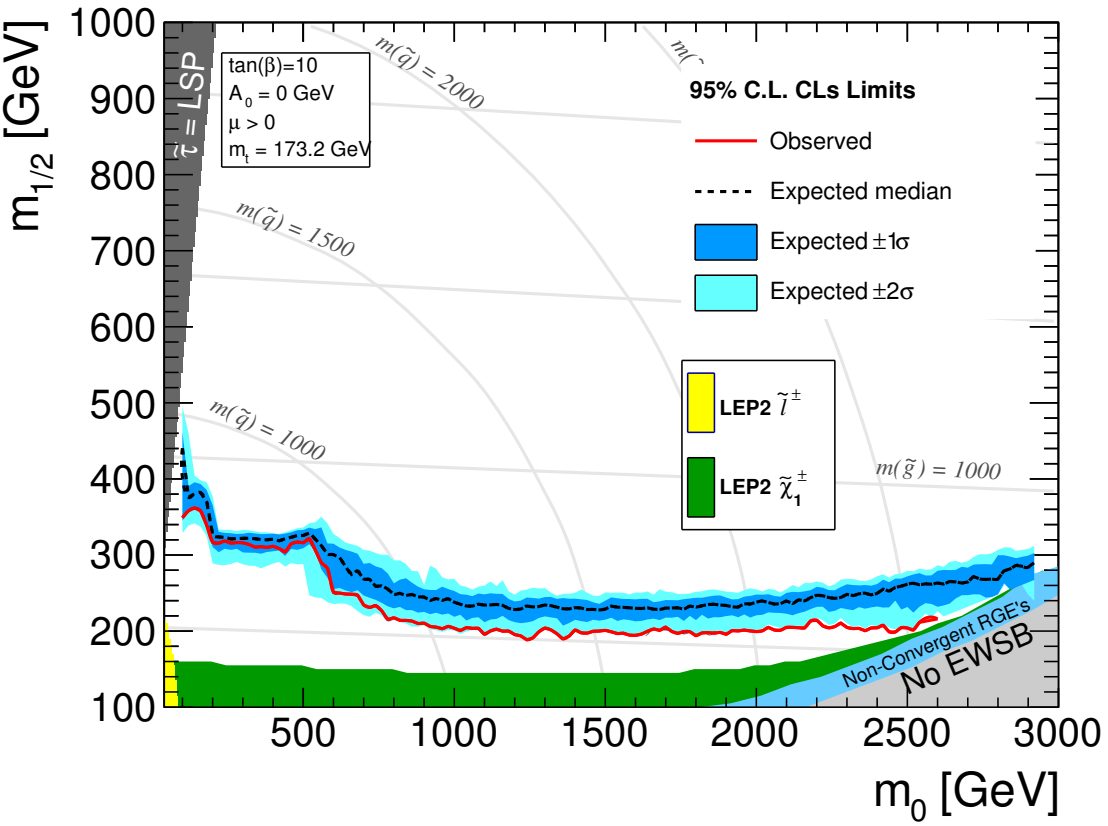

Figure 9.4: Excluded regions for the cMSSM scenarios with $tan\beta = 10$. Value of m_0, $m_{1/2}$ below the black curve (observed limit) are excluded at 95% confidence level by this analysis. The expected limit is indicated by the red line and the 1σ (2σ) by the blue (light blue) band. Excluded regions of former experiments are shown as well. The template cMSSM plane including various excluded regions described in the text can be found in [169].

$m_0 \approx 150\,\text{GeV}$ and $m_0 \approx 500\,\text{GeV}$, have to be discussed separately:

- The first drop to be discussed in the exclusion limit of Fig. 9.4 at m_0 values around 500 GeV is due to the changing signal contributions to the numerous channels examined and combined of Table 9.1. In Section 6.1 the different production and decay modes of the next to lightest neutralino and lightest chargino in the $m_0 - m_{1/2}$ plane have been discussed. It has been shown that for higher values of m_0, where the squarks and sleptons get heavy, the electroweak production of SUSY particles is dominant and the associated hadronic jet production decreases. For low m_0 masses the dominant signal contributions are in the channel (3L, (N(τ)=0), off-Z(on-Z), $H_T > 200\,\text{GeV}$, $E_T^{\text{miss}} > 50\,\text{GeV}$). Starting at $m_0 \approx 500\,\text{GeV}$ the dominant signal channel changes to (3L, (N(τ)=0), off-Z (on-Z), $H_T < 200\,\text{GeV}$, $E_T^{\text{miss}} > 50\,\text{GeV}$). Here the integrated SM background is higher with respect to the $H_T > 200\,\text{GeV}$ channel. Hence the exclusion limit decreases. The selection efficiency of the four main channels discussed are shown in Fig. 9.5, where the most sensitive regions can be seen. In Appendix F the selection efficiencies of all channels for $tan\beta = 40$ are presented.

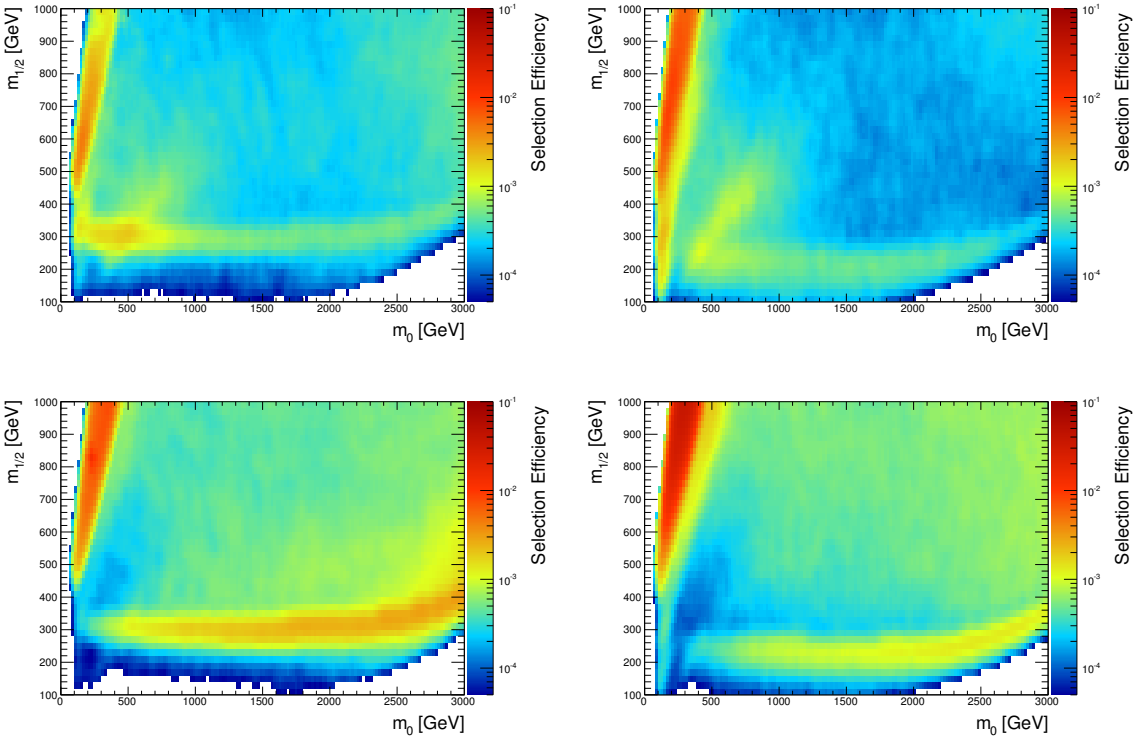

Figure 9.5: Signal ($tan\beta = 10$, $A_0 = 0$, $sign(\mu) = +1$) selection efficiency for the channels including 3 leptons (N(τ)=0), on-Z (left column), off-Z (right column), $E_T^{\text{miss}} > 50\,\text{GeV}$, $H_T > 200\,\text{GeV}$ (top row) and $H_T < 200\,\text{GeV}$ (bottom row).

- The other drop of the exclusion limit at $m_0 \approx 150\,\text{GeV}$ is due to the fact that at masses below, the next to lightest neutralino ($\tilde{\chi}_2^0$) decays via the slepton-lepton modes and the subsequent decay of the slepton into a lepton and the LSP. With increasing m_0 the sleptons get heavier and the decay via slepton-lepton modes is kinematically forbidden. Hence the next to lightest neutralino decays into two leptons and the LSP via a three body decay, either via a virtual slepton or a gauge boson into a lepton pair and neutralino. Increasing further the slepton masses (increasing m_0) the contribution of diagrams including virtual sleptons decreases and so does the branching fraction of the neutralino into leptons until it approaches a constant value corresponding to the Z boson branching fraction to two leptons. In addition some interference effects come into the game. The latter can be seen in Fig. 9.6 for the branching fraction of the next to lightest neutralino into two muons and the LSP. Shown is also the branching fraction of the lightest chargino.

Starting with m_0 masses of around 600 GeV the observed limit in Fig. 9.4 is $\Delta \approx 2\sigma$ off with respect to the expected limit. The dominant channel which defines the observed limit in this region is (3L, N(τ=0), off-Z, $E_T^{\text{miss}} > 50\,\text{GeV}$, $H_T < 200\,\text{GeV}$) with 42 observed events and 31.57 ± 11.98 expected. Despite the fact that the deviation in this particular channel is less than $\Delta \leq 1\sigma$, the correlation between the latter and the SM background dominated control channels (3L, N(τ=0), on-Z/off-Z, E_T^{miss}

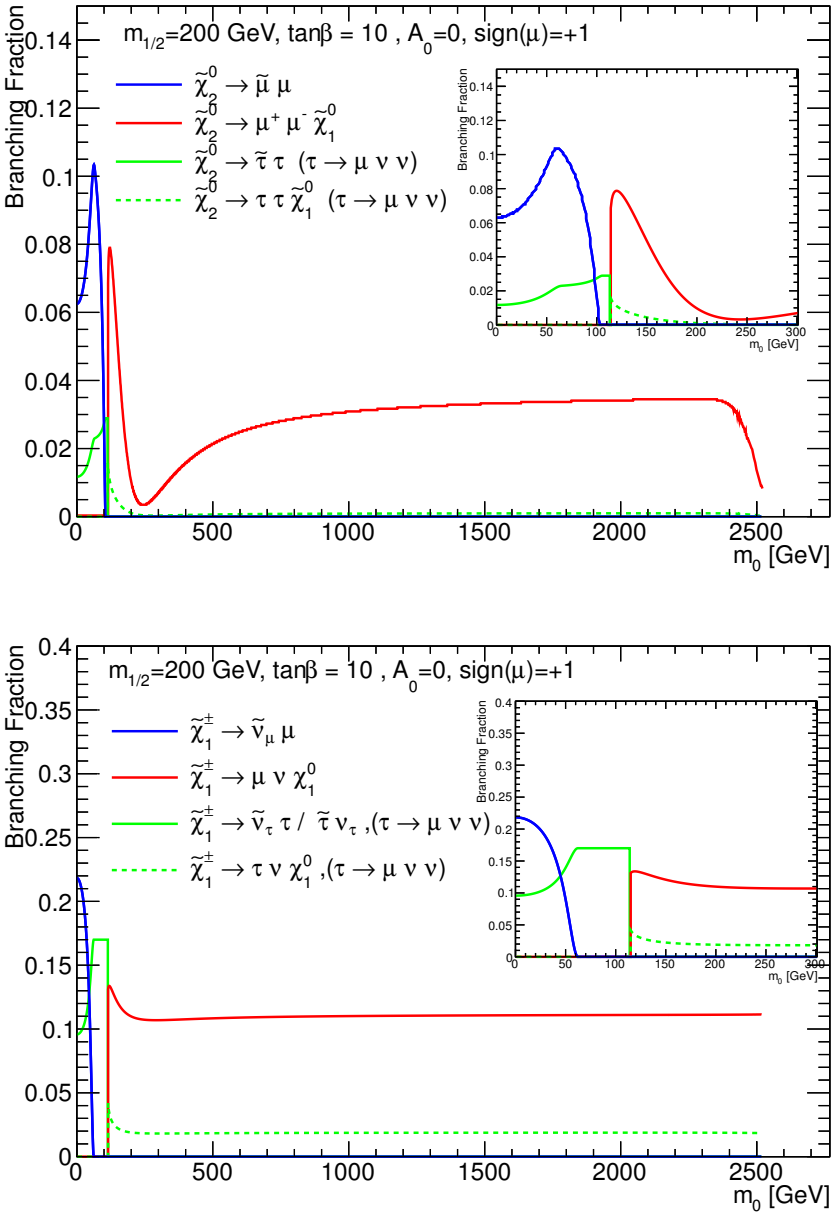

Figure 9.6: **Top**: Branching fraction of the next to lightest neutralino ($\tilde{\chi}_2^0$) into two muons via an intermediate smuon ($\tilde{\mu}$) for low m_0 masses (blue line) and via a three body decay for higher m_0 masses (red line). In addition the branching fraction into $\tilde{\tau}\tau$ with the subsequent decay $\tau \to \mu\nu_\mu\nu_\tau$ is added (green lines). In the box the region $m_0 = [0, 300]$ GeV is highlighted. The small gap at $m_0 = [106, 116]$ GeV between the decay modes (blue and red line) corresponds to the case where all slepton masses are higher with respect to the next to lightest neutralino except the lightest stau $\tilde{\tau}$, hence the decay $\tilde{\chi}_0^2 \to \tilde{\tau}\tau$ is the exclusive branching. The decrease of the branching fraction $\tilde{\chi}_0^2 \to \tilde{\chi}_0^1\mu^+\mu^-$ around $m_0 = 250$ GeV is due to interference effects of diagrams involving virtual sleptons and gauge bosons. **Bottom**: Branching fraction of the lightest chargino ($\tilde{\chi}_1^\pm$) into a muon (including also $\tau \to \mu\nu\nu$). For the given value $m_{1/2} = 200$ GeV the smuon ($\tilde{\mu}$) is for all values of m_0 heavier than the lightest chargino. Hence only $\chi_1^\pm \to \tilde{\nu}_\mu\mu^\pm$ is kinematically allowed (blue line). In the region $m_0 \approx [60, 115]$ GeV all sleptons are heavier except the lightest stau and the lightest chargino decays exclusively into $\tilde{\chi}_1^\pm \to \tilde{\tau}\nu_\tau$ (green line). For even higher m_0 masses the three body decay via virtual sleptons or gauge bosons is dominant (red line) approaching a constant value of $\sim 11\%$ corresponding to the branching fraction of a W boson into a muon and neutrino.

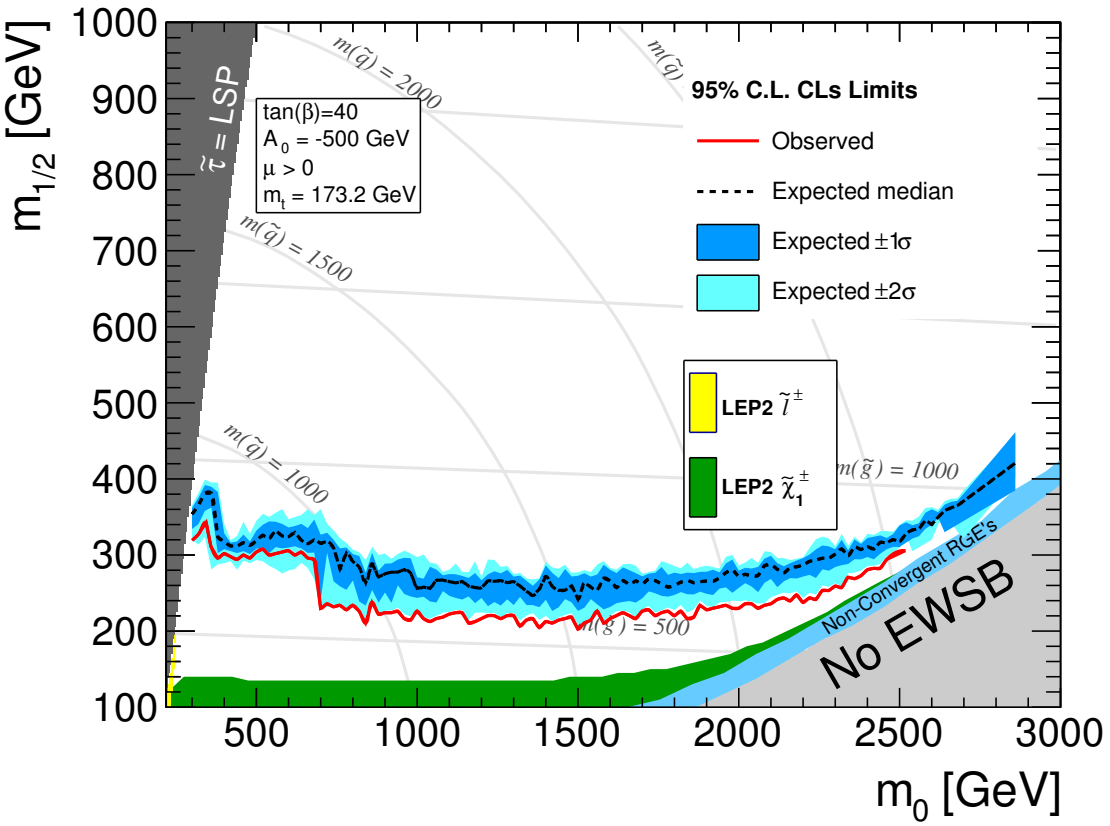

Figure 9.7: Excluded regions for the cMSSM scenario with $tan\beta = 40$. Values of m_0, $m_{1/2}$ below the black curve (observed limit) are excluded at 95% confidence level by this analysis. The expected limit is indicated by the red line and the 1σ (2σ) by the blue (light blue) band. Excluded regions of former experiments are shown as well. The template cMSSM plane including various excluded regions described in the text can be found in [169].

$< 50\,\text{GeV}$, $H_T < 200\,\text{GeV}$) fixes the nuisance parameters of the statistical model to lower values. Thus the seen deviation of the observed and expected limit is induced by this correlation.

9.2.2 cMSSM ($tan\beta = 40$)

In case of the exclusion limit for $tan\beta = 40$ shown in Fig. 9.7 a similar line of discussion can be followed as for $tan\beta = 10$ in Section 9.2.1. The main difference between both models occurs due to the higher value of $tan\beta$ and so the mass difference between selectron/smuon and the lightest stau is increased, as presented in Fig. 9.8. This results in enhanced tau final states. The effect on the observed limit in Fig. 9.7 is an increased excluded region for low m_0 masses (m_0 around 350 GeV). Analogous to the case of $tan\beta = 10$ with increasing values of m_0 the branching fraction of the next to lightest neutralino, which changes at a given mass from two body decays via intermediate sleptons to three body decays, into two leptons and the LSP decreases until it approaches a constant value corresponding to the branching fraction of the Z boson to leptons. The second drop of the observed

exclusion limit at $m_0 \approx 700$ GeV is due to a change of the dominant signal channel of Table 9.1 similar to the case of $tan\beta = 10$ described in more detail above. The selection efficiency of the four dominant channels is shown in Fig. 9.5, where the most sensitive regions for the different channels can be seen. In summary: over a wide range of m_0 masses $m_{1/2}$ masses below 220 GeV are excluded, except for low m_0, where also masses $m_{1/2} < 300$ GeV are excluded.
As for $tan\beta = 10$ a $\Delta \geq 2\sigma$ deviation of the observed limit with respect to the expected limit can be seen in Fig. 9.2.2 starting at m_0 masses of around 700 GeV. This deviation can be explained by the interplay of the correlation in the nuisance parameters for the dominant signal channel (3L, N(τ=0), off-Z, $E_T^{\text{miss}} > 50$ GeV, $H_T < 200$ GeV) and SM background dominanted control channels (3L, N(τ=0), on-Z/off-Z, $E_T^{\text{miss}} < 50$ GeV, $H_T < 200$ GeV).
In Appendix G the selection efficiencies of all channels for $tan\beta = 40$ are presented.

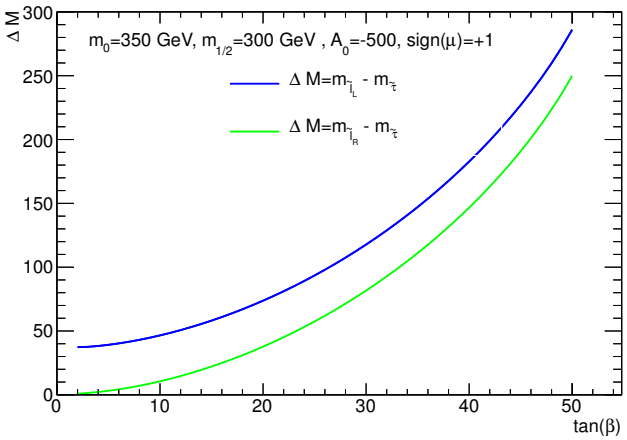

Figure 9.8: Mass difference ΔM between left (right)-handed sleptons ($\tilde{\mu}$, $\tilde{e}$) and the lightest stau ($\tilde{\tau}$) as a function of $\tan\beta$ for $m_0 = 350\,\text{GeV}$, $m_{1/2} = 300\,\text{GeV}$, $A_0 = -500$ and $sign(\mu) = +1$.

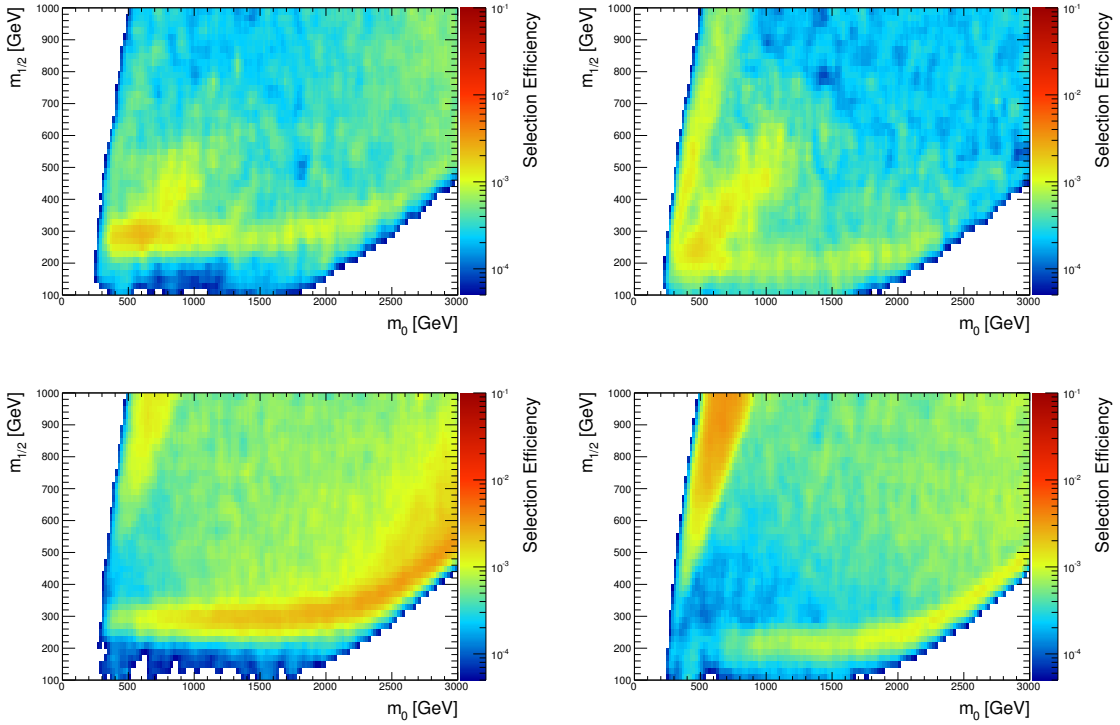

Figure 9.9: Signal ($tan\beta = 40$, $A_0 = 0$, $sign(\mu) = +1$) selection efficiency for the channels including 3 leptons (N(τ)=0), on-Z (left column), off-Z (right column), $E_T^{\text{miss}} > 50\,\text{GeV}$, $H_T > 200\,\text{GeV}$ (top row) and $H_T < 200\,\text{GeV}$ (bottom row).

9.2.3 Simplified Model Spectra (SMS)

Historically the results of searches for SUSY signals were interpreted in terms of specific models, e.g. the constrained minimal supersymmetric standard model (cMSSM) or the generalized gauge mediation models (GGM) [170]. A new kind of models was proposed for interpretation, which allow a more direct translation for theorists to apply the results to their models without a detailed knowledge of the detector. The so called *Simplified Model Spectra* (SMS) [168] are based on a small set of hypothetical particles. Within this approach several topology driven models have been defined, where the LSP is the lightest neutralino and stable (R-parity is conserved). Each model consists of a set of particles produced in the hard interaction and the decay chain. For this study three SMS models sensitive to multileptonic signatures are investigated: *TChiSlepSlep*, *TChiWZ* and *TChiZZ*.

TChiSlepSlep

The diagram describing the *TChiSlepSlep* SMS model is presented in Fig. 9.10. The model is driven by direct chargino-neutralino pair production decaying to slepton-lepton pairs with the subsequent decay of the slepton into the LSP and another lepton. In total three leptons, one neutrino and two LSP's are produced. The slepton masses are degenerated and hence the branching fractions of the neutralino/chargino into different slepton flavors is uniformly distributed. Also the chargino and neutralino masses are degenerated, which results in three model parameters: the mass of the neutralino/chargino, the LSP mass and the slepton mass. The latter is fixed by the requirement $m_{\tilde{l}} = (m_{\tilde{\chi}} - m_{LSP})/2$ reducing the degree of freedom to two parameters.

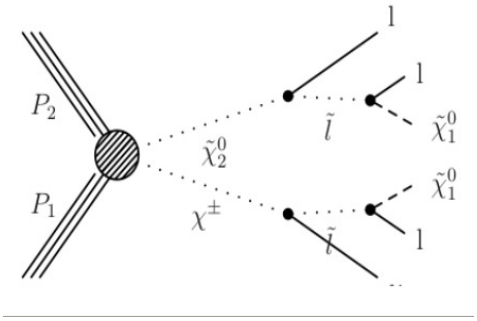

Figure 9.10: Schematic diagram for the SMS model TChiSlepSlep.

In total the TChiSlepSlep gives a strong three lepton yield without any contributions from Z and minor jet activity. Due to the undetected escaping LSP a high E_T^{miss} is expected. The dominant signal contribution in a wide range of the parameter space is suited in the channel (3L, N($\tau = 0$), off-Z, $H_T < 200\,\text{GeV}$ and $E_T^{\text{miss}} > 50\,\text{GeV}$). Fig. 9.11 demonstrates the acceptance $\times$ efficiency for the signal, and the 95% C.L. upper limit on the production cross section. All 48 examined channels are incorporated, despite the fact, that only a few channels give significant signal sensitivity. For high mass splittings, right bottom corner of Fig. 9.11, the acceptance $\times$ efficiency is mostly defined by the τ acceptance efficiency. Smaller mass splittings, close to the diagonal border, result in softer lepton spectra, where also the acceptance of electrons and muons decreases and so does the integrated

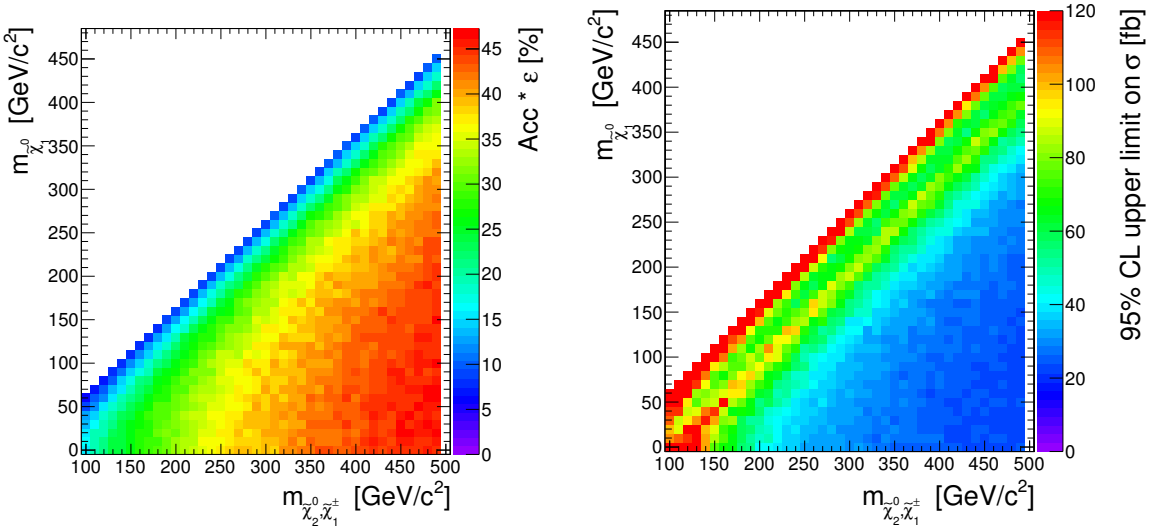

Figure 9.11: Acceptance $\times$ efficiency for the signal (left), and 95 C.L. upper limit on the production cross section (right) of the SMS model *TChiSlepSlep*.

acceptance.

The 95% C.L. upper limit on the production cross section is mostly driven by the observation and SM background prediction in the channel (3L, N($\tau = 0$), off-Z, $H_T < 200\,\text{GeV}$ and $E_T^{\text{miss}} > 50\,\text{GeV}$). Following the acceptance $\times$ efficiency distribution the upper limit gets higher for smaller mass splittings. Adjacent to the border one can observe a narrow band with a worse upper limit lying in the light green region. The sensitivity decreases because of the kinematic properties of the decay chain. Since the neutralino decays via a two body decay into a lepton-slepton pair and the slepton subsequently decays into the LSP and another lepton, the invariant mass distribution of the two leptons exhibits a particular edge with a kinematic end point corresponding to

$$M_{ll}^{max} = \sqrt{(m_{\tilde{\chi}_0^2}^2 - m_{\tilde{l}}^2)(m_{\tilde{l}}^2 - m_{\tilde{\chi}_0^1}^2)/m_{\tilde{l}}^2}\,. \tag{9.1}$$

Increasing the mass splitting of the neutralino and the LSP the kinematic end point crosses at some point the Z-veto window defined in the event selection. Those model points, where the kinematic endpoint lies in or close to the Z window contribute to the corresponding on-Z channel (3L, N($\tau = 0$), on-Z, $H_T < 200\,\text{GeV}$ and $E_T^{\text{miss}} > 50\,\text{GeV}$). Since here the SM background is higher compared to the off-Z channel, the upper limit on the production cross section in worsened to higher values[4].

TChiWZ

The second SMS model *TChiWZ* is also driven by chargino-neutralino production with the exception that all slepton masses are set to higher values and so the charginos/neutralinos decay via a two

[4]See Table 9.1: 3L, N($\tau = 0$), off-Z, $H_T < 200\,\text{GeV}$ and $E_T^{\text{miss}} > 50\,\text{GeV}$" - **42obs. vs 32exp** ; 3L, N($\tau = 0$), on-Z, $H_T < 200\,\text{GeV}$ and $E_T^{\text{miss}} > 50\,\text{GeV}$" - **162obs. vs 162exp**.

body decay into a LSP and gauge bosons. Thus this model depends on two parameters: the neutralino/chargino mass and the LSP.

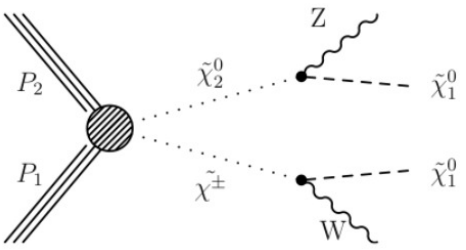

Figure 9.12: Schematic diagram for the SMS model TChiWZ.

Similar to the TChiSlepSlep model the TChiWZ gives a strong three lepton yield with minor jet activity. Here also the hadronic decay modes of the gauge bosons are included and hence the branching of both W and Z into leptons is around 3%.

Since the neutralino decays into a Z boson the dominant channel is (3L, N($\tau = 0$), on-Z, $E_T^{\text{miss}} > 50\,\text{GeV}$ and $H_T < 200\,\text{GeV}$). In comparison with the TChiSlepSlep model, where the upper limit on the production cross section is typically in the order of $\sigma_{UL,95\&C.L.} \approx 30 - 100\,\text{fb}$, the upper limit for TChiWZ is two orders of magnitude worse, namely in the order of $\sigma_{UL,95\&C.L.} \approx 2.5 - 3\,\text{pb}$. The reason for this is the lower branching fraction to three leptons and the higher background expectation in the dominant channel.

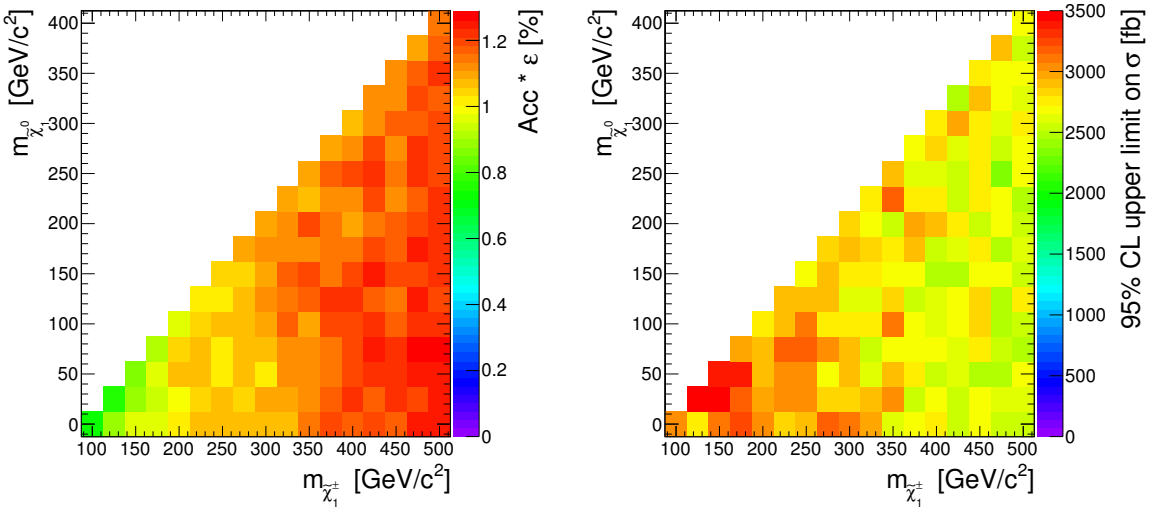

Figure 9.13: Acceptance $\times$ efficiency for the signal (left), and 95 C.L. upper limit on the production cross section (right) of the SMS model *TChiWZ*.

SMS: TChiZZ

The last SMS model to be discussed in this study is the *TChiZZ*. This model is driven by the direct neutralino-neutralino production for which the diagram is shown in Fig. 9.14. The model is parameterized by two independent parameters: the LSP mass and the neutralino mass. Each neutralino decays into a Z boson and a LSP.

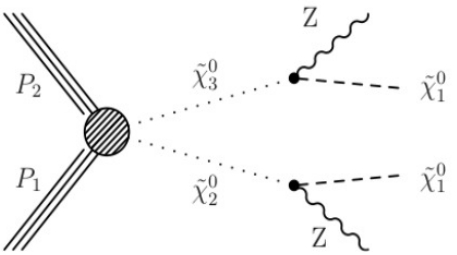

Figure 9.14: Schematic diagram for the SMS model TChiZZ.

In order to increase the simulated MC signal sample for multileptonic signatures one Z boson is forced to decay leptonically. Thus the TChiZZ is prone to produce 4L events with low H_T activity and high E_T^{miss}. The acceptance $\times$ efficiency for the signal and the 95% C.L. upper limit on the production cross section are presented in Fig. 9.15. The most sensitive channel is (4L, N($\tau = 0$), on-Z, $E_T^{\text{miss}} > 50\,\text{GeV}$ and $H_T < 200\,\text{GeV}$). For small mass splittings ($\Delta M \approx 100$ GeV) close to the border the E_T^{miss} distribution is shifted to lower values and the signal channel changes to $E_T^{\text{miss}} < 50\,\text{GeV}$ with higher SM background contributions. The upper limit on the production cross section is typically in the order of 0.5-1 pb. In comparison with the TChiWZ model discussed above, the upper limit is a factor $\approx$3 better, despite the worser selection efficiency. This is due to smaller background expectations in the 4L channels, which are the dominant signal channels for this model.

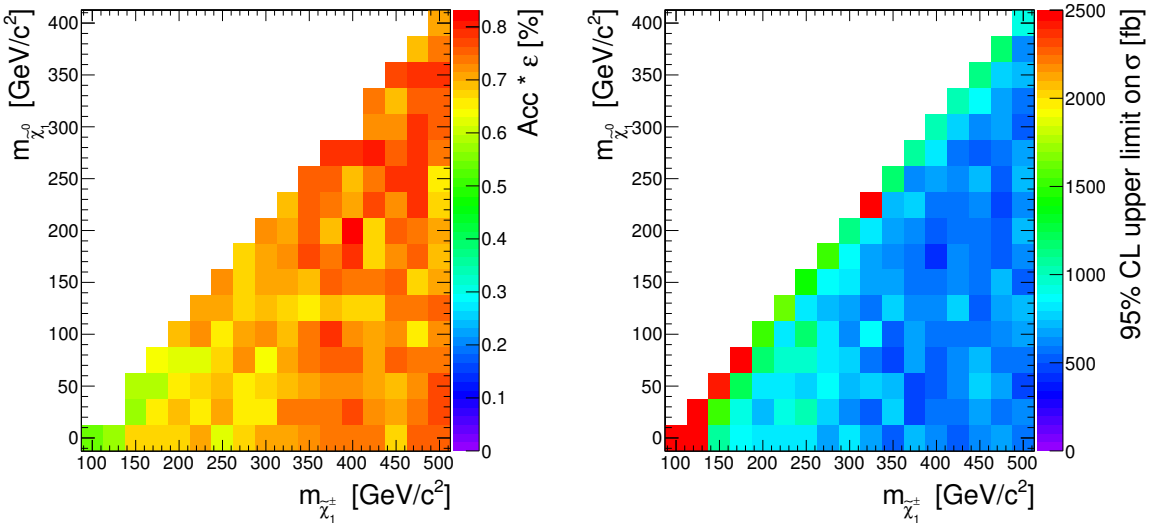

Figure 9.15: Acceptance × efficiency for the signal (left), and 95 C.L. upper limit on the production cross section (right) of the SMS model *TChiZZ*.

CHAPTER 10

Conclusion

Since the start of the LHC in 2009 an integrated luminosity $L_{int} = 4.7\,fb^{-1}$ of proton-proton collisions at a center-of-mass energy $\sqrt{s} = 7\,TeV$ has been recorded so far which allows to extend searches for physics beyond the SM far beyond regions in previous experiments. The multileptonic signatures including at least three leptons, either electrons, muons or taus, are often called *Golden Channels* due to the rare SM processes with multiple prompt leptons.

There are two types of SM processes for multileptonic searches: (i) The dominant irreducible background with three or more prompt leptons is formed by the double boson (WZ, ZZ incl.$\gamma*$) production with the subsequent decay to leptons. For each of these processes well defined control regions were investigated and good agreement between observations and expectations has been observed. A propagation of the background normalization determined in the control regions to H_T and/or E_T^{miss} signal regions yields large uncertainties up to 100%.

(ii) The dominant processes including fake leptons are Drell-Yan and $t\bar{t}$ with the subsequent decay to leptons plus an additional fake lepton, which can be either a fake electron, muon or tau. Fake leptons are predominantly produced in heavy flavor decays within jets. These can be suppressed by requiring leptons to be isolated from jet activity and associated to the primary vertex. A data driven method to predict the fake background was defined using the isolation side-band to predict the fake contributions in the signal region. An overall good agreement between data and the fake background predictions has been observed. An additional fake lepton background comes from initial/final state radiated photons converting into two leptons. Two kinds of photon conversions have been observed: (1) external conversion, where the photon interacts with the detector material and converts into an electron-positron pair and (2) internal conversion, where the conversion happens at the matrix element level in which case the decay into a muon pair has a similar branching as into electrons. A large fraction of the photon conversions into leptons, either external or internal, is asymmetric in p_T, so one lepton may fail the p_T cut and the 4L event is reconstructed as a 3L event. Those backgrounds can be suppresses by a requirement on the three body mass to be outside the Z mass window. A conservative systematic uncertainty on the remaining tails of 50% (100% internal conversion) has been assigned.

In total 48 exclusive channels have been examined. The events get classified by their jet activity H_T $\gtrless$ 200 GeV and missing transverse energy $E_T^{\text{miss}} \gtrless 50$ GeV. This classification accounts for different SUSY production modes like strong production via squarks and gluino or direct electroweak production of neutralinos and charginos. Furthermore the events get ordered by the number of hadronic tau candidates $N(\tau_h) = 0, 1, 2$, because with more hadronic tau decays the SM background rapidly rises. In addition tau final states can be enhanced in many SUSY models, especially for higher values of $tan\beta$ where the stau becomes lighter. Finally, the classification in multilepton events with and without a Z boson allows additional control of the dominant backgrounds.
The results presented in this thesis were also significant contributions to the official results published by the CMS collaboration [171]. In preparation for this publication a series of internal CMS notes have been published [172–181].
A good agreement between observations and expectations in channels dominated by SM processes has been seen. Some channels exhibit some tension: (I) two four lepton events in channels with particular low SM expectations, (II) 1.68σ deviation in one $N(\tau) = 1$ channel and (III) a smaller deviation of 1.27σ in a three lepton channel ($N(\tau) = 0$).
However given the probability for a statistical 2σ fluctuation in the measured cross sections in as many as 48 exclusive channels, the observation of the measured deviations above is expected. In spite of large systematic uncertainties more data and improved methods have to be incorporated in future studies to finally explain the observed deviations.
The overall observation is in agreement with the SM expectations within errors. Given the fact that there is no evidence for Physics Beyond the SM an upper limit on the $\sigma_{Prod.} \times BR(\geq 3l) \times \epsilon_{ac} \times \epsilon_{sel}$ can be set, where $\sigma_{Prod.}$ is the production cross section, $BR(\geq 3l)$ the branching fraction into three or more leptons, ϵ_{ac} the detector acceptance and ϵ_{sel} the selection efficiency for a particular SUSY model. This upper limit can be translated into an excluded region in the MSSM parameter space. Several different SUSY models have been investigated: (a) the gravity mediated SUSY breaking model cMSSM as a reference for previous results ($tan\beta = 10, 40$) and (b) three types of Simplified Model Spectra (SMS) including direct neutralino-chargino and neutralino-neutralino production sensitive to multileptonic signatures. In case of the cMSSM the excluded regions of previous experiments have been extended already with the first $L_{\text{int}} = 35\,\text{pb}^{-1}$ [182] and improvements including advanced background methods and control regions with the full data set of $L_{\text{int}} = 4.7\,\text{fb}^{-1}$ allow to exclude $m_{1/2} < 200$ GeV over a wide range of m_0 values. This corresponds to excluded gluino masses of $m_{\tilde{g}} \leq 500$ GeV.

Appendices

APPENDIX A

DATA and MC Samples

Table A.1: List of MC samples used in this study. The cross section and number of simulated events are given. Measured cross sections are used if available otherwise NLO calculations done with MCFM or Prospino in case of SUSY benchmark models are used. The ZZ+Jets including also $\gamma*$ and DY+Jets with additional internal conversions are simulated privately, due to insufficient official samples available so far.

MC sample	cross section [pb]	Sim Nevents
Summer11 Madgraph		
WJetsToLNu_TuneZ2_7TeV-madgraph-tauola	31314 pb	$45 \cdot 10^7$
DYJetsToLL_TuneZ2_M-10-50_7TeV-madgraph-tauola	11842 pb	$1.8 \cdot 10^7$
DYJetsToLL_TuneZ2_M-50_7TeV-madgraph-tauola	3050 pb	$3.5 \cdot 10^7$
TTJets_TuneZ2_7TeV-madgraph-tauola	168 pb	$3 \cdot 10^6$
WZJetsTo3LNu_TuneZ2_7TeV-madgraph-tauola	0.64 pb	$1.2 \cdot 10^6$
ZZJetsTo4L_TuneZ2_7TeV-madgraph-tauola	0.064 pb	$3 \cdot 10^5$
ZGToEEG_TuneZ2_7TeV-madgraph	42.7 pb	$3 \cdot 10^5$
ZGToMuMuG_TuneZ2_7TeV-madgraph	41.9 pb	$3 \cdot 10^5$
ZGToTauTauG_TuneZ2_7TeV-madgraph-tauola	38,4 pb	$3 \cdot 10^5$
WWJetsTo2L2Nu_TuneZ2_7TeV-madgraph-tauola	2.9 pb	$1.2 \cdot 10^6$
WWPhoton_TuneZ2_7TeV-madgraph	0.18 pb	$5.5 \cdot 10^4$
TTW_TuneZ2_7TeV-madgraph	0.16 pb	$9 \cdot 10^5$
TTZ_TuneZ2_7TeV-madgraph	0.14 pb	$2.5 \cdot 10^5$
Private Madgraph Ntuples		
$ZZ + 0, 1, 2$ Jets (including $\gamma*$)	0.2 pb	$2 \cdot 10^5$
Signal benchmark models (m_0, $m_{1/2}$, $tan\beta$, A_0, $sign(\mu)$)		
LM6 (85, 400, 10, 0, +1)	0.28 pb (0.5 pb NLO)	$4 \cdot 10^5$
LM9 (1450, 175, 50, 0, +1)	4.1 pb (7.1 pb NLO)	$4 \cdot 10^5$

Table A.2: List of data samples and the corresponding integrated luminosity used in this study. Data samples used within the trigger study are listed as well.

Data sample	Integrated luminosity
Data streams Run2011A	
/SingleMu/Run2011A-May10ReReco-v1/AOD	$200\,\mathrm{pb}^{-1}$
/SingleMu/Run2011A-05Aug2011-v1/AOD	$357\,\mathrm{pb}^{-1}$
/SingleMu/Run2011A-PromptReco-v4/AOD	$886\,\mathrm{pb}^{-1}$
/SingleMu/Run2011A-PromptReco-v6/AOD	$642\,\mathrm{pb}^{-1}$
/SingleElectron/Run2011A-May10ReReco-v1/AOD	$204\,\mathrm{pb}^{-1}$
/SingleElectron/Run2011A-05Aug2011-v1/AOD	$357\,\mathrm{pb}^{-1}$
/SingleElectron/Run2011A-PromptReco-v4/AOD	$886\,\mathrm{pb}^{-1}$
/SingleElectron/Run2011A-PromptReco-v6/AOD	$642\,\mathrm{pb}^{-1}$
/DoubleMu/Run2011A-May10ReReco-v1/AOD	$204\,\mathrm{pb}^{-1}$
/DoubleMu/Run2011A-05Aug2011-v1/AOD	$357\,\mathrm{pb}^{-1}$
/DoubleMu/Run2011A-PromptReco-v4/AOD	$886\,\mathrm{pb}^{-1}$
/DoubleMu/Run2011A-PromptReco-v6/AOD	$642\,\mathrm{pb}^{-1}$
/DoubleElectron/Run2011A-May10ReReco-v1/AOD	$204\,\mathrm{pb}^{-1}$
/DoubleElectron/Run2011A-05Aug2011-v1/AOD	$357\,\mathrm{pb}^{-1}$
/DoubleElectron/Run2011A-PromptReco-v4/AOD	$886\,\mathrm{pb}^{-1}$
/DoubleElectron/Run2011A-PromptReco-v6/AOD	$642\,\mathrm{pb}^{-1}$
/MuEG/Run2011A-May10ReReco-v1/AOD	$204\,\mathrm{pb}^{-1}$
/MuEG/Run2011A-05Aug2011-v1/AOD	$357\,\mathrm{pb}^{-1}$
/MuEG/Run2011A-PromptReco-v4/AOD	$886\,\mathrm{pb}^{-1}$
/MuEG/Run2011A-PromptReco-v6/AOD	$642\,\mathrm{pb}^{-1}$
Data streams Run2011B	
/SingleMu/Run2011B-PromptReco-v1/AOD	$2579\,\mathrm{pb}^{-1}$
/SingleElectron/Run2011B-PromptReco-v1/AOD	$2579\,\mathrm{pb}^{-1}$
/DoubleMu/Run2011B-PromptReco-v1/AOD	$2579\,\mathrm{pb}^{-1}$
/DoubleElectron/Run2011B-PromptReco-v1/AOD	$2579\,\mathrm{pb}^{-1}$
/MuEG/Run2011B-PromptReco-v1/AOD	$2579\,\mathrm{pb}^{-1}$
Data streams used for trigger study	
/HT/Run2011A-May10ReReco-v1/AOD	$204\,\mathrm{pb}^{-1}$
/HT/Run2011A-05Aug2011-v1/AOD	$357\,\mathrm{pb}^{-1}$
/HT/Run2011A-PromptReco-v4/AOD	$886\,\mathrm{pb}^{-1}$
/HT/Run2011A-PromptReco-v6/AOD	$642\,\mathrm{pb}^{-1}$
/HT/Run2011B-PromptReco-v1/AOD	$2579\,\mathrm{pb}^{-1}$

APPENDIX B

Private Madgraph Production

In this section the production of the private Madgraph sample will be discussed and a validation with official centrally produced samples are shown if possible. Two samples were produced privately to compensate too hard generator cuts in MC samples available so far.

B.1 $ZZ + 0, 1, 2$ Jets including $\gamma*$ and Internal Photon Conversions

The process to re-generate is the double boson production ZZ+Jets including also $\gamma*$ events and by doing so also internal photon conversions are included as well. The official Madgraph sample was produced with an internal generator cut on the invariant mass of all opposite sign same flavor lepton pairs $m_{ll} > 50\,\mathrm{GeV/c^2}$, which suppresses $\gamma*$ processes, internal photon conversion and off-shell Zs as well. Since the event selection is based on the splitting into on-Z and off-Z (see Section 7.5) and a fully data driven prediction of those processes is not possible due to lack of recoreded events so far, it is crucial to have a simulation covering the full phase space. For this purpose MadEvent/Madgraph5 [93] is used with following proc_card_mg5.dat:

```
#************************************************************
#*                        MadGraph 5                        *
#*                                                          *
#*                 *                       *                *
#*                   *         * *         *                *
#*                     * * * * 5 * * * *                    *
#*                   *         * *         *                *
#*                 *                       *                *
#*                                                          *
#*                                                          *
#*          VERSION 1.1.0.                2011-01-21        *
#*                                                          *
#*     The MadGraph Development Team - Please visit us at   *
#*     https://server06.fynu.ucl.ac.be/projects/madgraph    *
#*                                                          *
#************************************************************
```

```
#*                                                           *
#*               Command File for MadGraph 5                 *
#*                                                           *
#*     run as ./bin/mg5  filename                            *
#*                                                           *
#*     automaticaly generated the Tue Feb  8 11:44:43 2011   *
#*                                                           *
#************************************************************

import model sm
# Define multiparticle labels
define p u c d b s u~ c~ d~ b~ s~ g
define j = p
define l- =  e- mu- ta-
define l+ =  e+ mu+ ta+
# Specify process(es) to run
generate p p > l+ l- l+ l-  /t h
add process p p > l+ l- l+ l- j /t h
add process p p > l+ l- l+ l- j j /t h
# Output processes to MadEvent directory
output -f
```

The proper generation of internal conversion depends strongly on the generator cuts defined for the production. Dilepton processes with internal photon conversion contribute to the 3L channels, if the photon converts asymmetric, since one lepton is softer and fails the selection criteria. In order to not suppress such processes the transverse momentum p_T threshold of the fourth lepton (two from $Z/\gamma*$ and two from photon conversion) has been set as low as possible. Since the option to set different thresholds on individual leptons is not implemented in Madgraph5 so far, the overall threshold has to be set as low as possible, namely 0.

```
#*********************************************************************
#                       MadGraph/MadEvent                            *
#                   http://madgraph.hep.uiuc.edu                     *
#                                                                    *
#                        run_card.dat                                *
#                                                                    *
#  This file is used to set the parameters of the run.               *
#                                                                    *
#  Some notation/conventions:                                        *
#                                                                    *
#   Lines starting with a '# ' are info or comments                  *
#                                                                    *
#   mind the format:   value    = variable     ! comment             *
#*********************************************************************
#
#*******************
# Running parameters
#*******************
#
#*********************************************************************
# Tag name for the run (one word)                                    *
#*********************************************************************
  'fermi'     = run_tag ! name of the run
#*********************************************************************
# Run to generate the grid pack                                      *
```

```
#*********************************************************************
  .true.     = gridpack  !True = setting up the grid pack
#*********************************************************************
# Number of events and rnd seed                                      *
# Warning: Do not generate more than 100K event in a single run      *
#*********************************************************************
   1000       = nevents ! Number of unweighted events requested
      0       = iseed   ! rnd seed (0=assigned automatically=default))
#*********************************************************************
# Collider type and energy                                           *
#*********************************************************************
        1     = lpp1  ! beam 1 type (0=NO PDF)
        1     = lpp2  ! beam 2 type (0=NO PDF)
     3500     = ebeam1  ! beam 1 energy in GeV
     3500     = ebeam2  ! beam 2 energy in GeV
#*********************************************************************
# Beam polarization from -100 (left-handed) to 100 (right-handed)    *
#*********************************************************************
        0     = polbeam1 ! beam polarization for beam 1
        0     = polbeam2 ! beam polarization for beam 2
#*********************************************************************
# PDF CHOICE: this automatically fixes also alpha_s and its evol.    *
#*********************************************************************
 'cteq6l1'    = pdlabel     ! PDF set
#*********************************************************************
# Renormalization and factorization scales                           *
#*********************************************************************
 F        = fixed_ren_scale  ! if .true. use fixed ren scale
 F        = fixed_fac_scale  ! if .true. use fixed fac scale
 91.1880  = scale            ! fixed ren scale
 91.1880  = dsqrt_q2fact1    ! fixed fact scale for pdf1
 91.1880  = dsqrt_q2fact2    ! fixed fact scale for pdf2
 1        = scalefact        ! scale factor for event-by-event scales
#*********************************************************************
# Matching - Warning! ickkw > 1 is still beta
#*********************************************************************
 1        = ickkw            ! 0 no matching, 1 MLM, 2 CKKW matching
 1        = highestmult      ! for ickkw=2, highest mult group
 1        = ktscheme         ! for ickkw=1, 1 Durham kT, 2 Pythia pTE
 1        = alpsfact         ! scale factor for QCD emission vx
 F        = chcluster        ! cluster only according to channel diag
 T        = pdfwgt           ! for ickkw=1, perform pdf reweighting
#*********************************************************************
# Automatic ptj and mjj cuts if xqcut > 0
# (turn off for VBF and single top processes)
#*********************************************************
   T  = auto_ptj_mjj  ! Automatic setting of ptj and mjj
#*********************************************************
#
#*********************************
# BW cutoff (M+/-bwcutoff*Gamma)
#*********************************
  100  = bwcutoff      ! (M+/-bwcutoff*Gamma)
#*********************************************************
# Apply pt/E/eta/dr/mij cuts on decay products or not
# (note that etmiss/ptll/ptheavy/ht/sorted cuts always apply)
#*********************************************************
```

```
   T  = cut_decays    ! Cut decay products
#*********************************************************
# Number of helicities to sum per event (0 = all helicities)
# 0 gives more stable result, but longer run time (needed for
# long decay chains e.g.).
# Use >=2 if most helicities contribute, e.g. pure QCD.
#*********************************************************
   0  = nhel          ! Number of helicities used per event
#******************
# Standard Cuts
#******************
#
#*********************************************************************
# Minimum and maximum pt's                                           *
#*********************************************************************
 10  = ptj       ! minimum pt for the jets
 10  = ptb       ! minimum pt for the b
 10  = pta       ! minimum pt for the photons
  0  = ptl       ! minimum pt for the charged leptons
  0  = misset    ! minimum missing Et (sum of neutrino's momenta)
  0  = ptheavy   ! minimum pt for one heavy final state
1.0 = ptonium   ! minimum pt for the quarkonium states
1d5 = ptjmax    ! maximum pt for the jets
1d5 = ptbmax    ! maximum pt for the b
1d5 = ptamax    ! maximum pt for the photons
1d5 = ptlmax    ! maximum pt for the charged leptons
1d5 = missetmax ! maximum missing Et (sum of neutrino's momenta)
#*********************************************************************
# Minimum and maximum E's (in the lab frame)                         *
#*********************************************************************
  0  = ej     ! minimum E for the jets
  0  = eb     ! minimum E for the b
  0  = ea     ! minimum E for the photons
  0  = el     ! minimum E for the charged leptons
1d5  = ejmax ! maximum E for the jets
1d5  = ebmax ! maximum E for the b
1d5  = eamax ! maximum E for the photons
1d5  = elmax ! maximum E for the charged leptons
#*********************************************************************
# Maximum and minimum rapidity                                       *
#*********************************************************************
   5  = etaj    ! max rap for the jets
 1d2  = etab    ! max rap for the b
   5  = etaa    ! max rap for the photons
   5  = etal    ! max rap for the charged leptons
 0.6  = etaonium ! max rap for the quarkonium states
 0d0  = etajmin ! min rap for the jets
 0d0  = etabmin ! min rap for the b
 0d0  = etaamin ! min rap for the photons
 0d0  = etalmin ! main rap for the charged leptons
#*********************************************************************
# Minimum and maximum DeltaR distance                                *
#*********************************************************************
 0.1 = drjj    ! min distance between jets
 0   = drbb    ! min distance between b's
 0.1 = drll    ! min distance between leptons
 0.1 = draa    ! min distance between gammas
```

```
 0   = drbj    ! min distance between b and jet
 0.1 = draj    ! min distance between gamma and jet
 0.1 = drjl    ! min distance between jet and lepton
 0   = drab    ! min distance between gamma and b
 0   = drbl    ! min distance between b and lepton
 0.1 = dral    ! min distance between gamma and lepton
 1d2 = drjjmax ! max distance between jets
 1d2 = drbbmax ! max distance between b's
 1d2 = drllmax ! max distance between leptons
 1d2 = draamax ! max distance between gammas
 1d2 = drbjmax ! max distance between b and jet
 1d2 = drajmax ! max distance between gamma and jet
 1d2 = drjlmax ! max distance between jet and lepton
 1d2 = drabmax ! max distance between gamma and b
 1d2 = drblmax ! max distance between b and lepton
 1d2 = dralmax ! maxdistance between gamma and lepton
#*********************************************************************
# Minimum and maximum invariant mass for pairs                       *
#*********************************************************************
 0   = mmjj    ! min invariant mass of a jet pair
 0   = mmbb    ! min invariant mass of a b pair
 0   = mmaa    ! min invariant mass of gamma gamma pair
 5   = mmll    ! min invariant mass of l+l- (same flavour) lepton pair
 1d5 = mmjjmax ! max invariant mass of a jet pair
 1d5 = mmbbmax ! max invariant mass of a b pair
 1d5 = mmaamax ! max invariant mass of gamma gamma pair
 1d5 = mmllmax ! max invariant mass of l+l- (same flavour) lepton pair
#*********************************************************************
# Minimum and maximum invariant mass for all letpons                 *
#*********************************************************************
 0   = mmnl    ! min invariant mass for all letpons (l+- and vl)
 1d5 = mmnlmax ! max invariant mass for all letpons (l+- and vl)
#*********************************************************************
# Minimum and maximum pt for 4-momenta sum of leptons                *
#*********************************************************************
 0   = ptllmin  ! Minimum pt for 4-momenta sum of leptons(l and vl)
 1d5 = ptllmax  ! Maximum pt for 4-momenta sum of leptons(l and vl)
#*********************************************************************
# Inclusive cuts                                                     *
#*********************************************************************
 0  = xptj ! minimum pt for at least one jet
 0  = xptb ! minimum pt for at least one b
 0  = xpta ! minimum pt for at least one photon
 0  = xptl ! minimum pt for at least one charged lepton
#*********************************************************************
# Control the pt's of the jets sorted by pt                          *
#*********************************************************************
 0   = ptj1min ! minimum pt for the leading jet in pt
 0   = ptj2min ! minimum pt for the second jet in pt
 0   = ptj3min ! minimum pt for the third jet in pt
 0   = ptj4min ! minimum pt for the fourth jet in pt
 1d5 = ptj1max ! maximum pt for the leading jet in pt
 1d5 = ptj2max ! maximum pt for the second jet in pt
 1d5 = ptj3max ! maximum pt for the third jet in pt
 1d5 = ptj4max ! maximum pt for the fourth jet in pt
 0   = cutuse  ! reject event if fails any (0) / all (1) jet pt cuts
#*********************************************************************
```

```
# Control the Ht(k)=Sum of k leading jets                              *
#*********************************************************************
 0   = htjmin ! minimum jet HT=Sum(jet pt)
 1d5 = htjmax ! maximum jet HT=Sum(jet pt)
 0   = ihtmin  !inclusive Ht for all partons (including b)
 1d5 = ihtmax  !inclusive Ht for all partons (including b)
 0   = ht2min ! minimum Ht for the two leading jets
 0   = ht3min ! minimum Ht for the three leading jets
 0   = ht4min ! minimum Ht for the four leading jets
 1d5 = ht2max ! maximum Ht for the two leading jets
 1d5 = ht3max ! maximum Ht for the three leading jets
 1d5 = ht4max ! maximum Ht for the four leading jets
#*********************************************************************
# WBF cuts                                                            *
#*********************************************************************
 0   = xetamin ! minimum rapidity for two jets in the WBF case
 0   = deltaeta ! minimum rapidity for two jets in the WBF case
#*********************************************************************
# maximal pdg code for quark to be considered as a light jet          *
# (otherwise b cuts are applied)                                      *
#*********************************************************************
 5 = maxjetflavor    ! Maximum jet pdg code
#*********************************************************************
# Jet measure cuts                                                    *
#*********************************************************************
 0   = xqcut   ! minimum kt jet measure between partons
#*********************************************************************
```

An invariant mass cut of m_{ll} is sensitive to the internal conversion predictions as shown in Fig. B.1. For these events the invariant mass of all leptons with $p_T > 3\,\text{GeV}$ was required to be inside the Z-mass window as expected for FSR plus internal conversion. One observes a strong increase in the number of events if the cut is lowered from the default of $12\,\text{GeV/c}^2$ to $5\,\text{GeV/c}^2$. This implies, that a substantial part of the background is still suppressed and has to be corrected for.

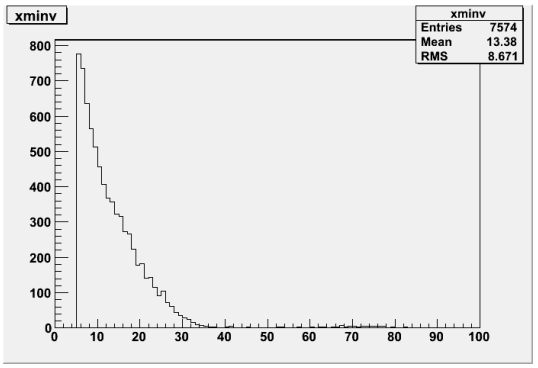

Figure B.1: Invariant mass pair m_{ll} of the two lepton from internal photon conversion on generator level in the privatly produced ZZ MC including DY events with FSR followed by internal photon conversion

APPENDIX C

Trigger Efficiency

The trigger efficieny of all used trigger paths in the various runs are presented for Single-Muon triggers in Fig. C.1, Single-Electron triggers in Fig. C.2, Doube-Electron trigger in Fig. C.3, Double-Muon trigger in Fig. C.4 and Electron-Muon cross trigger in Fig. C.5 measured in a H_T triggered data sample. In Table C.1 the measured trigger efficiencies are summarized.

Table C.1: Summary of the trigger efficiencies measured in H_T triggered data samples. The errors correspond to the statistical errors of the data sample. Throughout the different runs recorded in 2011 the trigger thresholds and trigger object requirements changed and hence various trigger paths have been used.

Trigger path	Trigger efficiency
Muon triggers	
HLT_IsoMu30_eta2p1	0.768 ± 0.02
HLT_IsoMu30	0.788 ± 0.02
HLT_IsoMu24	0.791 ± 0.02
HLT_IsoMu17	0.798 ± 0.03
HLT_Mu40_eta2p1	0.906 ± 0.02
HLT_Mu40	0.897 ± 0.02
HLT_Mu24	0.898 ± 0.04
HLT_Mu20	0.879 ± 0.09
HLT_Mu17_Mu8	0.907 ± 0.04
HLT_Mu13_Mu8	0.907 ± 0.04
Electron triggers	
HLT_Ele80_CaloIdVT_TrkIdT	0.917 ± 0.06
HLT_Ele65_CaloIdVT_TrkIdT	0.904 ± 0.02
HLT_Ele52_CaloIdVT_TrkIdT	0.896 ± 0.02
HLT_Ele45_CaloIdVT_TrkIdT	0.879 ± 0.03
HLT_Ele17_CaloIdL_CaloIsoVL...	0.993 ± 0.02
..._Ele8_CaloIdL_CaloIsoVL	
HLT_Ele17_CaloIdT_CaloIsoVL_TrkIdVL_TrkIsoVL...	0.970 ± 0.02
..._Ele8_CaloIdT_CaloIsoVL_TrkIdVL_TrkIsoVL	
HLT_Ele17_CaloIdT_TrkIdVL_CaloIsoVL_TrkIsoVL...	0.991 ± 0.02
..._Ele8_CaloIdT_TrkIdVL_CaloIsoVL_TrkIsoVL	
Electron-Muon-Crosstriggers	
HLT_Mu8_Ele17_CaloIdT_CaloIsoVL	0.940 ± 0.05
HLT_Mu8_Ele17_CaloIdL	0.934 ± 0.09
HLT_Mu17_Ele8_CaloIdT_CaloIsoVL	0.918 ± 0.06
HLT_Mu17_Ele8_CaloIdL	0.917 ± 0.08

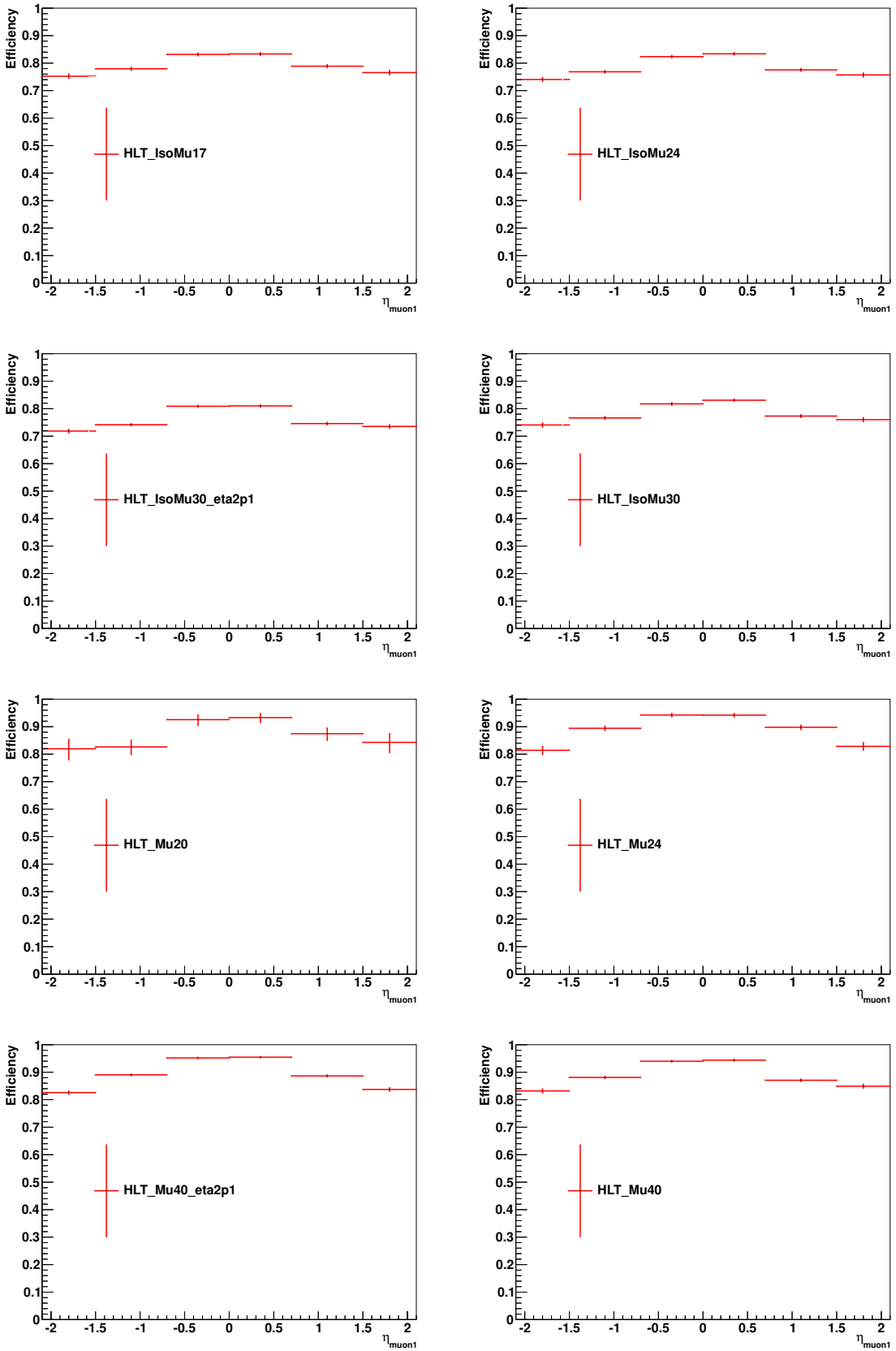

Figure C.1: Single-Muon trigger efficiency as a function of the muon pseudo rapidity η. The muon is required to pass all selection criteria given in Section 7.3.1 with increased transverse momentum threshold.

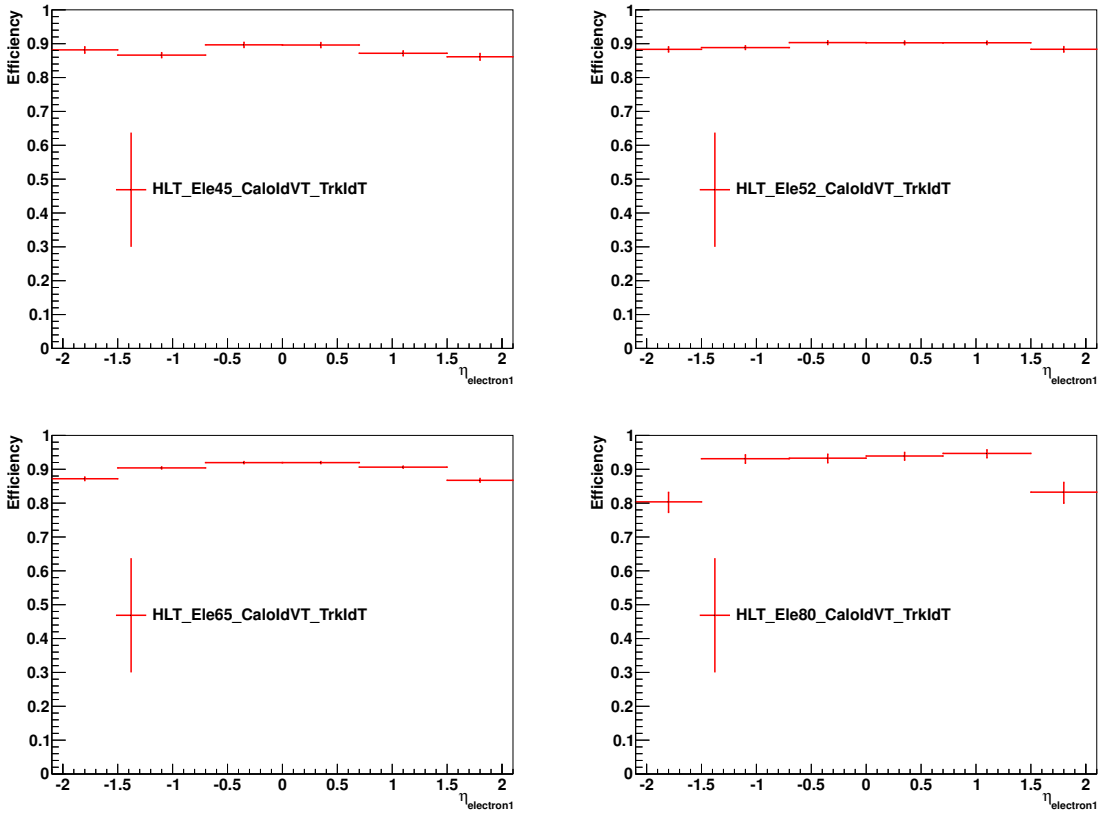

Figure C.2: Single-Electron trigger efficiency as a function of the electron pseudo rapidity η. The electron is required to pass all selection criteria given in Section 7.3.1 with increased transverse momentum threshold.

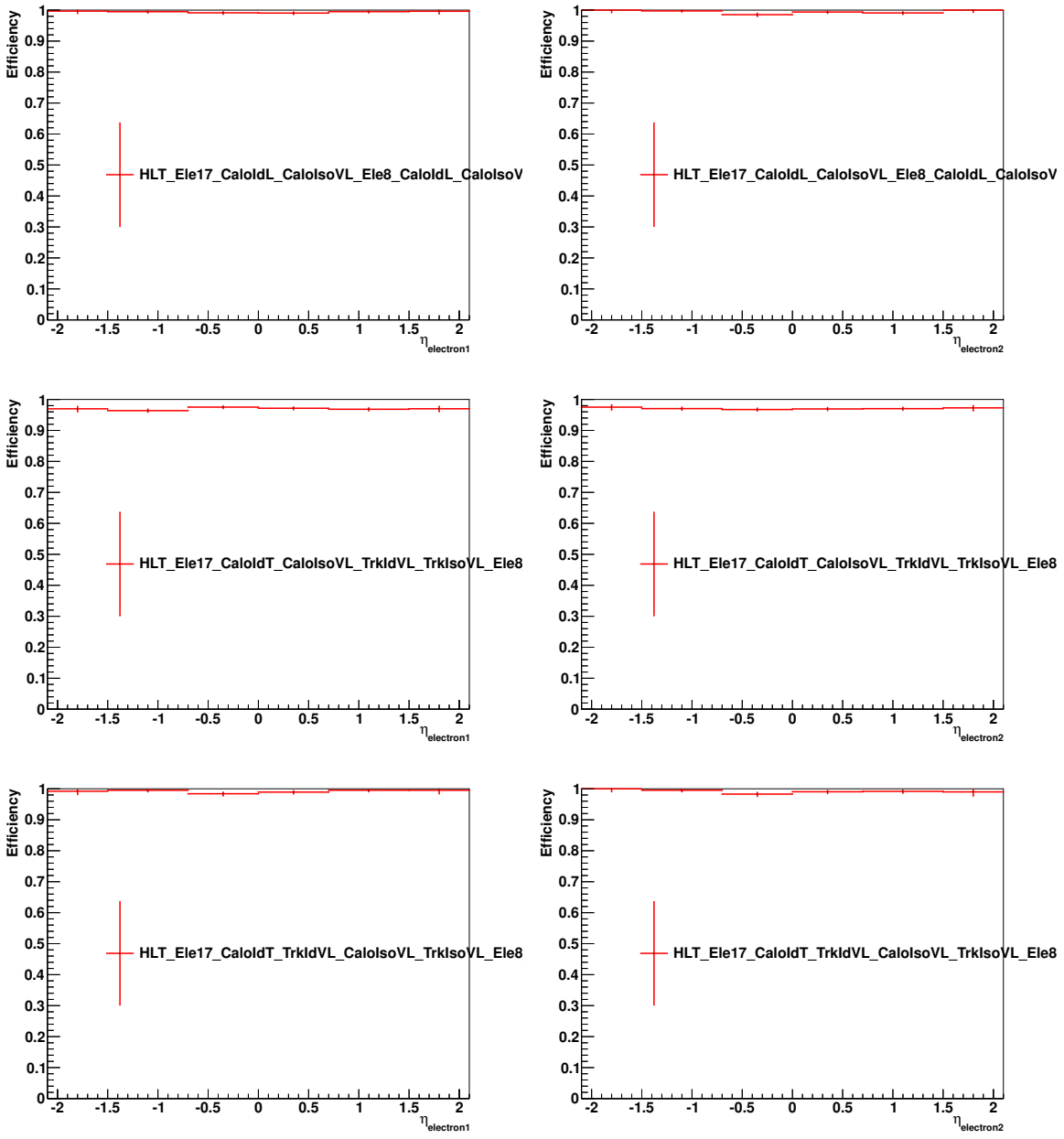

Figure C.3: Double-Electron trigger efficiency as a function of η of the leading (left) and second leading (right) electron. The electrons are required to pass all selection criteria given in Section 7.3.1 with increased transverse momentum threshold.

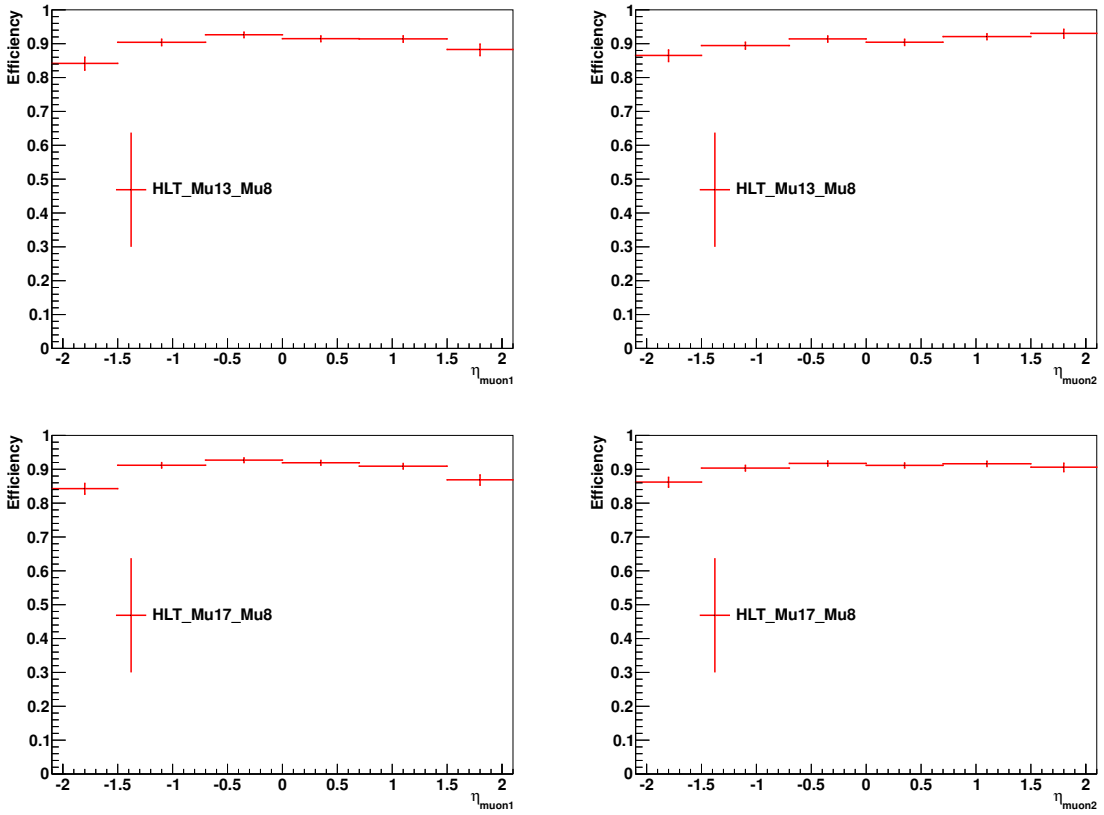

Figure C.4: Double-Muon trigger efficiency as a function of η of the leading (left) and second leading (right) muon. The muons are required to pass all selection criteria given in Section 7.3.1 with increased transverse momentum threshold.

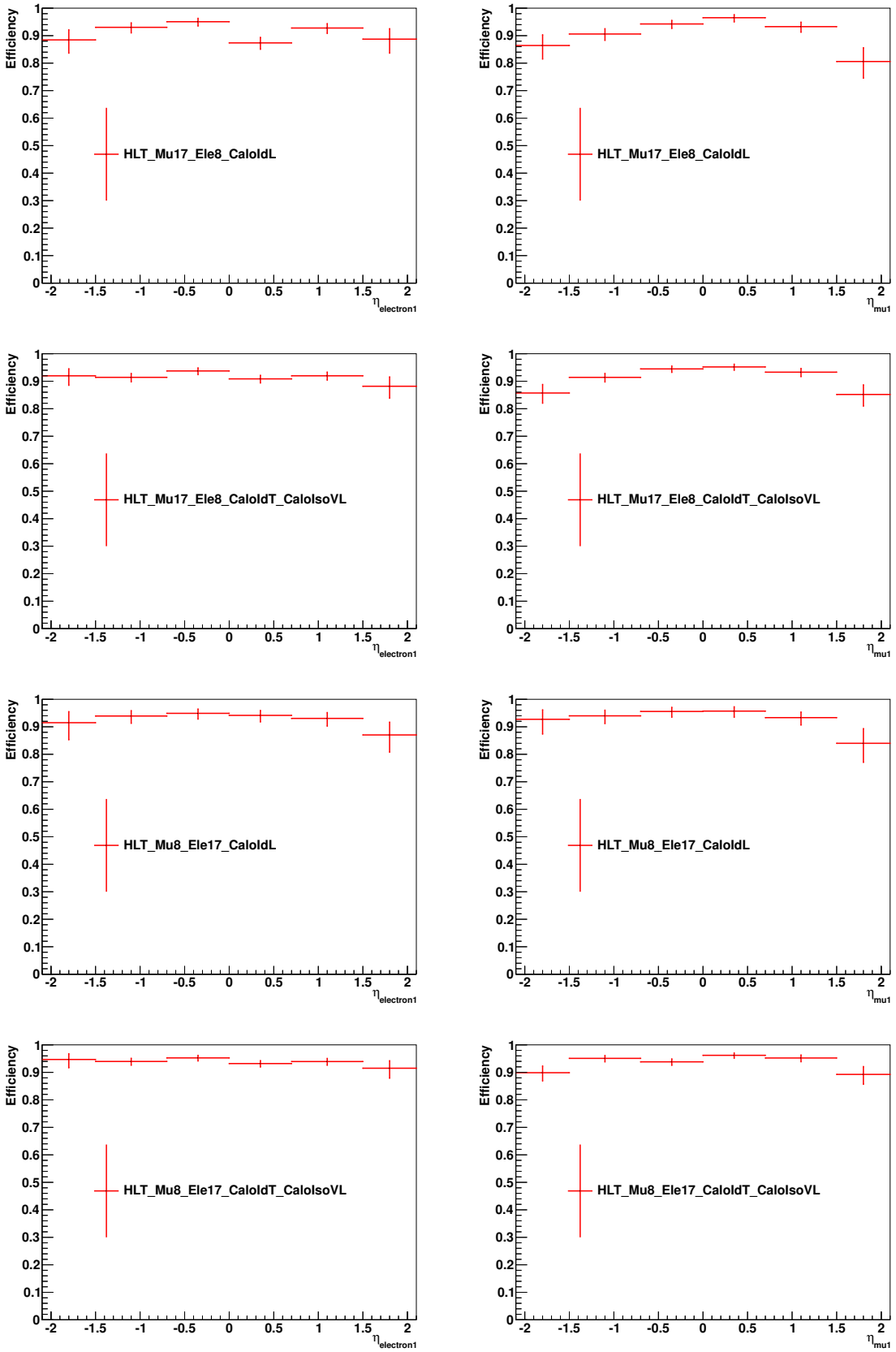

Figure C.5: Electron-Muon cross trigger efficiency as a function of η of the electron (left) or muon (right). The leptons are required to pass all selection criteria given in Section 7.3.1 with increased transverse momentum thresholds.

APPENDIX D

Vertex Reweighting

In Section 7.2 the pile up reweighting technique used in this study was discussed. Let's consider the impact of the vertex reweighting on the final result table. Since the final table is inclusive in E_T^{miss} , i.e. E_T^{miss} >50 GeV and E_T^{miss} <50 GeV is considered both, the total number of predicted events should not depend on the number of vertices in simulation, because the difference in vertex multiplicity only affects the shape of the E_T^{miss} distribution. The same counts for the prediction in subchannels which are split in E_T^{miss} e.g. on-Z, H_T >200 GeV, E_T^{miss} <50 GeV and E_T^{miss} >50 GeV. In order to guarantee that the total number of events in each channel is conserved, for each MC sample and subchannel a weighting factor has to be calculated. In Fig. D.1 the E_T^{miss} disribution of events selected with two tight leptons OS-SF forming an invariant mass consistent with the Z mass and a third loose lepton (e, μ, τ_h) with and without pile up reweighting is shown. Clearly, the reweigting is important for an improved description of E_T^{miss} .
Since the MC statistics in some subchannels is too small (<10 events) to allow for a meaningful calculation of weighting factor, the MC prediction in such channels is instead assigned with an extra 75% uncertainty corresponding to the maximum deviation in the E_T^{miss} distributions.

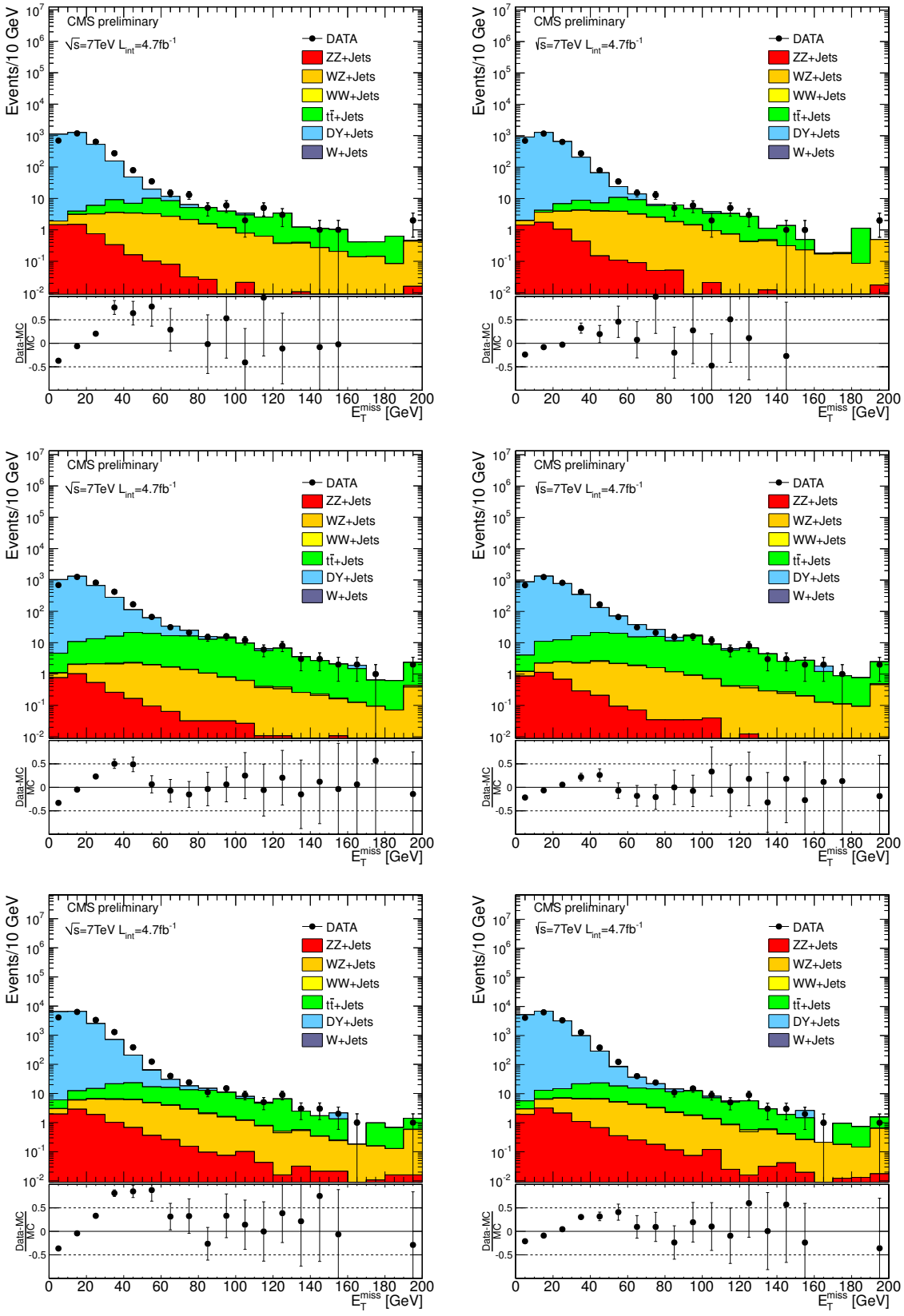

Figure D.1: E_T^{miss} distribution for events with two tight leptons OS-SF forming an invariant mass consistent with the Z mass and a third loose lepton (e (top), μ (middle), τ_h (bottom)) with (right) and without (left) pile up reweighting.

APPENDIX E

Detailed Result Tables

Table E.1: Results split in electron and muon flavors corresponding to an integrated luminosity $L_{int} = 4.7\,fb^{-1}$ recorded in 2011. The selection labels refer to whether there is an OS-SF lepton pair with a mass (in)consistent with the Z mass (off/on-Z) or not (no-OSSF), and the H_T and E_T^{miss} requirements. Four 4L N(τ)=0 channels of Table 9.1 are shown: (top block) off-Z, HT>200, MET>50; (second block) on-Z, HT>200, MET>50; (third block) off-Z, HT>200, MET<50 and (bottom block) on-Z HT>200 MET<50. The SM expectation is split into single processes (second to fifths columns). The total SM expectations and observations are given in the six and seventh columns and the signal expectations for the SUSY LM9 benchmark point in the last column. If given value is "$-$" no expectation for the process are given due to limited MC statistics.

Channel	DYJets	WZJets	TTJets	Rare	ZZ(incG)	SumSM	Data	LM9
N(τ)=0; 4 Leptons; OFF Z; HT>200; MET>50;								
$eeee$	-	-	-	-	-	-	0	-
$eee\mu$	-	-	-	0.008 ± 0.010	-	0.008 ± 0.010	0	0.209 ± 0.157
$ee\mu\mu$	-	-	-	0.022 ± 0.028	0.002 ± 0.003	0.024 ± 0.028	0	0.233 ± 0.231
$e\mu\mu\mu$	-	0.006 ± 0.007	-	0.003 ± 0.003	-	0.009 ± 0.008	0	0.003 ± 0.003
$\mu\mu\mu\mu$	-	-	-	0.002 ± 0.003	-	0.002 ± 0.003	0	-
Sum:	-	0.006 ± 0.007	-	0.035 ± 0.034	0.002 ± 0.003	0.043 ± 0.035	0	0.675 ± 0.364
N(τ)=0; 4 Leptons; ON Z; HT>200; MET>50;								
$eeee$	-	-	-	0.014 ± 0.016	-	0.014 ± 0.016	0	0.047 ± 0.047
$eee\mu$	-	-	-	0.037 ± 0.039	0.006 ± 0.011	0.044 ± 0.041	0	0.006 ± 0.006
$ee\mu\mu$	-	-	-	0.032 ± 0.035	0.007 ± 0.012	0.039 ± 0.037	0	0.386 ± 0.275
$e\mu\mu\mu$	-	-	-	0.044 ± 0.047	-	0.044 ± 0.047	0	0.221 ± 0.171
$\mu\mu\mu\mu$	-	-	-	0.040 ± 0.042	0.012 ± 0.020	0.052 ± 0.047	0	-
Sum:	-	-	-	0.167 ± 0.171	0.026 ± 0.039	0.193 ± 0.176	0	0.660 ± 0.329
N(τ)=0; 4 Leptons; OFF Z; HT<200; MET>50;								
$eeee$	-	-	-	0.001 ± 0.002	-	0.001 ± 0.002	0	-
$eee\mu$	-	0.002 ± 0.002	-	0.005 ± 0.007	-	0.007 ± 0.007	1	-
$ee\mu\mu$	-	-	-	0.012 ± 0.013	0.015 ± 0.019	0.027 ± 0.024	0	0.303 ± 0.303
$e\mu\mu\mu$	-	0.002 ± 0.002	-	0.031 ± 0.032	-	0.033 ± 0.033	0	-
$\mu\mu\mu\mu$	-	-	-	0.008 ± 0.010	0.014 ± 0.018	0.021 ± 0.021	0	0.143 ± 0.140
Sum:	-	0.004 ± 0.003	-	0.057 ± 0.057	0.029 ± 0.035	0.090 ± 0.068	1	0.575 ± 0.360
N(τ)=0; 4 Leptons; ON Z; HT<200; MET>50;								
$eeee$	-	0.005 ± 0.005	-	0.028 ± 0.029	0.041 ± 0.045	0.074 ± 0.055	0	0.006 ± 0.006
$eee\mu$	-	0.001 ± 0.001	-	0.065 ± 0.068	0.074 ± 0.078	0.140 ± 0.105	0	-
$ee\mu\mu$	-	0.005 ± 0.005	-	0.062 ± 0.065	0.209 ± 0.217	0.276 ± 0.228	2	0.184 ± 0.184
$e\mu\mu\mu$	-	0.002 ± 0.002	-	0.066 ± 0.069	0.095 ± 0.101	0.163 ± 0.124	0	0.230 ± 0.186
$\mu\mu\mu\mu$	-	0.005 ± 0.005	-	0.046 ± 0.049	0.131 ± 0.137	0.181 ± 0.146	0	1.385 ± 0.761
Sum:	-	0.019 ± 0.010	-	0.268 ± 0.271	0.549 ± 0.565	0.836 ± 0.633	2	1.806 ± 0.806

Table E.2: Results split in electron and muon flavors corresponding to an integrated luminosity $L_{int} = 4.7\,fb^{-1}$ recorded in 2011. The selection labels refer to whether there is an OS-SF lepton pair with a mass (in)consistent with the Z mass (off/on-Z) or not (no-OSSF), and the H_T and E_T^{miss} requirements. Four 4L N(τ)=0 channels of Table 9.1 are shown: (top block) off-Z, HT>200, MET<50; (second block) on-Z, HT>200, MET<50; (third block) off-Z, HT<200, MET<50 and (bottom block) on-Z HT<200 MET<50. The SM expectation is split into single processes (second to fifths columns). The total SM expectations and observations are given in the six and seventh columns and the signal expectations for the SUSY LM9 benchmark point in the last column. If given value is "$-$" no expectation for the process are given due to limited MC statistics.

Channel	DYJets	WZJets	TTJets	Rare	ZZ(incG)	SumSM	Data	LM9
N(τ)=0; 4 Leptons; OFF Z; HT>200; MET<50;								
$eeee$	-	-	-	0.002 ± 0.003	-	0.002 ± 0.003	0	-
$eee\mu$	-	-	-	-	-	-	0	0.140 ± 0.140
$ee\mu\mu$	-	-	-	-	0.012 ± 0.017	0.012 ± 0.017	0	-
$e\mu\mu\mu$	-	-	-	0.001 ± 0.002	-	0.001 ± 0.002	0	0.194 ± 0.195
$\mu\mu\mu\mu$	-	-	-	-	0.013 ± 0.017	0.013 ± 0.017	0	-
Sum:	-	-	-	0.003 ± 0.004	0.025 ± 0.031	0.028 ± 0.032	0	0.334 ± 0.240
N(τ)=0; 4 Leptons; ON Z; HT>200; MET<50;								
$eeee$	-	-	-	0.005 ± 0.007	0.048 ± 0.055	0.053 ± 0.055	0	-
$eee\mu$	-	-	-	0.017 ± 0.020	0.007 ± 0.010	0.024 ± 0.022	0	-
$ee\mu\mu$	-	-	-	0.017 ± 0.019	0.142 ± 0.149	0.159 ± 0.151	0	-
$e\mu\mu\mu$	-	0.005 ± 0.006	-	0.024 ± 0.027	0.011 ± 0.014	0.041 ± 0.031	1	-
$\mu\mu\mu\mu$	-	-	-	0.005 ± 0.007	0.143 ± 0.150	0.148 ± 0.150	0	0.053 ± 0.053
Sum:	-	0.005 ± 0.006	-	0.068 ± 0.072	0.358 ± 0.372	0.432 ± 0.381	1	0.237 ± 0.192
N(τ)=0; 4 Leptons; OFF Z; HT<200; MET<50;								
$eeee$	-	-	-	-	0.300 ± 0.165	0.300 ± 0.165	0	-
$eee\mu$	-	-	-	0.002 ± 0.002	0.063 ± 0.040	0.065 ± 0.040	0	-
$ee\mu\mu$	-	0.004 ± 0.005	-	0.006 ± 0.007	1.378 ± 0.734	1.388 ± 0.734	0	-
$e\mu\mu\mu$	-	0.006 ± 0.006	-	0.002 ± 0.003	0.127 ± 0.075	0.135 ± 0.075	0	-
$\mu\mu\mu\mu$	-	-	-	0.007 ± 0.009	1.291 ± 0.688	1.299 ± 0.688	1	-
Sum:	-	0.010 ± 0.009	-	0.018 ± 0.017	3.166 ± 1.678	3.194 ± 1.678	1	-
N(τ)=0; 4 Leptons; ON Z; HT<200; MET<50;								
$eeee$	-	0.013 ± 0.008	-	0.016 ± 0.018	6.461 ± 1.343	6.490 ± 1.344	3	-
$eee\mu$	-	-	-	0.040 ± 0.043	0.264 ± 0.072	0.304 ± 0.084	1	-
$ee\mu\mu$	-	0.006 ± 0.005	-	0.033 ± 0.036	17.314 ± 3.568	17.353 ± 3.569	16	0.177 ± 0.178
$e\mu\mu\mu$	-	0.005 ± 0.005	-	0.030 ± 0.032	0.490 ± 0.120	0.525 ± 0.124	1	0.184 ± 0.184
$\mu\mu\mu\mu$	0.016 ± 0.018	0.011 ± 0.008	-	0.022 ± 0.024	12.034 ± 2.485	12.084 ± 2.486	11	0.177 ± 0.178
Sum:	0.016 ± 0.018	0.035 ± 0.014	-	0.141 ± 0.144	36.647 ± 7.531	36.839 ± 7.535	32	0.723 ± 0.363

Table E.3: Results split in electron and muon flavors corresponding to an integrated luminosity $L_{int} = 4.7\,fb^{-1}$ recorded in 2011. The selection labels refer to whether there is an OS-SF lepton pair with a mass (in)consistent with the Z mass (off/on-Z) or not (no-OSSF), and the H_T and E_T^{miss} requirements. Four 3L N(τ)=0 channels of Table 9.1 are shown: (top block) no-OSSF, HT>200, MET>50; (second block) no-OSSF, HT<200, MET>50; (third block) no-OSSF, HT>200, MET<50 and (bottom block) no-OSSF HT<200 MET<50. The SM expectation is split into single processes (second to fifths columns). The total SM expectations and observations are given in the six and seventh columns and the signal expectations for the SUSY LM9 benchmark point in the last column. If given value is "$-$" no expectation for the process are given due to limited MC statistics.

Channel	DYJets	WZJets	TTJets	Rare	ZZ(incG)	SumSM	Data	LM9
N(τ)=0; 3 Leptons; no-OSSF; HT>200; MET>50;								
eee	-	0.017 ± 0.016	-	0.010 ± 0.011	-	0.027 ± 0.019	0	-
$ee\mu$	-	0.199 ± 0.149	-	0.169 ± 0.126	-	0.368 ± 0.199	1	0.489 ± 0.284
$e\mu\mu$	-	0.128 ± 0.097	0.272 ± 0.391	0.154 ± 0.133	-	0.554 ± 0.429	1	0.782 ± 0.407
$\mu\mu\mu$	-	-	-	-	-	-	0	-
Sum:	-	0.343 ± 0.254	0.272 ± 0.391	0.333 ± 0.265	-	0.948 ± 0.556	2	1.271 ± 0.499
N(τ)=0; 3 Leptons; no-OSSF; HT<200; MET>50;								
eee	-	0.147 ± 0.083	-	0.017 ± 0.026	0.006 ± 0.009	0.169 ± 0.088	1	-
$ee\mu$	-	0.798 ± 0.429	1.265 ± 1.014	0.289 ± 0.205	0.068 ± 0.079	2.420 ± 1.157	6	0.190 ± 0.149
$e\mu\mu$	-	0.448 ± 0.243	3.005 ± 1.211	0.273 ± 0.223	0.037 ± 0.044	3.763 ± 1.297	3	0.547 ± 0.322
$\mu\mu\mu$	-	-	-	-	-	-	0	-
Sum:	-	1.393 ± 0.746	4.271 ± 1.849	0.579 ± 0.427	0.110 ± 0.128	6.352 ± 2.145	10	0.737 ± 0.355
N(τ)=0; 3 Leptons; no-OSSF; HT>200; MET<50;								
eee	-	0.013 ± 0.013	-	0.003 ± 0.003	-	0.015 ± 0.014	0	-
$ee\mu$	-	0.044 ± 0.035	0.272 ± 0.411	0.048 ± 0.037	0.005 ± 0.010	0.369 ± 0.420	0	0.233 ± 0.230
$e\mu\mu$	-	0.016 ± 0.015	-	0.025 ± 0.022	-	0.041 ± 0.027	1	-
$\mu\mu\mu$	-	-	-	-	-	-	0	-
Sum:	-	0.073 ± 0.057	0.272 ± 0.411	0.076 ± 0.059	0.005 ± 0.010	0.426 ± 0.427	1	0.233 ± 0.230
N(τ)=0; 3 Leptons; no-OSSF; HT<200; MET<50;								
eee	0.399 ± 0.620	0.163 ± 0.087	-	0.030 ± 0.047	0.131 ± 0.097	0.723 ± 0.654	0	-
$ee\mu$	0.399 ± 0.604	0.884 ± 0.451	0.402 ± 0.450	0.198 ± 0.143	0.673 ± 0.458	2.557 ± 1.038	6	0.401 ± 0.297
$e\mu\mu$	0.790 ± 0.981	0.662 ± 0.339	1.673 ± 0.917	0.137 ± 0.091	0.375 ± 0.272	3.638 ± 1.442	5	0.431 ± 0.326
$\mu\mu\mu$	-	-	-	-	-	-	0	-
Sum:	1.588 ± 1.864	1.710 ± 0.867	2.076 ± 1.087	0.365 ± 0.255	1.180 ± 0.810	6.918 ± 2.585	11	0.832 ± 0.442

Table E.4: Results split in electron and muon flavors corresponding to an integrated luminosity $L_{int} = 4.7\,fb^{-1}$ recorded in 2011. The selection labels refer to whether there is an OS-SF lepton pair with a mass (in)consistent with the Z mass (off/on-Z) or not (no-OSSF), and the H_T and E_T^{miss} requirements. Four 3L N(τ)=0 channels of Table 9.1 are shown: (top block) off-Z, HT>200, MET>50; (second block) on-Z, HT>200, MET>50; (third block) off-Z, HT<200, MET>50 and (bottom block) on-Z HT<200 MET>50. The SM expectation is split into single processes (second to fifths columns). The total SM expectations and observations are given in the six and seventh columns and the signal expectations for the SUSY LM9 benchmark point in the last column. If given value is "$-$" no expectation for the process are given due to limited MC statistics.

Channel	DYJets	WZJets	TTJets	Rare	ZZ(incG)	SumSM	Data	LM9
N(τ)=0; 3 Leptons; OFF Z; HT>200; MET>50;								
eee	-	0.286 ± 0.212	-	0.089 ± 0.067	0.013 ± 0.021	0.388 ± 0.227	1	0.768 ± 0.400
$ee\mu$	-	0.615 ± 0.452	-	0.259 ± 0.192	0.010 ± 0.018	0.885 ± 0.499	1	0.856 ± 0.352
$e\mu\mu$	0.399 ± 0.727	0.886 ± 0.650	-	0.326 ± 0.243	0.026 ± 0.041	1.637 ± 1.023	3	1.004 ± 0.390
$\mu\mu\mu$	-	0.920 ± 0.674	0.816 ± 0.996	0.198 ± 0.146	0.014 ± 0.023	1.947 ± 1.232	1	3.446 ± 1.006
Sum:	0.399 ± 0.727	2.707 ± 1.977	0.816 ± 0.996	0.872 ± 0.636	0.063 ± 0.096	4.857 ± 2.610	6	6.074 ± 1.220
N(τ)=0; 3 Leptons; ON Z; HT>200; MET>50;								
eee	-	2.940 ± 1.568	0.272 ± 0.410	0.343 ± 0.330	0.027 ± 0.041	3.582 ± 1.681	3	1.585 ± 0.577
$ee\mu$	-	4.039 ± 2.153	-	0.502 ± 0.467	0.018 ± 0.028	4.559 ± 2.224	5	0.884 ± 0.386
$e\mu\mu$	-	4.894 ± 2.607	-	0.583 ± 0.552	0.032 ± 0.048	5.509 ± 2.690	5	1.450 ± 0.559
$\mu\mu\mu$	-	6.947 ± 3.699	-	0.627 ± 0.598	0.071 ± 0.104	7.646 ± 3.777	10	2.347 ± 0.703
Sum:	-	18.820 ± 10.013	0.272 ± 0.410	2.055 ± 1.939	0.149 ± 0.215	21.295 ± 10.310	23	6.266 ± 1.152
N(τ)=0; 3 Leptons; OFF Z; HT<200; MET>50;								
eee	-	2.695 ± 1.438	0.363 ± 0.324	0.162 ± 0.129	0.111 ± 0.130	3.331 ± 1.512	4	2.405 ± 0.660
$ee\mu$	0.442 ± 0.498	4.526 ± 2.412	1.356 ± 1.031	0.527 ± 0.354	0.379 ± 0.454	7.230 ± 2.845	9	2.172 ± 0.663
$e\mu\mu$	-	6.433 ± 3.427	3.045 ± 1.697	0.530 ± 0.390	0.966 ± 0.984	10.974 ± 4.150	15	6.340 ± 1.464
$\mu\mu\mu$	0.192 ± 0.189	6.728 ± 3.583	2.461 ± 1.255	0.279 ± 0.200	0.372 ± 0.431	10.483 ± 3.962	14	3.656 ± 1.056
Sum:	0.634 ± 0.532	20.383 ± 10.845	7.226 ± 3.204	1.499 ± 1.057	1.827 ± 1.708	31.569 ± 11.977	42	14.573 ± 2.100
N(τ)=0; 3 Leptons; ON Z; HT<200; MET>50;								
eee	0.332 ± 0.398	26.406 ± 4.884	0.073 ± 0.104	0.299 ± 0.248	0.861 ± 0.886	27.971 ± 5.167	32	1.797 ± 0.817
$ee\mu$	-	34.618 ± 6.399	0.392 ± 0.356	0.399 ± 0.344	1.895 ± 1.944	37.303 ± 7.005	35	0.910 ± 0.408
$e\mu\mu$	0.541 ± 0.630	37.594 ± 6.948	1.667 ± 0.918	0.520 ± 0.415	0.856 ± 0.880	41.178 ± 7.516	40	3.084 ± 0.971
$\mu\mu\mu$	-	51.754 ± 9.560	1.867 ± 1.055	0.501 ± 0.428	2.081 ± 2.134	56.203 ± 10.367	55	3.454 ± 0.989
Sum:	0.873 ± 0.842	150.372 ± 27.751	3.999 ± 1.706	1.719 ± 1.427	5.693 ± 5.833	162.656 ± 29.864	162	9.246 ± 1.684

Table E.5: Results split in electron and muon flavors corresponding to an integrated luminosity $L_{int} = 4.7\,fb^{-1}$ recorded in 2011. The selection labels refer to whether there is an OS-SF lepton pair with a mass (in)consistent with the Z mass (off/on-Z) or not (no-OSSF), and the H_T and E_T^{miss} requirements. Four 3L N(τ)=0 channels of Table 9.1 are shown: (top block) off-Z, HT>200, MET<50; (second block) on-Z, HT>200, MET<50; (third block) off-Z, HT<200, MET<50 and (bottom block) on-Z HT<200 MET<50. The SM expectation is split into single processes (second to fifths columns). The total SM expectations and observations are given in the six and seventh columns and the signal expectations for the SUSY LM9 benchmark point in the last column. If given value is "−" no expectation for the process are given due to limited MC statistics.

Channel	DYJets	WZJets	TTJets	Rare	ZZ(incG)	SumSM	Data	LM9
N(τ)=0; 3 Leptons; OFF Z; HT>200; MET<50;								
eee	0.534 ± 0.849	0.193 ± 0.145	0.272 ± 0.411	0.043 ± 0.038	0.030 ± 0.039	1.073 ± 1.105	0	-
$ee\mu$	-	0.387 ± 0.287	-	0.121 ± 0.091	0.058 ± 0.075	0.566 ± 0.318	1	0.050 ± 0.051
$e\mu\mu$	0.534 ± 0.849	0.454 ± 0.336	0.271 ± 0.390	0.115 ± 0.087	0.698 ± 1.098	2.072 ± 2.052	7	-
$\mu\mu\mu$	-	0.543 ± 0.401	-	0.104 ± 0.090	0.110 ± 0.156	0.757 ± 0.450	2	0.406 ± 0.249
Sum:	1.069 ± 1.316	1.577 ± 1.158	0.543 ± 0.699	0.383 ± 0.293	0.896 ± 1.154	4.467 ± 3.009	10	0.457 ± 0.254
N(τ)=0; 3 Leptons; ON Z; HT>200; MET<50;								
eee	0.743 ± 0.739	2.011 ± 1.082	-	0.273 ± 0.274	0.196 ± 0.207	3.223 ± 1.425	2	-
$ee\mu$	1.442 ± 1.083	2.139 ± 1.150	0.272 ± 0.411	0.323 ± 0.312	0.140 ± 0.147	4.316 ± 1.786	5	0.128 ± 0.128
$e\mu\mu$	2.385 ± 1.856	3.228 ± 1.734	-	0.348 ± 0.347	0.836 ± 1.120	6.797 ± 3.256	1	0.006 ± 0.006
$\mu\mu\mu$	-	3.586 ± 1.925	-	0.449 ± 0.446	0.249 ± 0.261	4.285 ± 2.038	5	0.006 ± 0.006
Sum:	4.570 ± 2.479	10.964 ± 5.877	0.272 ± 0.411	1.393 ± 1.373	1.422 ± 1.387	18.621 ± 7.330	13	0.140 ± 0.129
N(τ)=0; 3 Leptons; OFF Z; HT<200; MET<50;								
eee	11.829 ± 8.358	4.336 ± 2.192	0.245 ± 0.274	0.110 ± 0.073	4.144 ± 3.558	20.664 ± 9.396	16	2.756 ± 0.786
$ee\mu$	2.109 ± 1.124	6.903 ± 3.487	0.419 ± 0.324	0.184 ± 0.126	5.034 ± 4.051	14.650 ± 5.500	16	2.421 ± 0.727
$e\mu\mu$	26.494 ± 16.474	13.790 ± 6.963	0.241 ± 0.173	0.277 ± 0.160	11.594 ± 8.795	52.396 ± 20.913	48	2.804 ± 0.774
$\mu\mu\mu$	6.362 ± 4.244	15.772 ± 7.962	0.008 ± 0.008	0.118 ± 0.086	10.937 ± 9.950	33.197 ± 13.489	35	5.052 ± 1.147
Sum:	46.795 ± 26.276	40.802 ± 20.589	0.912 ± 0.503	0.690 ± 0.407	31.709 ± 26.214	120.907 ± 43.401	115	13.033 ± 1.810
N(τ)=0; 3 Leptons; ON Z; HT<200; MET<50;								
eee	68.888 ± 22.601	34.396 ± 2.612	-	0.183 ± 0.164	43.743 ± 15.409	147.210 ± 35	115	1.816 ± 0.712
$ee\mu$	64.927 ± 15.250	43.339 ± 3.284	0.094 ± 0.080	0.193 ± 0.161	16.766 ± 5.121	125.318 ± 16.998	139	0.966 ± 0.449
$e\mu\mu$	104.821 ± 35.293	53.685 ± 4.060	1.104 ± 0.751	0.277 ± 0.223	51.368 ± 16.851	211.256 ± 49.020	202	1.022 ± 0.504
$\mu\mu\mu$	100.049 ± 22.429	73.273 ± 5.530	0.560 ± 0.310	0.303 ± 0.279	23.821 ± 7.469	198.007 ± 25.234	197	3.272 ± 0.829
Sum:	338.686 ± 83.575	204.692 ± 15.386	1.758 ± 0.858	0.956 ± 0.817	135.698 ± 37.002	681.790 ± 107.995	653	7.075 ± 1.303

Table E.6: Results split in electron and muon flavors corresponding to an integrated luminosity $L_{int} = 4.7\,fb^{-1}$ recorded in 2011. The selection labels refer to whether there is an OS-SF lepton pair with a mass (in)consistent with the Z mass (off/on-Z) or not (no-OSSF), and the H_T and E_T^{miss} requirements. Four 4L N(τ)=1 channels of Table 9.1 are shown: (top block) off-Z, HT>200, MET>50; (second block) on-Z, HT>200, MET>50; (third block) off-Z, HT<200, MET>50 and (bottom block) on-Z HT<200 MET>50. The SM expectation is split into single processes (second to fifths columns). The total SM expectations and observations are given in the six and seventh columns and the signal expectations for the SUSY LM9 benchmark point in the last column. If given value is "−" no expectation for the process are given due to limited MC statistics.

Channel	DYJets	WZJets	TTJets	Rare	ZZ(incG)	SumSM	Data	LM9
N(τ)=1; 4 Leptons; OFF Z; HT>200; MET>50;								
eee	-	0.006 ± 0.008	-	0.008 ± 0.008	-	0.014 ± 0.011	0	-
$ee\mu$	-	0.005 ± 0.006	-	0.005 ± 0.004	-	0.009 ± 0.007	0	0.068 ± 0.068
$e\mu\mu$	-	-	-	-	-	-	0	-
$\mu\mu\mu$	-	-	-	0.003 ± 0.004	-	0.003 ± 0.004	0	0.194 ± 0.195
Sum:	-	0.011 ± 0.011	-	0.016 ± 0.013	-	0.027 ± 0.017	0	0.262 ± 0.206
N(τ)=1; 4 Leptons; ON Z; HT>200; MET>50;								
eee	-	0.019 ± 0.013	-	0.008 ± 0.010	0.007 ± 0.012	0.034 ± 0.021	0	0.184 ± 0.185
$ee\mu$	-	0.032 ± 0.022	-	0.005 ± 0.007	0.005 ± 0.009	0.043 ± 0.025	0	-
$e\mu\mu$	-	0.021 ± 0.015	-	0.005 ± 0.007	-	0.026 ± 0.016	0	-
$\mu\mu\mu$	-	0.037 ± 0.024	-	0.017 ± 0.019	0.011 ± 0.017	0.064 ± 0.036	0	-
Sum:	-	0.109 ± 0.062	-	0.035 ± 0.037	0.022 ± 0.034	0.167 ± 0.082	0	0.184 ± 0.185
N(τ)=1; 4 Leptons; OFF Z; HT<200; MET>50;								
eee	-	0.018 ± 0.014	-	0.017 ± 0.026	0.006 ± 0.009	0.041 ± 0.031	0	0.455 ± 0.340
$ee\mu$	-	0.050 ± 0.030	-	0.026 ± 0.018	0.059 ± 0.070	0.135 ± 0.080	1	0.003 ± 0.003
$e\mu\mu$	-	0.043 ± 0.026	-	0.008 ± 0.008	0.030 ± 0.036	0.080 ± 0.046	0	0.140 ± 0.140
$\mu\mu\mu$	-	0.045 ± 0.028	-	0.022 ± 0.024	0.047 ± 0.059	0.114 ± 0.071	0	0.302 ± 0.304
Sum:	-	0.156 ± 0.087	-	0.073 ± 0.048	0.141 ± 0.164	0.370 ± 0.196	1	0.900 ± 0.479
N(τ)=1; 4 Leptons; ON Z; HT<200; MET>50;								
eee	-	0.171 ± 0.043	-	0.011 ± 0.013	0.111 ± 0.116	0.293 ± 0.129	0	0.128 ± 0.129
$ee\mu$	-	0.273 ± 0.064	-	0.016 ± 0.018	0.199 ± 0.206	0.488 ± 0.223	0	0.047 ± 0.047
$e\mu\mu$	-	0.295 ± 0.067	-	0.028 ± 0.031	0.115 ± 0.120	0.438 ± 0.148	0	-
$\mu\mu\mu$	-	0.346 ± 0.077	-	0.023 ± 0.020	0.263 ± 0.272	0.633 ± 0.292	0	-
Sum:	-	1.086 ± 0.214	-	0.079 ± 0.074	0.687 ± 0.707	1.852 ± 0.767	0	0.175 ± 0.137

Table E.7: Results split in electron and muon flavors corresponding to an integrated luminosity $L_{int} = 4.7\,fb^{-1}$ recorded in 2011. The selection labels refer to whether there is an OS-SF lepton pair with a mass (in)consistent with the Z mass (off/on-Z) or not (no-OSSF), and the H_T and E_T^{miss} requirements. Four 4L N(τ)=1 channels of Table 9.1 are shown: (top block) off-Z, HT>200, MET<50; (second block) on-Z, HT>200, MET<50; (third block) off-Z, HT<200, MET<50 and (bottom block) on-Z HT<200 MET<50. The SM expectation is split into single processes (second to fifths columns). The total SM expectations and observations are given in the six and seventh columns and the signal expectations for the SUSY LM9 benchmark point in the last column. If given value is "−" no expectation for the process are given due to limited MC statistics.

Channel	DYJets	WZJets	TTJets	Rare	ZZ(incG)	SumSM	Data	LM9
N(τ)=1; 4 Leptons; OFF Z; HT>200; MET<50;								
eee	-	0.005 ± 0.006	-	-	0.009 ± 0.012	0.013 ± 0.013	0	-
$ee\mu$	-	-	-	-	-	-	0	-
$e\mu\mu$	-	-	-	0.005 ± 0.006	-	0.005 ± 0.006	0	-
$\mu\mu\mu$	-	0.005 ± 0.006	-	-	-	0.005 ± 0.006	0	0.138 ± 0.138
Sum:	-	0.009 ± 0.009	-	0.005 ± 0.006	0.009 ± 0.012	0.023 ± 0.017	0	0.138 ± 0.138
N(τ)=1; 4 Leptons; ON Z; HT>200; MET<50;								
eee	-	0.021 ± 0.016	-	0.010 ± 0.012	-	0.031 ± 0.020	0	-
$ee\mu$	-	0.014 ± 0.012	-	0.002 ± 0.003	-	0.017 ± 0.012	0	-
$e\mu\mu$	-	0.020 ± 0.014	-	0.001 ± 0.001	0.006 ± 0.009	0.027 ± 0.017	0	-
$\mu\mu\mu$	-	0.027 ± 0.019	-	0.014 ± 0.016	0.006 ± 0.008	0.048 ± 0.027	0	0.006 ± 0.006
Sum:	-	0.083 ± 0.049	-	0.027 ± 0.028	0.012 ± 0.015	0.123 ± 0.060	0	0.006 ± 0.006
N(τ)=1; 4 Leptons; OFF Z; HT<200; MET<50;								
eee	-	0.023 ± 0.015	-	0.003 ± 0.003	0.183 ± 0.104	0.209 ± 0.105	0	-
$ee\mu$	-	0.046 ± 0.028	-	0.020 ± 0.026	0.150 ± 0.087	0.215 ± 0.095	2	-
$e\mu\mu$	0.008 ± 0.011	0.099 ± 0.055	-	0.011 ± 0.010	0.220 ± 0.122	0.337 ± 0.135	1	0.438 ± 0.285
$\mu\mu\mu$	-	0.145 ± 0.078	-	0.002 ± 0.003	0.220 ± 0.122	0.368 ± 0.145	0	0.261 ± 0.261
Sum:	0.008 ± 0.011	0.313 ± 0.163	-	0.036 ± 0.031	0.772 ± 0.414	1.129 ± 0.448	3	0.698 ± 0.388
N(τ)=1; 4 Leptons; ON Z; HT<200; MET<50;								
eee	-	0.219 ± 0.036	-	0.004 ± 0.004	0.505 ± 0.118	0.728 ± 0.126	0	-
$ee\mu$	-	0.217 ± 0.035	-	0.001 ± 0.001	0.571 ± 0.132	0.788 ± 0.138	1	-
$e\mu\mu$	1.336 ± 1.487	0.299 ± 0.045	-	-	0.994 ± 0.232	2.629 ± 1.508	3	-
$\mu\mu\mu$	-	0.463 ± 0.059	-	0.026 ± 0.028	0.700 ± 0.164	1.189 ± 0.181	2	0.162 ± 0.163
Sum:	1.336 ± 1.487	1.198 ± 0.118	-	0.030 ± 0.033	2.769 ± 0.577	5.334 ± 1.611	6	0.162 ± 0.163

Table E.8: Results split in electron and muon flavors corresponding to an integrated luminosity $L_{int} = 4.7\,fb^{-1}$ recorded in 2011. The selection labels refer to whether there is an OS-SF lepton pair with a mass (in)consistent with the Z mass (off/on-Z) or not (no-OSSF), and the H_T and E_T^{miss} requirements. Four 3L N(τ)=1 channels of Table 9.1 are shown: (top block) no-OSSF, HT>200, MET>50; (second block) no-OSSF, HT<200, MET>50; (third block) no-OSSF, HT>200, MET<50 and (bottom block) no-OSSF HT<200 MET<50. The SM expectation is split into single processes (second to fifths columns). The total SM expectations and observations are given in the six and seventh columns and the signal expectations for the SUSY LM9 benchmark point in the last column. If given value is "−" no expectation for the process are given due to limited MC statistics.

Channel	DYJets	WZJets	TTJets	Rare	ZZ(incG)	SumSM	Data	LM9
N(τ)=1; 3 Leptons; no-OSSF; HT>200; MET>50;								
ee	-	0.171 ± 0.128	-	3.169 ± 4.432	0.011 ± 0.018	3.350 ± 4.437	2	0.341 ± 0.343
$e\mu$	1.135 ± 1.367	0.927 ± 0.679	18.359 ± 10.146	0.719 ± 0.313	0.020 ± 0.032	21.160 ± 10.383	20	0.520 ± 0.274
$\mu\mu$	0.381 ± 0.547	0.229 ± 0.170	0.297 ± 0.365	0.092 ± 0.069	-	0.999 ± 0.694	1	0.605 ± 0.425
Sum:	1.516 ± 1.761	1.328 ± 0.971	18.656 ± 10.355	3.979 ± 4.484	0.031 ± 0.048	25.509 ± 12.132	23	1.466 ± 0.616
N(τ)=1; 3 Leptons; no-OSSF; HT<200; MET>50;								
ee	0.607 ± 0.727	1.105 ± 0.594	0.012 ± 0.013	0.076 ± 0.058	0.101 ± 0.118	1.901 ± 0.971	6	0.298 ± 0.220
$e\mu$	8.263 ± 4.988	5.205 ± 2.776	86.224 ± 46.066	4.495 ± 0.826	0.914 ± 0.913	105.101 ± 47.266	118	1.380 ± 0.662
$\mu\mu$	-	1.342 ± 0.719	2.176 ± 0.972	0.088 ± 0.077	0.077 ± 0.090	3.683 ± 1.276	3	0.049 ± 0.049
Sum:	8.870 ± 5.161	7.653 ± 4.079	88.412 ± 46.589	4.659 ± 0.913	1.092 ± 1.034	110.686 ± 48.073	127	1.727 ± 0.703
N(τ)=1; 3 Leptons; no-OSSF; HT>200; MET<50;								
ee	0.389 ± 0.589	0.077 ± 0.060	-	0.025 ± 0.021	0.010 ± 0.014	0.501 ± 0.595	1	0.409 ± 0.292
$e\mu$	-	0.229 ± 0.171	4.792 ± 2.890	0.215 ± 0.118	0.030 ± 0.036	5.265 ± 2.925	13	0.395 ± 0.281
$\mu\mu$	-	0.051 ± 0.040	0.061 ± 0.064	0.011 ± 0.012	-	0.124 ± 0.078	0	0.300 ± 0.301
Sum:	0.389 ± 0.589	0.357 ± 0.264	4.853 ± 2.904	0.252 ± 0.143	0.040 ± 0.048	5.890 ± 3.041	14	1.104 ± 0.508
N(τ)=1; 3 Leptons; no-OSSF; HT<200; MET<50;								
ee	52.661 ± 27.171	1.660 ± 0.845	0.171 ± 0.191	0.044 ± 0.038	1.762 ± 1.471	56.297 ± 27.309	61	0.055 ± 0.056
$e\mu$	90.144 ± 46.344	7.067 ± 3.575	37.080 ± 19.351	7.081 ± 4.245	5.451 ± 4.025	146.823 ± 51.396	143	1.278 ± 0.587
$\mu\mu$	1.421 ± 0.940	1.867 ± 0.947	0.328 ± 0.362	0.074 ± 0.055	0.464 ± 0.251	4.154 ± 1.417	6	-
Sum:	144.226 ± 73.439	10.594 ± 5.357	37.578 ± 19.658	7.199 ± 4.249	7.677 ± 5.361	207.274 ± 77.324	210	1.333 ± 0.591

Table E.9: Results split in electron and muon flavors corresponding to an integrated luminosity $L_{int} = 4.7\,fb^{-1}$ recorded in 2011. The selection labels refer to whether there is an OS-SF lepton pair with a mass (in)consistent with the Z mass (off/on-Z) or not (no-OSSF), and the H_T and E_T^{miss} requirements. Four 3L N(τ)=1 channels of Table 9.1 are shown: (top block) off-Z, HT>200, MET>50; (second block) on-Z, HT>200, MET>50; (third block) off-Z, HT<200, MET>50 and (bottom block) on-Z HT<200 MET>50. The SM expectation is split into single processes (second to fifths columns). The total SM expectations and observations are given in the six and seventh columns and the signal expectations for the SUSY LM9 benchmark point in the last column. If given value is "$-$" no expectation for the process are given due to limited MC statistics.

Channel	DYJets	WZJets	TTJets	Rare	ZZ(incG)	SumSM	Data	LM9
N(τ)=1; 3 Leptons; OFF Z; HT>200; MET>50;								
ee	0.530 ± 0.598	0.261 ± 0.194	5.843 ± 3.519	0.224 ± 0.085	0.015 ± 0.025	6.873 ± 3.616	3	0.605 ± 0.384
$e\mu$	-	-	-	-	-	-	0	-
$\mu\mu$	0.608 ± 0.686	0.451 ± 0.332	10.309 ± 5.713	0.252 ± 0.131	0.016 ± 0.026	11.636 ± 5.819	11	0.687 ± 0.317
Sum:	1.139 ± 1.002	0.712 ± 0.523	16.151 ± 8.930	0.475 ± 0.204	0.031 ± 0.049	18.509 ± 9.100	14	1.292 ± 0.502
N(τ)=1; 3 Leptons; ON Z; HT>200; MET>50;								
ee	1.907 ± 1.420	1.011 ± 0.542	1.359 ± 0.995	0.150 ± 0.123	0.036 ± 0.054	4.463 ± 1.902	5	0.564 ± 0.293
$e\mu$	-	-	-	-	-	-	0	-
$\mu\mu$	2.005 ± 1.440	1.291 ± 0.691	3.242 ± 1.970	0.160 ± 0.129	0.030 ± 0.044	6.728 ± 2.660	4	1.248 ± 0.656
Sum:	3.912 ± 2.483	2.302 ± 1.229	4.601 ± 2.695	0.310 ± 0.249	0.066 ± 0.096	11.191 ± 4.102	9	1.812 ± 0.722
N(τ)=1; 3 Leptons; OFF Z; HT<200; MET>50;								
ee	2.780 ± 1.776	1.699 ± 0.910	20.268 ± 11.282	1.361 ± 0.269	0.269 ± 0.310	26.376 ± 11.733	39	0.709 ± 0.343
$e\mu$	-	-	-	-	-	-	0	-
$\mu\mu$	11.764 ± 6.833	2.382 ± 1.272	45.935 ± 25.031	2.418 ± 0.427	0.829 ± 0.870	63.328 ± 26.722	78	1.116 ± 0.508
Sum:	14.544 ± 8.099	4.082 ± 2.177	66.202 ± 35.992	3.779 ± 0.654	1.097 ± 1.040	89.704 ± 37.988	117	1.825 ± 0.618
N(τ)=1; 3 Leptons; ON Z; HT<200; MET>50;								
ee	11.827 ± 6.741	6.473 ± 1.225	6.611 ± 3.783	0.371 ± 0.109	0.987 ± 1.014	26.270 ± 8.544	44	0.490 ± 0.241
$e\mu$	-	-	-	-	-	-	0	-
$\mu\mu$	28.583 ± 15.637	9.725 ± 1.809	13.171 ± 7.218	3.766 ± 4.485	2.049 ± 1.603	57.294 ± 19.231	66	1.159 ± 0.645
Sum:	40.410 ± 21.766	16.198 ± 3.012	19.783 ± 10.668	4.138 ± 4.494	3.036 ± 2.469	83.564 ± 26.933	110	1.650 ± 0.691

Table E.10: Results split in electron and muon flavors corresponding to an integrated luminosity $L_{int} = 4.7\,fb^{-1}$ recorded in 2011. The selection labels refer to whether there is an OS-SF lepton pair with a mass (in)consistent with the Z mass (off/on-Z) or not (no-OSSF), and the H_T and E_T^{miss} requirements. Four 3L N(τ)=1 channels of Table 9.1 are shown: (top block) off-Z, HT>200, MET<50; (second block) on-Z, HT>200, MET<50; (third block) off-Z, HT<200, MET<50 and (bottom block) on-Z HT<200 MET<50. The SM expectation is split into single processes (second to fifths columns). The total SM expectations and observations are given in the six and seventh columns and the signal expectations for the SUSY LM9 benchmark point in the last column. If given value is "−" no expectation for the process are given due to limited MC statistics.

Channel	DYJets	WZJets	TTJets	Rare	ZZ(incG)	SumSM	Data	LM9
N(τ)=1; 3 Leptons; OFF Z; HT>200; MET<50;								
ee	3.489 ± 2.798	0.090 ± 0.069	0.176 ± 0.200	0.091 ± 0.050	0.009 ± 0.013	3.856 ± 2.823	5	0.006 ± 0.007
$e\mu$	-	-	-	-	-	-	0	-
$\mu\mu$	12.736 ± 8.322	0.108 ± 0.082	2.261 ± 1.509	0.156 ± 0.081	0.034 ± 0.051	15.295 ± 8.593	14	0.100 ± 0.100
Sum:	16.226 ± 10.119	0.198 ± 0.148	2.438 ± 1.595	0.247 ± 0.122	0.043 ± 0.060	19.152 ± 10.408	19	0.106 ± 0.101
N(τ)=1; 3 Leptons; ON Z; HT>200; MET<50;								
ee	37.216 ± 20.340	0.316 ± 0.174	0.848 ± 0.751	0.065 ± 0.058	0.020 ± 0.023	38.464 ± 20.436	38	-
$e\mu$	-	-	-	-	-	-	0	-
$\mu\mu$	53.955 ± 29.265	0.551 ± 0.300	1.203 ± 0.880	0.208 ± 0.194	0.047 ± 0.051	55.963 ± 29.409	63	0.246 ± 0.150
Sum:	91.171 ± 49.120	0.867 ± 0.469	2.051 ± 1.386	0.272 ± 0.248	0.066 ± 0.071	94.428 ± 49.354	101	0.246 ± 0.150
N(τ)=1; 3 Leptons; OFF Z; HT<200; MET<50;								
ee	1109.532 ± 560.573	2.362 ± 1.200	13.104 ± 7.012	4.109 ± 4.432	5.155 ± 4.247	1134.261 ± 560.863	973	0.737 ± 0.342
$e\mu$	-	-	-	-	-	-	0	-
$\mu\mu$	2302.325 ± 1159.875	3.911 ± 1.980	20.853 ± 11.297	7.638 ± 6.850	11.391 ± 5.234	2346.119 ± 1160.169	2281	1.622 ± 0.497
Sum:	3411.856 ± 1718.184	6.273 ± 3.174	33.958 ± 17.975	11.747 ± 10.084	16.546 ± 8.180	3480.380 ± 1718.730	3254	2.359 ± 0.613
N(τ)=1; 3 Leptons; ON Z; HT<200; MET<50;								
ee	4771.145 ± 2407.786	7.763 ± 0.702	2.818 ± 1.696	0.358 ± 0.088	93.743 ± 45.984	4875.827 ± 2409.114	4759	0.014 ± 0.014
$e\mu$	-	-	-	-	-	-	0	-
$\mu\mu$	7754.467 ± 3896.475	12.830 ± 0.998	7.120 ± 3.903	0.640 ± 0.125	119.507 ± 57.519	7894.564 ± 3897.491	7483	0.094 ± 0.081
Sum:	12525.612 ± 6299.197	20.593 ± 1.633	9.938 ± 5.313	0.998 ± 0.178	213.250 ± 102.590	12770.391 ± 6301.316	12242	0.108 ± 0.082

Table E.11: Results split in electron and muon flavors corresponding to an integrated luminosity $L_{int} = 4.7\,fb^{-1}$ recorded in 2011. The selection labels refer to whether there is an OS-SF lepton pair with a mass (in)consistent with the Z mass (off/on-Z) or not (no-OSSF), and the H_T and E_T^{miss} requirements. Four 4L N(τ)=2 channels of Table 9.1 are shown: (top block) off-Z, HT>200, MET>50; (second block) on-Z, HT>200, MET>50; (third block) off-Z, HT<200, MET>50 and (bottom block) on-Z HT<200 MET>50. The SM expectation is split into single processes (second to fifths columns). The total SM expectations and observations are given in the six and seventh columns and the signal expectations for the SUSY LM9 benchmark point in the last column. If given value is "−" no expectation for the process are given due to limited MC statistics.

Channel	DYJets	WZJets	TTJets	Rare	ZZ(incG)	SumSM	Data	LM9
N(τ)=2; 4 Leptons; OFF Z; HT>200; MET>50;								
ee	-	-	-	0.002 ± 0.003	-	0.002 ± 0.003	0	-
$e\mu$	-	0.003 ± 0.005	-	0.007 ± 0.010	-	0.010 ± 0.013	0	-
$\mu\mu$	-	0.004 ± 0.006	-	0.003 ± 0.004	-	0.006 ± 0.009	0	-
Sum:	-	0.007 ± 0.010	-	0.011 ± 0.015	-	0.018 ± 0.022	0	-
N(τ)=2; 4 Leptons; ON Z; HT>200; MET>50;								
ee	-	0.007 ± 0.010	-	0.003 ± 0.004	-	0.010 ± 0.012	0	-
$e\mu$	-	-	-	-	-	-	0	-
$\mu\mu$	-	-	-	0.003 ± 0.005	-	0.003 ± 0.005	1	-
Sum:	-	0.007 ± 0.010	-	0.005 ± 0.008	-	0.012 ± 0.015	1	-
N(τ)=2; 4 Leptons; OFF Z; HT<200; MET>50;								
ee	-	0.032 ± 0.020	-	0.003 ± 0.005	-	0.035 ± 0.021	0	-
$e\mu$	-	0.028 ± 0.019	1.083 ± 1.632	0.006 ± 0.008	0.004 ± 0.007	1.122 ± 1.636	2	-
$\mu\mu$	-	0.020 ± 0.015	0.813 ± 1.248	0.028 ± 0.033	0.012 ± 0.016	0.873 ± 1.267	1	-
Sum:	-	0.080 ± 0.047	1.896 ± 2.789	0.037 ± 0.042	0.016 ± 0.021	2.030 ± 2.816	3	-
N(τ)=2; 4 Leptons; ON Z; HT<200; MET>50;								
ee	-	0.034 ± 0.014	0.263 ± 0.457	0.003 ± 0.004	0.120 ± 0.128	0.420 ± 0.479	0	-
$e\mu$	-	-	-	-	-	-	0	-
$\mu\mu$	-	0.079 ± 0.025	-	0.009 ± 0.013	0.163 ± 0.170	0.250 ± 0.174	0	-
Sum:	-	0.113 ± 0.031	0.263 ± 0.457	0.011 ± 0.016	0.283 ± 0.294	0.670 ± 0.556	0	-

Table E.12: Results split in electron and muon flavors corresponding to an integrated luminosity $L_{int} = 4.7\,fb^{-1}$ recorded in 2011. The selection labels refer to whether there is an OS-SF lepton pair with a mass (in)consistent with the Z mass (off/on-Z) or not (no-OSSF), and the H_T and E_T^{miss} requirements. Four 4L N(τ)=2 channels of Table 9.1 are shown: (top block) off-Z, HT>200, MET<50; (second block) on-Z, HT>200, MET<50; (third block) off-Z, HT<200, MET<50 and (bottom block) on-Z HT<200 MET<50. The SM expectation is split into single processes (second to fifths columns). The total SM expectations and observations are given in the six and seventh columns and the signal expectations for the SUSY LM9 benchmark point in the last column. If given value is "−" no expectation for the process are given due to limited MC statistics.

Channel	DYJets	WZJets	TTJets	Rare	ZZ(incG)	SumSM	Data	LM9
N(τ)=2; 4 Leptons; OFF Z; HT>200; MET<50;								
ee	-	-	-	-	-	-	0	-
$e\mu$	-	-	-	0.001 ± 0.001	0.005 ± 0.010	0.006 ± 0.010	0	-
$\mu\mu$	0.387 ± 0.674	-	-	0.001 ± 0.001	0.005 ± 0.010	0.393 ± 0.678	1	-
Sum:	0.387 ± 0.674	-	-	0.002 ± 0.003	0.011 ± 0.018	0.399 ± 0.682	1	-
N(τ)=2; 4 Leptons; ON Z; HT>200; MET<50;								
ee	0.788 ± 1.255	0.004 ± 0.006	-	0.008 ± 0.012	-	0.800 ± 1.262	0	-
$e\mu$	-	-	-	-	-	-	0	-
$\mu\mu$	0.399 ± 0.695	0.003 ± 0.005	-	-	0.005 ± 0.009	0.407 ± 0.700	1	-
Sum:	1.187 ± 1.826	0.007 ± 0.010	-	0.008 ± 0.012	0.005 ± 0.009	1.207 ± 1.840	1	-
N(τ)=2; 4 Leptons; OFF Z; HT<200; MET<50;								
ee	5.862 ± 7.280	0.056 ± 0.035	-	0.006 ± 0.006	0.112 ± 0.065	6.035 ± 7.281	5	-
$e\mu$	0.128 ± 0.181	0.037 ± 0.023	-	0.017 ± 0.021	0.078 ± 0.048	0.260 ± 0.190	0	-
$\mu\mu$	5.256 ± 6.663	0.025 ± 0.016	0.271 ± 0.469	0.005 ± 0.005	0.208 ± 0.124	5.764 ± 6.795	6	-
Sum:	11.245 ± 13.354	0.117 ± 0.065	0.271 ± 0.469	0.028 ± 0.028	0.399 ± 0.221	12.060 ± 13.490	11	-
N(τ)=2; 4 Leptons; ON Z; HT<200; MET<50;								
ee	12.162 ± 12.427	0.057 ± 0.017	-	0.011 ± 0.016	2.409 ± 2.269	14.639 ± 12.645	16	-
$e\mu$	-	-	-	-	-	-	0	-
$\mu\mu$	18.127 ± 18.406	0.060 ± 0.017	-	0.003 ± 0.005	0.775 ± 0.173	18.965 ± 18.409	18	-
Sum:	30.289 ± 30.581	0.117 ± 0.025	-	0.014 ± 0.018	3.184 ± 2.286	33.604 ± 30.677	34	-

APPENDIX F

cMSSM $tan\beta = 10$: Selection Efficiencies

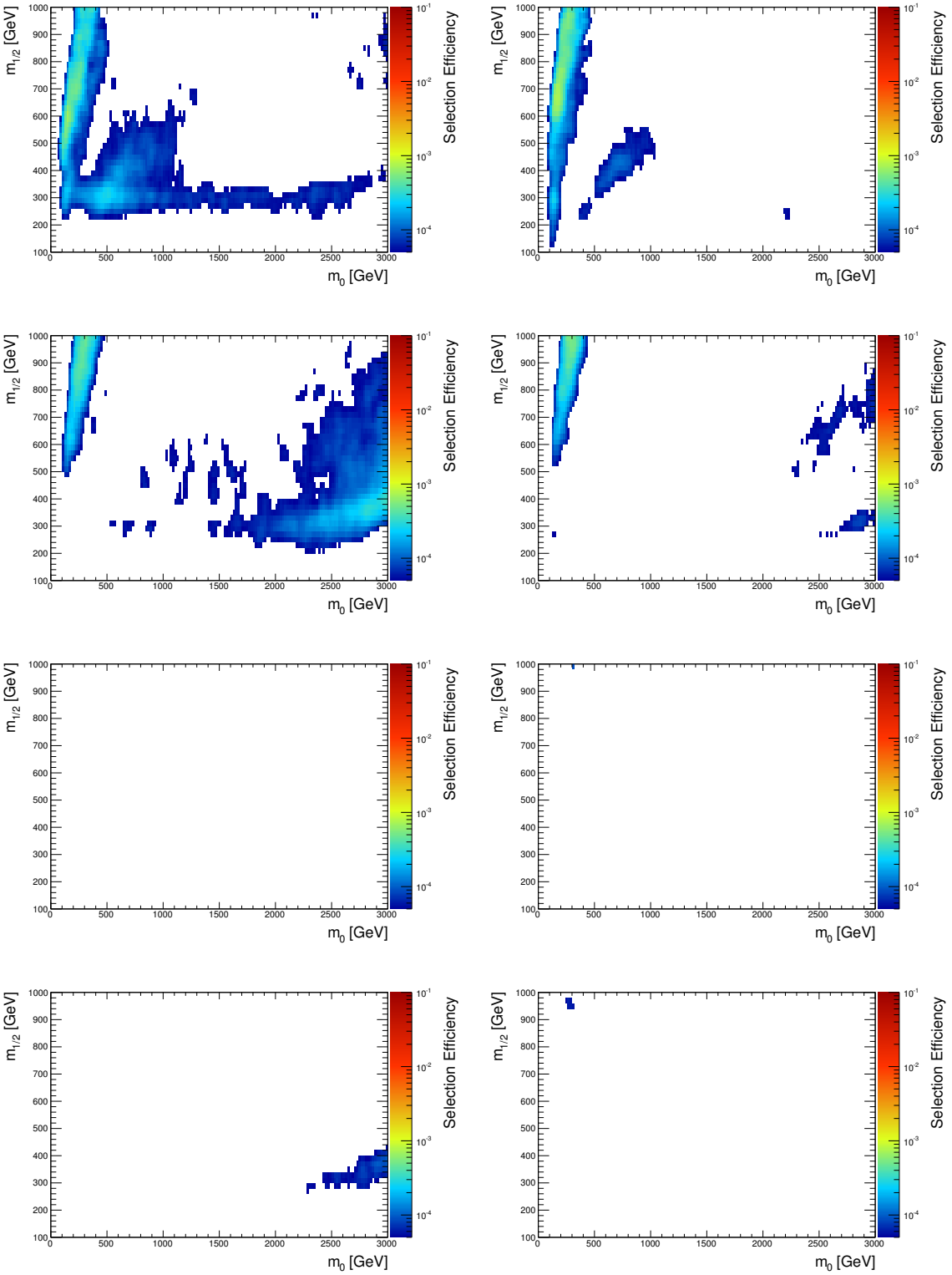

Figure F.1: Signal ($tan\beta = 10$, $A_0 = 0$, $sign(\mu) = +1$) selection efficiency for the channels including 4 leptons (N(τ)=0), on-Z (left column), off-Z (right column), $E_T^{\text{miss}} > 50\,\text{GeV}$, $H_T > 200\,\text{GeV}$ (top row), $E_T^{\text{miss}} > 50\,\text{GeV}$, $H_T < 200\,\text{GeV}$ (second row), $E_T^{\text{miss}} < 50\,\text{GeV}$, $H_T > 200\,\text{GeV}$ (third row) and $E_T^{\text{miss}} < 50\,\text{GeV}$, $H_T < 200\,\text{GeV}$ (forth row). White spaces correspond to selection efficiencies below $\epsilon_{sel} < 0.00005$.

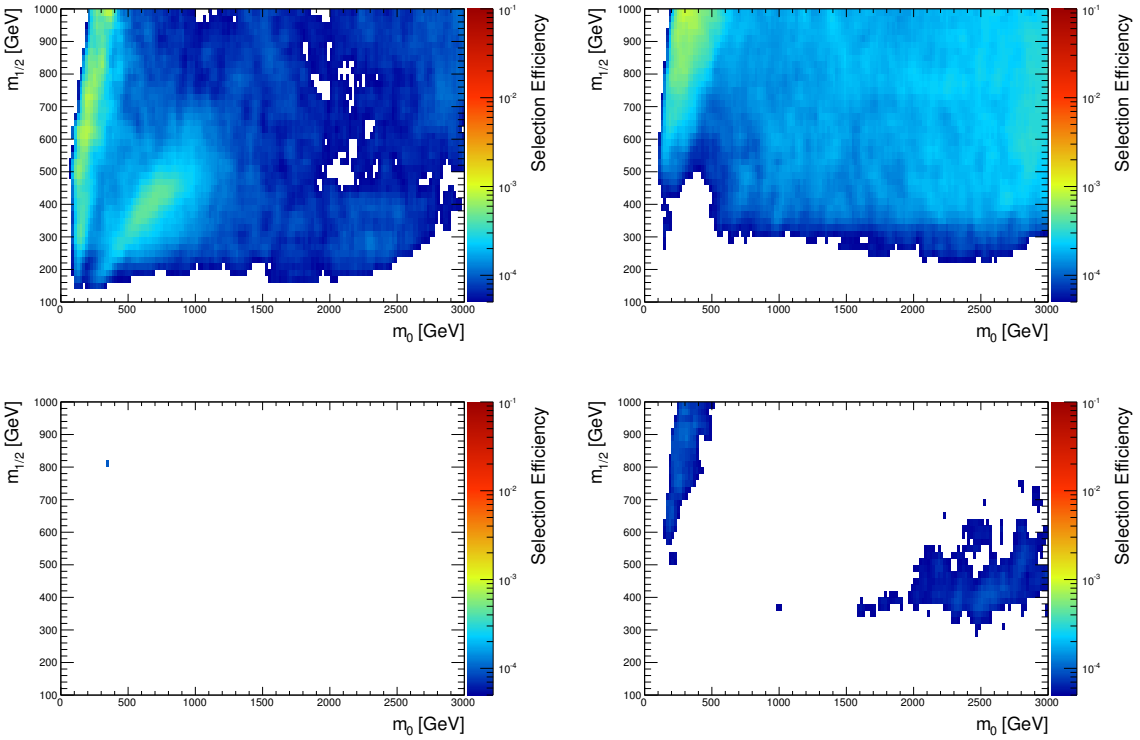

Figure F.2: Signal ($tan\beta = 10$, $A_0 = 0$, $sign(\mu) = +1$) selection efficiencies for the channels including 3 leptons (N(τ)=0), no-OSSF , $E_T^{\text{miss}} > 50\,\text{GeV}$, $H_T > 200\,\text{GeV}$ (top left), $E_T^{\text{miss}} > 50\,\text{GeV}$, $H_T < 200\,\text{GeV}$ (top right), $E_T^{\text{miss}} < 50\,\text{GeV}$, $H_T > 200\,\text{GeV}$ (bottom left) and $E_T^{\text{miss}} < 50\,\text{GeV}$, $H_T < 200\,\text{GeV}$ (botoom right). White spaces correspond to selection efficiencies below $\epsilon_{sel} < 0.00005$.

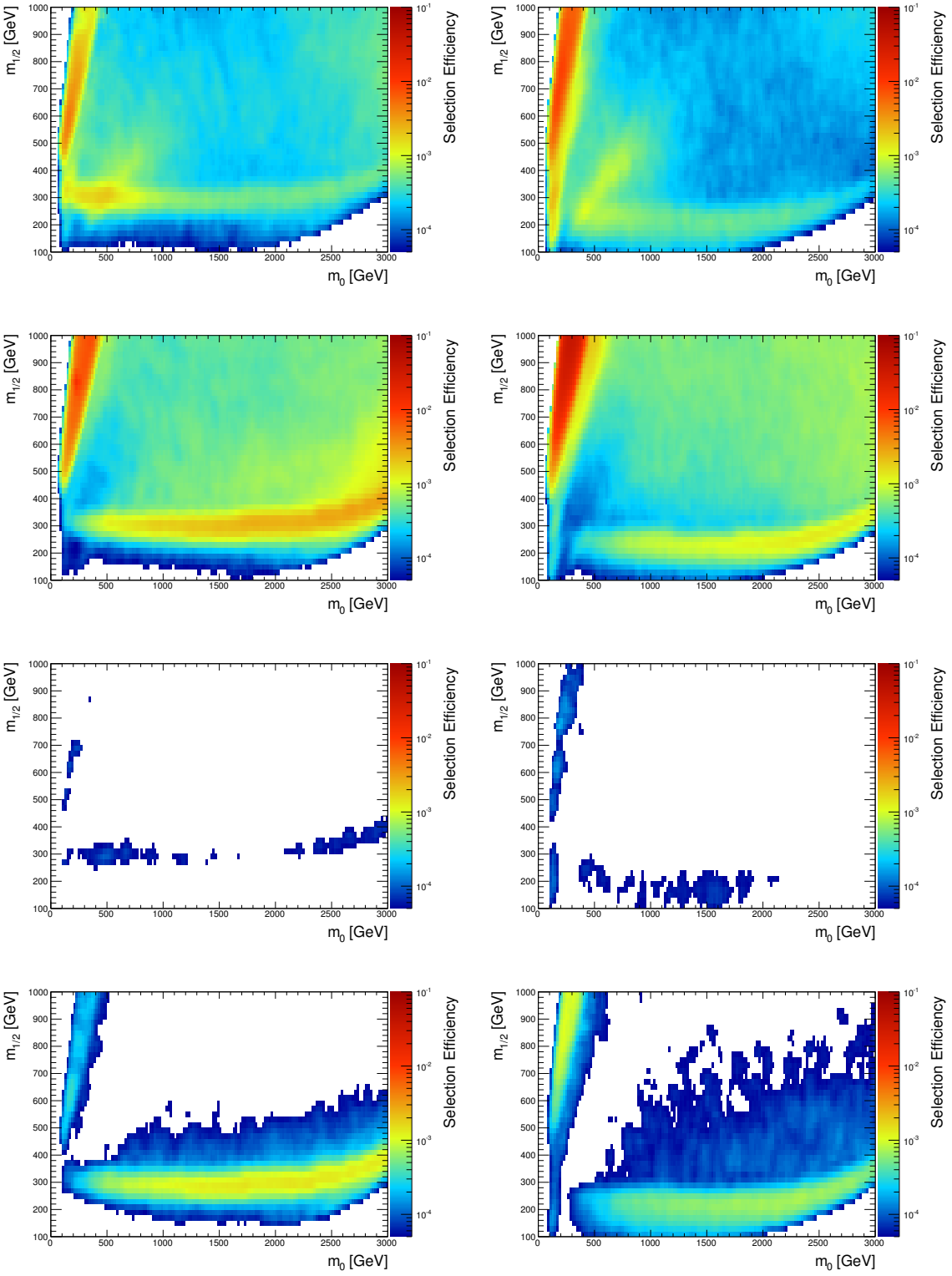

Figure F.3: Signal ($tan\beta = 10$, $A_0 = 0$, $sign(\mu) = +1$) selection efficiencies for the channels including 3 leptons (N(τ)=0), on-Z (left column), off-Z (right column), $E_T^{\text{miss}} > 50\,\text{GeV}$, $H_T > 200\,\text{GeV}$ (top row), $E_T^{\text{miss}} > 50\,\text{GeV}$, $H_T < 200\,\text{GeV}$ (second row), $E_T^{\text{miss}} < 50\,\text{GeV}$, $H_T > 200\,\text{GeV}$ (third row) and $E_T^{\text{miss}} < 50\,\text{GeV}$, $H_T < 200\,\text{GeV}$ (bottom row). White spaces correspond to selection efficiencies below $\epsilon_{sel} < 0.00005$.

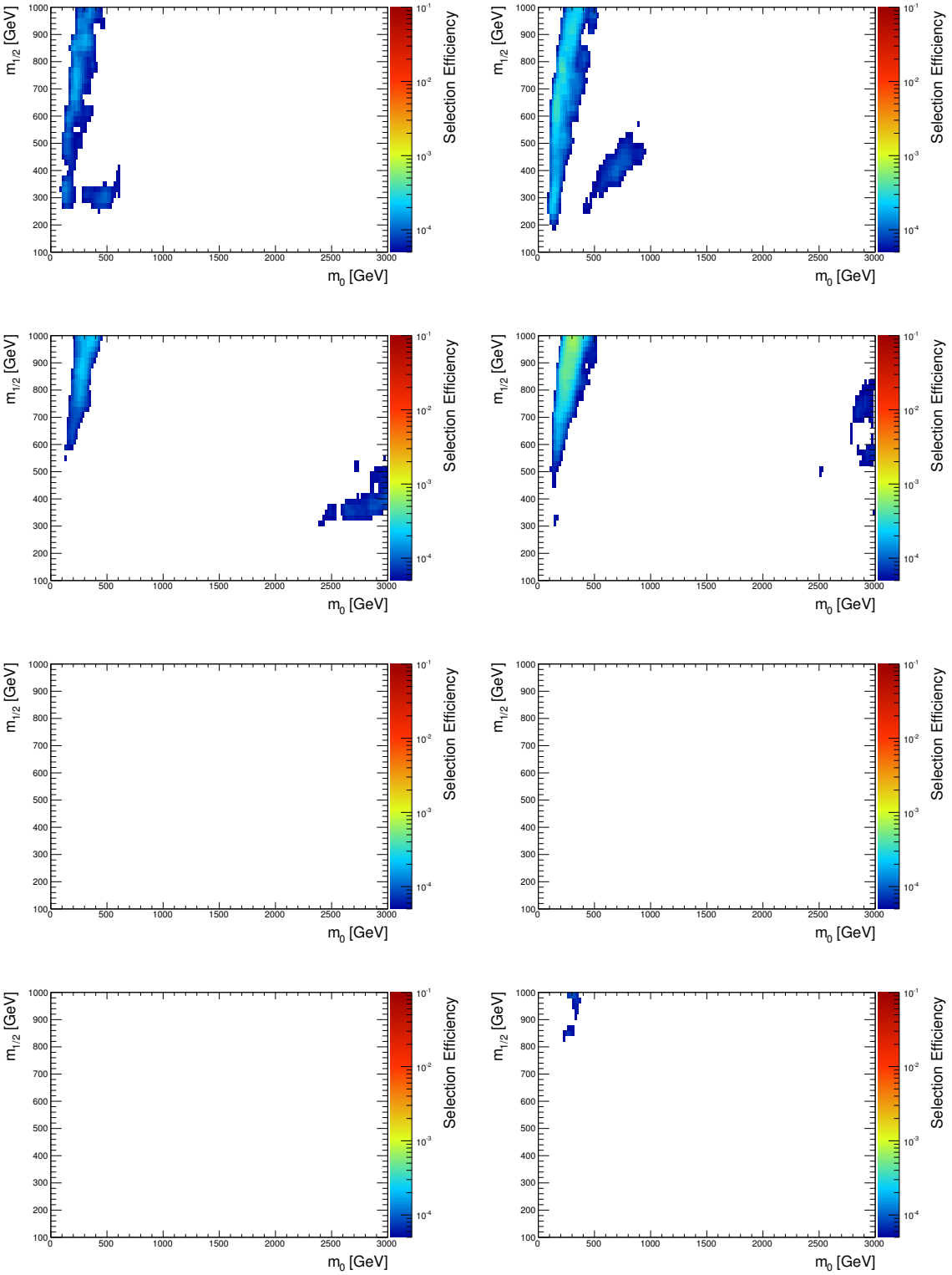

Figure F.4: Signal ($tan\beta = 10$, $A_0 = 0$, $sign(\mu) = +1$) selection efficiencies for the channels including 4 leptons (N(τ)=1), on-Z (left column), off-Z (right column), $E_T^{\text{miss}} > 50\,\text{GeV}$, $H_T > 200\,\text{GeV}$ (top row), $E_T^{\text{miss}} > 50\,\text{GeV}$, $H_T < 200\,\text{GeV}$ (second row), $E_T^{\text{miss}} < 50\,\text{GeV}$, $H_T > 200\,\text{GeV}$ (third row) and $E_T^{\text{miss}} < 50\,\text{GeV}$, $H_T < 200\,\text{GeV}$ (bottom row). White spaces correspond to selection efficiencies below $\epsilon_{sel} < 0.00005$.

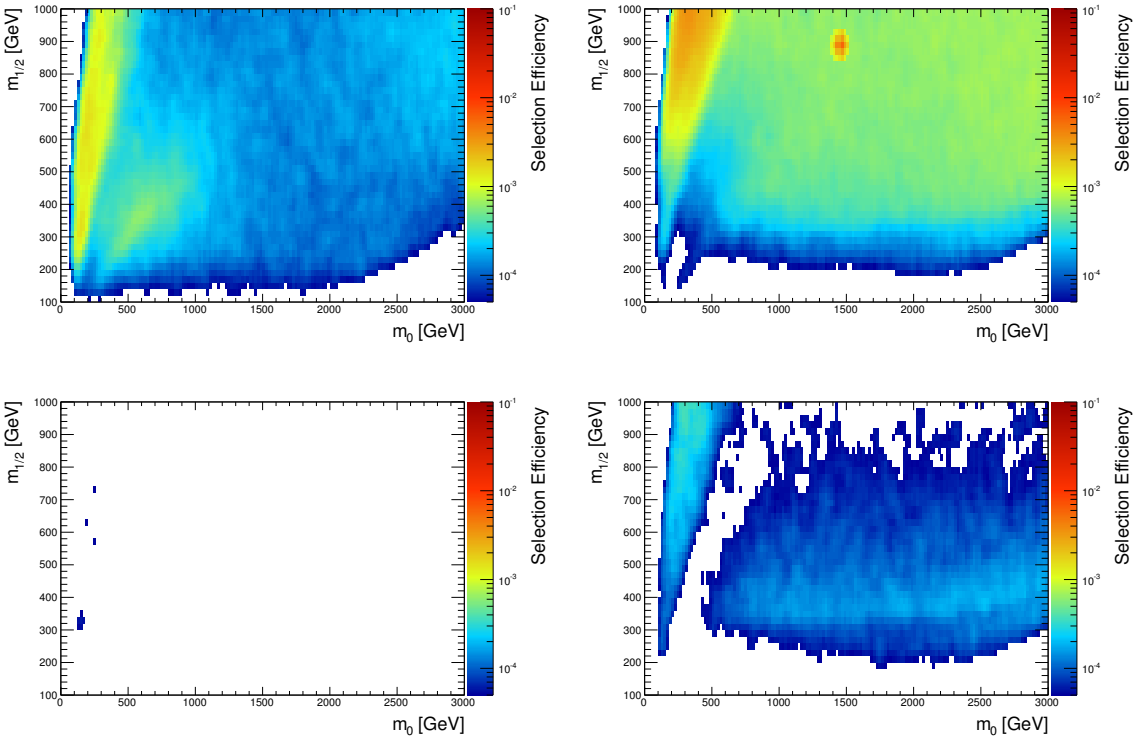

Figure F.5: Signal ($tan\beta = 10$, $A_0 = 0$, $sign(\mu) = +1$) selection efficiencies for the channels including 3 leptons (N(τ)=1), no-OSSF , $E_T^{\text{miss}} > 50\,\text{GeV}$, $H_T > 200\,\text{GeV}$ (top left), $E_T^{\text{miss}} > 50\,\text{GeV}$, $H_T < 200\,\text{GeV}$ (top right), $E_T^{\text{miss}} < 50\,\text{GeV}$, $H_T > 200\,\text{GeV}$ (bottom left) and $E_T^{\text{miss}} < 50\,\text{GeV}$, $H_T < 200\,\text{GeV}$ (botoom right). White spaces correspond to selection efficiencies below $\epsilon_{sel} < 0.00005$.

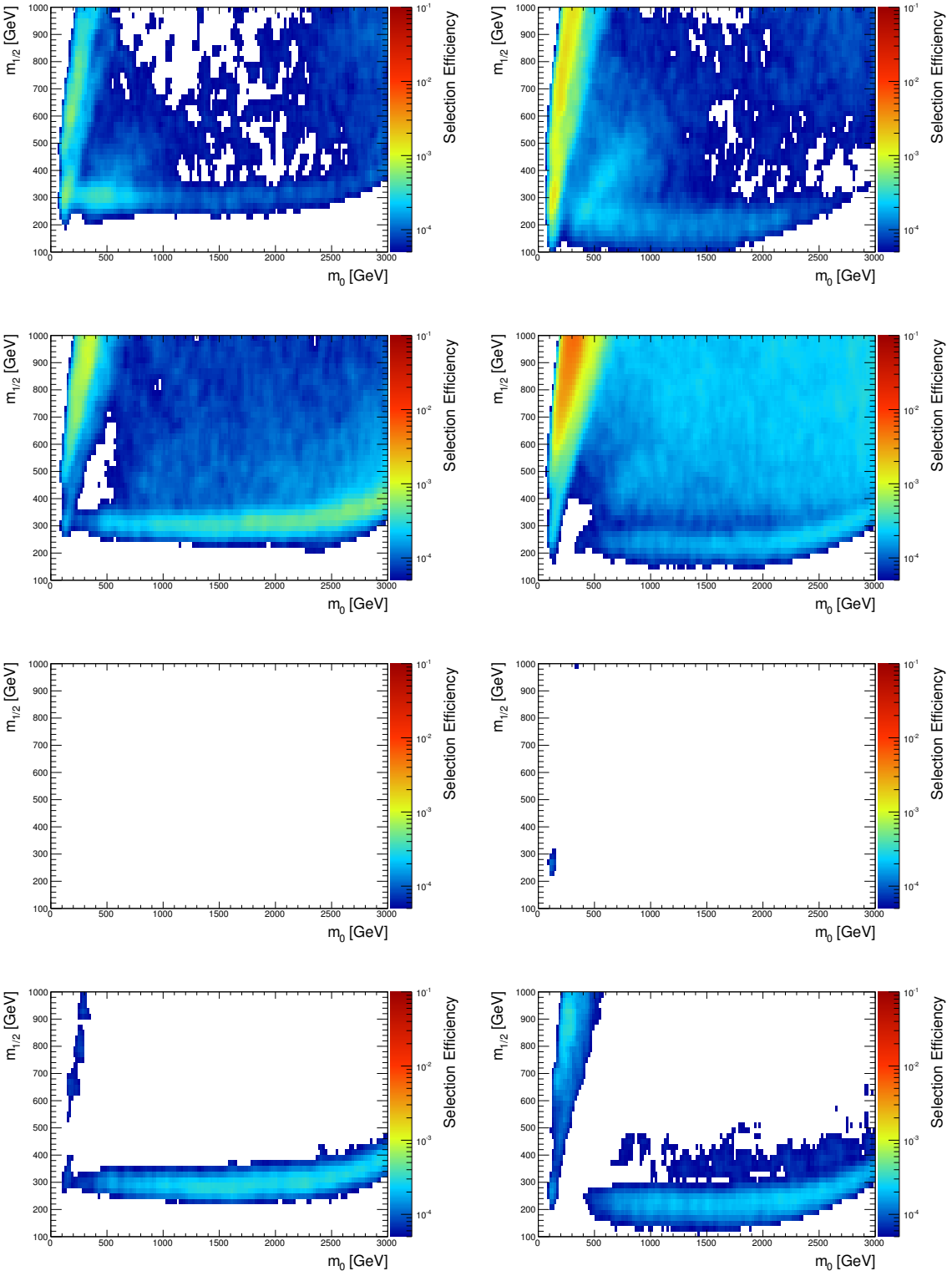

Figure F.6: Signal ($tan\beta = 10$, $A_0 = 0$, $sign(\mu) = +1$) selection efficiencies for the channels including 3 leptons (N(τ)=1), on-Z (left column), off-Z (right column), $E_T^{\text{miss}} > 50\,\text{GeV}$, $H_T > 200\,\text{GeV}$ (top row), $E_T^{\text{miss}} > 50\,\text{GeV}$, $H_T < 200\,\text{GeV}$ (second row), $E_T^{\text{miss}} < 50\,\text{GeV}$, $H_T > 200\,\text{GeV}$ (third row) and $E_T^{\text{miss}} < 50\,\text{GeV}$, $H_T < 200\,\text{GeV}$ (bottom row). White spaces correspond to selection efficiencies below $\epsilon_{sel} < 0.00005$.

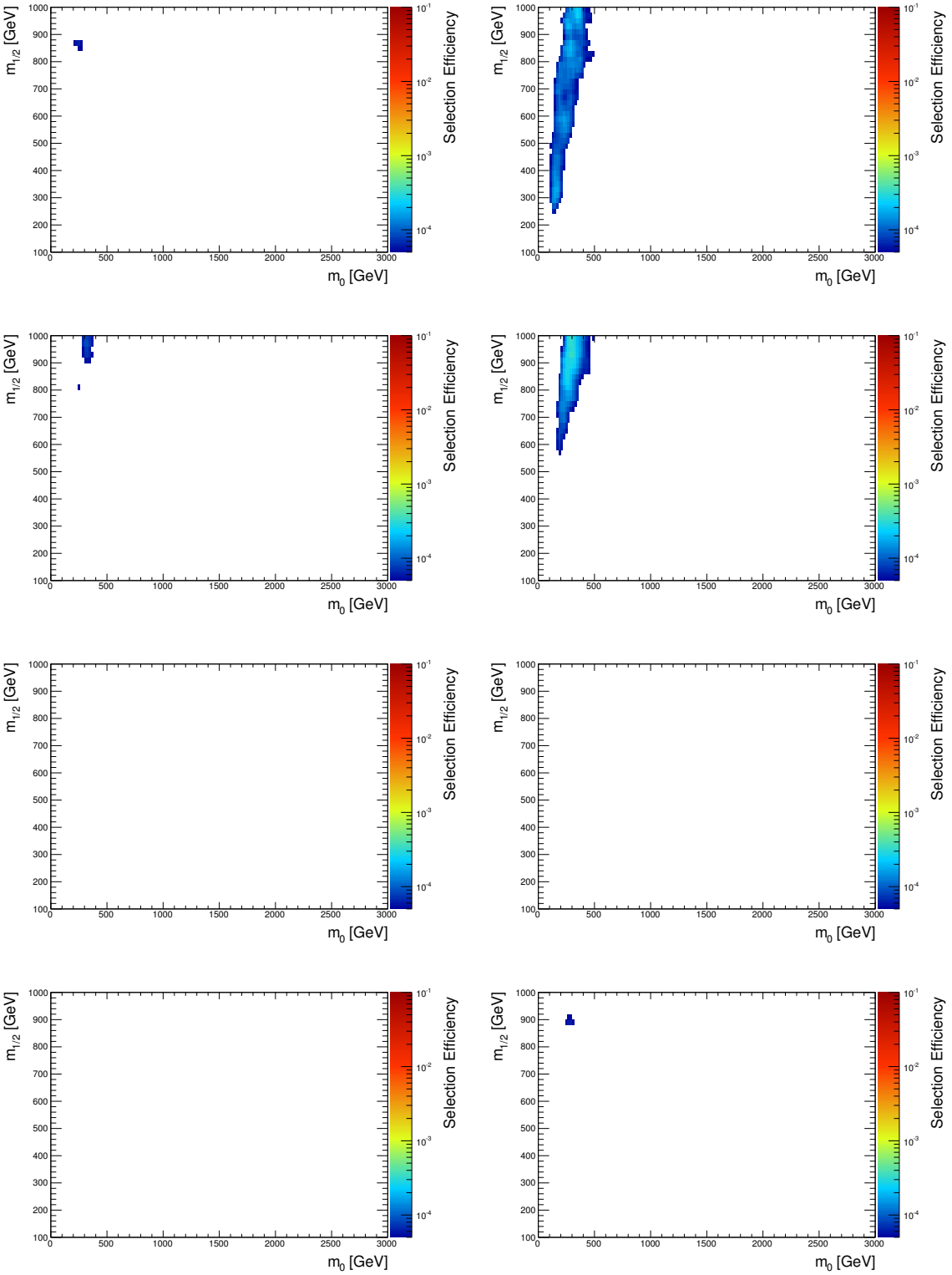

Figure F.7: Signal ($tan\beta = 10$, $A_0 = 0$, $sign(\mu) = +1$) selection efficiencies for the channels including 4 leptons (N(τ)=2), on-Z (left column), off-Z (right column), $E_T^{\text{miss}} > 50\,\text{GeV}$, $H_T > 200\,\text{GeV}$ (top row), $E_T^{\text{miss}} > 50\,\text{GeV}$, $H_T < 200\,\text{GeV}$ (second row), $E_T^{\text{miss}} < 50\,\text{GeV}$, $H_T > 200\,\text{GeV}$ (third row) and $E_T^{\text{miss}} < 50\,\text{GeV}$, $H_T < 200\,\text{GeV}$ (fourth row). White spaces correspond to selection efficiencies below $\epsilon_{sel} < 0.00005$.

APPENDIX G

cMSSM $tan\beta = 40$: Selection Efficiencies

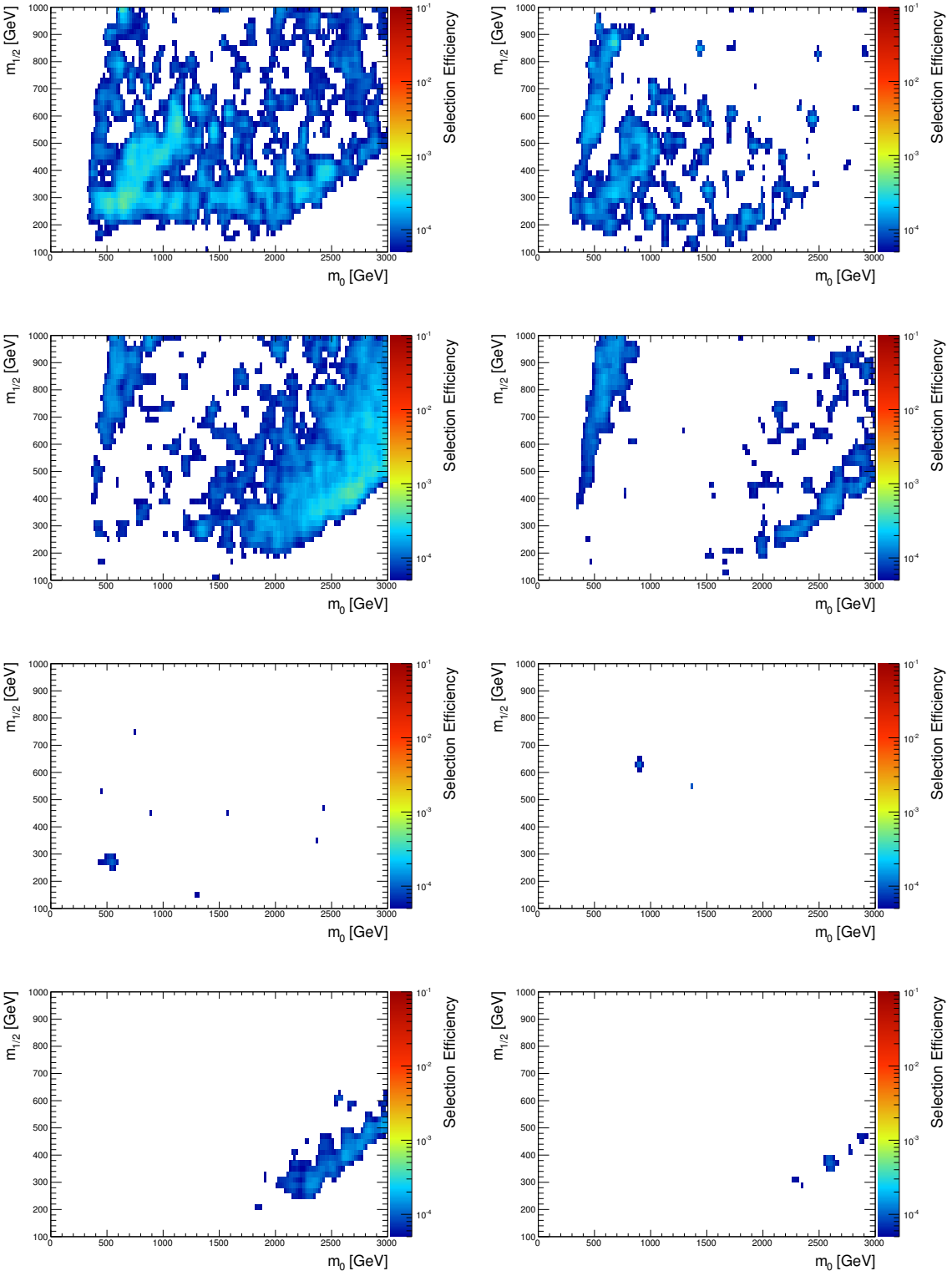

Figure G.1: Signal ($tan\beta = 40$, $A_0 = 0$, $sign(\mu) = +1$) selection efficiencies for the channels including 4 leptons (N(τ)=0), on-Z (left column), off-Z (right column), $E_T^{\text{miss}} > 50\,\text{GeV}$, $H_T > 200\,\text{GeV}$ (top row), $E_T^{\text{miss}} > 50\,\text{GeV}$, $H_T < 200\,\text{GeV}$ (second row), $E_T^{\text{miss}} < 50\,\text{GeV}$, $H_T > 200\,\text{GeV}$ (third row) and $E_T^{\text{miss}} < 50\,\text{GeV}$, $H_T < 200\,\text{GeV}$ (forth row). White spaces correspond to selection efficiencies below $\epsilon_{sel} < 0.00005$.

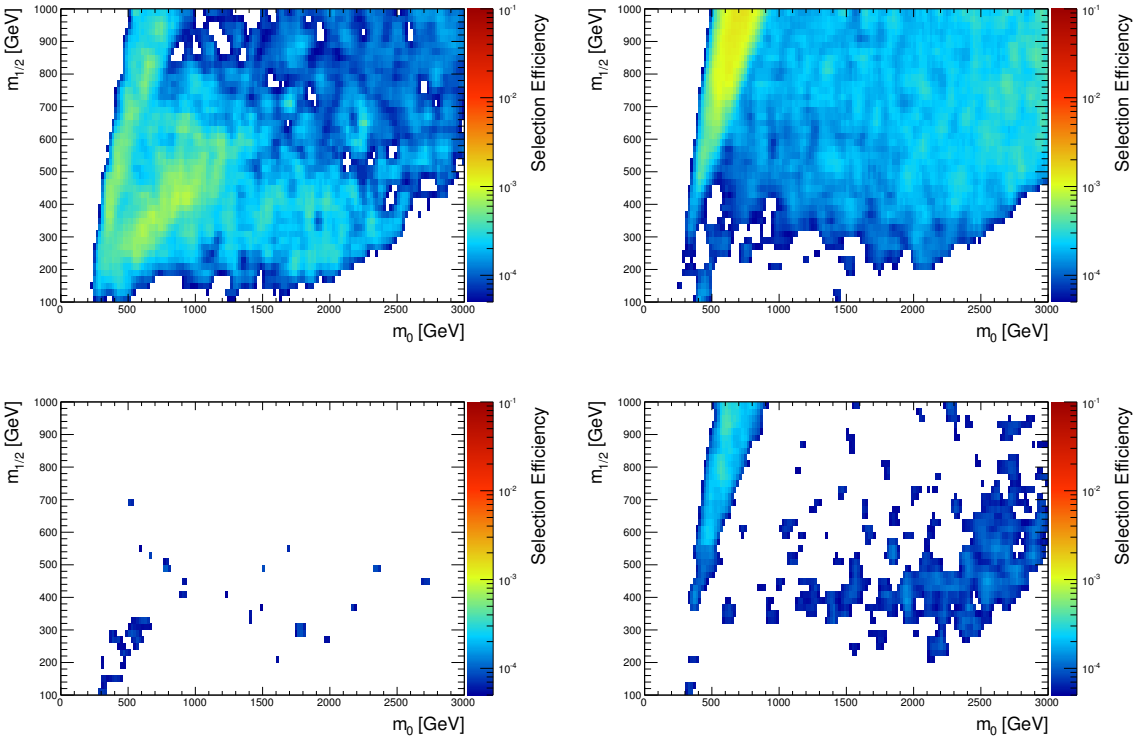

Figure G.2: Signal ($tan\beta = 40$, $A_0 = 0$, $sign(\mu) = +1$) selection efficiencies for the channels including 3 leptons (N(τ)=0), no-OSSF , $E_T^{\text{miss}} > 50\,\text{GeV}$, $H_T > 200\,\text{GeV}$ (top left), $E_T^{\text{miss}} > 50\,\text{GeV}$, $H_T < 200\,\text{GeV}$ (top right), $E_T^{\text{miss}} < 50\,\text{GeV}$, $H_T > 200\,\text{GeV}$ (bottom left) and $E_T^{\text{miss}} < 50\,\text{GeV}$, $H_T < 200\,\text{GeV}$ (botoom right). White spaces correspond to selection efficiencies below $\epsilon_{sel} < 0.00005$.

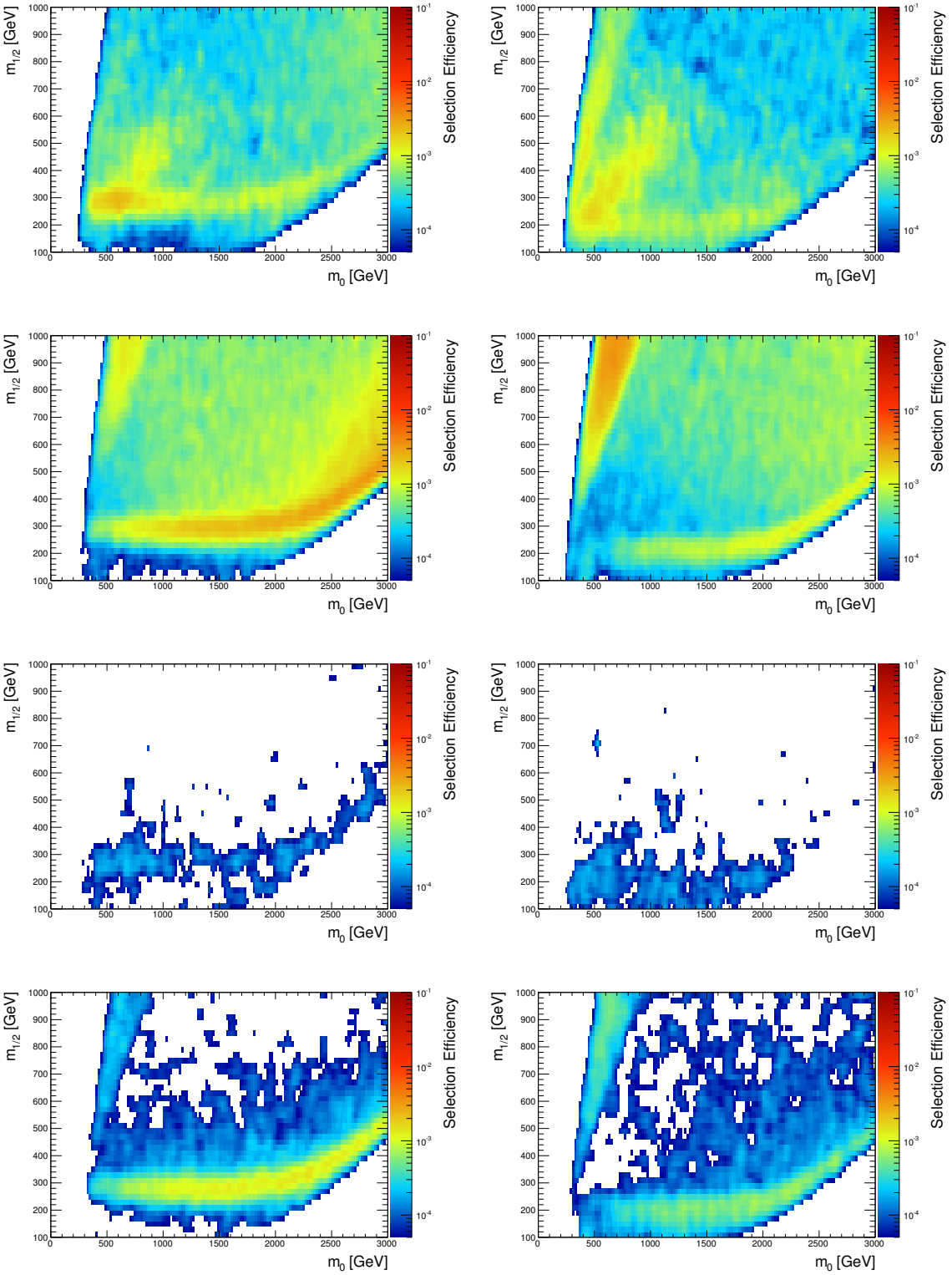

Figure G.3: Signal ($tan\beta = 40$, $A_0 = 0$, $sign(\mu) = +1$) selection efficiencies for the channels including 3 leptons (N(τ)=0), on-Z (left column), off-Z (right column), $E_T^{\text{miss}} > 50\,\text{GeV}$, $H_T > 200\,\text{GeV}$ (top row), $E_T^{\text{miss}} > 50\,\text{GeV}$, $H_T < 200\,\text{GeV}$ (second row), $E_T^{\text{miss}} < 50\,\text{GeV}$, $H_T > 200\,\text{GeV}$ (third row) and $E_T^{\text{miss}} < 50\,\text{GeV}$, $H_T < 200\,\text{GeV}$ (bottom row). White spaces correspond to selection efficiencies below $\epsilon_{sel} < 0.00005$.

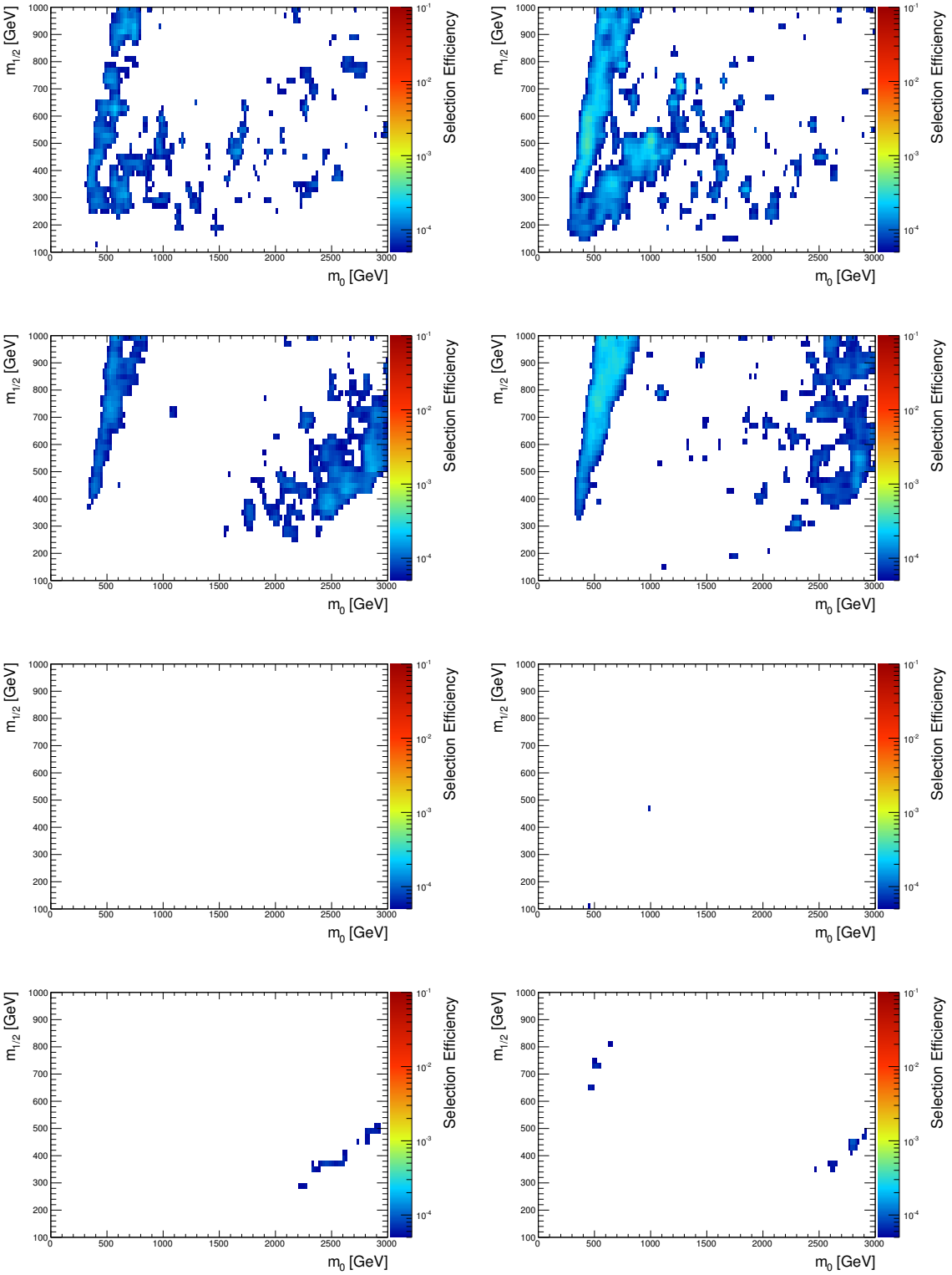

Figure G.4: Signal ($tan\beta = 40$, $A_0 = 0$, $sign(\mu) = +1$) selection efficiencies for the channels including 4 leptons (N(τ)=1), on-Z (left column), off-Z (right column), $E_T^{\text{miss}} > 50\,\text{GeV}$, $H_T > 200\,\text{GeV}$ (top row), $E_T^{\text{miss}} > 50\,\text{GeV}$, $H_T < 200\,\text{GeV}$ (second row), $E_T^{\text{miss}} < 50\,\text{GeV}$, $H_T > 200\,\text{GeV}$ (third row) and $E_T^{\text{miss}} < 50\,\text{GeV}$, $H_T < 200\,\text{GeV}$ (bottom row). White spaces correspond to selection efficiencies below $\epsilon_{sel} < 0.00005$.

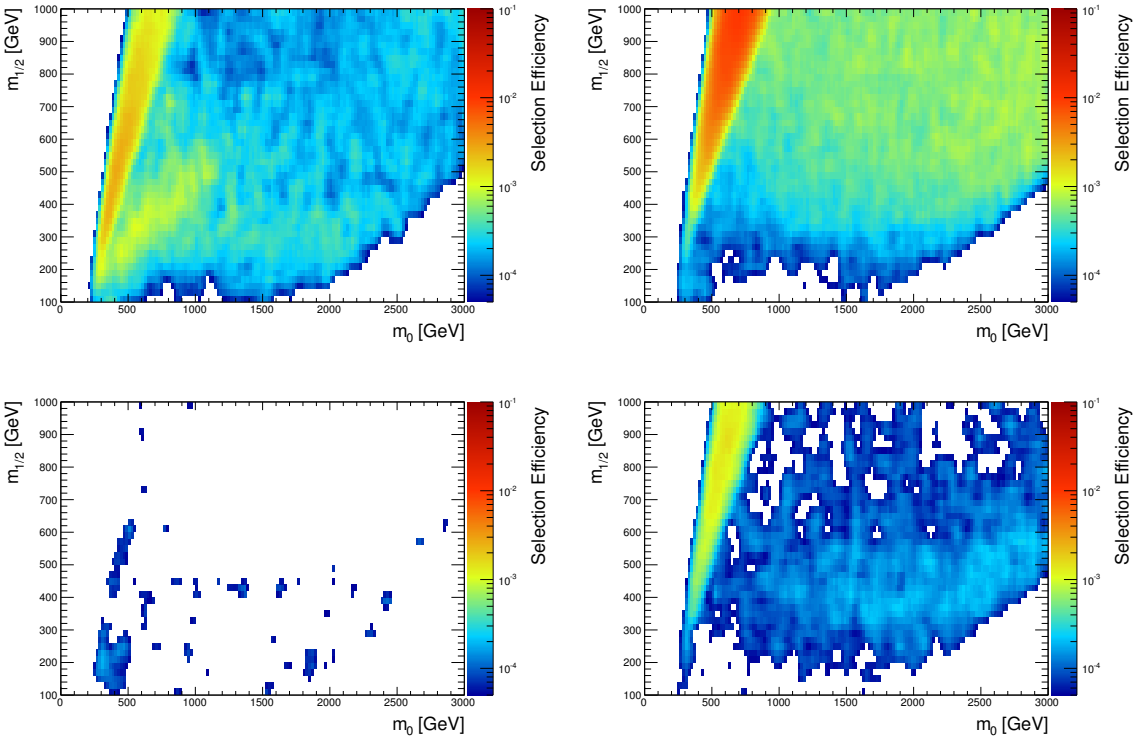

Figure G.5: Signal ($tan\beta = 40$, $A_0 = 0$, $sign(\mu) = +1$) selection efficiencies for the channels including 3 leptons (N(τ)=1), no-OSSF , $E_T^{\text{miss}} > 50\,\text{GeV}$, $H_T > 200\,\text{GeV}$ (top left), $E_T^{\text{miss}} > 50\,\text{GeV}$, $H_T < 200\,\text{GeV}$ (top right), $E_T^{\text{miss}} < 50\,\text{GeV}$, $H_T > 200\,\text{GeV}$ (bottom left) and $E_T^{\text{miss}} < 50\,\text{GeV}$, $H_T < 200\,\text{GeV}$ (botoom right). White spaces correspond to selection efficiencies below $\epsilon_{sel} < 0.00005$.

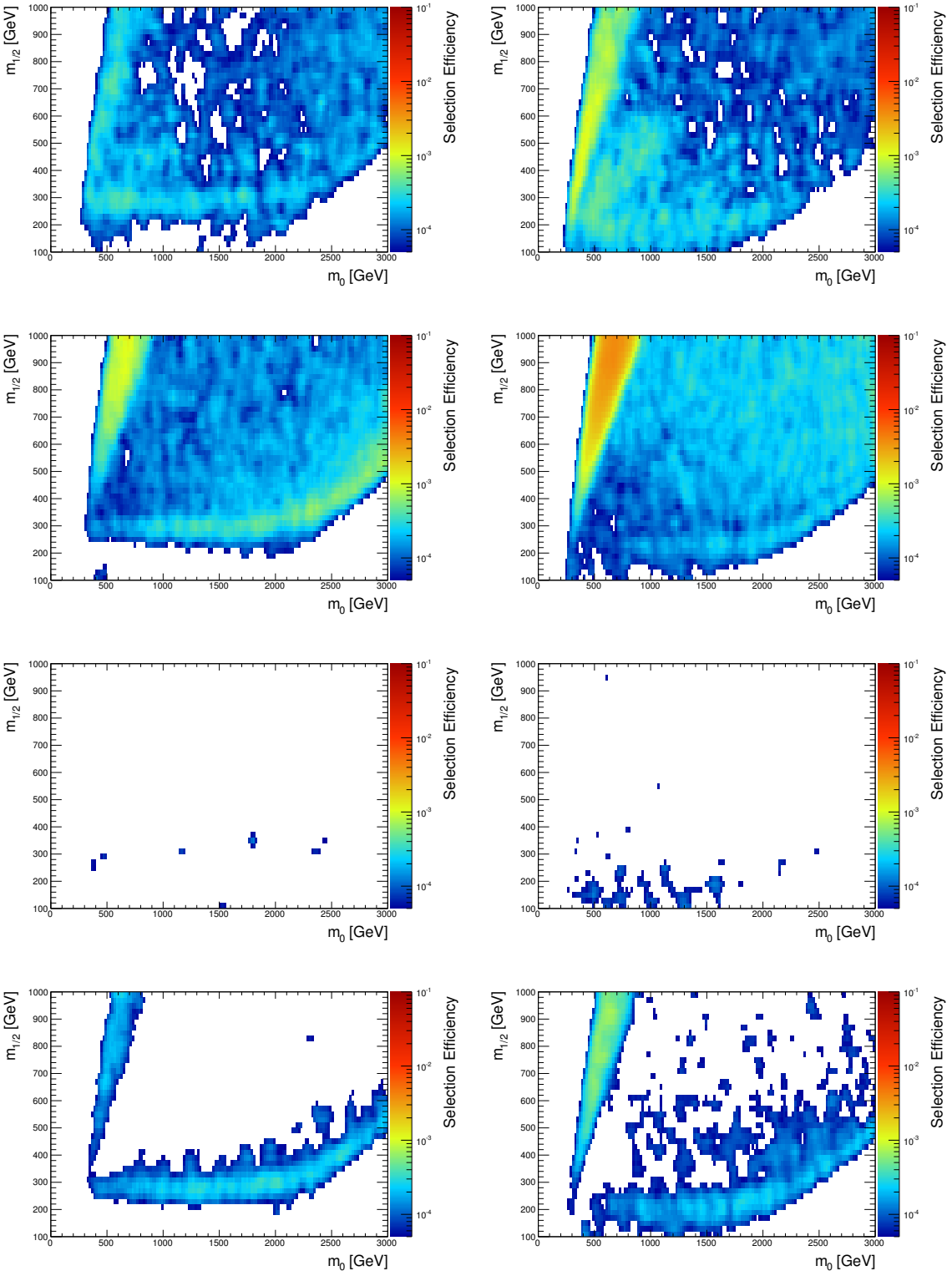

Figure G.6: Signal ($tan\beta = 40$, $A_0 = 0$, $sign(\mu) = +1$) selection efficiencies for the channels including 3 leptons (N(τ)=1), on-Z (left column), off-Z (right column), $E_T^{\text{miss}} > 50\,\text{GeV}$, $H_T > 200\,\text{GeV}$ (top row), $E_T^{\text{miss}} > 50\,\text{GeV}$, $H_T < 200\,\text{GeV}$ (second row), $E_T^{\text{miss}} < 50\,\text{GeV}$, $H_T > 200\,\text{GeV}$ (third row) and $E_T^{\text{miss}} < 50\,\text{GeV}$, $H_T < 200\,\text{GeV}$ (bottom row). White spaces correspond to selection efficiencies below $\epsilon_{sel} < 0.00005$.

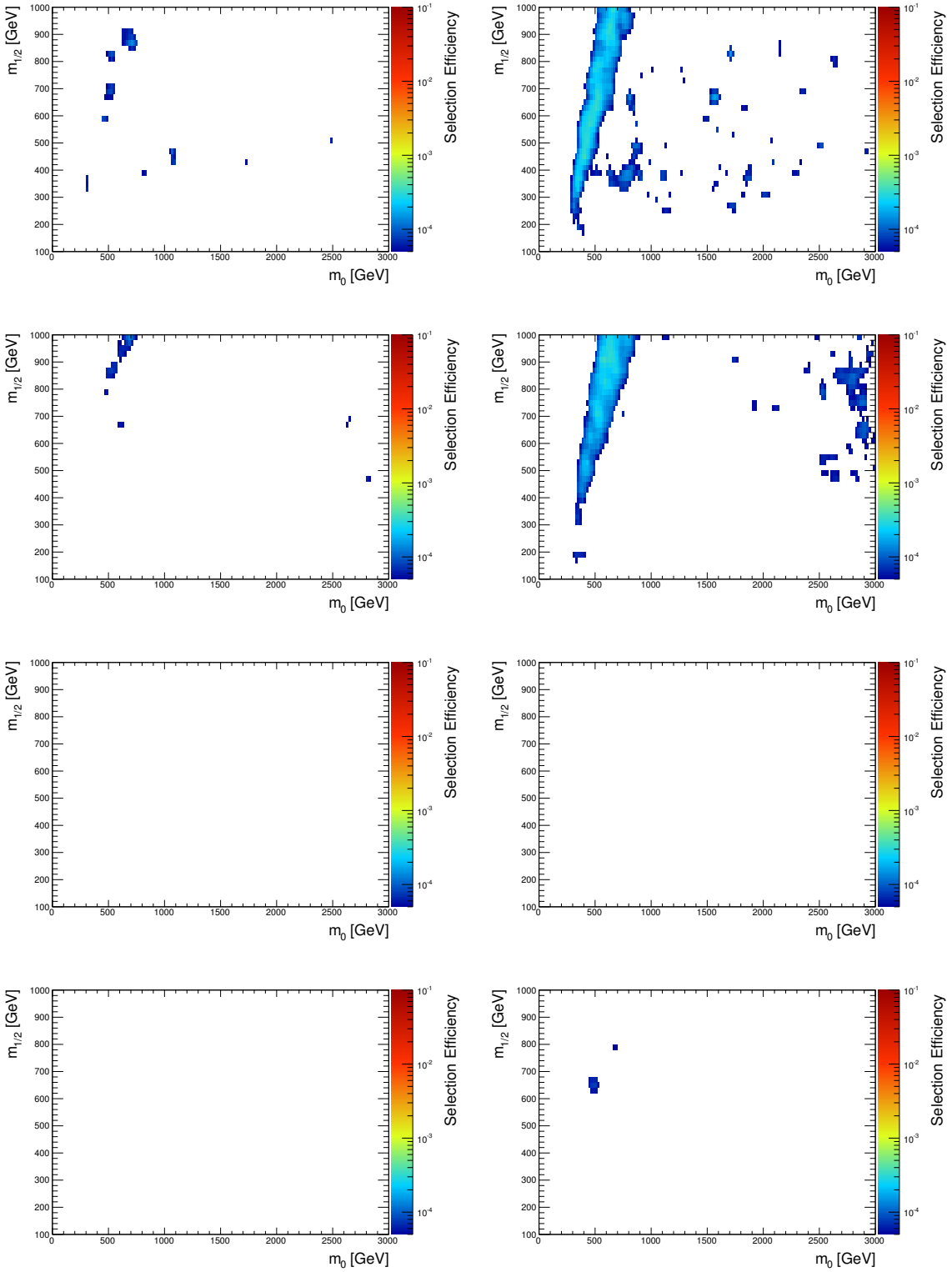

Figure G.7: Signal ($tan\beta = 40$, $A_0 = 0$, $sign(\mu) = +1$) selection efficiencies for the channels including 4 leptons (N(τ)=2), on-Z (left column), off-Z (right column), $E_T^{\text{miss}} > 50\,\text{GeV}$, $H_T > 200\,\text{GeV}$ (top row), $E_T^{\text{miss}} > 50\,\text{GeV}$, $H_T < 200\,\text{GeV}$ (second row), $E_T^{\text{miss}} < 50\,\text{GeV}$, $H_T > 200\,\text{GeV}$ (third row) and $E_T^{\text{miss}} < 50\,\text{GeV}$, $H_T < 200\,\text{GeV}$ (fourth row). White spaces correspond to selection efficiencies below $\epsilon_{sel} < 0.00005$.

APPENDIX H

Event Displays

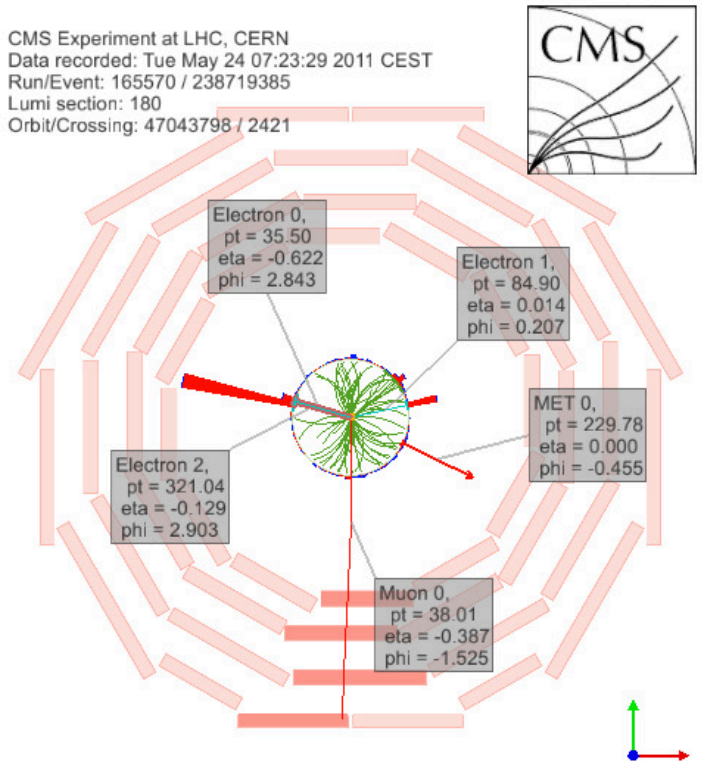

Figure H.1: Event display of the interesting 4 lepton (3 electrons and 1 muon) event with $H_T \approx 84\,\text{GeV}$ and $E_T^{\text{miss}} \approx 231\,GeV$ shown in the Rho-Phi coordinate system. The values differ from shown once in the display, due to energy corrections not applied. The invariant masses of the OS electron pairs are $m_{e_0e_2} \approx 322\,\text{GeV/c}^2$ and $m_{e_1e_2} \approx 54\,\text{GeV/c}^2$.

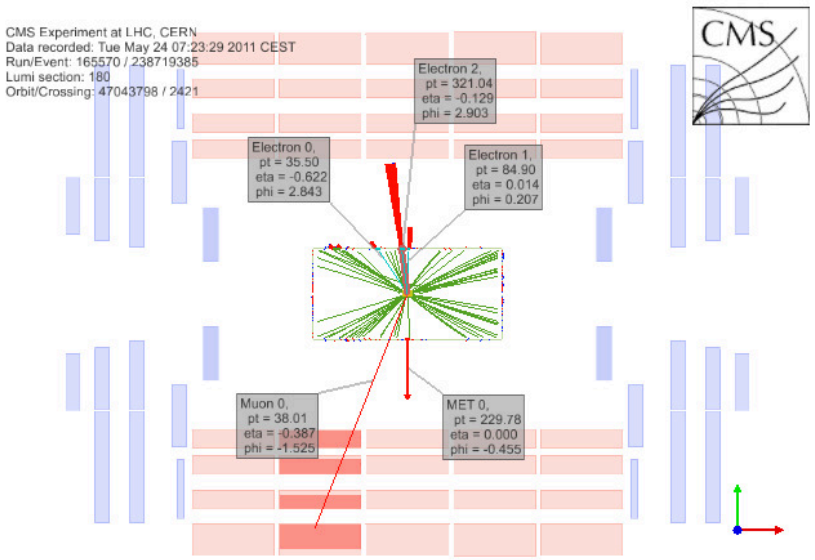

Figure H.2: Event display of the interesting 4 lepton (3 electrons and 1 muon) event with $H_T \approx 84\,\text{GeV}$ and $E_T^{\text{miss}} \approx 231\,GeV$ shown in the Rho-Z coordinate system. Same event as shown in Fig. H.1. Event display are made with Fireworks [183].

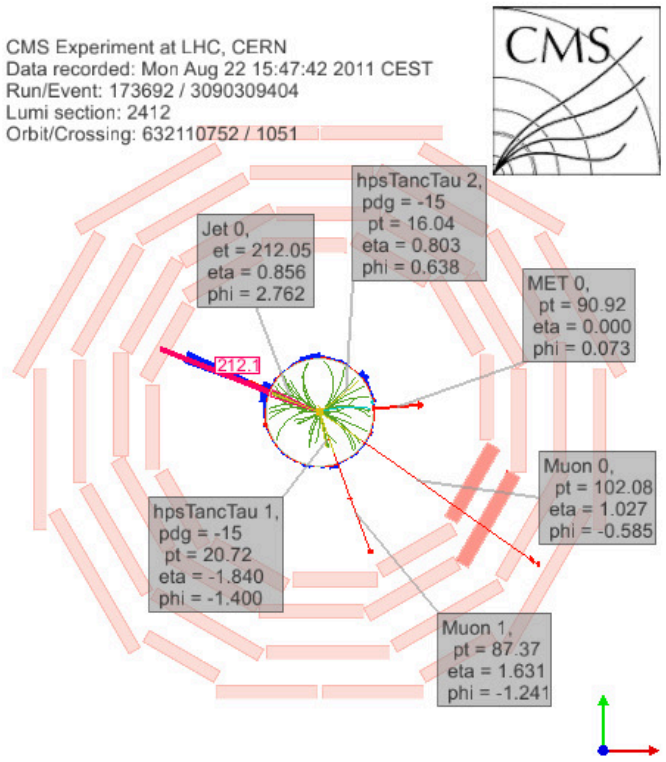

Figure H.3: Event display of the interesting 4 lepton (2 muons and 2 taus) event with $H_T \approx 223\,\text{GeV}$ and $E_T^{\text{miss}} \approx 81\,GeV$ shown in the Rho-Phi coordinate system. The values differ from shown once in the display, due to energy corrections not applied. The invariant masses of the OS muon pair is $m_{\mu_0\mu_1} \approx 84\,\text{GeV/c}^2$.

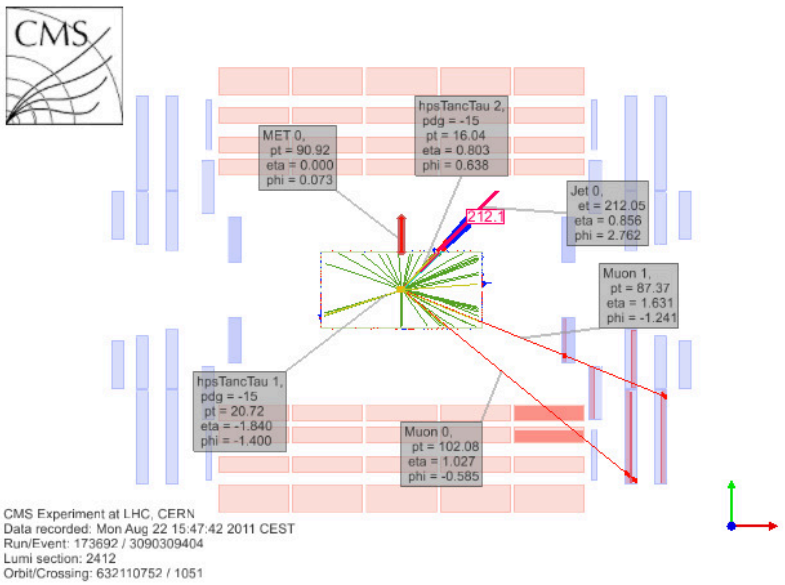

Figure H.4: Event display of the interesting 4 lepton (2 muons and 2 taus) event with $H_T \approx 84\,\text{GeV}$ and $E_T^{\text{miss}} \approx 231\,GeV$ shown in the Rho-Z coordinate system. Same event as shown in Fig. H.3.

Bibliography

[1] **CMS** Collaboration, S. Chatrchyan et al., "Combined results of searches for the standard model Higgs boson in pp collisions at sqrt(s) = 7 TeV," arXiv:1202.1488, 2012.

[2] **ATLAS** Collaboration, G. Aad et al., "Combined search for the Standard Model Higgs boson using up to 4.9 fb-1 of pp collision data at sqrt(s) = 7 TeV with the ATLAS detector at the LHC," *Phys.Lett.* **B710** 49–66, arXiv:1202.1408, 2012.

[3] **WMAP** Collaboration, D. Spergel et al., "First year Wilkinson Microwave Anisotropy Probe (WMAP) observations: Determination of cosmological parameters," *Astrophys.J.Suppl.* **148** 175–194, arXiv:astro-ph/0302209, doi:10.1086/377226, 2003.

[4] S. P. Martin, "A Supersymmetry Primer," arXiv:hep-ph/9709356v6, 2011.

[5] W. de Boer, "Grand unified theories and supersymmetry in particle physics and cosmology," *Prog.Part.Nucl.Phys.* **33** 201–302, arXiv:hep-ph/9402266, doi:10.1016/0146-6410(94)90045-0, 1994.

[6] M. Drees and M. M. Nojiri, "The Neutralino relic density in minimal $N = 1$ supergravity," *Phys.Rev.* **D47** 376–408, arXiv:hep-ph/9207234, doi:10.1103/PhysRevD.47.376, 1993.

[7] U. Amaldi, W. de Boer, and H. Furstenau, "Comparison of grand unified theories with electroweak and strong coupling constants measured at LEP," *Phys.Lett.* **B260** 447–455, doi:10.1016/0370-2693(91)91641-8, 1991.

[8] **CDF** Collaboration, A. Abulencia et al., "Search for anomalous production of multi-lepton events in $p\bar{p}$ collisions at $\sqrt{s}$ = 1.96-TeV," *Phys.Rev.Lett.* **98** 131804, arXiv:0706.4448, doi:10.1103/PhysRevLett.98.131804, 2007.

[9] S. Dube, J. Glatzer, S. Somalwar, A. Sood, and S. Thomas, "Addressing the Multi-Channel Inverse Problem at High Energy Coliders: A Model Independent Approach to the Search for New Physics with Trileptons," arXiv:0808.1605, 2008.

[10] **D0** Collaboration, V. Abazov et al., "Search for associated production of charginos and neutralinos in the trilepton final state using 2.3 fb^{-1} of data," *Phys.Lett.* **B680** 34–43, arXiv:0901.0646, doi:10.1016/j.physletb.2009.08.011, 2009.

[11] **CDF** Collaboration, R. Forrest, "Search for Supersymmetry in p anti-p Collisions at s**(1/2) =1.96-TeV Using the Trilepton Signature of Chargino-Neutralino Production," arXiv:0910.1931, 2009.

[12] **CMS** Collaboration, S. Chatrchyan et al., "Search for Physics Beyond the Standard Model Using Multilepton Signatures in pp Collisions at sqrt(s)=7 TeV," *Phys.Lett.* **B704** 411–433, arXiv:1106.0933, doi:10.1016/j.physletb.2011.09.047, 2011.

[13] S. Maruyama, "Supersymmetry Search in Multilepton Final States with Taus Using the CMS Detector at the LHC," 2011.

[14] D. Hits, "Multi-lepton search for new physics in 35 pb-1 proton-proton collisions at the LHC with the center mass energy of $\sqrt{s} = 7$ TeV with CMS detector". PhD thesis, Rutgers Univ., 2011.

[15] **CMS** Collaboration, "Search for supersymmetry in events with three or more leptons and missing energy," CMS PAS SUS-11-013, 2011.

[16] **Particle Data Group** Collaboration, R. Kelly et al., "Review of Particle Properties. Particle Data Group," *Rev.Mod.Phys.* **52** S1–S286, doi:10.1103/RevModPhys.52.S1, 1980.

[17] A. F. Falk, "The CKM matrix and the heavy quark expansion," arXiv:hep-ph/0007339, 2000.

[18] V. E. Barnes, P. L. Connolly, D. J. Crennell, B. B. Culwick, W. C. Delaney, W. B. Fowler, P. E. Hagerty, E. L. Hart, N. Horwitz, P. V. C. Hough, J. E. Jensen, J. K. Kopp, K. W. Lai, J. Leitner, J. L. Lloyd, G. W. London, T. W. Morris, Y. Oren, R. B. Palmer, A. G. Prodell, D. Radojičić, D. C. Rahm, C. R. Richardson, N. P. Samios, J. R. Sanford, R. P. Shutt, J. R. Smith, D. L. Stonehill, R. C. Strand, A. M. Thorndike, M. S. Webster, W. J. Willis, and S. S. Yamamoto, "Observation of a Hyperon with Strangeness Minus Three," *Phys. Rev. Lett.* **12** 204–206, doi:10.1103/PhysRevLett.12.204, 1964.

[19] C.-N. Yang and R. L. Mills, "Conservation of Isotopic Spin and Isotopic Gauge Invariance," *Phys.Rev.* **96** 191–195, doi:10.1103/PhysRev.96.191, 1954.

[20] M. E. Peskin and D. V. Schroeder, "An Introduction to quantum field theory," 1995.

[21] S. Glashow, "Partial Symmetries of Weak Interactions," *Nucl.Phys.* **22** 579–588, doi:10.1016/0029-5582(61)90469-2, 1961.

[22] S. Weinberg *Phys. Rev. Lett.* **19** 1264, 1967.

[23] A. Salam *Phys. Rev.* **127** 331., 1962.

[24] H. Fritzsch, M. Gell-Mann, and H. Leutwyler, "Advantages of the Color Octet Gluon Picture," *Phys.Lett.* **B47** 365–368, Introduces the term 'color', doi:10.1016/0370-2693(73)90625-4, 1973.

[25] D. Gross and F. Wilczek, "Asymptotically Free Gauge Theories. 1," *Phys.Rev.* **D8** 3633–3652, doi:10.1103/PhysRevD.8.3633, 1973.

[26] S. Weinberg, "Nonabelian Gauge Theories of the Strong Interactions," *Phys.Rev.Lett.* **31** 494–497, doi:10.1103/PhysRevLett.31.494, 1973.

[27] A. Oehler, "Strategy for an Initial Measurement of the Inclusive Jet Cross Section with the CMS Detector". PhD thesis, Karlsruher Institut fuer Technologie (KIT), 2009. IEKP-KA/2009-34.

[28] C. Wu, E. Ambler, R. Hayward, D. Hoppes, and R. Hudson, "Experimental test of Parity Conservation in Beta Decay," *Phys.Rev.* **105** 1413–1414, doi:10.1103/PhysRev.105.1413, 1957.

[29] F. Englert and R. Brout, "Broken Symmetry and the Mass of Gauge Vector Mesons," *Phys.Rev.Lett.* **13** 321–322, doi:10.1103/PhysRevLett.13.321, 1964.

[30] G. Guralnik, C. Hagen, and T. Kibble, "Global Conservation Laws and Massless Particles," *Phys.Rev.Lett.* **13** 585–587, doi:10.1103/PhysRevLett.13.585, 1964.

[31] P. W. Higgs, "Broken Symmetries and the Masses of Gauge Bosons," *Phys.Rev.Lett.* **13** 508–509, doi:10.1103/PhysRevLett.13.508, 1964.

[32] A. Djouadi, "The Anatomy of electro-weak symmetry breaking. I: The Higgs boson in the standard model," *Phys.Rept.* **457** 1–216, arXiv:hep-ph/0503172, doi:10.1016/j.physrep.2007.10.004, 2008.

[33] "https://twiki.cern.ch/twiki/bin/view/CMSPublic/PhysicsResults,".

[34] D. Kazakov, "Beyond the Standard Model (In search of Supersymmetry)", 2001.

[35] C. Sander, "Interpretation des Überschusses in diffuser galaktischer Gamma-Strahlung oberhalb 1 GeV als Annihilationssignal dunkler Materie". PhD thesis, Universitaet Karlsruhe (TH), 2005. IEKP-KA/2005-12.

[36] S. Dimopoulos and D. W. Sutter, "The Supersymmetric flavor problem," *Nucl.Phys.* **B452** 496–512, arXiv:hep-ph/9504415, doi:10.1016/0550-3213(95)00421-N, 1995.

[37] L. Alvarez-Gaume, J. Polchinski, and M. B. Wise, "Minimal Low-Energy Supergravity," *Nucl.Phys.* **B221** 495, Revised version, doi:10.1016/0550-3213(83)90591-6, 1983.

[38] W. de Boer, G. Burkart, R. Ehret, J. Lautenbacher, W. Oberschulte-Beckmann, et al., "Combined fit of low-energy constraints to minimal supersymmetry and discovery potential at

LEP-2," *Z.Phys.* **C71** 415–430, arXiv:hep-ph/9603350, doi:10.1007/s002880050187, 1996.

[39] **LEP Working Group for Higgs boson searches, ALEPH , DELPHI, L3 , OPAL** Collaboration, R. Barate et al., "Search for the standard model Higgs boson at LEP," *Phys.Lett.* **B565** 61–75, arXiv:hep-ex/0306033, doi:10.1016/S0370-2693(03)00614-2, 2003.

[40] **WMAP** Collaboration, E. Komatsu et al., "Five-Year Wilkinson Microwave Anisotropy Probe (WMAP) Observations: Cosmological Interpretation," *Astrophys.J.Suppl.* **180** 330–376, arXiv:0803.0547, doi:10.1088/0067-0049/180/2/330, 2009.

[41] C. Beskidt, W. de Boer, T. Hanisch, E. Ziebarth, V. Zhukov, et al., "Constraints on Supersymmetry from Relic Density compared with future Higgs Searches at the LHC," *Phys.Lett.* **B695** 143–148, arXiv:1008.2150, doi:10.1016/j.physletb.2010.10.048, 2011.

[42] **CDMS-II, CDMS** Collaboration, Z. Ahmed et al., "Search for inelastic dark matter with the CDMS II experiment," *Phys.Rev.* **D83** 112002, arXiv:1012.5078, doi:10.1103/PhysRevD.83.112002, 2011.

[43] **XENON100** Collaboration, E. Aprile et al., "Implications on Inelastic Dark Matter from 100 Live Days of XENON100 Data," *Phys.Rev.* **D84** 061101, arXiv:1104.3121, doi:10.1103/PhysRevD.84.061101, 2011.

[44] **EDELWEISS** Collaboration, E. Armengaud et al., "Final results of the EDELWEISS-II WIMP search using a 4-kg array of cryogenic germanium detectors with interleaved electrodes," *Phys.Lett.* **B702** 329–335, arXiv:1103.4070, doi:10.1016/j.physletb.2011.07.034, 2011.

[45] **HPQCD** Collaboration, E. Gamiz, C. T. Davies, G. Lepage, J. Shigemitsu, and M. Wingate, "Neutral B Meson Mixing in Unquenched Lattice QCD," *Phys.Rev.* **D80** 014503, arXiv:0902.1815, doi:10.1103/PhysRevD.80.014503, 2009.

[46] **CDF** Collaboration, T. Aaltonen et al., "Search for $B_s \to \mu^+\mu^-$ and $B_d \to \mu^+\mu^-$ Decays with CDF II," *Phys.Rev.Lett.* **107** 191801, arXiv:1107.2304, doi:10.1103/PhysRevLett.107.191801, 2011.

[47] **CMS + LHCb** Collaboration, "'Search for the rare decay $B_s^0 \to \mu^+\mu^-$ at the LHC with the CMS and LHCb experiments Combination of LHC results of the search for $B_s \to \mu^+\mu^-$ decays," CMS-PAS-BPH-11-019, LHCb-CONF-2011-047.

[48] C. Beskidt, W. de Boer, D. Kazakov, F. Ratnikov, E. Ziebarth, et al., "Constraints from the decay $B_s^0 \to \mu^+\mu^-$ and LHC limits on Supersymmetry," *Phys.Lett.* **B705** 493–497, arXiv:1109.6775, doi:10.1016/j.physletb.2011.10.053, 2011.

[49] **Muon G-2** Collaboration, G. Bennett et al., "Final Report of the Muon E821 Anomalous Magnetic Moment Measurement at BNL," *Phys.Rev.* **D73** 072003, arXiv:hep-ex/0602035, doi:10.1103/PhysRevD.73.072003, 2006.

[50] D. Stockinger, "The Muon Magnetic Moment and Supersymmetry," *J.Phys.G* **G34** R45–R92, arXiv:hep-ph/0609168, doi:10.1088/0954-3899/34/2/R01, 2007.

[51] S. P. Martin and J. D. Wells, "Muon anomalous magnetic dipole moment in supersymmetric theories," *Phys.Rev.* **D64** 035003, arXiv:hep-ph/0103067, doi:10.1103/PhysRevD.64.035003, 2001.

[52] "https://twiki.cern.ch/twiki/bin/view/CMSPublic/PhysicsResultsSUS,".

[53] "https://twiki.cern.ch/twiki/bin/view/AtlasPublic/SupersymmetryPublicResults,".

[54] O. Buchmueller, R. Cavanaugh, A. De Roeck, M. Dolan, J. Ellis, et al., "Supersymmetry in Light of 1/fb of LHC Data," arXiv:1110.3568, 2011.

[55] C. Beskidt, "Massengrenzen auf supersymmetrischen Teilchen aus kosmologischen und elektroschwachen Präzisionsdaten im Vergleich zu den Erwartungen am LHC," 2011. IEKP-KA/2011-25.

[56] O. Buchmueller, R. Cavanaugh, D. Colling, A. De Roeck, M. Dolan, et al., "Frequentist Analysis of the Parameter Space of Minimal Supergravity," *Eur.Phys.J.* **C71** 1583, arXiv:1011.6118, doi:10.1140/epjc/s10052-011-1583-8, 2011.

[57] P. Bagnaia et al., "http://user.web.cern.ch/public/en/About/History-en.html,".

[58] F. J. Hasert et al., "Search for elastic muon neutrino electron scattering," *Phys. Lett.* **B46** 121–124, doi:10.1016/0370-2693(73)90494-2, 1973.

[59] **Gargamelle Neutrino** Collaboration, F. J. Hasert et al., "Observation of neutrino-like interactions without muon or electron in the Gargamelle neutrino experiment," *Phys. Lett.* **B46** 138–140, doi:10.1016/0370-2693(73)90499-1, 1973.

[60] **UA1** Collaboration, G. Arnison et al., "Experimental Observation of Isolated Large Transverse Energy Electrons with Associated Missing Energy at s**(1/2) = 540-GeV," *Phys.Lett.* **B122** 103–116, 1983.

[61] **UA2** Collaboration, P. Bagnaia et al., "Evidence for Z0 $\rightarrow$ e+ e- at the CERN anti-p p Collider," *Phys.Lett.* **B129** 130–140, doi:10.1016/0370-2693(83)90744-X, 1983.

[62] E. Lyndon and B. Philip, "LHC Machine," *JINST* **3** S08001, doi:10.1088/1748-0221/3/08/S08001, 2008.

[63] **ATLAS** Collaboration, G. Aad et al., "The ATLAS Experiment at the CERN Large Hadron Collider," *JINST* **3** S08003, doi:10.1088/1748-0221/3/08/S08003, 2008.

[64] **LHCb** Collaboration, A. Alves et al., "The LHCb Detector at the LHC," *JINST* **3** S08005, doi:10.1088/1748-0221/3/08/S08005, 2008.

[65] **ALICE** Collaboration, K. Aamodt et al., "The ALICE experiment at the CERN LHC," *JINST* **3** S08002, doi:10.1088/1748-0221/3/08/S08002, 2008.

[66] **OPERA** Collaboration, M. Guler et al., "OPERA: An appearance experiment to search for nu/mu $\leftrightarrow$ nu/tau oscillations in the CNGS beam. Experimental proposal," 2000.

[67] **OPERA** Collaboration, T. Adam et al., "Measurement of the neutrino velocity with the OPERA detector in the CNGS beam," arXiv:1109.4897, 2011.

[68] S. van der Meer, "Calibration of the effective beam height in the ISR.," 1968.

[69] **CMS** Collaboration, "Absolute Calibration of Luminosity Measurement at CMS: Summer 2011 Update," CMS PAS EWK-11-001, 2011.

[70] **CMS** Collaboration, R. Adolphi et al., "The CMS experiment at the CERN LHC," *JINST* **3** S08004, doi:10.1088/1748-0221/3/08/S08004, 2008.

[71] **CMS** Collaboration, G. Bayatian et al., "CMS physics: Technical design report," 2006.

[72] D. Kotlinski, "The design of the CMS pixel detector system," *Nucl. Instrum. Methods Phys. Res., A* **477** no. 1-3, 446–50, 2002.

[73] **CMS** Collaboration, "The Tracker Project Technical Design Report," *CERN/LHCC 98-6, CMS TDR 5* 1998.

[74] **CMS** Collaboration, "Addendum to the Technical Design Report," *CERN/LHCC 2000-016, CMS TDR 5 Addendum 1* 2000.

[75] **CMS** Collaboration, "The CMS electromagnetic calorimeter project: Technical Design Report," 1997.

[76] **CMS** Collaboration, "Electromagnetic calorimeter calibration with 7 TeV data," CMS PAS EGM-10-003, 2010.

[77] **CMS** Collaboration, "The CMS hadron calorimeter project: Technical Design Report," 1997.

[78] **CMS** Collaboration, S. Chatrchyan et al., "Performance of the CMS Hadron Calorimeter with Cosmic Ray Muons and LHC Beam Data," *JINST* **5** T03012, arXiv:0911.4991, doi:10.1088/1748-0221/5/03/T03012, 2010.

[79] **ECAL/HCALs** Collaboration, E. Yazgan, "The CMS barrel calorimeter response to particle beams from 2-GeV/c to 350-GeV/c," *J.Phys.Conf.Ser.* **160** 012056, doi:10.1088/1742-6596/160/1/012056, 2009.

[80] G. Bayatian, A. Sirunian, I. Emelyanchik, V. Massolov, N. Shumeiko, et al., "Design, performance and calibration of the CMS forward calorimeter wedges," *Eur.Phys.J.* **C53** 139–166, doi:10.1140/epjc/s10052-007-0459-4, 2008.

[81] **CMS** Collaboration, G. Acquistapace et al., "CMS, the magnet project: Technical design report," 1997.

[82] **CMS** Collaboration, "The CMS muon project: Technical Design Report", Technical Design Report CMS, CERN, Geneva, 1997.

[83] **CMS** Collaboration, S. Dasu et al., "CMS. The TriDAS project. Technical design report, vol. 1: The trigger systems," 2000.

[84] **CMS** Collaboration, e. Sphicas, P., "CMS: The TriDAS project. Technical design report, Vol. 2: Data acquisition and high-level trigger," 2002.

[85] R. Wilkinson, B. Hegner, and C. Jones, "Usage of the python programming language in the CMS experiment," *J.Phys.Conf.Ser.* **219** 042026, doi:10.1088/1742-6596/219/4/042026, 2010.

[86] R. Brun, F. Rademakers, and S. Panacek, "ROOT, an object oriented data analysis framework," 2000.

[87] C. Jones et al., "The new CMS Event Data Model and Framework," in *Proceedings of the CHEP06 Conference*. CERN, Mumbia, India, 2006.

[88] T. Sjostrand, S. Mrenna, and P. Z. Skands, "PYTHIA 6.4 Physics and Manual," *JHEP* **0605** 026, arXiv:hep-ph/0603175, doi:10.1088/1126-6708/2006/05/026, 2006.

[89] T. Sjostrand, S. Mrenna, and P. Z. Skands, "A Brief Introduction to PYTHIA 8.1," *Comput.Phys.Commun.* **178** 852–867, arXiv:0710.3820, doi:10.1016/j.cpc.2008.01.036, 2008.

[90] M. Bahr, S. Gieseke, M. Gigg, D. Grellscheid, K. Hamilton, et al., "Herwig++ Physics and Manual," *Eur.Phys.J.* **C58** 639–707, arXiv:0803.0883, doi:10.1140/epjc/s10052-008-0798-9, 2008.

[91] M. L. Mangano, M. Moretti, F. Piccinini, R. Pittau, and A. D. Polosa, "ALPGEN, a generator for hard multiparton processes in hadronic collisions," *JHEP* **0307** 001, arXiv:hep-ph/0206293, 2003.

[92] T. Gleisberg, S. Hoeche, F. Krauss, M. Schonherr, S. Schumann, et al., "Event generation with SHERPA 1.1," *JHEP* **0902** 007, arXiv:0811.4622, doi:10.1088/1126-6708/2009/02/007, 2009.

[93] J. Alwall, M. Herquet, F. Maltoni, O. Mattelaer, and T. Stelzer, "MadGraph 5 : Going Beyond," *JHEP* **1106** 128, arXiv:1106.0522, doi:10.1007/JHEP06(2011)128, 2011.

[94] B. Allanach, "SOFTSUSY: a program for calculating supersymmetric spectra," *Comput.Phys.Commun.* **143** 305–331, arXiv:hep-ph/0104145, doi:10.1016/S0010-4655(01)00460-X, 2002.

[95] A. Djouadi, M. Muhlleitner, and M. Spira, "Decays of supersymmetric particles: The Program SUSY-HIT (SUspect-SdecaY-Hdecay-InTerface)," *Acta Phys.Polon.* **B38** 635–644, arXiv:hep-ph/0609292, 2007.

[96] B. Andersson, G. Gustafson, G. Ingelman, and T. Sjostrand, "Parton Fragmentation and String Dynamics," *Phys.Rept.* **97** 31–145, doi:10.1016/0370-1573(83)90080-7, 1983.

[97] S. Hoeche, F. Krauss, N. Lavesson, L. Lonnblad, M. Mangano, et al., "Matching parton showers and matrix elements," arXiv:hep-ph/0602031, 2006.

[98] A. Djouadi, J. Kalinowski, and M. Spira, "HDECAY: A Program for Higgs boson decays in the standard model and its supersymmetric extension," *Comput.Phys.Commun.* **108** 56–74, arXiv:hep-ph/9704448, doi:10.1016/S0010-4655(97)00123-9, 1998.

[99] M. Muhlleitner, A. Djouadi, and Y. Mambrini, "SDECAY: A Fortran code for the decays of the supersymmetric particles in the MSSM," *Comput.Phys.Commun.* **168** 46–70, arXiv:hep-ph/0311167, doi:10.1016/j.cpc.2005.01.012, 2005.

[100] **GEANT4** Collaboration, S. Agostinelli et al., "GEANT4: A Simulation toolkit," *Nucl.Instrum.Meth.* **A506** 250–303, doi:10.1016/S0168-9002(03)01368-8, 2003.

[101] **CMS** Collaboration, "Particle-Flow Event Reconstruction in CMS and Performance for Jets, Taus, and MET," CMS PAS PFT-09-001, 2009.

[102] T. Speer, W. Adam, R. Fruhwirth, A. Strandlie, T. Todorov, et al., "Track reconstruction in the CMS tracker," *Nucl.Instrum.Meth.* **A559** 143–147, doi:10.1016/j.nima.2005.11.207, 2006.

[103] **CMS** Collaboration, "Tracking and Primary Vertex Results in First 7 TeV Collisions," CMS PAS TRK-10-005, 2010.

[104] R. Fruhwirth, "Application of Kalman filtering to track and vertex fitting," *Nucl.Instrum.Meth.* **A262** 444–450, doi:10.1016/0168-9002(87)90887-4, 1987.

[105] T. Speer, K. Prokofiev, R. Fruhwirth, W. Waltenberger, and P. Vanlaer, "Vertex fitting in the CMS tracker," 2006.

[106] R. Fruhwirth, W. Waltenberger, and P. Vanlaer, "Adaptive vertex fitting," *J.Phys.G* **G34** N343, doi:10.1088/0954-3899/34/12/N01, 2007.

[107] **CMS** Collaboration, R. Salerno, "Electron reconstruction in CMS at the LHC," *Nucl.Phys.Proc.Suppl.* **172** 257–259, doi:10.1016/j.nuclphysbps.2007.08.149, 2007.

[108] W. Adam, R. Fruhwirth, A. Strandlie, and T. Todorov, "Reconstruction of electrons with the Gaussian sum filter in the CMS tracker at LHC," *eConf* **C0303241** TULT009, arXiv:physics/0306087, doi:10.1088/0954-3899/31/9/N01, 10.1088/0954-3899/31/9/N01, 2003.

[109] H. Bethe and W. Heitler, "On the Stopping of fast particles and on the creation of positive electrons," *Proc.Roy.Soc.Lond.* **A146** 83–112, 1934.

[110] **CMS** Collaboration, "https://twiki.cern.ch/twiki/bin/view/CMSPublic/PhysicsResultsEGM,".

[111] **CMS** Collaboration, "Measurement of the Inclusive Upsilon production cross section in pp collisions at $\sqrt{s} = 7$ TeV," CMS PAS BPH-10-003, 2010.

[112] "https://twiki.cern.ch/twiki/bin/view/CMSPublic/PhysicsResultsMUO,".

[113] CMS, "Performance of tau-lepton reconstruction and identification in CMS," arXiv:1109.6034, 2011.

[114] M. Cacciari, G. P. Salam, and G. Soyez, "The Anti-k(t) jet clustering algorithm," *JHEP* **0804** 063, arXiv:0802.1189, doi:10.1088/1126-6708/2008/04/063, 2008.

[115] S. D. Ellis and D. E. Soper, "Successive combination jet algorithm for hadron collisions," *Phys.Rev.* **D48** 3160–3166, arXiv:hep-ph/9305266, doi:10.1103/PhysRevD.48.3160, 1993.

[116] S. Catani, Y. L. Dokshitzer, M. Seymour, and B. Webber, "Longitudinally invariant K_t clustering algorithms for hadron hadron collisions," *Nucl.Phys.* **B406** 187–224, doi:10.1016/0550-3213(93)90166-M, 1993.

[117] Y. L. Dokshitzer, G. Leder, S. Moretti, and B. Webber, "Better jet clustering algorithms," *JHEP* **9708** 001, arXiv:hep-ph/9707323, 1997.

[118] **CMS** Collaboration, "Jet Plus Track Algorithm for Calorimeter Jet Energy Corrections in CMS," CMS PAS JME-09-002, 2009.

[119] **CMS** Collaboration, S. Chatrchyan et al., "Determination of Jet Energy Calibration and Transverse Momentum Resolution in CMS," *JINST* **6** P11002, arXiv:1107.4277, doi:10.1088/1748-0221/6/11/P11002, 2011.

[120] **CMS** Collaboration, "Jet Energy Corrections determination at 7 TeV ," CMS PAS JME-10-013, 2011.

[121] **CMS** Collaboration, "Missing E_T performance in CMS," CMS PAS JME-07-001, 2007.

[122] **CMS** Collaboration, "Performance of Track-Corrected Missing Transverse Energy in CMS," CMS PAS JME-09-010, 2009.

[123] **CMS** Collaboration, "CMS MET Performance in Events Containing Electroweak Bosons from pp Collisions at sqrt(s)=7 TeV.," CMS PAS JME-10-005, 2010.

[124] **CMS** Collaboration, "Missing Transverse Energy Performance in Minimum-Bias and Jet Events from Proton-Proton Collisions at $\sqrt{s} = 7$ TeV.," CMS PAS JME-10-004, 2010.

[125] G. L. Bayatyan, M. Della Negra, Foà, H. A, and A. Petrilli, "CMS computing: Technical Design Report," Submitted on 31 May 2005, 2005.

[126] **German CMS** Collaboration, A. Scheurer, "German contributions to the CMS computing infrastructure," *J.Phys.Conf.Ser.* **219** 062064, doi:10.1088/1742-6596/219/6/062064, 2010.

[127] V. Buege, "Virtualisation of Grid Resources and Prospects of the Measurement of Z Boson Production in Association with Jets at the LHC", Vdm Verlag, 2008.

[128] A. L. Read, "Modified frequentist analysis of search results (The CL(s) method)," 2000.

[129] **CMS** Collaboration, "Statistical model for the combined SUSY search," CMS AN-2010-236, 2010.

[130] M. Bonsch, "A Statistical Model for combining Muonic SUSY Searches with the CMS Detector at the LHC," 2010. IEKP-KA/2010-11.

[131] "https://mschen.web.cern.ch/mschen/LandS/,".

[132] L. Moneta, K. Belasco, K. S. Cranmer, S. Kreiss, A. Lazzaro, et al., "The RooStats Project," *PoS* **ACAT2010** 057, arXiv:1009.1003, 2010.

[133] K. S. Cranmer, "Statistics for the LHC: Progress, challenges, and future," 2007.

[134] R. D. Cousins, J. T. Linnemann, and J. Tucker, "Evaluation of three methods for calculating statistical significance when incorporating a systematic uncertainty into a test of the background-only hypothesis for a Poisson process," *Nucl.Instrum.Meth.* **A595** 480–501, doi:10.1016/j.nima.2008.07.086, 2008.

[135] G. Cowan, K. Cranmer, E. Gross, and O. Vitells, "Asymptotic formulae for likelihood-based tests of new physics," *Eur.Phys.J.* **C71** 1554, arXiv:1007.1727, doi:10.1140/epjc/s10052-011-1554-0, 2011.

[136] T. Junk, "Confidence level computation for combining searches with small statistics," *Nucl.Instrum.Meth.* **A434** 435–443, arXiv:hep-ex/9902006, doi:10.1016/S0168-9002(99)00498-2, 1999.

[137] **CMS** Collaboration, S. Chatrchyan et al., "Search for Supersymmetry at the LHC in Events with Jets and Missing Transverse Energy," arXiv:1109.2352, 2011.

[138] **CMS** Collaboration, G. Lungu, "Search for supersymmetry at the CMS in all-hadronic final state," arXiv:0910.3310, 2009.

[139] **CMS** Collaboration, S. Chatrchyan et al., "Search for supersymmetry in pp collisions at sqrt(s)=7 TeV in events with a single lepton, jets, and missing transverse momentum," arXiv:1107.1870, 2011.

[140] **CMS** Collaboration, "Search for new physics with same-sign isolated dilepton events with jets and missing energy," CMS-PAS-SUS-11-010, 2011.

[141] **CMS** Collaboration, "Search for new physics in events with opposite-sign dileptons and missing transverse energy," CMS-PAS-SUS-11-011, 2011.

[142] **CMS** Collaboration, "Search for Physics Beyond the Standard Model in Z + MET + Jets events at the LHC," CMS-PAS-SUS-11-012, 2011.

[143] W. Beenakker, R. Hopker, M. Spira, and P. Zerwas, "Squark and gluino production at hadron colliders," *Nucl.Phys.* **B492** 51–103, arXiv:hep-ph/9610490, doi:10.1016/S0550-3213(97)00084-9, 1997.

[144] W. Beenakker, M. Klasen, M. Kramer, T. Plehn, M. Spira, et al., "The Production of charginos / neutralinos and sleptons at hadron colliders," *Phys.Rev.Lett.* **83** 3780–3783, arXiv:hep-ph/9906298, doi:10.1103/PhysRevLett.83.3780, 10.1103/PhysRevLett.100.029901, 1999.

[145] W. Beenakker, R. Hopker, and M. Spira, "PROSPINO: A Program for the production of supersymmetric particles in next-to-leading order QCD," arXiv:hep-ph/9611232, 1996.

[146] **CMS** Collaboration, G. Bayatian et al., "CMS technical design report, volume II: Physics performance," *J.Phys.G* **G34** 995–1579, doi:10.1088/0954-3899/34/6/S01, 2007.

[147] A. Buckley, "http://www.insectnation.org/projects/pyslha,".

[148] **CMS** Collaboration, "Open beauty production cross section with muons in pp collisions at a center-of-mass energy of 7TeV," CMS-PAS-BPH-10-007, 2010.

[149] **CMS** Collaboration, "First Results on the Search for Stopped Gluinos in pp collisions at $\sqrt{s} = 7$ TeV," CMS-PAS-EXO-10-003, 2010.

[150] **CMS** Collaboration, "Electron reconstruction and identification at sqrt s =7 TeV," CMS PAS EGM-10-004, 2010.

[151] **CMS** Collaboration, "Performance of tau-lepton reconstruction and identification in CMS," arXiv:1109.6034, 2011.

[152] **CMS** Collaboration, "Performance of muon identification in pp collisions at $\sqrt{s} = 7$ TeV," CMS PAS MUO-10-002, 2010.

[153] J. M. Campbell, R. Ellis, and C. Williams, "Vector boson pair production at the LHC," *JHEP* **1107** 018, arXiv:1105.0020, doi:10.1007/JHEP07(2011)018, 2011.

[154] **CMS** Collaboration, "Top pair cross section in dileptons," CMS-PAS-TOP-11-005, 2011.

[155] **CMS** Collaboration, "Measurement of the WW, WZ and ZZ cross sections at CMS ," CMS PAS EWK-11-010, 2011.

[156] M. Niegel, "Search for Supersymmetry in Trimuon Final States with the CMS Detector," 2009. IEKP-KA/2009-37.

[157] D. Troendle, "Myonenidentifikation im CMS-Detektor am LHC," 2008. IEKP-KA/2008-29.

[158] **CMS** Collaboration, "Isolated Photon Reconstruction and Identification at $\sqrt{s} = 7$ TeV," CMS PAS EGM-10-006, 2010.

[159] "https://twiki.cern.ch/twiki/bin/view/CMSPublic/WorkBookCollisionsDataAnalysis,".

[160] **CMS** Collaboration, "Measurement of the ttbar production cross section in the fully hadronic decay channel in pp collisions at 7 TeV," CMS-PAS-TOP-11-007, 2011.

[161] **CMS** Collaboration, "Measurement of ttbar Pair Production Cross Section at sqrt(s)=7 TeV using b-quark Jet Identification Techniques in Lepton + Jet Events ," CMS-PAS-TOP-11-003, 2011.

[162] **CMS** Collaboration, "Status of b-tagging tools for 2011 data analysis.," CMS PAS BTV-11-002, 2011.

[163] **CMS** Collaboration, "Performance of b-jet identification in CMS," CMS PAS BTV-11-001, 2011.

[164] R. C. Gray, C. Kilic, M. Park, S. Somalwar, and S. Thomas, "Backgrounds To Higgs Boson Searches from $W\gamma^* \to l\nu l(l)$ Asymmetric Internal Conversion," arXiv:1110.1368, 2011.

[165] **CMS** Collaboration, S. Chatrchyan et al., "Measurement of W+W- Production and Search for the Higgs Boson in pp Collisions at sqrt(s) = 7 TeV," *Phys.Lett.* **B699** 25–47, arXiv:1102.5429, doi:10.1016/j.physletb.2011.03.056, 2011.

[166] **CMS** Collaboration, "Search for the Higgs Boson in the Fully Leptonic W^+W^- Final State," 2011.

[167] **CMS** Collaboration, "Search for a Standard Model Higgs boson produced in the decay channel 4l," 2011.

[168] **CMS** Collaboration, "Interpretation of Searches for Supersymmetry," CMS PAS SUS-11-016, 2012.

[169] K. Matchev and R. Remington, "Updated templates for the interpretation of LHC results on supersymmetry in the context of mSUGRA," arXiv:1202.6580, 2012.

[170] G. Giudice and R. Rattazzi, "Theories with gauge mediated supersymmetry breaking," *Phys.Rept.* **322** 419–499, arXiv:hep-ph/9801271, doi:10.1016/S0370-1573(99)00042-3, 1999.

[171] **CMS** Collaboration, "Search for supersymmetry in events with three or more leptons and missing energy," *CMS PAS SUS-11-013* 2011.

[172] **CMS** Collaboration, "Search for Supersymmetry with Trimuons," CMS AN-2009/077, 2009.

[173] **CMS** Collaboration, "Generators comparison for Z/W/ T - T+jets production at 10 TeV," CMS AN-2010/002, 2010.

[174] **CMS** Collaboration, "Side band measurements in SUSY search with muons," CMS AN-2010/075, 2010.

[175] **CMS** Collaboration, "Search for SUSY with one, two and three muons at 10 TeV," CMS AN-2010/001, 2010.

[176] **CMS** Collaboration, "Systematic Uncertainties for SUSY Searches in CMS," CMS AN-2010/232, 2010.

[177] **CMS** Collaboration, "Statistical model for the combined SUSY search," CMS AN-2010/236, 2010.

[178] **CMS** Collaboration, "Background study for the RA7 multileptonic SUSY search using the ABCD method and reach in mSUGRA," CMS AN-2010/302, 2010.

[179] **CMS** Collaboration, "Multileptonic SUSY searches with Jets and MET," CMS AN-2011/288, 2011.

[180] **CMS** Collaboration, "The ST distribution reconsidered," CMS AN-2011/309, 2011.

[181] **CMS** Collaboration, "Interpretations of Multileptonic SUSY searches with Jets and MET for EWKino Production," CMS AN-2012/10, 2012.

[182] **CMS** Collaboration, S. Chatrchyan et al., "Search for Physics Beyond the Standard Model Using Multilepton Signatures in pp Collisions at sqrt(s)=7 TeV," arXiv:1106.0933, 2011.

[183] D. Kovalskyi, M. Tadel, A. Mrak-Tadel, B. Bellenot, V. Kuznetsov, C. D. Jones, L. Bauerdick, M. Case, J. Mülmenstädt, and A. Yagil, "Fireworks: A physics event display for CMS," *Journal of Physics: Conference Series* **219** no. 3, 032014, 2010.

List of Figures

2.1 The Higgs potential for $\lambda > 0$ and $\mu^2 > 0$ and $\mu^2 < 0$ 16
2.2 Electroweak production cross section measured with the CMS experiment. 17
2.3 $t\bar{t}$ production cross section measured with the CMS experiment. 18

3.1 Evolution of the three coupling constants of the electroweak and strong interaction . 21
3.2 MSSM RGEs solutions 25
3.3 Allowed regions in the cMSSM m_0-$m_{1/2}$ plane for correct relic density in the universe 29
3.4 CMS and ATLAS exclusion limits in the context of the cMSSM model ($tan\beta = 10$, $A_0 = 0$, $sign(\mu) = +1$) 31
3.5 The best-fit point after incorporation constraints including the LHC 1 fb^{-1} results . . 32

4.1 CERN accelerator facility 43
4.2 The daily peak instantaneous and integrated luminosity delivered by the LHC. 44
4.3 A schematic overview of the Compact Muon Solenoid detector with its various subsystems 45
4.4 Schematic overview of the CMS inner tracking system 46
4.5 Schematic transverse overview of the ECAL configuration in the CMS experiment. . 47
4.6 Schematic overview of the CMS hadron calorimeter 48
4.7 The muon system of the CMS detector 49
4.8 The CMS data acquisition and trigger systems 50

5.1 A sample module chain in the CMSSW frameworw 52
5.2 Vertex resolution as a function of number of tracks 56
5.3 Dielectron/photon invariant mass spectrum 57
5.4 Invariant mass spectrum for pairs of muon. 63
5.5 Central Jet ($|\eta| < 0.5$) p_T resolution measured in data compared to MC predictions for caloJets and PFJets 64
5.7 Schematic view of the WLCG tier structure of CMS. 65

6.1 Squark/gluino production at hadron colliders. 70
6.2 Gaugino production at hadron colliders 70
6.3 Sparticle production cross section in the m_0-$m_{1/2}$ plane. 72
6.4 Squark/gluino and chargino/neutralino production cross sections 73
6.5 Regions in the m_0-$m_{1/2}$ plane for fixed $tan\beta = 10$, $A_0 = 0$ and $sign(\mu) = +1$ corresponding the dominant decay modes of the lightest charginos $\tilde{\chi}_1^{\pm}$ and next-to-lightest neutralinos $\tilde{\chi}_2^0$ 74
6.6 Gluino-gluino and direct neutralino-chargino decay 75
6.7 Mass spectrum of LM6 SUSY benchmark points 77
6.8 Mass spectrum of LM9 SUSY benchmark points 78
6.9 Kinematic distribution for the benchmark points LM6 and LM9 79
6.10 Fake lepton production mechanism. 80
6.11 Double boson production at hadron colliders. 81
6.12 Typical diagrams for Drell-Yan+Jets and $t\bar{t}$ production. 81
6.13 Third loose lepton (e, μ) transverse momentum p_T, relative isolation Riso and transverse impact parameter dxy for LM9 and SM processes 82
6.14 H_T , E_T^{miss} , L_T, S_T, m_{ll} and jet multiplicity for LM9 and SM processes 83

7.1 E_T^{miss} and H_T distribution for different PU scenarios 87
7.2 Number of primary vertices in data and MC events 88
7.3 Muon ID and ISO efficiency 93
7.4 Electon ID and ISO efficiency 94
7.5 τ_h isolation and identification efficiency control sample for HPS τ_h candidates . . . 96
7.6 Average trigger efficiency of Double-Muon, Double-Electron and Electron-Muon cross trigger paths 97
7.7 H_T distribution for SM backgrounds and a SUSY benchmark model 99
7.8 Average $<E_T^{\text{miss}}>$ and $< H_T >$ in the cMSSM parameter space 100
7.9 Event Selection Strategy 101

8.1 Invariant mass distributions of two tight leptons OS-SF 106
8.2 Transverse momentum p_T and pseudo rapidity η distribution of fake leptons (e, μ) in Drell-Yan events 107
8.3 Relative isolation Riso distribution of fake leptons in Drell-Yan events 109
8.4 Transverse momentum p_T and pseudo rapidity η distribution of a third vloose HPS τ_h candidates in DY+Jets events 110
8.5 Relative isolation Riso distribution for loose leptons (e, μ) in Z events, where also the transverse impact parameter is inverted $> dxy| > 0.02$. 111
8.6 H_T and E_T^{miss} distribution for two tight leptons opposite sign opposite flavor ($e^{\pm}, \mu^{\mp}$) 113
8.7 Transverse momentum p_T and pseudo rapidity η distributions for loose fake leptons (e, μ) in leptonic $t\bar{t}$ events 114
8.8 Transverse momentum p_T and pseudo rapidity η distribution for fake HPS τ_h candidates in leptonic $t\bar{t}$ events 115
8.9 Relative isolation distribution for fake leptons (e, μ) in the $t\bar{t}$ events 116

8.10 Relative isolation Riso distribution for fake leptons (e, μ) with the inverted transverse impact parameter requirement in the leptonic $t\bar{t}$ fake enriched data sample 116
8.11 H_T and E_T^{miss} distribution in $t\bar{t}$ events with one prompt lepton events 118
8.12 Relative isolation distribution of a second but loose lepton (e, μ) in $t\bar{t}$ events with one prompt lepton. 119
8.13 Relative isolation distribution of a second but loose lepton (e, μ) with inverted d_{xy} requirement in $t\bar{t}$ events with one prompt lepton. 119
8.14 Transverse momentum p_T distributions for τ_h candidates in the isolation side-band and isolation signal region in $t\bar{t}$ events with one prompt lepton. 120
8.15 H_T and E_T^{miss} distributions for three lepton events including two tight and one loose lepton. 122
8.16 Asymmetric Photon Conversion in Drell-Yan events 123
8.17 Three body mass $m_{ll\gamma}$ distribution of $Z \to l^+l^- + \gamma$ events. 124
8.18 Events selected with two tight OF-SF leptons and an additional tight photon distributed in the $m_{l^+l^-}$-$m_{l^+l^-\gamma}$ plane 125
8.19 Three body mass distribution for $l^+l^-e^\pm$ and $\mu^+\mu^-\mu^\pm$ events with low H_T and low E_T^{miss} 126
8.20 H_T and E_T^{miss} distribution for events including $l^+l^-e^\pm$ and $\mu^+\mu^-\mu^\pm$, where the OS-SF lepton pair should be off-Z. 127
8.21 Four body mass of events with four leptons 128
8.22 Invariant mass distribution m_{ll} of all OS-SF lepton pairs in the $WZ/\gamma*$ control sample 130
8.23 Example diagrams for WZ + 0, 1 and 2 Jets in the final state used within the Madgraph MC production. 131
8.24 H_T and E_T^{miss} distribution of WZ events 132
8.25 ZZ control sample with four tight leptons. 132
8.26 H_T and E_T^{miss} distribution of ZZ events 133
8.27 Relative background composition of different SM processes contributing to the three lepton (e, μ) channels with one OS-SF pair on-Z 135
8.28 Relative background composition of different SM processes contributing to the three lepton (e, μ) channels with one OS-SF pair off-Z 136
8.29 Relative background composition of different SM processes contributing to the three lepton (e, μ) channels without OS-SF pairs 137

9.1 E_T^{miss} and H_T distributions for three lepton events 142
9.2 E_T^{miss} distributions for three lepton events including one τ 143
9.3 E_T^{miss} and H_T distribution for three lepton events including signal prediction for the SUSY benchmark model LM9 144
9.4 Excluded regions for the cMSSM scenarios with $tan\beta = 10$ 150
9.6 Branching Fraction of the next to lightest neutralino ($\tilde{\chi}_2^0$) and lightest chargino 154
9.7 Excluded regions for the cMSSM scenario with $tan\beta = 40$ 155
9.8 Mass difference ΔM between left (right)-handed sleptons and the lightest stau as a function of $\tan\beta$ 156
9.10 Schematic diagram for the SMS model TChiSlepSlep. 157

9.11 Acceptance × efficiency for the signal, and 95 C.L. upper limit on the production cross section of the SMS model *TChiSlepSlep* 158
9.12 Schematic diagram for the SMS model TChiwz. 159
9.13 Acceptance × efficiency for the signal, and 95 C.L. upper limit on the production cross section of the SMS model *TChiWZ* 160
9.14 Schematic diagram for the SMS model TChiZZ. 160
9.15 Acceptance × efficiency for the signal, and 95 C.L. upper limit on the production cross section of the SMS model *TChiZZ* 161

B.1 Invariant mass pair m_{ll} of the two lepton from internal photon conversion on generator level 175

C.1 Single-Muon trigger efficiency as a function of the muon pseudo rapidity η. 179
C.2 Single-Electron trigger efficiency as a function of the electron pseudo rapidity η. . . 180
C.3 Double-Electron trigger efficiency as a function of the leading (second leading) electron pseudo rapidity η. 181
C.4 Double-Muon trigger efficiency as a function of the leading (second leading) muon pseudo rapidity η. 182
C.5 Electron-Muon cross trigger efficiency as a function of η of the electron or muon. . . 183

D.1 E_T^{miss} distribution for events with two tight leptons OS-SF forming an invariant mass consistent with the Z mass and a third loose lepton (e, μ, τ_h) with and without pile up reweighting. 186

H.1 Event display (Rho-Phi) of the interesting 4 lepton (3 electrons and 1 muon) event . . 218
H.2 Event display (Rho-Z) of the interesting 4 lepton (3 electrons and 1 muon) event . . . 218
H.3 Event display (Rho-Phi) of the interesting 4 lepton (2 muons and 2 taus) event 219
H.4 Event display (Rho-Z) of the interesting 4 lepton (2 muons and 2 taus) event 219

List of Tables

2.1 Particle spectrum of the Standard Model 6

3.1 The particle spectrum of the MSSM 22

5.1 Summary of the information of the CMS sub-detectors used in the reconstruction of physics objects 54
5.2 Efficiency for τ_h to pass the HPS and TaNC identification criteria 60

7.1 Summary Muon Selection 89
7.2 Summary Electron Selection 90
7.3 Tau Selection Summary 91
7.4 Summary of the Photon Selection 91
7.5 Summary of the measured ID and ISO efficiency for muons and electrons 92

9.1 Results summed over electron and muon flavors corresponding to an integrated luminosity $L_{int} = 4.7\,fb^{-1}$ recorded in 2011 140
9.2 Results split in electron and muon flavors corresponding to an integrated luminosity $L_{int} = 4.7\,fb^{-1}$ recorded in 2011 145
9.3 The sources and values of systematic uncertainties associated with this analysis . . . 148

A.1 Summary of MC Samples. 167
A.2 List of Data Samples. 168

C.1 Summary Trigger Paths and Efficiency. 178

Acknowledgements

There is no perfect work which can be done without any help.

First, I would like to thank my supervisor Prof. Dr. Wim de Boer for giving me the opportunity to perform my PhD studies as a member of his group. Thank you for always beeing available with solutions and motivations whenever i got stuck.

Many thanks also to Prof. Dr. Günter Quast for co-supervising this thesis.

Special mention for supporting and accompanying me on my way through this dissertation deserves Dr. Martin Niegel and Stefan Wayand, without whom i would have never been able to finish.

I would like to thank also Dr. Fedor Ratnikov for plenty of discussion time and Dr. Valery Zhukov for his patience and guidance since the very beginning of my studies.

Additionally i would like to thank Felix Frensch, Thorsten Serr, Simon Lemaire, Conny Beskidt, Simon Kunz, Markus Weber, Markus Bonsch, Christian Skole, Dr. Eva Ziebarth, Dr. Altan Cakir and Dr. Iris Gebauer for the help with correcting this thesis and the friendly and productive atmosphere in our working group.

Last, but of course not least, I would like to thank my friends, especially Mirjana Spinner, and my family for their help and support.

Hiermit erkläre ich, dass ich die Dissertationsschrift mit dem Titel

Search for Supersymmetry using Multileptonic Signatures in Proton-Proton Collisions with the CMS Detector at the LHC

selbständig und unter ausschliesslicher Verwendung der angegebenen Hilfsmittel angefertigt habe.

Daniel Troendle